Atomistic Simulations of Precipitation Kinetics in Multicomponent Interstitial/Substitutional Alloys

David Bombač

A thesis submitted for the degree of
Doctor of Science

Department of Materials and Metallurgy
Faculty of Natural Sciences and Engineering
University of Ljubljana

Ljubljana, MMXII

Univerza v Ljubljani
Naravoslovnotehniška Fakulteta
Oddelek za materiale in metalurgijo

Atomistične simulacije kinetike izločanja v večkomponentnih zlitinah z atomi legirnih elementov na intersticijskih in/ali substitucijskih mestih kristalne mreže

David Bombač

Predloženo za pridobitev naziva
doktor znanosti

Ljubljana, MMXII

Copyright © 2012 by David Bombač. All rights reserved. No part of this publication may be reproduced, stored in a retrieval system, or transmitted, in any form or by any means, electronic, mechanical, photocopying, recording, or otherwise, without the prior written permission of the publisher. Printed in Slovenia. Typeset using LaTeX.

Per Aspera Ad Astra

✠

To May.

Statement

This dissertation is submitted for the degree of Doctor of Science at the Faculty of Natural Sciences and Engineering, University of Ljubljana. The research described herein was conducted under the mentoring of Assoc. Prof. Dr. Goran Kugler and co-mentoring of Prof. Dr. Radomir Turk in the Department of Materials and Metallurgy, Faculty of Natural Sciences and Engineering, University of Ljubljana, between October 2008 and April 2011.

Part of the research was conducted during visit in the Department of Materials Science and Metallurgy, University of Cambridge under supervision of Professor H. K. D. H. Bhadeshia between May 2009 to September 2009 and July 2010 to November 2010.

Except where acknowledgement and reference are made to previous work, the work is, to the best of my knowledge, original. This dissertation is the result of my own work and includes nothing which is the outcome of work done in collaboration except where specifically indicated in the text.

David Bombač

Mentor: Assoc. Prof. Dr. Goran Kugler

Co mentor: Prof. Dr. Radomir Turk

Acknowledgements

I would like to acknowledge and express my sincere gratitude to my supervisor Associate Professor Dr. Goran Kugler for all his support, guidance, inspiration and encouragement during the work at Chair for Materials Forming, Department of Materials and Metallurgy at University of Ljubljana. I also express my gratitude to the Professor Dr. Radomir Turk under whom my doctoral study started. I would like to thank Professor H. K. D. H. Bhadeshia from the Department of Materials Science and Metallurgy at University of Cambridge who accepted me into Phase Transformations Group where part of my work was conducted. I shall cherish for long the memory of being with the Phase Transformations Group. I earnestly acknowledge financial support from Slovenian Research Agency (ARRS) and Slovene Human Resources Development and Scholarship Fund. I would like to thank to every member of the Department for being kind to me. I thank every member of the Chair for Materials Forming for their help and friendship. All the help from Miha Brojan, Dr. Peter Fajfar, Dr. Milan Terčelj, Dr. Tomaž Rodič, Bostjan Bradaškja, Matevž Fazarinc, Alenka Šalej, Mathew J. Peet, Pei Yan, Javen Chen, Arijit Saha Podder, John Garnham is also gratefully acknowledged. I am sure there are some I may have missed, but they are no less appreciated! Many thanks to all! I am greatly indebted to my parents and family for their support, devotion and understanding.

Abstract

This thesis deals with mechanisms of the precipitates nucleation and growth which are not sufficiently understood in the multicomponent alloys. An atomistic simulation package for computer experiments developed and implemented here, enables study of the diffusive phase transformations at a detailed atomistic spatial scale. A developed atomistic simulations package enables both quantitative and 3D topographical simulations of evolution of microstructure during precipitation in interstitial/substitutional alloys and consequently a better understanding of the precipitation and kinetic pathways. Emphasis is on the formation and decomposition of subcritical nuclei and their role on the nucleation growth, coarsening and coalescence. Within the framework of the study detailed simulations were employed aiming to predict the influence of temperature, chemical composition, asymmetry of interatomic potentials, mixing energies and initial microstructure on evolutions of precipitate fraction and density, volume fractions of chemical elements, precipitate size, shape (moments of inertia), concentration profiles, short range order and pair correlations. First a simple model based on the binary Fe-Cu alloy system with BCC crystal structure was studied in detail. The simulated microstructures closely resemble typical microstructures observed with 3D APT and HRTEM. It was found, that influence of the mixing energy on evolutions of the short range order parameter and number of clusters are similar to influence of the temperature, i.e. increased mixing energy accelerates clustering and consequently the value of short range order parameter. Furthermore, with higher mixing energy clear distinction between growth and coarsening stages was observed. Simulations show that precipitation and kinetic pathways are very sensitive to the asymmetry of interatomic potentials, which was studied through definition of the asymmetry parameters. In the present work new asymmetry model has been

proposed, which beside energies between atoms considers also ghost energies between vacancy and atoms. It was observed that for the negative asymmetry parameters, coarsening by diffusion and direct coagulation of clusters dominated over Ostwald ripening mechanism, while the opposite holds for positive asymmetry parameters or symmetrical model. For long times, the time exponent of the mean radius of clusters obtained from simulations were compared to the prediction of LSW theory. Deviations from this theory were attributed to the influence of clusters mobilities. It was also revealed that negative asymmetry results in increase of required computation time to achieve the same real physical time. This was attributed to the preferred environment where vacancy prefers to reside, i.e. the vacancy trapping effect in Cu rich areas. In order to further elucidate cluster evolution, computer experiments with seeded spherical clusters on the defined positions and slightly supersaturated environment were conducted. The aim was to study evolution of the shape and size of clusters, with different initial sizes during growth stage of precipitation. It was recognized that initial spherical shape changes dramatically over time, which was identified visually as well as quantified by calculation of the moment of inertia tensors for growing clusters. Since in all simulations full periodic boundary conditions were employed, which can cause periodicity effects on the evolving microstructure, influences of the simulation box size on precipitation were assessed. It was found that reliable and repeatable results can be obtained with box size of 40^3 BCC lattices. However, since number of formed precipitates is too small for adequate statistical post-processing, all simulations were performed on larger box sizes.

The simulation package and underlying model parameters were then made more complex by introduction of other substitutional elements to simulate ternary and quaternary alloys with BCC crystal structure. Precipitation and kinetic pathways of ternary Fe-Cu-Mn, Fe-Cu-Ni and quaternary Fe-Cu-Ni-Mn alloys were compared to the binary Fe-Cu alloy. During these simulations, evolution of the short range order parameters and mean cluster sizes were monitored at temperature of 873 K. It was found that addition of Ni and Mn increased incubation time for nucleation and have influence on

the growth rates. The highest and the lowest growth rates were observed when only Ni and only Mn were added, respectively. For quaternary system the growth rate lies between those obtained for ternary systems. In order to study phase separation, the simulations package was upgraded to FCC crystal structure and model for Ni-Cr-Al alloy system. At 873 K two types of γ' phases were recognized, i.e. Ni_3Al and Ni_3Cr, which is in agreement with 3D APT experiments found in literature. Phases exhibit different fractions and evolution kinetics. Fraction of the Ni_3Al is increasing throughout simulations, while fraction of Ni_3Cr is increasing until it reaches maximum and then starts to decrease. Two methods of detection of these two phases were developed. The first is based on calculation of local concentrations around given atoms, while the second searches for exact crystal structure. It was found that these two methods yield different results, which suggest that special care must be put when analysing obtained data either from computer or atom probe experiments. The ability of developed simulation package and underlying model parameters was also tested with coupled substitutional/interstitial diffusion in Fe-C alloy system. Although expected realistic Fe_3C phase cannot be reproduced with the rigid lattice approximation, much faster interstitial diffusion and slower substitutional diffusion were correctly reproduced. Pair correlation functions for this example were calculated for initial disordered and two later states. It identified that carbon pairs form bonds on the third nearest neighbour, which is an expected results according to the selected interaction energies.

Keywords:
statistical mechanics, atomistic Monte Carlo methods, rigid lattice approximation, diffusional phase transformations, precipitation

PACS numbers: 68.43.De, 05.10.Ln, 81.30.Mh, 66.30.Lw, 64.70.kd

Contents

Contents ix

List of Figures xiii

List of Tables xxiii

Nomenclature and abbreviations xxv

1 Introduction 1
- 1.1 Definition of the research problem . . . 1
- 1.2 Scope, aim and outline of the thesis . . . 3

2 Nucleation theory 7
- 2.1 Classical Nucleation Theory . . . 8
  - 2.1.1 Homogeneous Nucleation . . . 10
  - 2.1.2 Heterogeneous Nucleation . . . 12
  - 2.1.3 Rate of Nucleation . . . 15
- 2.2 Atomic Jumps and Diffusion . . . 18
  - 2.2.1 Vacancy diffusion . . . 22
  - 2.2.2 Interstitial diffusion . . . 23
  - 2.2.3 Tracer diffusion and Self-diffusion . . . 23
- 2.3 Growth and Coarsening . . . 24
  - 2.3.1 Diffusion-Controlled Growth . . . 26
    - 2.3.1.1 Zener model for diffusion controlled growth . . . 26
    - 2.3.1.2 Gibbs-Thomson effect . . . 28
  - 2.3.2 Coarsening . . . 29
    - 2.3.2.1 The Lifshitz-Slyozov-Wagner theory . . . 30
- 2.4 Clusters . . . 32
  - 2.4.1 Cluster analysis . . . 33
    - 2.4.1.1 Cluster size distribution . . . 34
    - 2.4.1.2 Mean cluster size . . . 34
    - 2.4.1.3 Pair Correlation Function . . . 34

2.4.1.4 Short Range Order 36
2.4.1.5 Moment of inertia 37
2.5 Beyond classical theories 37
2.5.1 Computational metallurgy 38
2.5.1.1 Monte Carlo methods 39
2.5.1.2 Cluster Dynamics 39
2.5.2 Phase Field Models 41

3 Statistical Mechanics and Monte Carlo methods 43
3.1 Statistical mechanics 43
3.1.1 Entropy 46
3.1.2 Statistical ensembles and partition function 47
3.1.2.1 General statistical ensembles 48
3.1.2.2 Canonical ensemble 48
3.1.2.3 Partition function 50
3.1.3 Ising Model 51
3.2 Boundary Conditions 52
3.3 Monte Carlo methods 52
3.3.1 Monte Carlo integration 53
3.3.2 Importance sampling 55
3.4 Markov Master Equation 55
3.5 Monte Carlo methods in statistical physics 56
3.5.1 Metropolis Monte Carlo algorithm 57
3.5.2 Glauber and Kawasaki Dynamics 59
3.5.3 Thermally activated processes 59
3.6 Kinetic Monte Carlo method 60

4 Diffusion kinetic Monte Carlo model 65
4.1 Crystal lattice 65
4.1.1 Rigid lattice 67
4.1.2 Lattice size 67
4.2 Transition probabilities models 68
4.3 Vacancy concentration and time adjustment 73
4.3.1 Vacancy concentration 73

4.3.2 Physical time 74
4.4 Random number generator 75
4.5 Complexity of the model used in this work 76

5 Clustering in binary Fe-Cu alloy 77
5.1 Parametrization of the simulation model 79
5.1.1 Model Asymmetry 83
5.2 Analysis of obtained atomic configurations 84
5.2.1 Identification and analysis of the clusters 84
5.2.1.1 Identification with average concentrations 84
5.2.1.2 Identification with neighbouring atoms 85
5.3 Results of the kMC simulations in the binary Fe-Cu system 85
5.3.1 Influence of the simulation box size 85
5.3.2 Influence of the temperature and chemical composition 88
5.3.3 Influence of the mixing energy 98
5.3.4 Influence of the model asymmetry 102
5.3.5 Evolution of seeded clusters 108
5.3.6 Evolution of microstructure with initial conditions previously annealed at high temperature 119

6 Clustering in the ternary Fe-Cu-Ni and Fe-Cu-Mn and in the quaternary Fe-Cu-Ni-Mn alloys 121
6.1 Model parametrization 121
6.2 Results 124

7 The phase separation in Ni-Cr-Al alloy 139
7.1 Model parametrization 140
7.2 Results 141

8 The simulation of coupled interstitial/substitutional diffusion in Fe-C alloy 149
8.1 Model parametrization 149
8.2 Results 152

9 Conclusions 157

A Description of the developed kMC code **161**

B Extended summary in Slovene (Povzetek v slovenskem jeziku) **165**

References **173**

List of Figures

2.1 Phase diagram for binary AB alloy and nucleation of β phase inside α matrix. 9

2.2 Schematic representation of solid-solid precipitates; a) an incoherent precipitate, b) a semicoherent precipitate, c) a coherent particle, and c) a fully coherent particle, [49]. 11

2.3 The activation energy barrier ΔG* and the critical nucleus size r* according to classical nucleation theory based on heterophase fluctuations, [50]. 12

2.4 The critical nucleus size for heterogeneous nucleation. 13

2.5 The free energy change needed for homogeneous (ΔG_{hom}) and heterogeneous (ΔG_{het}) nucleation, [50]. 14

2.6 Dependence of $\Delta G_{\mathrm{hom}}/\Delta G_{\mathrm{het}}$ on $\cos\theta$ for various heterogeneous nucleation sites, [51]. 15

2.7 Flow of monomers to form dimers, trimers, tetramers, pentamers and finally critical sized clusters consisting of n particles, where f_n is attachment frequency and g_n is detachment frequency of monomers to n sized cluster. 15

2.8 Schematic representation of the radius $r^*_{k_{\mathrm{B}}T}$, at which stable precipitates nucleate in the graph of the free energy change needed associated with nucleation. 18

2.9 Proposed solid-state diffusion mechanisms; a) direct interchange mechanism, b) Zener ring mechanism, c) vacancy diffusion mechanism and d) interstitial diffusion. 19

2.10 An atom jump in a crystalline solid from an initial configuration i (1) to a final configuration j (3), through a saddle point position (2). 21

2.11 The energy barrier associated with the growth of a precipitate in the solid state. 25

2.12 Schematic representation of concentration profile at an α/β interface for; a) diffusion–controlled interface, b) interface–controlled interface and c) mixed interface. 25
2.13 Schematic representation of the; a) concentration field in the matrix surrounding a precipitate with radius R, b) simplification of the same concentration field profile. 26
2.14 Gibbs-Thomson effect shown in free energy curves at temperature T, [50]. 28
2.15 Schematic presentation of the coarsening or Ostwald ripening on droplets in two dimensions. 29
2.16 Schematic presentation of pair correlation function in binary solution. . 35
2.17 Time and dimension scales achieved using various atomistic methods . . 38

3.1 Two dimensional periodic conditions system. 52
3.2 Schematic representation of MC integration method to determine grey area. 54
3.3 Schematic representation of migration barrier energy for broken bond model. 63
3.4 Flow chart of kinetic Monte Carlo simulation 64
3.5 Schematic representation of step 5 for process with 8 possible events, e.g. diffusion in BCC lattice. 64

4.1 Simple cubic crystal structure with substitutional and interstitial atoms; a) body centred cubic (BCC) crystal and b) face centred cubic (FCC) crystal. 65
4.2 Schematic representation of migration barrier energy for broken bond model. 70
4.3 Schematic representation of migration barrier energy for kinetic Ising barrier energy model. 71

5.1 Equilibrium phase diagram of Fe-Cu alloys, [1]. Dashed line represents metastable miscibility gap of liquids. 77
5.2 HREM micrograph of Cu precipitate; a) twinned 9R structure, [158] and b) structure partially transformed to FCC structure, [161]. 78

5.3 Schematic representation of the interaction energies in BCC crystal lattice; a) only X atoms on first $\epsilon^{(1)}_{\mathrm{XX}}$ and second $\epsilon^{(2)}_{\mathrm{XX}}$ nearest neighbour shells and b) mixed X and Y atoms on first and second nearest neighbour shells. 80

5.4 Influence of the simulation box size on the evolution of number density of clusters larger than $n > 2$. 86

5.5 Evolution of the short range order parameter $\alpha^{1}_{\mathrm{CuCu}}$ at various simulation box sizes. 87

5.6 Influence of the simulation box size on the time evolution of the average cluster size. 88

5.7 Snapshots of Fe-Cu alloy with 1 at.% Cu, obtained from kMC simulations during annealing at 923 K. Size of the simulation box is 80^3 BCC lattices (23^3 nm) and only Cu atoms are displayed due to visibility reasons; a) initial disordered configuration, b) at 4.5 s, c) at 15 s, d) at 30 s, e) at 90 s, f) at 227 s. 90

5.8 Snapshots of Fe-Cu alloy with 1 at.% Cu, obtained from kMC simulations during annealing at 873 K. Size of the simulation box is 80^3 BCC lattices (23^3 nm) and only Cu atoms are displayed due to visibility reasons; a) initial disordered configuration, b) at 9 s, c) at 26 s, d) at 44 s, e) at 87 s, f) at 850 s. 91

5.9 Snapshots of Fe-Cu alloy with 1.5 at.% Cu, obtained from kMC simulations during annealing at 873 K. Size of the simulation box is 80^3 BCC lattices (23^3 nm) and only Cu atoms are displayed due to visibility reasons; a) initial disordered configuration, b) at 8 s, c) at 24 s, d) at 40 s, e) at 79 s, f) at 790 s. 92

5.10 Snapshots of Fe-Cu alloy with 1 at.% Cu, obtained from kMC simulations during annealing at 773 K. Size of the simulation box is 80^3 BCC lattices (23^3 nm) and only Cu atoms are displayed due to visibility reasons; a) initial disordered configuration, b) at 181 s, c) at 596 s, d) at 2780 s, e) at 5431 s, f) at 53092 s. 93

5.11 Snapshots of Fe-Cu alloy with 1 at.% Cu, obtained from kMC simulations during annealing at 673 K. Size of the simulation box is 80^3 BCC lattices (23^3 nm) and only Cu atoms are displayed due to visibility reasons; a) initial disordered configuration, b) at 28345 s, c) at 358598 s, d) at 1.1×10^6 s, e) at 2.2×10^6 s, f) at 9.6×10^6 s. 94
5.12 Evolution of the short range order parameter in Fe-Cu alloys at different temperatures and various chemical compositions. 95
5.13 Time evolution of Cu concentration in the matrix at different temperatures and various chemical compositions. 96
5.14 Number of clusters, including dimers in Fe-Cu alloys at different conditions. 96
5.15 Evolution of the average cluster size in time for simulated conditions in Fe-Cu alloys. 98
5.16 Snapshots of Fe-Cu alloy with 1 at.% Cu, obtained from kMC simulations during annealing at 873 K and increased mixing energy. Size of the simulation box is 80^3 BCC lattices (23^3 nm) and only Cu atoms are displayed due to visibility reasons; a) initial disordered configuration, b) at 1.7 s, c) at 7.9 s, d) at 73 s, e) at 289 s, f) at 724 s. 99
5.17 Influence of mixing energy on the evolution of the short range order parameter. 100
5.18 Influence of mixing energy on number of clusters in time. 101
5.19 Influence of mixing energy on evolution of the average cluster size in time. 101
5.20 Influence on the real time for asymmetry parameter $a* = -1$, with and without vacancy trapping adjustment. 105
5.21 Influence of the asymmetry parameter $a*$ on the evolution of the SRO parameter α^1_{CuCu}. 106
5.22 Influence of the asymmetry parameter $a*$ on the average cluster size evolution in time. 106
5.23 Influence the asymmetry parameter $a*$ on the number of clusters larger than pentamers. 107

5.24 Snapshots of cluster evolution with seeded clusters of various dimensions in Fe-Cu alloy, obtained during annealing at 873 K. Size of the simulation box is 50^3 BCC lattices (14.35^3 nm) and only Cu atoms are displayed due to visibility reasons; a) initial configuration R=2, b) at 88.3 s, c) at 439 s, d) initial configuration R=2.5, e) at 84.6 s, f) at 423 s, g) initial configuration R=3, h) at 80 s, i) at 400 s, j) initial configuration R=3.5, k) at 77.8 s, l) at 388 s. 109

5.25 Evolution of the average cluster size for various initial sizes of seeded clusters. 110

5.26 Size of clusters in time for seeded clusters with starting radius size R=2 lattice sites. 111

5.27 a) Moment of inertia evolution in time, b) clusters centre of mass deviation from seed position in time; for seeded clusters with starting radius size 2 lattice sites. 111

5.28 Evolution of seeded cluster P2 with initial radius 2 lattice sites and its components of moment of inertia tensor in time at a) initial configuration with 66 Cu atoms and eigenvalues (2213.87, 2196.79, 2097.23), b) at 176.2 s with 404 Cu atoms and eigenvalues (52008.3, 47038.2, 42883.1), c) at 439 s with 583 Cu atoms and eigenvalues (96062.6, 90184.7, 75491). 112

5.29 Size of clusters in time for seeded clusters with starting radius size R=2.5 lattice sites. 113

5.30 a) Moment of inertia evolution in time, b) clusters centre of mass deviation from seed position in time; for seeded clusters with starting radius size 2.5 lattice sites. 114

5.31 Evolution of seeded cluster P3 with initial radius 2.5 lattice sites and its components of the moment of inertia tensor in time at a) initial configuration with 140 Cu atoms and eigenvalues (7921.07, 7801.8, 7479.45), b) at 169 s with 428 Cu atoms and eigenvalues (54891.2, 52377.6, 47256.1), c) at 423 s with 762 Cu atoms and eigenvalues (145193, 134421, 122176). 114

5.32 Snapshots seeded cluster P8 with initial radius R=2.5 lattice sites a) differently coloured superposition b)-k), b) initial configuration (137 atoms), c) at 42.2 s (182 atoms), d) at 84.6 s (187 atoms), e) at 126.8 s (216 atoms), f) at 169 s (217 atoms), g) at 211.2 s (214 atoms), h) at 253.5 s (263 atoms), i) at 296 s (287 atoms), j) at 338.2 s (323 atoms), k) at 380.5 s (294 atoms), l) at 423 s (287 atoms). 115

5.33 Concentration around seeded clusters with starting radius size 2.5 lattice sites at various times and following initial seed center coordinates; a) P1, b) P2, c) P3, d) P4, e) P5, f) P6, g) P7, h) P8. 116

5.34 Size of clusters in time for seeded clusters with starting radius size R=3 lattice sites. 117

5.35 a) Moment of inertia evolution in time, b) clusters centre of mass deviation from seed position in time; for seeded clusters with starting radius size 3 lattice sites. 117

5.36 Evolution of seeded cluster P7 with initial radius 3 lattice sites and its components of moment of inertia tensor in time at a) initial configuration with 259 Cu atoms and eigenvalues (21355.6, 21355.6, 21355.6), b) at 159.9 s with 459 Cu atoms and eigenvalues (60567.4, 56659.7, 54812.8), c) at 400.2 s with 670 Cu atoms and eigenvalues (122955, 110917, 94401.7).118

5.37 Evolution of the SRO parameter for random and previously annealed initial conditions in Fe-Cu alloys with 1 at.% Cu isothermally treated at 873 K. 119

5.38 Evolution of the average cluster size for random and previously annealed initial conditions in Fe-Cu alloys with 1 at.% Cu isothermally treated at 873 K. 120

6.1 Snapshots of clusters in Fe-Cu-Mn alloy with 1 at.% Cu and 1 at.% Mn, obtained from kMC simulations during annealing at 873 K. Size of the simulation box is 80^3 BCC lattices (23^3 nm), Cu atoms are orange and Mn are blue. Fe atoms are not shown due to visibility reasons; a) initial disordered configuration, b) at 66.5 s, c) at 133.2 s, d) at 334.7 s, e) at 1356 s, f) at 2720 s. 125

6.2 Snapshots of individual atom group clusters from kMC simulations during isothermal treatment at 873 K for Fe-Cu-Mn alloy with 1 at.% Cu and 1 at.% Mn. Size of the simulation box is 80^3 BCC lattices (23^3 nm), Cu atoms are orange and Mn atoms are blue; a)-c) at 66.5 s, d)-e) at 133.2 s, f)-h) at 334.7 s, i)-k) at 1356 s, l)-m at 2720 s. 126
6.3 Evolution of the short range order parameters in Fe-Cu-Mn alloy with 1 at.% Cu and 1 at.% Mn at 873 K. Dashed line presents evolution of the short range order parameter in binary Fe-Cu alloy at same conditions. . 127
6.4 Evolution of the average cluster size in time for Fe-Cu-Mn alloy isothermally annealed at 873 K. 128
6.5 Snapshots from kMC simulations of Fe-Cu-Ni alloy with 1 at.% Cu and 1 at.% Ni, obtained from kMC simulations during annealing at 873 K. Size of the simulation box is 80^3 BCC lattices (23^3 nm), Cu atoms are orange and Ni atoms are green. Fe atoms are not shown due to visibility reasons; a) initial disordered configuration, b) at 67.9 s, c) at 244.5 s, d) at 680.7 s, e) at 1368 s, f) at 2743 s. 130
6.6 Snapshots of individual atom group clusters from kMC simulations during isothermal treatment at 873 K for Fe-Cu-Ni alloy with 1 at.% Cu and 1 at.% Ni. Size of the simulation box is 80^3 BCC lattices (23^3 nm), Cu atoms are orange and Ni atoms are green; a)-c) at 67.9 s, d)-e) at 244.5 s, f)-h) at 680.7 s, i)-k) at 1368 s, l)-m at 2743 s. 131
6.7 Evolution of the short range order parameter in Fe-Cu-Ni alloy with 1 at.% Cu and 1 at.% Ni at 873 K. Dashed line presents evolution of the short range order parameter in binary Fe-Cu alloy at same conditions. . 132
6.8 Evolution of the average cluster size in time for Fe-Cu-Ni alloy isothermally annealed at 873 K. 132
6.9 Snapshots of precipitation in Fe-Cu-Ni-Mn alloy with 1 at.% Cu, 1 at.% Ni and 1 at.% Mn, obtained from kMC simulations during isothermal treatment at 873 K. Size of the simulation box is 80^3 BCC lattices (23^3 nm), Cu atoms are orange, Ni atoms are blue and Mn atoms are red, Fe atoms are not shown due to visibility reasons; a) initial disordered configuration, b) at 80.7 s, c) at 134.7 s, d) at 202 s, e) at 476 s, f) at 2623 s. 133

6.10 Snapshots of individual atom group clusters from kMC simulations during isothermal treatment at 873 K for Fe-Cu-Ni-Mn alloy with 1 at.% Cu, 1 at.% Ni and 1 at.% Mn. Size of the simulation box is 80^3 BCC lattices (23^3 nm), Cu atoms are orange, Ni atoms are blue and Mn atoms are red; a)-d) at 80.7 s, e)-h) at 134.7 s, i)-l) at 202 s, m)-p) at 476 s, q)-u) at 2623 s. 134

6.11 Evolution of the short range order parameter in Fe-Cu-Ni-Mn alloy with 1 at.% Cu, 1 at.% Ni and 1 at.% Mn at 873 K. Dashed line presents evolution of the short range order parameter in binary Fe-Cu alloy at same conditions. 135

6.12 Evolution of the average cluster size in time for Fe-Cu-Ni-Mn alloy isothermally annealed at 873 K. 135

6.13 Evolution of the short range order parameter α^1_{CuCu} in time for Fe-Cu-Ni, Fe-Cu-Mn and Fe-Cu-Ni-Mn alloy systems. Dashed line presents evolution of the short range order parameter in binary Fe-Cu alloy at same conditions. 136

6.14 Evolution of the average cluster size in time for Fe-Cu-Ni, Fe-Cu-Mn and Fe-Cu-Ni-Mn alloy systems. 136

7.1 Ni part of equilibrium ternary phase diagram of Ni-Cr-Al alloy at 873 K, [179]. 139

7.2 Schematic presentation of Ni_3Al with $L1_2$ crystallographic structure. . . 140

7.3 Snapshots of isothermally treated Ni-Cr-Al alloy with 15.2 at% Cr, 5.2 at% Al, at 873 K obtained from kMC simulations. Due to visibility reasons only Cr (blue) and Al (red) atoms are displayed; a) initial disordered configuration, b) at 0.04 s, c) at 0.18 s, d) at 0.28 s, e) at 0.39 s, f) at 0.49 s. 142

7.4 Time evolution of the amount of Ni_3Al and Ni_3Cr precipitates. 143

7.5 Snapshots of obtained Ni_3Al precipitates in isothermally treated Ni-Cr-Al alloy with 15.2 at% Cr, 5.2 at% Al, at 873 K. Al atoms are red and Ni atoms are silver; a) at 0.18 s, b) at 0.28 s, c) at 0.39 s, d) at 0.49 s. . 144

7.6 Snapshots of obtained Ni_3Cr precipitates in isothermally treated Ni-Cr-Al alloy with 15.2 at% Cr, 5.2 at% Al, at 873 K. Cr atoms are blue and Ni atoms are silver; a) at 0.18 s, b) at 0.28 s, c) at 0.39 s, d) at 0.49 s. . 145
7.7 Snapshots of obtained γ' precipitates using threshold concentration around Ni atoms in isothermally treated Ni-Cr-Al alloy with 15.2 at% Cr, 5.2 at% Al, at 873 K. Cr atoms are blue, Al atoms are red and Ni atoms are silver; a) at 0.18 s, b) at 0.28 s, c) at 0.39 s, d) at 0.49 s. 146
7.8 Evolution of the short range order parameter in Ni-Cr-Al alloy at 873 K for homoatomic combinations. 147
7.9 Evolution of the short range order parameter in Ni-Cr-Al alloy at 873 K for heteroatomic combinations. 147

8.1 The Fe-C phase diagram, [191]. 150
8.2 Schematic presentation of Fe_3C structure on the simple cubic lattice. Three variants, a), b), and c) are possible, with C atoms occupying various interstitial positions. 151
8.3 Snapshots of Fe-C alloy with 1 at.% C, obtained from kMC simulations during annealing at 873 K. Size of the simulation box is 32^3 BCC lattices (9.2^3 nm), only C atoms are displayed due to visibility reasons; a) initial disordered configuration, b) at 0.9 s, c) at 2 s. 152
8.4 Carbon-carbon pair correlation function of initial disordered state. . . . 153
8.5 Snapshots of FeC precipitates in Fe-C alloy with 1 at.% C, obtained from kMC simulations during annealing at 873 K; a) at 0.9 s, b) at 2 s. . . . 153
8.6 Carbon-carbon pair correlation function at 0.9 s. 154
8.7 Carbon-carbon pair correlation function at 2 s. 154

A.1 Flowchart of the developed kMC simulation software 162

List of Tables

3.1 Summary of microcanonical, canonical and grand canonical ensembles . 48

4.1 Unit vectors of the first nearest substitutional neighbours in the BCC and FCC lattices. 66
4.2 Unit vectors of the second nearest substitutional neighbours in the BCC and FCC lattices. 66

5.1 Material properties of Fe and Cu used for calculation of interaction energies and kinetic parameters. 79
5.2 Calculated interaction energies and kinetic parameters for binary FeCu alloy used in kMC simulations. 82
5.3 Various simulation box sizes used to investigate size effects. 86
5.4 The equilibrium matrix concentrations at various temperatures for different mixing energies. 89
5.5 Number of cluster at the initial disordered state ($t = 0$ s) for various temperature and chemical compositions. 97
5.6 Simulation parameters with mixing energy $E_{\text{mixFeCu}} = -0.60$ eV. 98
5.7 Simulation parameters with asymmetry parameter $a* = 45.27$. 102
5.8 Simulation parameters with asymmetry parameter $a* = -2.5$. 104
5.9 Simulation parameters with asymmetry parameter $a* = -1$. 104
5.10 Simulation parameters with asymmetry parameter $a* = 0.25$. 104
5.11 Simulation parameters with asymmetry parameter $a* = 0.5$. 104
5.12 Coordinates of seeded clusters centre in lattice constants, used for subsequent analysis. 108
5.13 Number of cluster obtained from isothermal annealing at 1123 K. 119

6.1 Material properties of Fe, Cu, Ni and Mn used for calculation of interaction energies and kinetic parameters. 122
6.2 Calculated simulations parameters used in ternary and quaternary alloy systems. 123
6.3 Possible asymmetry parameters $c*$ for simulated alloy systems. 124

6.4 Chemical compositions in at.% used in kMC simulations. 124
6.5 Values of exponent x for growth stage according to the $L^2(t) \propto t^x$, with average cluster size expressed as radii. 137

7.1 Simulation parameters used for kMC simulations in NiCrAl alloy 141

8.1 Interaction energies and kinetic parameters used for the kMC simulations of Fe-C alloy. 151

Nomenclature and abbreviations

a	Lattice parameter
h	Planck constant ($6.62606957(29) \times 10^{-34}$ eVs)
k_B	Boltzmann constant ($8.617343(15) \times 10^{-5}\ \mathrm{eV\,K^{-1}}$)
c	Concentration
D	Diffusivity
D_0	Diffusion coefficient
E_coh	Cohesive energy
E_mig	Migration energy
e_SP	Saddle point binding energy or energy of the bonds created in the saddle point configuration
$E_{\mathrm{V}_\mathrm{for}}$	Vacancy formation energy
$E_{\mathrm{V}_\mathrm{mig}}$	Vacancy migration energy
E_mixXY	Mixing energy between X and Y atoms
G	Gibbs free energy
$\mathcal{H}$	Hamiltonian of the system
H	Enthalpy
J	Atomic flux
M	Onsager mobility matrix
p	Pressure
Q	Activation energy
R	Gas constant

r	Precipitate radius
r^*	Critical precipitate radius
S	Entropy
t	Time
T	Temperature
ΔT	Supercooling
t_{MC}	Monte Carlo time
V	Volume
$c_{\mathrm{V}_{\mathrm{real}}}$	Real vacancy concentration in the alloy
$c_{\mathrm{V}_{\mathrm{sim}}}$	Vacancy concentration in the simulation
X_i	Solute mole fraction of component i
Z	Zeldovich factor
ϵ^i_{XY}	Chemical binding energy between X and Y atoms, at i-th nearest neighbour.
ϵ^i_{XV}	Chemical binding energy between X atom and vacancy, at i-th nearest neighbour.
α	Ferrite
$\beta = \frac{1}{k_{\mathrm{B}}T}$	Boltzmann factor
δ	Delta function
ε	Misfit strain
γ	Austenite
$\gamma_{\alpha\alpha}$	Specific interfacial energy on α/α boundary
μ	Shear modulus

μ_i	Chemical potential
ρ	Average density
Γ	Transition probability
2D	Two dimensional
3D	Three dimensional
BCC	Body centred cubic
d	Dimensionality
DFT	Density Functional Theory
EAM	Embedded Atom Method
FCC	Face centred cubic
kMC	kinetic Monte Carlo
MC	Monte Carlo
MD	Molecular Dynamics
MMC	Metropolis Monte Carlo
PBC	Periodic Boundary Conditions
SPEM	Saddle Point Energy Model
SPEM2	Saddle Point Energy Model 2
Z	Coordination number

A fact is a simple statement that everyone believes. It is innocent, unless found guilty. A hypothesis is a novel suggestion that no one wants to believe. It is guilty, until found effective.

Edward Teller (1908-2003)

1

Introduction

1.1 Definition of the research problem

Breakthroughs and advances in materials science are closely connected to the basic research to interpret meso-, micro- and nano-scopic mechanisms. Basic research facilitates the prediction of results for proposed models, which are later validated through experimental observations. Usually experimental validation becomes more complex with decreased scale of observation. Many physical properties of metals depend on defects and their concentration in the crystal. The simplest defects are point defects i.e. self interstitials and vacancies. The formation energies of these types of defects are of the order of electron volts and vacancies also have low equilibrium concentrations. The movement of point defects is governed by diffusion; substitutional for vacancies and interstitial for interstices. Additional properties of alloys can depend on precipitation of various phases. For example, pure iron exhibits three transformations during cooling from the melting point of 1538 °C. It transforms from liquid to solid δ-Fe with body centred cubic (BCC) crystal structure at 1535 °C. At 1403 °C it undergoes solid-state transformation to face centred cubic (FCC) crystal structure (γ-Fe). Pure iron then finally transforms from γ-Fe to α-Fe with BCC crstal structure at 910 °C [1]. Alloy of iron and carbon is known as steel. To obtain desired properties also other elements are added to obtain special steels. Their strength and toughness varies with the changes and constituents of the microstructure, i.e. size and shape of contained phases and on the detailed arrangements of the atoms in them. Almost all steels rely on the transformation between austenite and ferrite for obtaining the desired microstructure. Furthermore, the mechanical properties of steels can depend on carbides, nitrides, carbonitrides,…, precipitated from austenite at high temperatures and from ferrite at lower temperatures. With addition of Nb, V or Ti in low carbon steels, e.g. like high strength low alloy (HSLA) steels one can increase yield strength. With addition of these elements kinetics of carbide precipitation and recrystallization can be altered. Alloys where precipitation is also very important are aluminium alloys with addition of Cu (series 2xxx) and with addition of Mg, Si and Zn (series 6xxx and 7xxx). These have complex formation and decomposition of metastable phases dependent on temperature, time and chemical composition. In the past these alloys were extensively studied experimentally and theoretically. Huge steps forward in understanding of precipitation mechanisms accompanied the development of modern experimental techniques, such as scanning electron microscopy (SEM), transmission electron microscopy (TEM), X-ray diffraction (XRD), 3D atom probe tomography (3DAPT), etc.

Study of precipitation and its kinetics from oversaturated metastable solid solution can be divided in three regimes: *(i)* nucleation, *(ii)* diffusional controlled growth of clusters and *(iii)* clusters coarsening (Ostwald ripening) and coalescence where larger clusters grow on expense of smaller ones because of decrease of a system total surface energy. In reality those three idealized regimes often overlap which consequentially make it difficult to interpret obtained results. A better understanding of the precipitation and its kinetics presents a real theoretical challenge. In particular, much more remains to be done to gain a more accurate knowledge of precipitation and a better understanding of the parameters governing the composition, size and density of precipitates. Phase transformations can be solved analytically for binary solutions up to 2D square lattice by Ising model assuming only first nearest neighbours. It is known that models based on classical nucleation theory with suitable parameter selection can satisfactory describe time evolution of the number and size of the precipitates in regimes where they grow and coarsen. These simplified models necessarily contain questionable assumptions, for example, that the precipitates are spherical and stoichiometric, or that surface energies are independent of temperature and size of the precipitates, etc. Current models account only for the growth of the precipitates with size over a critical threshold whilst ignoring unstable clusters with subcritical size. Even in unsaturated solid solutions some kind of a stationary distribution exists and has influence on the kinetic pathways. At higher temperatures and/or low surface energies these unstable subcritical clusters could significantly influence the concentration of solute atoms in alloys and consequently have an influence on the nucleation, growth and coarsening of the precipitates and kinetic pathways. On the other hand, computer aided atomistic simulations explicitly consider diffusion of particular atoms and do not need the simplifications and assumptions mentioned above. Temperature, time and chemical composition dependent atomistic simulations of the precipitation, contribute considerably to a better comprehension of nucleation of the nuclei and their subsequent growth and coarsening. High power computers have become more accessible as hardware costs fall and computing power increases. That makes atomistic simulations an excellent tool as their predictive capability is helpful with the design of alloys, especially for systems studied at extreme conditions (e.g. extreme pressures, temperatures, dangerous elements, etc.) where experimental work is difficult and expensive or impossible.

1.2 Scope, aim and outline of the thesis

Mechanisms of the precipitate nucleation and growth are not sufficiently understood in the multicomponent interstitial/substitutional alloys. Within the scope of the thesis, an atomistic simulation package has been developed and implemented to enable studies at a detailed atomistic, spatial scale of the diffusion processes. These processes lead to the nucleation, growth, coarsening and coalescence of precipitates. A developed atomistic simulation package enables a better understanding of the nucleation physics. Emphasis is on formation and decomposition of subcritical nuclei and their role on the nucleation. Furthermore, it enables more accurate forecasting of the nucleation kinetics, dependent on the temperature, time and chemical composition.

Dynamic and kinetic development of molecular (atomic) systems using computational materials science is the main focus of the thesis. Atomistic modeling and simulations have their roots in molecular dynamics (MD) simulations developed within theoretical physics in the late 1950s and early 1960s [2, 3]. In MD simulation, atoms and molecules are allowed to interact for a period of time by approximations of classical physics (Newton's laws of motion) and the simulation is totally deterministic. The potential energy of all systems is calculated using force fields. MD is limited to small time increments due to lattice thermal vibrations, as the method follows trajectories of all particles. This means integration step dt is very small, somewhere in the range of approximately 10^{-15} s. On contemporary high performance computer clusters, MD simulations can achieve time scales up to milliseconds in reasonable simulation times. In the next development stage, electronic structure calculation methods were developed to achieve an even more accurate result. They are based on solving an equation that describes how the quantum state of a physical system changes in time, based on approximation of the Schrödinger equation, formulated in 1926 [4]. Today many computer methodologies exists which solve the Schrödinger equation. These are often called *ab-initio* or first principles methods, with Density Functional Theory (DFT) being mostly used in materials science since the 1970s. Conceptual roots of DFT are based on the Thomas-Fermi model, which is a statistical model used to approximate the distribution of electrons in an atom, [5, 6], but it was put on a firm theoretical foundation with the Hohenberg-Kohn theorems, which reduce the many-body problem of N electrons with $3N$ spatial coordinates to 3 spatial coordinates with the electron density functionals and defines an energy functional for the system and proves that the correct ground state electron density minimizes energy functional, [7] and Kohn–Sham equations, where intractable many-body problem of interacting electrons in a static external potential is reduced to a tractable problem of non-interacting electrons moving in an effective potential, [8]. Despite gaining in accuracy, due to electronic structure calculation the biggest downside of first principles methods is their huge computational power demand. In order to increase time scale, a combined approach using both first principles and MD was proposed in 1985 [9], where electronic behaviour is obtained from first principles and later used in MD to achieve greater sizes and times. To achieve even longer times in order to study diffusional processes which are the scope of the thesis, more averaged methods are needed. The atomistic simulation methods used to extend length and time scales are the group of Monte Carlo (MC) methods used in materials science first in late 1940s and early 1950s to solve thermodynamic state equations [10, 11]. Particular MC method used in this thesis is the kinetic Monte Carlo method (kMC), where development of the system can be simulated in real time. Atomistic kMC simulations are much more appropriate for the study of nucleation and kinetic pathways, as the kMC method does not follow exact thermal excitation trajectories but only diffusional hops from state to state. This allows for greater simulation times which are important for the study of nucleation and kinetic pathways in real alloys [12–38]. The main scope of the thesis is therefore the use of the kMC method for detailed study of nucleation, growth, coarsening and coalescence of precipitates. Particular emphasis is put on the formation and dissolution of unstable clusters with subcritical dimensions and their effect on the nucleation and kinetic pathways, which can not be described by classical nucleation theory.

A brief outline and organization of the thesis in chronological order is laid out in the next chapter. In this second chapter a review of classical nucleation theory and diffusion in crystals is presented. Chapter 3 provides an introduction to statistical mechanics and a historical overview of Monte Carlo methods with emphasis on the kinetic Monte Carlo method. In the fourth chapter, an atomistic kinetic Monte Carlo model is constructed for rigid lattice substitutional/interstitial systems. This model represents BCC and FCC crystal structures and is intended to describe the thermodynamical behaviour and kinetics of the simulated system. Chapter 4 also reviews various possible parametrizations for kinetic Monte Carlo simulations. In Chapter 5, the Fe-Cu alloy system is addressed and its parametrization is described. The Fe-Cu alloy system is simple binary model and serves as starting point. It was extensively studied theoretically, experimentally and by computer simulations which enables comparison of obtained results and addressing issues that were not given any attention previously. Correct representation of intra-atomic and inter-atomic interactions are required for accurate simulations. In this chapter results of few simulations, performed at different conditions, which focuses on the precipitation kinetics are shown together with a comparison and assessment of experimental data from literature. Also a detailed analysis of obtained results is presented. In chapter 6 the simple binary model is made more complex and focuses on the ternary Fe-Cu-Ni and Fe-Cu-Mn, and quaternary Fe-Cu-Ni-Mn alloys. Similar to the chapter 5, first focus is placed on the parametrization of the fore mentioned systems and then to the detailed analysis of obtained results. Chapters 7 and 8 provide kMC simulations of a Ni-Cr-Al alloy with FCC structure and Fe-C alloy with BCC structure and octahedral interstitials, respectively. Chapter 9 summarizes the thesis by discussing the overall contribution of the research. Additionally, limitations of the approach and general ideas to the future research directions are discussed. Finally, Appendix A provides an overview of kMC simulation package, whilst Appendix B provides extended summary in the Slovene.

A scientific truth does not triumph by convincing its opponents and making them see the light, but rather because its opponents eventually die and a new generation grows up that is familiar with it.

Max Planck (1858-1947)

2

Nucleation theory

Phase transformations play an important role in a wide variety of physical process occurring in nature. Their better understanding helps us to predict behaviour and kinetic development of materials especially in solid state conditions. In 1876, J. W. Gibbs published *On the Equilibrium of Heterogeneous Substances*, [39] where he proposed that growth of a new phase from an existing phase is commenced by a formation of a smallest stable cluster of the new phase, which then spontaneously grows. The formation of these smallest stable cluster or critical nuclei is known as nucleation. Phase transition from an initial system in thermodynamic equilibrium is destabilized by change in state variables like temperature, pressure, magnetic field, …The system rather than becoming unstable stays metastable if that perturbation is small enough. In the nucleation theory there is distinguish between homogeneous and heterogeneous nucleation. Homogeneous nucleation is the spontaneous formation of critical nuclei from individual atoms of the parent phase. Heterogeneous nucleation is the formation of nuclei of the new phase on impurities or other pre-existing surfaces in order to reduce the free energy barrier. The Gibbs free energy of a solution is a function of temperature T, pressure p and molar quantities of solutes n_i. In the differential form it is defined as

$$\mathrm{d}G = \left(\frac{\partial G}{\partial T}\right)_{p,n_i} \mathrm{d}T + \left(\frac{\partial G}{\partial p}\right)_{T,n_i} \mathrm{d}p + \sum_i \left(\frac{\partial G}{\partial n_i}\right)_{T,p,n_{j\neq i}} \mathrm{d}n_i \tag{2.1}$$

If T and p are constant, the equation 2.1 can be written as

$$\mathrm{d}G = \sum_i \left(\frac{\partial G}{\partial n_i}\right)_{T,p,n_{j\neq i}} \mathrm{d}n_i \tag{2.2}$$

where the partial molar quantity $\left(\frac{\partial G}{\partial n_i}\right)_{T,p,n_{j\neq i}}$ is known as a chemical potential μ_i.

2.1 Classical Nucleation Theory

Under the framework of the classical nucleation theory (CNT) one is able to yield the incubation time and the nucleation rate of precipitates. Combined with diffusion equations, modeling of the concentration time evolution and field of various components of the alloy is possible.

In diffusive transformations a second phase occurs either by nucleation or spinodal decomposition, followed by growth and coarsening. Observations and theoretical interpretation of experimental results on the phase transformations are despite number of modern developments, [40] still carried out widely based on the classical nucleation theory, formulated in 1926, [41, 42] and its extensions and modifications in 1935, [43], 1942, [44] and 1984, [45]. The idea behind classical nucleation theory is very simple and is based on the properties of the critical cluster. It was first formulated for the condensation of a vapour to form liquid, which is the simplest nucleation process. Later theory became convenient for more complex problems of nucleation in liquid and solid phases. In an ordinary nucleation process, within another phase a small amount of new phase is formed. The main driving force behind that is the difference in the free energies of initial and final configurations. Furthermore, when a small amount of new phase is formed, the free energy rises initially. With the creation of an embryo of the new phase, the associated event is formation of boundary, which separates two phases. Observation and defining of the boundary is very difficult when there are only few particles in the embryo. However, there is a critical particle size when these clusters become stable. Before particle clusters reach critical size they are called *embryos*, and above it they are known as *nuclei*. The embryos or small clusters are unstable initially due to their high surface-to-volume ratio. After they grow beyond the critical size they are biased toward further growth. It is important to note, that formation of a solid crystal from a vapour or liquid is much more complicated compared to the formation of a liquid droplet from a vapour. Complexity increases due to the shape of crystal when it is growing, since its surface energy is function of the orientation. Considering this, the crystal nucleus of a minimum surface energy can have very complicated shape. Furthermore, in a solid crystals, atoms need to fit into the fixed pattern of the crystal lattice, [46]. Under the nucleation theory two basic ways of nucleation are known. New phase can form on pre-existing interface (particle, grain boundary, dislocation,...), which is known as *heterogeneous nucleation* and occurs more easily. The other way of forming a new phase is know as *homogeneous nucleation*, where new phase is result of a concentration fluctuation of atoms. In figure 2.1, nucleation of β phase precipitate in α matrix is depicted in phase diagram of binary alloy. Nucleation of β in α matrix occurs after sufficient amount of B-atoms diffuse through it together to form small volume. After the nucleation, the growth of new phase can commence. From an atomistic point of view that happens by two successive processes, [47]. First, long range transport by diffusion over distances of many atomic spacings, known as *diffusion process.* Secondly, atomic transport across the interface i.e. normally a thermally activated short range diffusional process, known as *interface process.*

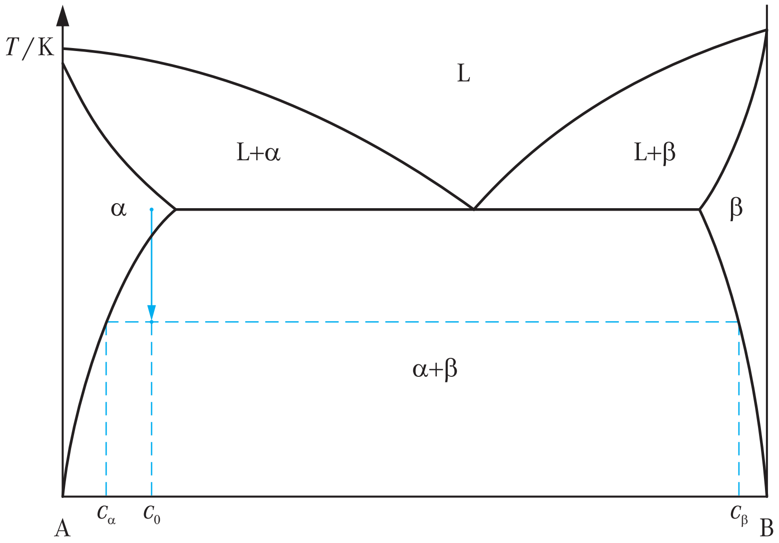

Figure 2.1: Phase diagram for binary AB alloy and nucleation of β phase inside α matrix.

The nucleation and growth depends on some important characteristics. The velocity of nucleation and growth is dependent on rate at which stable nuclei form, and on their subsequent growth rate. While in some transformations only important and limiting factor for nucleation is an activation energy for nucleation, in condensed phases equally important is the activation energy for atom migration or diffusion. The general characteristics of the nucleation can be summarized as follows:

- dependence on time
- dependence on temperature
- effect of stresses
- composition, atomic volume, and shape of the new phase
- orientation relations
- and stabilization, [46].

The basic kinetic mechanism assumed under the framework of CNT is that small clusters grow and decay by the absorption or emission of single atoms. In this theory the clusters are treated as spherical droplets, due to simplification of theory derivation.

2.1.1 Homogeneous Nucleation

Homogeneous nucleation happens in the interior of a uniform phase. When nuclei of the new phase (β) is formed, the interface at the boundaries (α/β) is created. The free energy change (ΔG) associated with the homogeneous nucleation process have several contributions and is given as

$$\Delta G = -V\Delta G_V + A\gamma + V\Delta G_s \tag{2.3}$$

where $V\Delta G_V$ is reduction of volume free energy due to the creation of a volume V of new phase β, $A\gamma$ is increase of the free energy due to the creation of an area A on interface α/β with specific interfacial energy γ, and $V\Delta G_s$ is rise of the strain energy as newly created volume does not fit perfectly into the space previously occupied by the matrix. If we assume that the nucleus is spherical with radius r, the equation (2.3) becomes

$$\Delta G\left(r\right) = -\frac{4}{3}\pi r^3\left(\Delta G_V - \Delta G_s\right) + 4\pi r^2\gamma_{\alpha\beta} \tag{2.4}$$

The main difference between nucleation in solids and nucleation in vapours or liquids (solidification) is the role of an elastic energy, estimated as $\Delta G_s = 6\mu_\alpha U\varepsilon^2$, [48], where ε is misfit strain arising from the difference in lattice parameters and $U \equiv 3E_\beta/(3E_\beta + 4\mu_\alpha)$. E_β is the bulk modulus and μ_α is shear modulus, denoted for the corresponding phase. Precipitated new solid phases from supersaturated solid solution are classified either as coherent, incoherent or something in-between (semi coherent). Figure 2.2 depicts all possible types of precipitates, [49]. An incoherent precipitate is shown in figure 2.2a, where crystal structure of precipitating β-phase has different crystal structure than parent phase. Figure 2.2b shows semicoherent precipitate, where dislocations array acts as relief of the elastic strain due to lattice mismatch. This type of interference is intermediate between coherent and incoherent. Figure 2.2c ilustrates coherent precipitate, where its lattice planes are continuous with the matrix. No structural discontinuity is between two phases, although they have different composition and lattice parameters. Figure 2.2d depicts fully coherent precipitate with same lattice parameters and different composition.

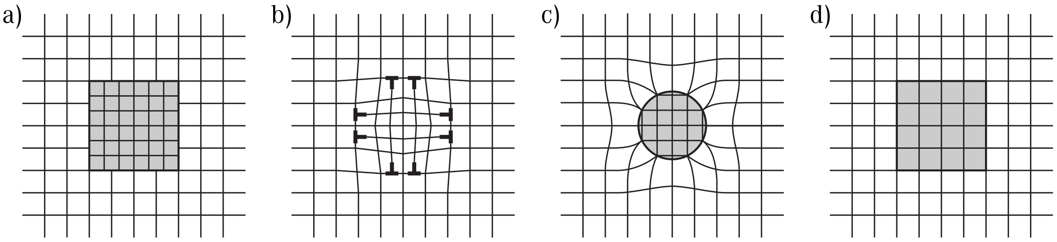

Figure 2.2: Schematic representation of solid-solid precipitates; a) an incoherent precipitate, b) a semicoherent precipitate, c) a coherent particle, and c) a fully coherent particle, [49].

The free energy change as a function of radius is depicted in figure 2.3, [50]. The critical nucleus size is determined from the first derivative of the function in equation (2.4). This criterion yields the critical nucleus radius

$$\left.\frac{\mathrm{d}\Delta G}{\mathrm{d}r}\right|_{r=r^*} = 0 \quad \Rightarrow \quad r^* = \frac{2\gamma_{\alpha\beta}}{(\Delta G_V - \Delta G_s)} \tag{2.5}$$

Nuclei smaller than the critical size tend to decay because the free energy hill goes down toward smaller cluster sizes. However, after clusters reach critical size they tend

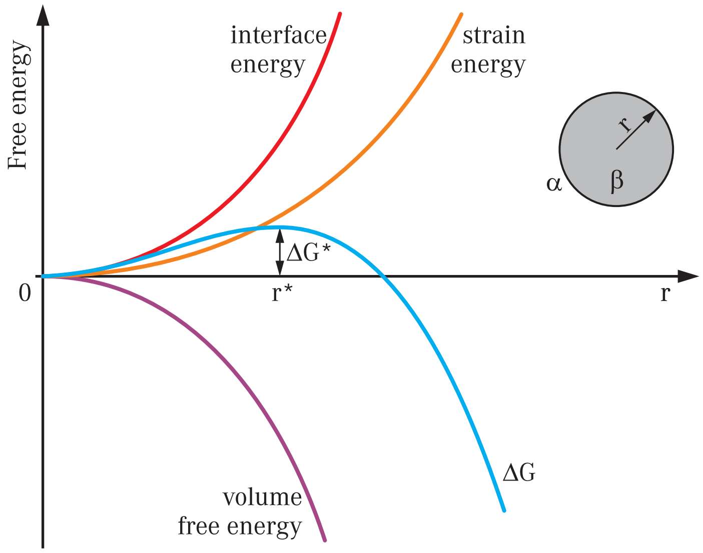

Figure 2.3: The activation energy barrier ΔG* and the critical nucleus size r* according to classical nucleation theory based on heterophase fluctuations, [50].

to grow since downhill is now toward larger sizes. After nuclei reaches critical point their growth is afterwards governed by diffusion or by reaction kinetics. The free energy needed to form critical nucleus is

$$\Delta G^{*} = \frac{16\pi\gamma_{\alpha\beta}^{3}}{3\left(\Delta G_V - \Delta G_s\right)^2} \tag{2.6}$$

The formation of critical clusters is *nucleation* and the formation rate is the *nucleation rate*, which describes how many clusters per unit time and volume grow over the hill top.

2.1.2 Heterogeneous Nucleation

Heterogeneous nucleation can occur on imperfections when nucleating particle effectively “replaces” some energetic feature of the original configuration. For instance, nucleation on a grain boundary removes grain boundary area, and replaces it with an interphase boundary area, that would have been created anyway by formation of the new phase. Thus, pre existing imperfections effectively “catalyze” nucleation process.

Compared to the homogeneous nucleation, the heterogeneous nucleation is usually favoured. However, it is believed that homogeneous nucleation of Guinier-Preston zones is possible, as long as vacancy concentration exists, [49]. Nucleation in solids is preferentially heterogeneous. It occurs on pre-existing imperfections, which are suitable nucleation sites and are non-equilibrium defects, e.g. vacancies, dislocations, grain boundaries, inclusions, stacking faults or free surfaces. At these preferential sites, the effective surface energy is lower. Therefore, the free energy barrier is diminished and facilitates nucleation process. The free energy change (ΔG_{het}) associated with the heterogeneous nucleation is given as

$$\Delta G_{\text{het}} = -V\left(\Delta G_V - \Delta G_s\right) + A\gamma_{\alpha\beta} - \Delta G_d \tag{2.7}$$

where ΔG_d is reduction of the free energy due to destruction of defect where nucleation occurs. Preferential sites are favoured because of wetting, cf. figure 2.4, where contact or wetting angle θ is given by

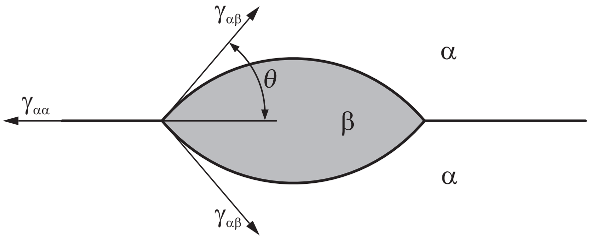

Figure 2.4: The critical nucleus size for heterogeneous nucleation.

$$\cos\theta = \frac{\gamma_{\alpha\alpha}}{2\gamma_{\alpha\beta}} \tag{2.8}$$

if we assume that $\gamma_{\alpha\beta}$ is isotropic.

The free energy change for heterogeneous nucleation is then

$$\Delta G_{\text{het}} = -V\left(\Delta G_V - \Delta G_s\right) + A_{\alpha\beta}\gamma_{\alpha\beta} - A_{\alpha\alpha}\gamma_{\alpha\alpha} \tag{2.9}$$

where V is the volume of nucleus, $A_{\alpha\beta}$ is the area of the α/β interface with interfacial energy $\gamma_{\alpha\beta}$ and $A_{\alpha\alpha}$ the area of α/α interface which is annihilated during process. The heterogeneous nucleation free energy is equal to the homogeneous nucleation free energy scaled with a function of the wetting angle

$$\Delta G_{\text{het}} = \Delta G_{\text{hom}} f(\theta) \tag{2.10}$$

where $f(\theta)$ is given by

$$f(\theta) = \frac{1}{2}(2 + \cos\theta)(1 - \cos\theta)^2 \tag{2.11}$$

Equation 2.10 also holds for free energy needed for critical nucleus.

Function of wetting angle is not dependant on the radius, meaning that critical size radius is the same for both types of nucleation, only change is the difference in the free energy, needed for nucleation. In figure 2.5 difference in the free energies needed for both types of nucleation is shown. Heterogeneous nucleation can occur on various heterogeneous sites, such as grain boundaries, grain edges or grain corners. In figure 2.6, the effect of $\Delta G_{\text{hom}}/\Delta G_{\text{het}}$ on the $\cos\theta$ for various nucleation sites is depicted, [51]. It is clearly shown that nucleation on the grain corners is preferred site, since the activation energy for nucleation here is reduced.

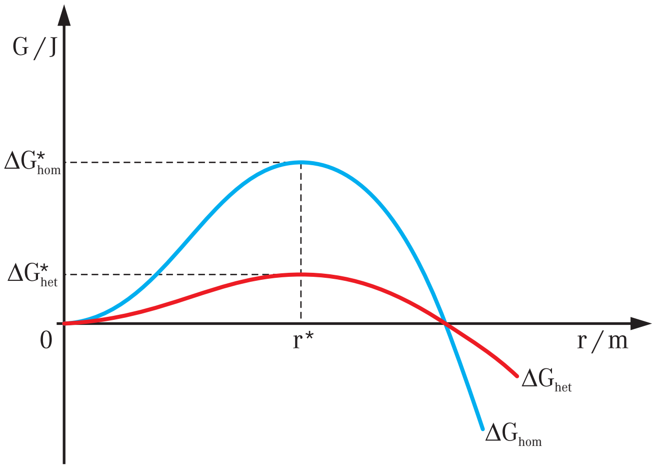

Figure 2.5: The free energy change needed for homogeneous (ΔG_{hom}) and heterogeneous (ΔG_{het}) nucleation, [50].

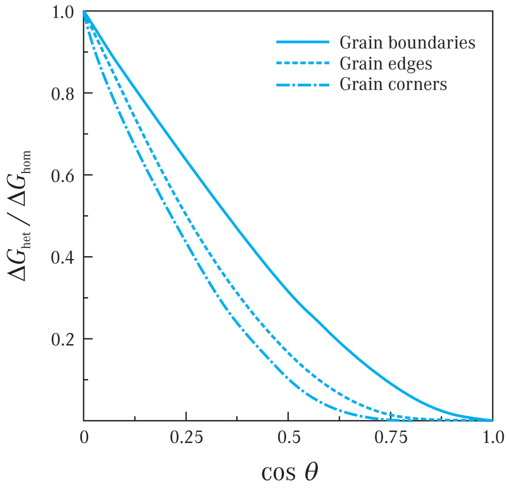

Figure 2.6: Dependence of $\Delta G_{\mathrm{hom}}/\Delta G_{\mathrm{het}}$ on $\cos\theta$ for various heterogeneous nucleation sites, [51].

2.1.3 Rate of Nucleation

In previous sections, the critical values needed for an embryo to become a nucleus were derived. The key insight into the nucleation process was presented. However, the very important feature not addressed, was the rate at which nuclei of a new phase appear in the system. The nucleation rate is critical in the prediction of the phase transformation behaviour. Hereafter, critical nuclei and clusters will be described by the number of particles (atoms or molecules) in them and not by their radii. In the figure 2.7, atomistic view of formation of the critical cluster is depicted. Basic idea for

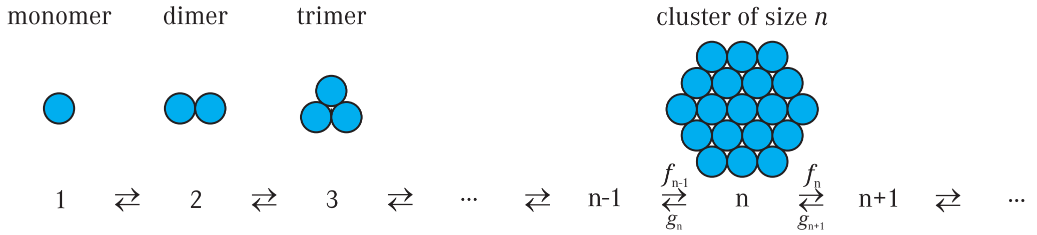

Figure 2.7: Flow of monomers to form dimers, trimers, tetramers, pentamers and finally critical sized clusters consisting of n particles, where f_n is attachment frequency and g_n is detachment frequency of monomers to n sized cluster.

cluster formation was given by L. Szilard, as a series of consecutive attachments and detachments of single atoms, [40, 42, 52, 53]. Clusters consisting of n atoms are formed by the growth of clusters consisting of $n-1$ atoms and the decay of clusters of $n+1$ atoms and disappear by the growth and decay into clusters of $n+1$ and $n-1$ atoms, respectively. The change with time of the concentration $X_n(t)$ of clusters consisting of n atoms is given by

$$\frac{\mathrm{d}X_n(t)}{\mathrm{d}t} = J_n(t) - J_{n+1}(t) \tag{2.12}$$

where $J_n(t)$ is the net flux of clusters through the size n given by

$$J_n(t) = f_{n-1}X_{n-1}(t) + g_{n+1}X_{n+1}(t) - f_nX_n(t) - g_nX_n(t) \tag{2.13}$$

where, f_n is attachment frequency or rate and g_n is detachment frequency of monomers from the cluster of the size n. Attachment and detachment rates are connected with

$$g_{n+1} = f_n \frac{X_n}{X_{n+1}} \tag{2.14}$$

where, the cluster concentration X_n is concentration that would develop when equilibrium between these cluster concentrations would be achieved. When attachment and detachment rates are equal, a steady-state concentration of the clusters in the system can be assumed, and holds

$$J_n(t) = J_{n+1}(t) = J_0 \tag{2.15}$$

where J_0 is the time averaged frequency of formation of clusters of any size. Hence, J_0 is equal to the frequency of formation of the clusters with the critical size n^* and thus is equal to the steady-state nucleation rate. After employing some simple mathematics on the Szilard scheme for J_0 we obtain, [52]

$$J_0 = X_1 \sum_{n=1}^{N-1} \left(\frac{1}{f_n} \frac{g_2\, g_3 \cdots g_n}{f_1\, f_2 \cdots f_{n-1}} \right)^{-1} \tag{2.16}$$

Attachment and detachment rates are connected to the cluster formation energy by

$$\frac{g_2\, g_3 \cdots g_n}{f_1\, f_2 \cdots f_{n-1}} = \exp\left(\frac{\Delta G(n)}{k_\mathrm{B}T} \right) \tag{2.17}$$

where, $\Delta G(n)$ is the energy associated to form a cluster consisting of n atoms. Comparison of equations (2.16) and (2.17) leads to the expression for nucleation rate. A long time ago, Volmer and Weber proposed the celebrated expression for nucleation rate, [41] given with

$$J \propto \exp\left(-\frac{\Delta G^*}{k_\mathrm{B}T}\right) \tag{2.18}$$

where, ΔG^* is the free energy required to form critical nucleus. To estimate the nucleation rate, population density of the critical nuclei is needed. According to the Volmer and Weber, the density of critical sized nuclei N is given by the Boltzmann distribution as

$$N = N_0 \exp\left(-\frac{\Delta G^*}{k_\mathrm{B}T}\right) \tag{2.19}$$

where, N is the number of critical sized nuclei containing n atoms per unit volume that exist in the system, N_0 is the total number of nucleation sites (monomers) per unit volume of the system. Under Volmer and Weber theory, formation of clusters is governed by monomer fluctuations. The problem arises here due to possibility of critical sized cluster to lose monomers and thus be reduced to subcritical. Important improvement of equation (2.18), especially insight into the kinetic prefactor was studied by Becker and Döring [43] and Zeldovich [44]. They expressed nucleation rate as

$$J = \beta^* N_0 Z \exp\left(-\frac{\Delta G^*}{k_\mathrm{B}T}\right) \tag{2.20}$$

where, β^* is the rate of the reaction of solute atoms to form a critical cluster ($n-1 \rightarrow n^*$) and Z is the Zeldovich factor, given by

$$Z = \sqrt{-\frac{1}{2\pi k_\mathrm{B}T}\frac{\partial^2 G}{\partial n^2}\bigg|_{n=n^*}} \tag{2.21}$$

Zeldovich factor accounts for the possibility that critical cluster nucleus with n^* particles, can with equal probability either grow or shrink. It also accounts that larger nuclei have probability of shrinking. Further improvement of previous approaches was then by Kampmann and Wagner, [45] introduction of the incubation time τ. The incubation time is approximately the time, elapsing from the moment of supersaturating the old phase until the moment of appearance of a detectable amount of the new phase, or simply put the amount of time before particles begin reaching the critical size. After

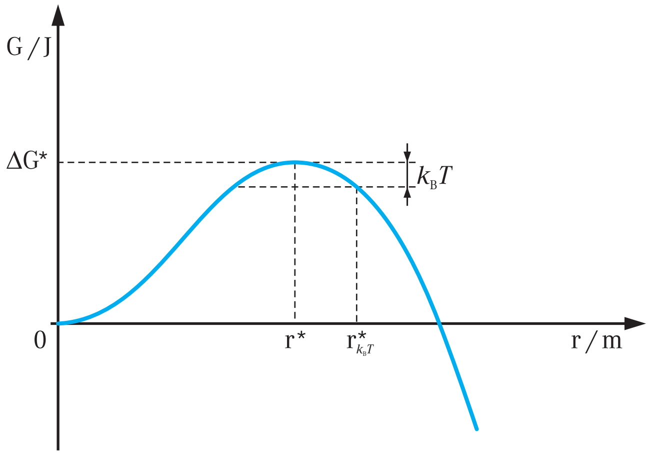

Figure 2.8: Schematic representation of the radius $r^*_{k_\mathrm{B}T}$, at which stable precipitates nucleate in the graph of the free energy change needed associated with nucleation.

introduction of τ, the following expression for the nucleation rate was given

$$\left.\frac{\mathrm{d}N}{\mathrm{d}t}\right|_{nuc.} = N_0 Z \beta^* \exp\left(-\frac{\Delta G^*}{k_\mathrm{B}T}\right) \exp\left(-\frac{\tau}{t}\right) \tag{2.22}$$

where, $\tau = 4/2\pi\beta^* Z^2$. Here the critical nuclei size is given with equation (2.23) and is show in Figure 2.8

$$r^*_{k_\mathrm{B}T} = r^* + \frac{1}{\sqrt{\pi}Z} \tag{2.23}$$

2.2 Atomic Jumps and Diffusion

Phenomena of diffusion can be introduced in two ways. A phenomenological approach starting with Fick's laws and their mathematical consequences, or an atomistic one by considering the random walk of the diffusing particles or atoms, [54]. A knowledge of solid state diffusion is essential for understanding of countless microstructural changes occurring at elevated temperatures. For example, solid state diffusion is fundamental for processes like diffusional phase transformations, precipitation, dissolution of second phase, recrystallization, oxidation, creep, annealing and others. The atomistic mechanisms for solid state diffusion rely on defects in crystals e.g. point defects like vacancies, divacancies and interstitials, [55]. Diffusion is also important to study how atoms move in solids. Movements of atoms in matter are thermally activated and results in the net transport of atoms. The jumps are assumed to be entirely random and the probability of jumping depends on the surrounding atom configurations. Furthermore, diffusion can be represented by random walks of particles, [56]. Experimental work has shown that atomic diffusion in the solid-state occurs by vacancy mechanism, [57]. The vacancies are voids on the substitutional lattice sites. Their movements are associated with distortion of the lattice and are linked to a energy barrier which needs to be overcome. Historically, various diffusion mechanisms were proposed and are schematically shown in figure 2.9. Direct interchange mechanism (figure 2.9a) and Zener ring mechanism (figure 2.9b) are associated with high strain energies, and thus probability of their occurrence is very low, especially at lower temperatures. On the other hand, the vacancy diffusion mechanism (figure 2.9c) proposed by H. B. Huntington and F. Seitz in 1942, [58] is associated with much lower energy barrier, [58, 59]. Vacancy diffusion mechanism is associated with vacancy concentration. The equilibrium vacancy concentration given by

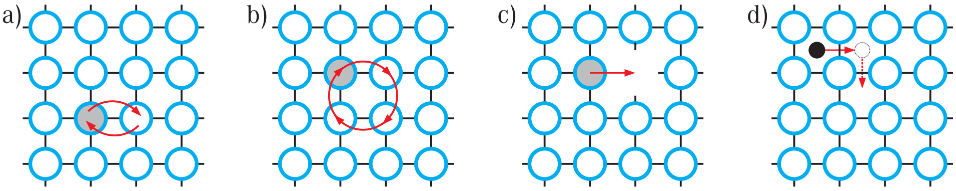

Figure 2.9: Proposed solid-state diffusion mechanisms; a) direct interchange mechanism, b) Zener ring mechanism, c) vacancy diffusion mechanism and d) interstitial diffusion.

$$c_V^{eq} = \exp\left(-\frac{\Delta G_V^{for}}{k_\mathrm{B}T}\right) \tag{2.24}$$

is very small, typically about $10^{-1} - 10^{-2}$ at.% for most metals at their melting point, and it decreases with decreasing temperature. In equation (2.24), ΔG_V^{for} is vacancy formation energy, sometimes denoted as E_V^{for}, which can be split into enthalpy and entropy terms which yields

$$c_V^{eq} = \exp\left(\frac{\Delta S_V^{for}}{k_\mathrm{B}}\right)\exp\left(-\frac{\Delta H_V^{for}}{k_\mathrm{B}T}\right) \tag{2.25}$$

Existence of the the vacancy diffusion mechanism was disputable, because of the low vacancy concentrations at temperature interesting for diffusional phase transformations. The theory was generally accepted after a diffusion seminar in 1950 where validity of E. Kirkendall seminal experiment conducted in 1947, [57] was approved.

Net diffusion rate of atoms across area perpendicular to flux vector is described by Fick's first law, written in general form as

$$\vec{J} = -D\nabla c \tag{2.26}$$

where, $\vec{J}$ is the total atomic flux vector, D is a symmetric second rank tensor denoted as the diffusion coefficient tensor and c is the concentration of the same atoms, [60, 61]. However, if concentration is time dependent, use of continuity equation

$$\nabla\vec{J} = -\frac{\partial c}{\partial t} \tag{2.27}$$

with equation (2.26) yields the diffusion equation (Fick's second law), [60]

$$\nabla\left(-D\nabla c\right) = -D\left(\nabla^2 c\right) - \left(\nabla c\right)\left(\nabla c\right) = \frac{\partial c}{\partial t} \tag{2.28}$$

for the case without sources and sinks. Since diffusion is thermally activated process, jumps of vacancies and interstitials are also thermally activated and they occur at rate

$$\Gamma = \nu\exp\left(-\frac{E^\mathrm{m}}{k_\mathrm{B}T}\right) \tag{2.29}$$

where, ν is an attempt frequency and E^m is activation energy for the jump, [62]. Therefore, due to the vacancy jumps, atoms change their positions on the crystal lattice with frequency, that depends on the local configuration, attempt frequencies, temperature, …For example, in alloy where clustering is favoured, same atoms tend to have more energetically favourable bonds, and same pair bonds are easily formed.

In figure 2.10 jump of atom from an initial configuration i to final configuration j

through saddle point is depicted. Whenever an atom jumps from one site to another, configuration of the alloy changes from configuration i to j (cf. figure 2.10). Transition probability for occurrence of this event, at temperature T is given by

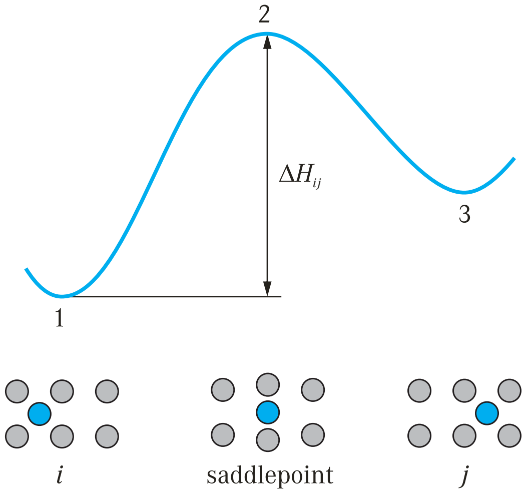

Figure 2.10: An atom jump in a crystalline solid from an initial configuration i (1) to a final configuration j (3), through a saddle point position (2).

$$\Gamma_{i \to j} = \nu_{ij} \exp\left(-\frac{\Delta H_{ij}}{k_{\mathrm{B}} T}\right) \tag{2.30}$$

where, ΔH_{ij} is the activation barrier for the transition from configuration i in the point 1, to j in the point 3, through saddle position in the point 2. Transition $i \to j$ results in change of interatomic potential i.e. change in alloys atomic arrangement. In equation (2.30), ν_{ij} represent attempt frequency for event $i \to j$. The attempt frequency ν_{ij}, are usually obtained using the rate theory for solids, [63–65], which offers a conceptually straightforward approximation to the attempt frequencies, and is reviewed in detail in [66]. The attempt frequency ν_{ij} is for crystal with N atoms in a *quasi harmonic approximation* given as

$$\nu_{ij} = \frac{\prod_{k=1}^{3N} \nu_i}{\prod_{k=1}^{3N-1} \nu_{ij}^{'}} \tag{2.31}$$

where, ν_i and $\nu_{ij}^{'}$ are $3N$ normal mode vibrational frequencies at the minimum or initial state i and $3N-1$ nonimaginary normal mode vibrational frequencies at the saddle point, respectively. In a 3D periodic system where all atoms are moving, discarding the translational modes leaves $3N-3$ and $3N-4$ real normal mode vibrational frequencies at the minimum and saddle point, respectively. If the system is free to rotate, there are $6N-6$ and $6N-7$ relevant modes, [67].

Under the framework of the quasi harmonic approximation it is assumed that the anharmonicity is restricted to thermal expansion, so that the temperature dependence of the phonon frequencies arises only from dependence on the crystal structure and volume, [68]. The quasi harmonic approximation is used in the lattice dynamics theory to obtain the thermodynamic properties of crystals. In the system with N atoms, the total potential energy is expanded in the atomic displacements using Taylor series, and then in the quasi harmonic approximation the terms with order higher than two are neglected.

2.2.1 Vacancy diffusion

Atoms in solids usually diffuse by the motion of vacant lattice sites. Diffusion in the solids is relatively simple and happens via vacancy mechanism, illustrated in figure 2.9c. A substitutional atom either foreign or self, diffuses by jumping into adjacent vacancy. The motion of the atoms in solids is much slower than the motion of the vacancies, because motion of the atoms depends on having neighbouring vacancy, with which it can exchange positions. In the solid-state the motion of an atom depends on the probability, that it is adjacent to the vacancy, multiplied with the atom-vacancy exchange rate. The atom-vacancy exchange rate is dependent on the energy barrier for jump of atom to vacant site. Furthermore, higher the vacancy concentration, the more exchanges occur. Equilibrium vacancy concentration in an alloy given by equation (2.24), depends on the temperature, pressure and chemical potential between atoms, constituting the alloy. For the system with N_V vacancies and N atoms, the vacancy concentration can be written as

$$c_V^{eq} = \frac{N_V}{N + N_V} \tag{2.32}$$

In alloys, vacancies are formed and annihilated on free surfaces, dislocations and other defects in order to maintain their equilibrium concentration.

2.2.2 Interstitial diffusion

As depicted in the figure 2.9d, some elements have ability to move in the spaces between the atoms, as they can fit into the interstitial spaces in the lattice of other elements. This allows them to move through the lattice much faster, since they do not require the presence of a vacancy as is the case with substitutional atoms, since most of interstitial sites is unoccupied. Typical examples where interstitial diffusion takes place are Si in Cu, H in Pt, C and N in Fe, [69].

2.2.3 Tracer diffusion and Self-diffusion

Diffusion processes described above are called also chemical diffusion, which results in net transport of mass and occurs because of a gradient of chemical potential. Result is increase of the system entropy and system evolves towards equilibrium. Beside the chemical diffusion there also tracer diffusion and self-diffusion. This type of the diffusion, takes place in the absence of the gradient of chemical potential. Name tracer diffusion comes from using isotopic tracers to observe evolution and measure self-diffusion coefficients. The diffusion coefficient D_i^* for tracer diffusion is related to the chemical diffusion coefficient D_i as

$$D_i^* = D_i \frac{\partial \ln c_i}{\partial \ln a_i} \tag{2.33}$$

where, c_i is concentration and a_i is activity of atoms i, [70]. As already noted diffusion can be represented by random walks of particles. The time-dependent diffusion coefficient is given by Einstein expression, [71, 72] as

$$D(t) = \frac{1}{2\mathrm{d}} \frac{\delta}{\delta t} \left\langle R^2(t) \right\rangle \tag{2.34}$$

where, d is the system dimensionality $(d = 1, 2, 3)$ and $\left\langle R^2(t) \right\rangle$ is the average of particles displacement in time t, [73]. This equation provides very useful method to calculate the diffusion coefficient in the framework of diffusivity models from random walks. Einstein equation is very useful for providing the basic theory that describes diffusion of particles in solid state, where atoms are jumping from one lattice site to another and is given as

$$D_x = \frac{\left\langle X^2 \right\rangle}{2t} \tag{2.35}$$

For isotropic crystals the diffusion coefficient is the same in every direction

$$D = \frac{\left\langle S^2 \right\rangle}{6t} \tag{2.36}$$

where S is the vector displacement of an atom in time t. In the terms of transition probability, the traced diffusion coefficient in 3D is given as

$$D = \frac{ns^2 f}{6t} = \frac{\Gamma f s^2}{6} \tag{2.37}$$

where, s is the transition or jump distance and f is correlation factor, connected to the direction of the jumps [56] and is given as

$$f = \lim_{n \to \infty} \frac{\left\langle S^2 \right\rangle}{ns^2} \tag{2.38}$$

The correlation factor can be expressed as the ratio of the actual displacement vector $\left\langle S^2 \right\rangle$ and the resulting displacement vector of a complete random walk, [74]. For example, if each jump in the random walk is completely independent of previous, then $f = 1$. For the vacancy diffusion mechanism the correlation factor f is approximately

$$f \approx 1 - \frac{2}{\mathrm{Z}} \tag{2.39}$$

where, Z is the local coordination number.

2.3 Growth and Coarsening

In the phase transformations an initial stage of nucleation is followed by growth of the new phase. During growth stage, new atoms are added to an existing cluster. In figure 2.11, energy curve associated with the free energy of an atom as it passes through the boundary from the α matrix into the β phase precipitate is depicted, [46].

In general, two various growth models are distinguished. One is for diffusion-controlled growth which occurs in phase transformations with long range compositional changes. Other growth model is known as interface controlled growth where growth is determined by the kinetics of atomic processes in vicinity of the interface, e.g. $\gamma \to \alpha$ transformation during cooling in binary Fe-Mn alloys, [75]. The interface controlled growth does not involve a composition change as growth proceeds with the interface motion. The boundary migration kinetics involve local atomic rearrangements, where

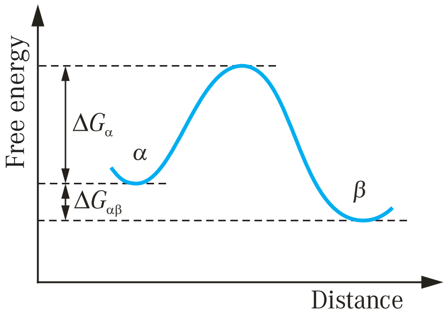

Figure 2.11: The energy barrier associated with the growth of a precipitate in the solid state.

atoms jump from one side of the interface to the other side. Usually in the interface-controlled growth processes, the interface motion occurs at constant velocity hence the particle size increases linearly in time ($r \propto t$). In the diffusion-controlled growth processes, the particle size often increases parabolic in time ($r \propto \sqrt{t}$). Typical concentration profiles for various growth processes are depicted in Figure 2.12.

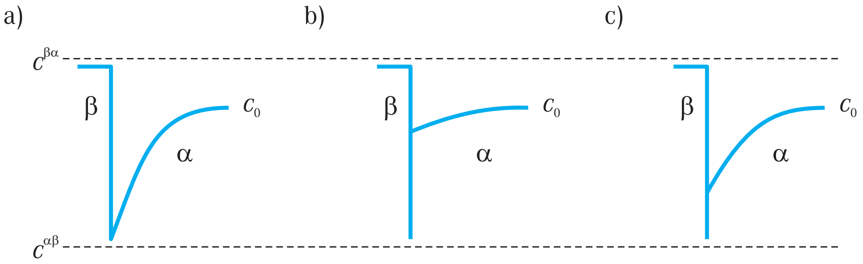

Figure 2.12: Schematic representation of concentration profile at an α/β interface for; a) diffusion–controlled interface, b) interface–controlled interface and c) mixed interface.

The growth of clusters causes drain of solutes in the surrounding matrix. Growth ceases when concentration of solutes in the matrix reaches its equilibrium value. From this point on, size increase of clusters is governed by coarsening. Coarsening is thermodynamically driven spontaneous process, known also as Ostwald ripening or competitive growth. It occurs because larger particles are energetically more favoured compared to small particles, Gibbs-Thomson effect. In the coarsening stage, large particles grow at the expense of small particles, [76, 77].

Growth and coarsening are common features of all structural transformations in multi-phase mixtures. Their principles will be discussed next.

2.3.1 Diffusion-Controlled Growth

After nuclei becomes large enough, further growth factor controlling mechanism if the interface mobility is sufficiently high, becomes the volume diffusion and growth rate is from this point limited by the diffusion rate. Growth of clusters with monomer addition, must satisfy the diffusion equation

$$\frac{\partial c(r,t)}{\partial t} = \sum_{i=1}^{3}\sum_{j=1}^{3}\frac{\partial}{\partial x_i}\left[D_{ij}(c,r)\frac{\partial c(r,t)}{\partial x_j}\right] \tag{2.40}$$

where, D_{ij} is the diffusion coefficient which dependant on the local concentration $c(r,t)$ and consequently on position r.

2.3.1.1 Zener model for diffusion controlled growth

This section describes Zener model for the growth, [78]. Solute concentration profile as a function of the distance is schematically illustrated in figure 2.13a. Zener assumed linear gradient, shown schematically in figure 2.13b, and that the phases at the interface have equilibrium composition. At the interface, the diffusion equation (2.40) must be satisfied. For sake of simplicity, the diffusion coefficient D_{ij} from equation (2.40) is assumed constant, which yields diffusion equation as

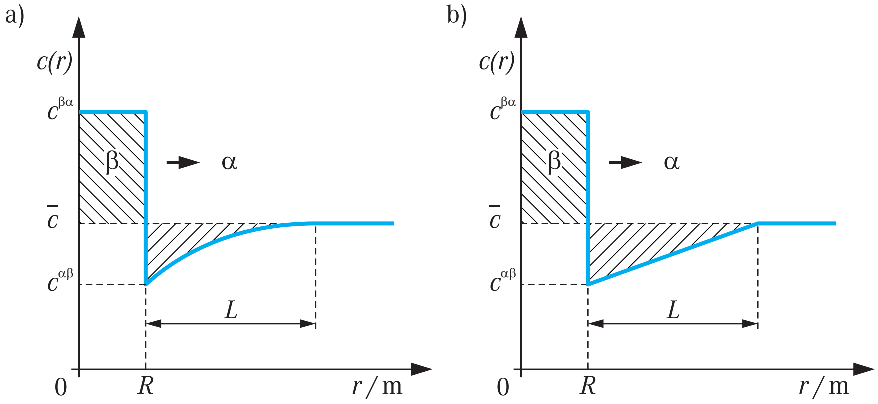

Figure 2.13: Schematic representation of the; a) concentration field in the matrix surrounding a precipitate with radius R, b) simplification of the same concentration field profile.

$$\frac{\partial c(r,t)}{\partial t} = D\nabla^2 c(r,t) \tag{2.41}$$

where, first boundary condition at the time $t = 0$, is $c(r, 0) = \bar{c}$. $\bar{c}$ is average solute concentration in the matrix (cf. Figure 2.13). However, in order to get the solute distribution from the diffusion equation, additional boundary conditions have to be specified.

In figure 2.13, $c^{\beta\alpha}$ is solute concentration in the precipitate β which is in equilibrium with α, $c^{\alpha\beta}$ is solute concentration in the matrix which is in equilibrium with β and $\bar{c}$ is mean solute concentration in the alloy. In incrementally small amount of time $\mathrm{d}t$, the boundary of the precipitate moves into the matrix for a distance $\mathrm{d}x$. The flux at the interface $r = R$ is from Fick's first law given as

$$-J_{r=R} = -D\left.\frac{\partial c}{\partial r}\right|_{r=R} = -D\frac{\bar{c} - c^{\alpha\beta}}{L} \tag{2.42}$$

and must be equal to the rate, at which the solute is partitioned. L can be estimated by mass conservation equation at the interface

$$R(c^{\alpha\beta}) = \frac{1}{2}L(\bar{c} - c^{\beta\alpha}) \tag{2.43}$$

Velocity at interface is given by

$$\frac{\mathrm{d}R}{\mathrm{d}t} = \frac{D}{2}\Omega\frac{\bar{c} - c^{\alpha\beta}}{c^{\beta\alpha} - \bar{c}}\frac{1}{R} \tag{2.44}$$

where, Ω is dimensionless supersaturation defined as

$$\Omega = \frac{\bar{c} - c^{\alpha\beta}}{c^{\beta\alpha} - c^{\alpha\beta}} \tag{2.45}$$

In the most cases it can be assumed $(c^{\alpha\beta} - \bar{c})(c^{\beta\alpha} - c^{\alpha\beta})$, then velocity is

$$\frac{\mathrm{d}R}{\mathrm{d}t} = \frac{D}{2}\Omega^2\frac{1}{R} \tag{2.46}$$

Integration of equation (2.46) leads to the relation for position of the boundary as function of time

$$R = \Omega\sqrt{Dt} \tag{2.47}$$

The precipitate size changes with the square root of time, yielding parabolic growth law for one dimensional growth (thickening of a plate) in binary system.

The solution of the diffusion equation (equation 2.41), for the spherical precipitate growth was derived by C. Zener in 1949, [78] and F. S. Frank in 1950, [79]. For more general shaped particles, treatment of diffusion problem was solved by F. S. Ham in 1959, [80] and G. Horvay and J. W. Gahn in 1961, [81]. All mentioned solutions assume smooth interfaces with constant diffusion flux over a planar interface. By considering an origin in the moving boundary in the direction of growth and normal to the plane of the precipitate, M. Hilert, [82] improved solution derived by C. Zener.

2.3.1.2 Gibbs-Thomson effect

In diffusion controlled growth described in previous section, the interface compositions are given by the equilibrium phase diagram which are calculated with assumption that phases extends indefinitely, i.e. without surfaces. This assumption is often not true, and influence of the surface energy needs to be considered. For the curved interfaces, additional surface energy terms is present, and results in a modification of the expected composition. This is the so called Gibbs-Thomson effect or capillary effect which causes modification of the solubility limits. In the case of nucleation, growth or coarsening, the capillary effect must be included into the solubility limits, [83]. In figure 2.14 effect of the interface curvature on the solubility of small particles is presented in the free energy curve at temperature T. In the binary alloy, correct solubility limit X_{eq}, of B atoms in α matrix in the equilibrium with β phase spherical particle with the radius r, is given as a function of the radius, [50, 83] by

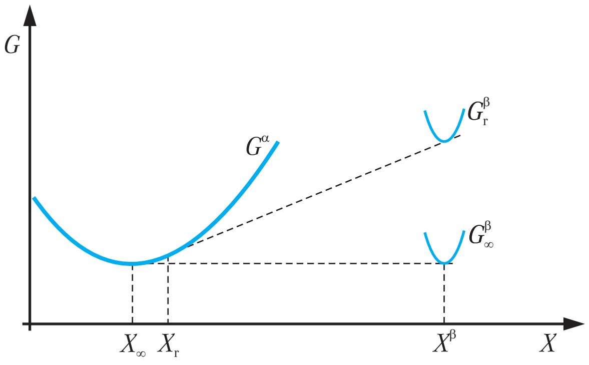

Figure 2.14: Gibbs-Thomson effect shown in free energy curves at temperature T, [50].

$$X_r^{\alpha} = X_{\infty}^{\alpha} \exp\left(\frac{2\gamma V_m}{r\mathrm{R}T}\right) \tag{2.48}$$

where, V_m is molar volume, γ is the surface energy, R is the molar gas constant and T is temperature.

2.3.2 Coarsening

The theory of coarsening or Ostwald ripening in alloys, describes the late stages of the formation and growth of a new phase particles, from a supersaturated solution. In the coarsening the dissolution of small particles proceeds and they than redeposit on the surfaces of larger particles, [76]. Furthermore, W. Ostwald discovered that driving force for the process is Gibbs-Thomson effect. The process occurs as smaller particles have a higher surface energy and therefore higher total Gibbs energy than larger particles, giving rise to an apparent higher solubility. During these stage, no new grains can form, and governing process for the growth of the particles is diffusional mass exchange, [84, 85]. In figure 2.15 is a schematic display of coarsening in two dimensions in time. As time evolves from a) to c) total number of droplets decreases, with increase of average radius. However, volume fraction of droplets is constant.

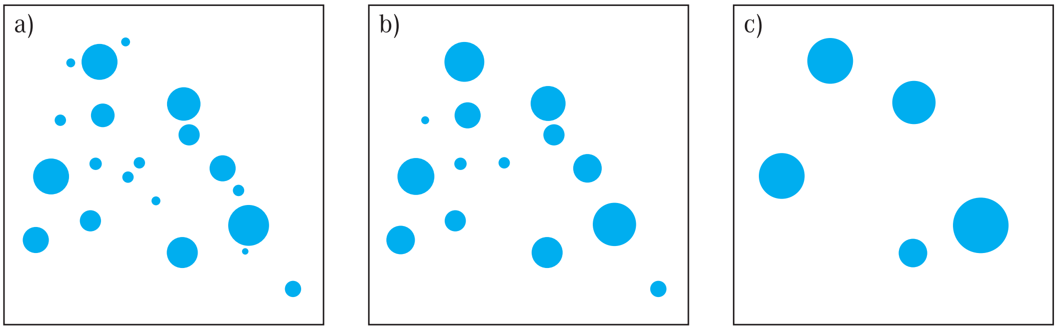

Figure 2.15: Schematic presentation of the coarsening or Ostwald ripening on droplets in two dimensions.

Theories of particle coarsening must be statistical in nature since experimental data are essentially statistical samples. In the theory three fundamental equations which require solution arise:

- *a kinetic equation*, describing the growth or shrinkage rate of an individual particle of given size,
- *a continuity equation*, describing the temporal evolution of a particle size distribution function,
- *a mass conservation equation*, which the solutions to the first two must satisfy to be acceptable.

The major progress in the theory of coarsening was done 1961 by I. M. Lifshitz and V. V. Slyozov, [84] and independently C. Wagner [85]. They quantitatively analysed asymptotic behaviour of the particle-size distribution in three dimensions. Their theory will be discussed in detail in the next section.

2.3.2.1 The Lifshitz-Slyozov-Wagner theory

The Lifshitz-Slyozov-Wagner theory of coarsening is used for description of the late stages of the growth by diffusional mass transfer in the supersaturated solution. Theory was discussed in 1961 by I. M. Lifshitz and V. V. Slyozov, [84] and independently C. Wagner [85]. They derived exact results, assuming that the minority phase occupies a negligible volume fraction. They showed that the characteristic size of the minority phase particles increases as $r \propto t^{1/3}$, and their number decreases as $N \propto t^{-1}$, [86]. Theory became known as the Lifshitz-Slyozov-Wagner (LSW) theory in 1975, when M. Kahlweit discovered that theories in papers from I. M. Lifshitz and V. V. Slyozov, [84] and C. Wagner, [85] are identical, [87].

All systems, where dispersed particles have certain solubility and are statistically distributed in a medium, are due to a large interface area, thermodynamically unstable. Interface surface decrease is described by the Gibbs-Thomson equation, when particles are approaching equilibrium through coarsening. Starting point of the LSW theory is diffusion equation for concentration c in the steady-state limit, given as

$$\nabla^2 c(r) = 0 \tag{2.49}$$

where, $\partial c/\partial t$ can be neglected. This determines the flow of material between particles, subjected to the Gibbs-Thomson boundary condition at the interface surface of a particle with radius r'

$$c(r)|_{r=r'} = c_\infty \left(1 + \frac{\nu}{r'}\right) \tag{2.50}$$

$$\lim_{r\to\infty} c(r) = \bar{c} \tag{2.51}$$

where, $\nu = 2\gamma\Omega c_\infty/RT$ is the capillary length and $\bar{c}$ is mean concentration in the bulk. Ω is the mean molar volume of the particle. The mass balance

$$\frac{\mathrm{d}}{\mathrm{d}t}\left(\frac{4\pi}{3}r'^3\right) = 4\pi r'^2 D \left.\frac{\mathrm{d}c(r)}{\mathrm{d}r}\right|_{r=r'} \tag{2.52}$$

satisfies criterion that volume change of the spherical particles is due to change in concentration. The evolution of the second phase is characterized by the particle-radius distribution $N(r', t)$, where $N(r', t)\mathrm{d}r$ is the number of particles per unit volume at time t with radius between r' and $r' + \mathrm{d}r$. The particle distribution function $f(r', t)$ determines averages

$$\overline{(\cdots)} = \frac{\int \mathrm{d}r' f(r', t)(\cdots)}{\int \mathrm{d}r' f(r', t)} \tag{2.53}$$

and with normalization, the total number of particles is given by

$$\int \mathrm{d}r' f(r', t) = N(t) \tag{2.54}$$

Distribution function satisfies the continuity equation (equation 2.55), as nucleation of new particles can be neglected, since nuclei are so small that they disappear immediately. Creation of new particles by fusion of two existing can be neglected due to large distances between particles.

$$\frac{\partial f(r', t)}{\partial t} + \frac{\partial}{\partial r'}(\dot{r'} f(r', t)) = 0 \tag{2.55}$$

where, $\dot{r'}$ is a time derivative. Furthermore, the distribution function must satisfy the conservation equation, thus

$$\Delta(t) + \frac{4\pi}{3} \int_0^\infty r'^3 f(r', t)\mathrm{d}r' = \phi V' \tag{2.56}$$

where, $\Delta(t) = \bar{c} - c_\infty$ is the supersaturation of the solution and vanishes as $t \to \infty$, $\phi V'$ is the initial concentration, and V' is the volume of the system. In the limit, where $\phi \to 0$, solution of the steady-state diffusion equation in equation (2.49), is given as

$$c(r) = \bar{c} - \frac{(\bar{c} - c(r'))r'}{r} \tag{2.57}$$

and only one droplet needs to be considered. The growth law in this limit is with equation for mass balance given as

$$\frac{\mathrm{d}r'}{\mathrm{d}t} = \frac{D}{r'}\left(\Delta - \frac{\nu}{r'}\right) \tag{2.58}$$

shows clearly, that droplets larger than time dependant critical radius $\nu/\Delta(t)$ grow and vice versa. Theory was derived for asymptotic behaviour of the particle-size distribution in three dimensions. Many particles in the system were assumed, with distances between particles grater than the size of the particles. Asymptotic solution of equation (2.58) yields average particle radius as

$$\bar{r}(t) = \left(\frac{4D\nu t}{9} \right)^{1/3} \tag{2.59}$$

where, factor 4/9 is dimensionless coarsening rate. Obtained was also analytical form of the particle size distribution function for very long times, given by

$$f(r', t) \propto \frac{g(r'/\bar{r})}{\bar{r}^4} \tag{2.60}$$

The explicit form of the scaled normalized distribution function is given by

$$g(z) = \begin{cases} \dfrac{\left(\dfrac{3^4 e}{2^{5/3}} z^2 \right) \exp\left(-\dfrac{1}{1 - 2/3z} \right)}{(z+3)^{7/3}(3/2 - z)^{11/3}} & \text{if} \quad 0 < z < 3/2 \\ 0 & \text{otherwise} \end{cases} \tag{2.61}$$

where, $z \equiv r'/\bar{r'}$.

It is worth to mention that in the case of heterogeneous precipitation, the coarsening is affected by short range diffusion on the grain boundaries and dislocations. If coarsening is controlled entirely by the grain boundary diffusion, the other phase particles size increases as $r \propto t^{1/4}$, [88]. However, if coarsening is controlled entirely by the pipe diffusion, the other phase particle size increases as $r \propto t^{1/5}$, [89, 90].

2.4 Clusters

A cluster is term to describe an assembly which lacks the well defined composition, geometric structure and chemical bonds, typical for molecules and lack in properties of typical bulk material, [91]. The main reason for their research is understanding their influence on the alloy kinetics. Interesting is to observe their changes in properties when they grow from monomers into various groups made of different number of particles. Sometimes, the property change is so minimal when clusters grow, that it can not be distinguished from a solid. All these properties needs to be thoroughly analysed from data sets from experiments or simulations.

Clusters form from atoms during nucleation process and subsequent growth and coarsening phases. They are found in various sizes, from very small to macroscopic. The cluster is defined as a set of identical atoms or molecules, occupying crystal sites and connected by at least one nearest neighbour bond, [92, 93]. Particular cluster of n atoms, changes its size as a result, of a series of attachments and detachments from it. The critical cluster with n^* atoms is also known as the critical nucleus. Atoms attach and detach to the critical cluster with equal frequency, [94]. As it was already explained previously, a subnuclei ($n < n^*$) tends to decay into monomers, because in the unit of time, more atoms are detached than attached to them. On the other hand, a supernuclei ($n > n^*$) tends to grow, because more atoms are attached to them than detached. Since atomic attachments and detachments are random events, any cluster of the size n, can either decay or grow into cluster with macroscopic size. This is happening with certain probability $P(n)$. Critical clusters have growth probability of $P(n = n^*) = 1/2$, whereas subnuclei and supernuclei evolve with the growth probability of $P(n < n^*) < 1/2$ and $P(n > n^*) > 1/2$, respectively.

It was shown, that between thermodynamically defined critical nucleus size (r^*) and kinetically defined critical size (n^*) exists difference, [95]. Kinetically defined clusters are polyhedrons with N solute atoms. Radii of the cluster in the BCC lattice, without interstitial atoms can be obtained with calculation of the sphere having the same volume as cluster. The BCC lattice cell have two atoms and volume of $V_{sub} = a^3$. If the number of atoms N in the cluster is known, and spherical shape of the cluster is assumed, the volume is given as

$$V_{cluster} = \frac{4}{3}\pi r^3 = \frac{N}{2}a^3 \tag{2.62}$$

which holds for $N > 20$, and is basis for calculation of the cluster radius, [20] given as

$$r = \left(\frac{3a^3}{8\pi}N\right)^{1/3} \tag{2.63}$$

Similar procedure can also be done for FCC crystal lattice.

2.4.1 Cluster analysis

Huge amount of data is obtained after the experiment or simulation is finished. This data configurations must be analysed in a way that informations contained in wast amount of raw data are retained, but are represented more simply. This is usually done with various averages and correlation functions.

2.4.1.1 Cluster size distribution

Determination of the size distributions is very important in cluster analysis, as the size distribution determines many bulk properties and provides detailed information about the mechanisms governing both, the kinetics and the thermodynamics of the nucleation, growth and coarsening of a new phase. Another important feature of the size distribution is that it can be compared between the classical nucleation theory and measured size distributions obtained from simulations and experiments. In the latter, the size distribution is given with a counts of the number of clusters with a given size defined, either with number of particles, $n(i)$ or radius of clusters, $n(r)$. Alternatively, the cluster size distribution can be defined in time t, as $n(t)$. Furthermore, obtained function obeys power law and is frequently normalized to get volume independent function, [96].

2.4.1.2 Mean cluster size

As alloys evolves in time, so the mean cluster size evolves. The mean cluster size enables description of the evolution kinetics. The mean cluster sizes $L(t)$ and $L^2(t)$ as a functions of time t, can be defined as first or second moment of the cluster size distribution, normalized by the cluster size distribution or by the first moment of the cluster size distribution, respectively. The first moment of the cluster size distribution is given as

$$L(t) = \frac{\sum_{l=l_c}^{\infty} l n_l(t)}{\sum_{l=l_c}^{\infty} n_l(t)} \tag{2.64}$$

whereas the second moment of the cluster size distribution is given as

$$L^2(t) = \frac{\sum_{l=l_c}^{\infty} l^2 n_l(t)}{\sum_{l=l_c}^{\infty} l n_l(t)} \tag{2.65}$$

where, $n_l(t)$ is the number of clusters what have l atoms at time t, and l_c is the cut off criterion, [17, 92, 96, 97].

2.4.1.3 Pair Correlation Function

The particle correlation functions, measure the extent to which the structure of a matter deviates from the complete randomness, [98]. The spatial correlation functions characterize structure of the system, and gives more detailed informations than thermodynamic quantities. Therefore, it is very important to be able to do their comparison, to the experimental data from various scattering techniques. The particle densities. and the closely related equilibrium particle correlation functions, provide a complete description of the structure of a matter, [98, 99] In general, the n-particle correlation function $g_N^{(n)}(r^n)$, defined in terms of the particle densities is given as

$$g_N^{(n)}(r^n) = \frac{\rho_N^{(n)}(r_1, \ldots, r_n)}{\prod_{i=1}^{n} \rho_N^{(1)}(r_i)} \tag{2.66}$$

where, $\rho_N^{(1)}(r)$ is the single particle density and $\rho_N^{(n)}(r^n)$ is the n-particle density, [100]. The pair correlation or radial distribution function $g_N^{(2)}(r_1, r_2)$, is the second order particle correlation function, and is the simplest of the correlation functions. For the homogeneous and isotropic systems, the pair correlation function $g_N^{(2)}(r_1, r_2)$, is a function only of the distance $r_{12} = |r_2 - r_1|$, and is written as $g(r)$. It provides a measure of local spatial ordering in the matter, and describes the probability of finding a pair of the particles at a distance r from each other, relative to the probability for a complete random distribution at the same density, cf. figure (2.16), [100]. The particle densities in equation (2.66) can be expressed with δ functions of position. The single particle density expressed with Dirac δ functions of position is given as

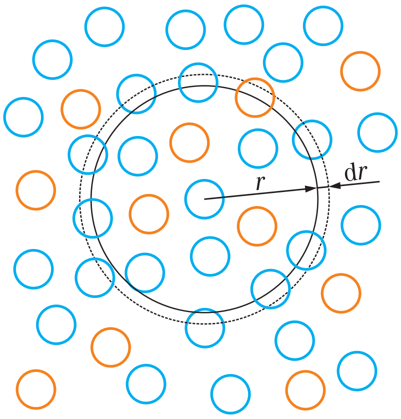

Figure 2.16: Schematic presentation of pair correlation function in binary solution.

$$\rho_N^{(1)}(r) = \left\langle \sum_{i=1}^{N} \delta(r - r_i) \right\rangle \tag{2.67}$$

and represents the ensemble average of a microscopic particle density $\rho(r)$. Similar notation can be used for second order particle density, which then gives pair correlation function $g(r)$ as

$$g(r) = \rho^{-2} \left\langle \sum_{i} \sum_{j \neq i} \delta(r_i)\delta(r_j - r) \right\rangle = \frac{V}{4\pi r^2 N^2} \left\langle \sum_{i} \sum_{j \neq i} \delta(r - r_{ij}) \right\rangle \tag{2.68}$$

where, ρ is average number density of particles, [100]. By definition of the $g(r)$, on average the number of particles at a distance between r and $r + \mathrm{d}r$, from the reference particle is $4\pi r^2 \rho g(r)\mathrm{d}r$ and the peaks in $g(r)$ represents neighbouring shells from the reference particle, [100]. Furthermore, for totally disordered state, a value of the pair correlation function is $g(r) = 1$.

2.4.1.4 Short Range Order

A short range order (SRO) parameter is directly related to the pair correlation functions. In the binary AB alloys, the most used short range order parameter α^n_{AB} is known as Warren-Cowley parameter, [101], which is for the n-th neighbour shell defined as

$$\alpha^n_{\mathrm{AB}} = 1 - \frac{p^n_{\mathrm{BA}}}{c_{\mathrm{A}}} \tag{2.69}$$

where, p^n_{BA} is the probability of finding an atom A in the neighbourhood of an atom B, c_{A} is the concentration of A atoms, and it must hold $c_{\mathrm{A}} + c_{\mathrm{B}} = 1$. In the fully disordered systems it is by definition $\alpha^n_{\mathrm{AB}} = 0$, whereas in the perfectly ordered systems it reaches its absolute value, which is dependent on the system. If the system has tendency toward clustering $\alpha^n_{\mathrm{AB}} > 0$, and $\alpha^n_{\mathrm{AB}} < 0$ when system has tendency of forming unlike pairs.

More convenient definition of the short range order parameter, used to analyse local atomic arrangement in the lattice computer simulations is given as

$$\alpha^n_{\mathrm{AB}} = \frac{N^n_{\mathrm{AB}}}{N_{\mathrm{A}} Z^n} \tag{2.70}$$

where, N^n_{AB} is the number of AB atom pairs in the n-th neighbour shell, N_{A} is the number of A atoms, and Z^n is the n-th neighbour coordination number, [102]. The short range order parameter from equation (2.70) is similar to the original Warren-Cowley parameter (cf. equation (2.69)), and characterizes tendency of the A atoms, to form bonds with the B atoms on the desired distance or neighbouring shell.

2.4.1.5 Moment of inertia

The moment of inertia of an object is a measure which describes how difficult it is to change rotation of an object. It is connected to the objects mass and distance of each bit of mass from the centre of the mass. The moment of inertia can be applied to the clusters as a sum of mass points at a distance from axis as

$$J = \sum_i m_i r_i^2 \tag{2.71}$$

where, r_i is the distance of an atom i from the mass centre, and m_i is mass of the atom i. The moment of inertia defined above depends on the orientation of the axis relative to the cluster. For clearness of presentation is it sometimes necessary to express J as a tensor. In the Cartesian coordinate system, components of the moment of inertia tensor are given as

$$\begin{aligned}
J_{xx} &= \textstyle\sum_i m_i(y_i^2 + z_i^2)\\
J_{yy} &= \textstyle\sum_i m_i(z_i^2 + x_i^2)\\
J_{zz} &= \textstyle\sum_i m_i(x_i^2 + y_i^2)\\
J_{xy} &= J_{yx} = -\textstyle\sum_i m_i x_i y_i\\
J_{yz} &= J_{zy} = -\textstyle\sum_i m_i y_i z_i\\
J_{zx} &= J_{xz} = -\textstyle\sum_i m_i z_i y_i
\end{aligned} \tag{2.72}$$

and are then used as components of the moment of inertia tensor as

$$\boldsymbol{J} = \begin{pmatrix} I_{xx} & I_{xy} & I_{xz} \\ I_{yx} & I_{yy} & I_{yz} \\ I_{zx} & I_{zy} & I_{zz} \end{pmatrix} \tag{2.73}$$

Tensor $\boldsymbol{J}$ permits the calculation of the moment of inertia about any axis relative to the orientation of the cluster.

2.5 Beyond classical theories

Materials that surround us are frequently found in nonequilibrium states. They are produced in this states because designer wanted to exploit and achieve some particular useful properties. However, when alloys are subjected to some energy input, its configuration adapts to the environment. Energy inputs can vary, and are usually imposed chemical gradient, high temperature, flow of high energy particles, mechanical strains, etc. For example, materials in the energy reactors are subjected to the high temperatures, and/or to the flow of high energy particles. Whenever, alloys in nonequilibrium are subjected to these energy inputs, they tend to evolve toward equilibrium state over time. When designers are choosing alloys for applications they must know great deal on the kinetic pathways on which materials in question will try to evolve. In the past, a lot of physical experiments were conducted before alloy was allowed to be used in these kind applications. With increasing costs of physical experiments and increased difficulty even to conduct them, designers need different tools to test alloy behaviour under driven environment. The modeling of alloys under certain types of energy inputs need to be based on the real kinetics, and must preserve classical thermodynamics.

2.5.1 Computational metallurgy

Atomistic modeling has its roots in molecular dynamics (MD) simulations [2, 9]. In MD simulation atoms and molecules are allowed to interact for a period of time by approximations of classical physics (Newton's laws of motion) and is totally deterministic. MD follows all events and is for materials science limited to small time increments due to the atomic vibrations. On contemporary computer clusters MD simulations can achieve time scales up to milliseconds in reasonable simulation times. This downside of MD was successfully solved using Monte Carlo (MC) methods. This is also called a second principles approach due to use of results from first principles methods i.e. MD, density functional theory (DFT) and *ab initio* methods to extend the time scale (cf.

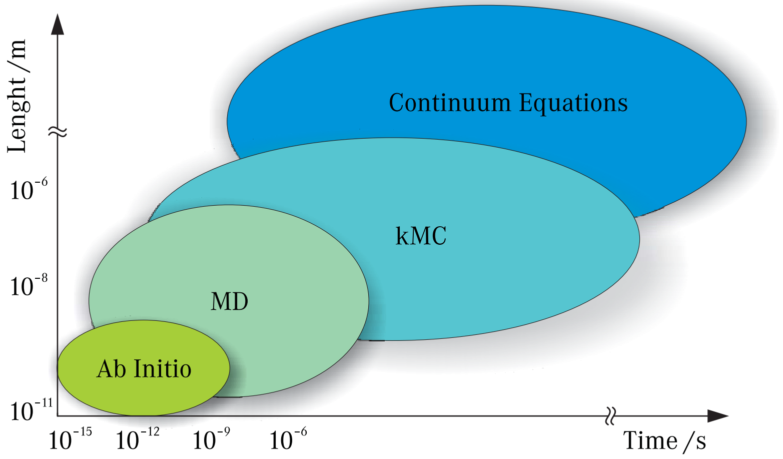

Figure 2.17: Time and dimension scales achieved using various atomistic methods

figure 2.17).

2.5.1.1 Monte Carlo methods

Nucleation of coherent precipitates in an isothermal or anisothermal environment is governed by diffusion. Atoms change sites on the crystal lattice with some frequency due to the vacancy jumps. Frequency at which jumps occur depend on the local configuration. For example, in the alloy where clustering is favoured, same atoms tend to have more energetically favourable bonds, and same pair bonds are easily formed. Atom jumps are easily simulated with a Monte Carlo (MC) simulations, where input parameters depend only on jump frequencies as functions of the local atom configuration. The set of jump frequencies defines the thermodynamics for the alloy. However, reverse is not true, as several kinetic pathways are possible for a given thermodynamics. If we define the equilibrium probability $p_e(i)$ of configuration i, and the transition probability per unit time $W(i \to j)$ from configuration i to j, detailed balance gives next equation

$$p_e(i)W(i \to j) = p_e(j)W(j \to i) \tag{2.74}$$

The atomic jumps in solids are thermally activated processes, [48], therefore it holds

$$W(i \to j) = \frac{\prod_\alpha \omega_i^\alpha}{\prod_{\alpha'} \omega_{ij}^{\alpha'}} \exp\left(-\beta(E_{ij}^{\mathrm{sp}} - E(i))\right) \tag{2.75}$$

where E_{ij}^{sp} is the saddle point energy, for which holds $E_{ij}^{\mathrm{sp}} = E_{ji}^{\mathrm{sp}}$ and ω_i and ω_{ij} are stable eigen vibrational frequencies of configuration i and at the saddle point between configurations i and j, respectively. Putting equation (2.75) in the equation (2.74) one yields

$$\frac{p_e(i)}{p_e(j)} = \exp\left(-\beta(E(i) - E(j))\right) \tag{2.76}$$

where $E(i)$ is configurational energy of state i.

More detailed explanation of the Monte Carlo methods used for simulations in the isothermal or anisothermal environment will be given in next chapter.

2.5.1.2 Cluster Dynamics

For description of the kinetic pathways several tools are available. One of them is Cluster Dynamics (CD), where the output is a time-dependent size distribution of clusters.

Cluster Dynamics is very efficient way to describe the fluctuations in the alloy at equilibrium and also relaxation towards the equilibrium. CD implies a thermodynamic model for the alloy which is viewed as a lattice gas of solute clusters, [48, 103–105]. Cluster is characterized by the number of solute atoms, vacancies or self interstitial atoms, from which it is made. Therefore, it is a set of n solute atoms, where each has at least one nearest neighbour belonging to the cluster. Each cluster with n atoms, can be arranged into several configurations. From most simple, with n atoms in a row, to the most compact. Therefore, each cluster has its own free energy. Furthermore, at the equilibrium the gas of clusters has a free energy with two distinct contributions. One is the sum of free energies of the each cluster with n atoms, and other is the mixing entropy of the same clusters on the lattice. The evolution of the number density of each type of clusters with particular number of particles n is treated under the framework of the chemical rate theory. Evolution is described by differential equations for cluster density, given by

$$\frac{\mathrm{d}C_n}{\mathrm{d}t} = \sum_m J_{m\to n} - \sum_q J_{n\to q} + G_n - K_n C_n \tag{2.77}$$

where C_n is cluster density of size n, $J_{m\to n}$ is the cluster flux from class of size m to class of the size n, given with

$$J_{m\to n} = \sum_m w_{m\to n} C_m \tag{2.78}$$

where $w_{m\to n}$ is the transition rate per unit from the class size m to the class size n. G_n is the production rate of clusters of size n and K_n is loss of the clusters of the size n at for example surfaces, dislocations or grain boundaries. K_n is accounted only in simulations with vacancies or self interstitials. When equation (2.78) is applied in equation (2.77), the evolution of the number density is then

$$\frac{\mathrm{d}C_n}{\mathrm{d}t} = G_n + \sum_m w_{m\to n} C_m - \sum_q w_{n\to q} C_n - K_n C_n \tag{2.79}$$

Cluster distributions can be solved numerically in short computation time, when number of the differential equations in the set is considered. Equation (2.79) gives a detailed description, which is important for small clusters, while for larger clusters an approximated description can be used, [104, 105].

2.5.2 Phase Field Models

Kinetics in the evolution of alloys to the equilibrium often leads through non-equilibrium states. Well known fact is that non-equilibrium states provides different physical properties of alloys which are often in advantage for engineering use. Therefore, the optimization at the mesoscopic level concentrates on the control and prediction of kinetics. Utilization of the non-equilibrium effects associated with phase transformations largely relayed on the empirical model in the past. Nowadays, high power computers allows numerical solutions for theoretical approaches that have been know for a long time, for various phase transformations, with spatial and temporal changes in the structural, chemical and crystallographic fields. These state variable are often called phase field variables.

In terms of field changes, Fick's first law can be written as

$$J = -M \frac{\partial}{\partial x} \frac{\partial f}{\partial c} \tag{2.80}$$

where, f is free energy density and M is Onsager mobility matrix. Using equation (2.80) and continuity equation

$$\frac{\partial c}{\partial t} + \frac{\partial J}{\partial x} = 0 \tag{2.81}$$

the Fick's second law can be written as

$$\frac{\partial c}{\partial t} = \frac{\partial}{\partial x} \left(M \frac{\partial}{\partial x} \frac{\partial f}{\partial c} \right) \tag{2.82}$$

which, can be interpreted as a diffusional form of more general Onsager or Ginzburg–Landau equation given as

$$\frac{\partial \psi_i}{\partial t} = -\hat{M}_{ij} \frac{\delta \tilde{F}}{\delta \psi_j} \tag{2.83}$$

where $\tilde{F}$ is the free energy functional of the functions ψ_j, t is time, $\delta\tilde{F}/\delta\psi_j$ is the thermodynamic driving force, $\hat{M}$ is the symmetric Onsager kinetic operator matrix, and $i = 1, 2, \ldots, \vartheta$ is the variable of the ϑ dynamic fields and the Einstein summation rule is implied. Equation (2.83) provides a fundamental means of describing the kinetic equations of dynamic fields as a function of the thermodynamic driving force. Although, equation (2.83) is linear with respect to the driving force, it can be nonlinear with respect to the fields ψ_i, and therefore its solution is very sensitive on the starting conditions, [106].

Mostly exploited phase field models are Chan-Hilliard, [107] and Allen–Cahn, [108] kinetic models. Both models are based on the theories of Onsager, [109, 110] and Ginzburg–Landau, [111, 112] adapted to the materials science. The Cahn–Hilliard model describes the kinetics of transformation phenomena with conserved field variables (e.g. chemical concentration). The Allen–Cahn model describes transformations with nonconserved variables (e.g. crystal orientation, long-range order, crystal structure). The original Ginzburg–Landau approach was directed at calculating electromagnetic second-order phase transition phenomena, advanced metallurgical variants are capable of addressing a variety of transformations in metals, ceramics, and polymers, such as spinodal decomposition, competitive particle ripening, non-isostructural precipitation and growth phenomena, grain growth, solidification, and dendrite formation in terms of corresponding chemical and structural phase field variables, [106].

Anyone who attempts to generate random numbers by deterministic means is, of course, living in a state of sin.

John von Neumann
(1903-1957)

3

Statistical Mechanics and Monte Carlo methods

3.1 Statistical mechanics

Statistical mechanics was initiated by Ludwig Eduard Boltzmann in 1870, [113] and deals with interpretation of the measurable macroscopic properties of matter, in terms of the properties of their constituent particles and interactions between them. In the middle of the 19^{th} century a question of burning importance was the proposed existence of the atom. This was related to use of the steam power, which was rapidly changing the world. Steam powered the factories, trains and ships of the Industrial Revolution. How to use it more effectively was of crucial significance and became the key question of the 19^{th} century science. The demand to build more powerful and efficient steam engines, in turn created an urgent need to understand and predict the behaviour of water and steam at high temperatures and pressures. Physicists believed that matter can not be infinitely divisible into ever smaller pieces and argued that ultimately everything is made of the basic building blocks - atoms. Boltzmann showed that if you imagined steam as being made of millions of tiny rigid spheres or atoms, then you could create some powerful mathematical equations.

Statistical mechanics provides a connection between the microscopic properties of individual atoms and bulk macroscopic properties of matter. Properties of every atomic/molecular system can be described at two levels, either by classical thermodynamics which is in macroscopic quantities e.g. p, V, n, c_V, H, G, etc., or at microscopic level. At microscopic level, the state of each atom/molecule is specified by using classical or quantum mechanics and is therefore very detailed. For example, in classical mechanics descriptions, 1 mole of matter contains approximately 10^{23} particles and their positions have to be updated every 10^{-15} s. This shows that both approaches are impractical. When we are performing computer simulations at an atomistic or molecular level in materials science, the bridge is needed between the microscopic properties of individual particles and the macroscopic properties of simulated material. Bridge between the over elaborate details of mechanics, and obscure generalities of the thermodynamics is statistical mechanics, which describes macroscopic quantities in the statistical terms. These statistical terms are averages or the most probable results. The name 'statistical mechanics' comes from dealing with the probabilities of the systems being in one or another state, instead of calculating exact solutions. Statistical mechanics provides an atomistic or molecular level interpretation of the macroscopic thermodynamics quantities, e.g. entropy, free energy, work and heat. It's main advantage compared to the classical thermodynamics is ability to predict macroscopic quantities based on the microscopic properties. Furthermore, entropy is a distribution function of the systems micro state in statistical mechanics, whereas in the classical thermodynamics is known only empirically, as a function of the state of a system associated with the second law of thermodynamics [114–116]. In the late 19th century L. Boltzmann initiated the kinetic theory of gases [113], following earlier work by D. Bernoulli, J. Herapath, J. P. Joule, A. K. Krönig, R. Clausius, and J. C. Maxwell. In the early 20th century this was turned into what is known today as 'statistical mechanics' through the work of J. W. Gibbs [117].

Due to an inherently probabilistic description of the system in the statistical mechanics, where the probabilities play central role of importance, the following conditions must be satisfied:

- The probability $p(A)$ of event A, must be positive $p(A) \geq 0$.
- If we have two independent events A and B, with probabilities $p(A)$ and $p(B)$, they must satisfy law of additivity $p(A + B) = p(A) + p(B)$, respectively.
- Normalization of the probabilities, where sum of all probabilities is equal to 1, $(\sum_i p_i = 1)$.

The key concept of the statistical mechanics is an ensemble, which is a collection of all microstates of the system (atoms or molecules) subject to at least one extensive constraint. The ensemble defines a probability p_i, which describes the likelihood of observing each state. For example, if we have very large collection of time evolving systems, the ensemble is formed by a snapshot of the state of each of these systems at some time instant. This key concept requires some important notions. A macrostate is defined by controllable macroscopic parameters. For example, macroscopic parameters for a thermal and mechanical system are the number of particles N, volume of the system V and total energy E. If the particles that compose the system are non interacting, the total energy E is sum of the energies ε_i of all individual particles

$$E = \sum_i n_i \varepsilon_i \tag{3.1}$$

where, n_i is i-th particle with energy ε_i. Evidently, the number of particles in the system is

$$N = \sum_i n_i \tag{3.2}$$

Quantities are differentiated between extensive, which scale linearly with V on N, and intensive which do not scale. The quantity $\Omega(N, V, E)$ is the number of microstates in a particular macrostate, and is function of N, V and E. A microstate is a particular state of the system which is consistent with the macrostate of that system. For an thermally isolated system, possible macrostate of the system have the same energy and the same probability to be in any given microstate. Any microstate will include all atom/molecule positions and momenta, consistent with N, V and E, where unconstrained extensive quantities are represented by full range of possible values. This is called a microcanonical or NVE ensemble.

Statistical mechanics rest on two fundamental postulates. The first postulate states that given isolated system in equilibrium is found with equal probability in each of its accessible microstates. This is known as *the equal a priori probability postulate* and it denotes that for possible states with the same number of particles N, the same volume V and the same energy E, all states are equally likely. The second postulate is known as the postulate of ergodicity and this declares that the time averaged properties of a thermodynamic system, i.e. the properties manifested by the collection of atoms/molecules as they proceed through their natural dynamics, are equal to the properties obtained by weighted averaging over all microstates in the ensemble and we obtain measurable macroscopic quantities. The second postulate has a practical use, since we do not exactly know in which one of the Ω microstates the system is in, at the time of interest, we simply average equally over all microstates.

Another important statistical mechanics notion is the principle of detailed balance, cf. equation (3.3), which is saying that the transition rate from one microstate to another must be equal to the rate of the reverse process

$$\pi_i P_{ij} = \pi_j P_{ji} \tag{3.3}$$

where π_i and π_j are the equilibrium probabilities of being in states i and j, respectively. P_{ij} is transition probability from the state i to j and P_{ji} is transition probability of reverse process.

3.1.1 Entropy

Classical thermodynamic definition of entropy was introduced by R. Clausius in 1865, and is defined as the amount of heat reversibly exchanged at a temperature T, cf. equations (3.4) and (3.5). For reversible processes entropy is;

$$dS = \frac{\partial Q_{rev}}{T} \tag{3.4}$$

For an arbitrary transformation, entropy is

$$S_1 - S_0 \geq \int_0^1 \frac{\partial Q}{T} \tag{3.5}$$

where the equality is valid, if the transformation is reversible. If a system is thermally isolated the entropy never decreases $S_1 - S_0 \geq 0$, where the equality holds if transformation is reversible [118]. As it was already mentioned, entropy in classical thermodynamics is known empirically. Besides this classical definition which do not make reference to the microscopic nature of the system, also exists statistical mechanics definition. Latter was developed from analysis of the statistical behaviour of the microscopic constituents of the system by L. Boltzmann in the late 19^{th} century [113]. Boltzmann showed that the thermodynamic entropy is identical to the statistical, scaled by constant number k_B, now known as Boltzmann's constant ($8.617343(15) \times 10^{-5}$ eV K^{-1}). The entropy in the statistical mechanics is essentially a measure of the number of states in which the system can be arranged. In the statistical mechanics the entropy is governed by the probability, and therefore allows for a disorder decrease even in the closed systems. More specifically the entropy

$$S = -k_B \ln \Omega \tag{3.6}$$

is logarithmic measure of the total number of microstates consistent with the given macrostate, Ω. Equation (3.6) is famous Boltzmann equation of entropy, where all probabilities are the same. If we treat probabilities individually the entropy, is called Gibbs entropy

$$S = -k_B \sum_i p_i \ln p_i \tag{3.7}$$

and is logarithmic measure of the density of states, summed over all the microstates the system can be in, multiplied with the probability distribution p_i that the system is in a particular microstate i with energy E_i. By functional optimisation from the Gibbs entropy, the probability distribution p_i for the system can be derived. Contrary to the classical thermodynamics definition of entropy in the statistical mechanical description, the temperature or heat does not appear in the definition.

3.1.2 Statistical ensembles and partition function

A system with given macrostate (N, V, E), is equally likely to be in any one of the distinct microstates, at any time t. As time advances, the system evolves from one mircrostate to the another. Each considered microstate is represented in its phase space as a representative point (q_i, p_i). In an ensemble of systems, as time passes, every member of the ensemble undergoes a change of microstates. This means that the representative points move along their trajectories.

Now we need to define a density function $\rho(q, p, t)$ in a way that, at any time t, the number of representative points in the volume element $(d^{3N}qd^{3N}p)$ around the point (q, p) of the phase space is given with $\rho(q, p, t)d^{3N}qd^{3N}p$. This density function represents how the members of the ensemble are distributed over all possible microstates at particular time. At an equilibrium, the ensemble is stationary if the density function ρ, does not depend on the time explicitly

$$\frac{\partial \rho}{\partial t} = 0 \tag{3.8}$$

According to the Liouville's theorem which states; *the distribution function is constant along any trajectory in phase space* in terms of the Poisson brackets, it holds

$$\frac{d\rho}{dt} = \frac{\partial \rho}{\partial t} + \rho, H = 0 \tag{3.9}$$

This means that the local density of the representative points, according to an observer moving with a representative point, stays constant in time. For the system in the equilibrium, it states

$$\rho, H = \sum_{i=1}^{3N} \left(\frac{\partial \rho}{\partial q_i} \dot{q}_i + \frac{\partial \rho}{\partial p_i} \dot{p}_i \right) = 0 \tag{3.10}$$

and demonstrates the conservation of the density in the phase space.

3.1.2.1 General statistical ensembles

In the statistical mechanics three general types of ensembles are usually applied, ordered by increased complexity:

- **Microcanonical ensemble** - fixed N, V and E, corresponds to an isolated system. With constant energy E the system can not exchange energy or mass with its surroundings.
- **Canonical ensemble** - fixed N, V and T describes a system in thermal equilibrium with environment. This system is allowed to exchange heat with the surroundings.
- **Grand canonical ensemble** - fixed V, T and μ corresponds to an open system. The system as such is able to exchange energy and mass with the outside.

Table 3.1: Summary of microcanonical, canonical and grand canonical ensembles

	Microcanonical	Canonical	Grand canonical
Constant variables	N, V, E	N, V, T	V, T, μ
Microscopic features	Number of microstates Ω	Canonical partition function $Z = \sum_k e^{-\beta E_k}$	Grand canonical partition function $\Xi = \sum_k e^{-\beta(E_k - \mu N_k)}$
Macroscopic function	$S = k_B \ln \Omega$	$F = -k_B T \ln Z$	$F - G = -pV = -k_B T \ln \Xi$

In Table 3.1 summary of properties for these three mostly used ensembles in statistical mechanics is presented. Although, only three basic statistical ensembles are presented, the number of various ensemble types is unlimited. When somebody is constructing specific ensemble, they just need to follow rules for good ensembles.

3.1.2.2 Canonical ensemble

Since all simulations herein were performed under the canonical ensemble, this ensemble is described in more detail. The macrostate of the canonical ensemble is characterized by N, V, T. The number of particles N, a volume V and a temperature T, are fixed for all systems in the same ensemble. The fixed temperature T of the system is easily controllable by keeping the system in contact with a heat reservoir or heath bath. The energy E of the system is in the canonical ensemble a variable and can in principle have values on interval $[0, \infty]$. The probability p_i of finding the system in a particular microscopic state, with an energy E_i at any time t, is given by Boltzmann distribution. If we consider a system A with the energy E in a very large heat bath A' with an energy E' and $E^{(0)} = E' + E$. $E^{(0)}$ is constant, since the combined system is isolated. Note that heat bath is very large, thus E'_i is almost constant and have number of microstates $\Omega'(E'_i)$. The probability p_i, of the system A being in the i-th state is proportional to the corresponding number of microstates

$$p_i \propto \Omega'(E'_i) \equiv (E^{(0)} - E_i) \tag{3.11}$$

Probability p_i can be written as

$$p_i = C'\Omega'(E'_i) \tag{3.12}$$

where C' is constant. The logarithm then gives

$$\ln p_i = \ln C' \ln \Omega'(E'_i) = \ln C' \ln \Omega'(E^{(0)} - E_i) \tag{3.13}$$

Since E_i is small compared to $E^{(0)}$, it can be expanded in a Taylor series around the energy $E^{(0)}$, which yields

$$\begin{aligned} \ln \Omega'(E'_i) &= \sum_{k=0}^{\infty} \frac{\left(E_i{}' - E^{(0)}\right)^k}{k!} \frac{\partial^k \ln \Omega'(E^{(0)})}{\partial E'^k} \\ &= \ln \Omega'(E^{(0)}) - \frac{\partial}{\partial E_i{}'} \ln \Omega'(E^{(0)}) E_i + \cdots \\ &= \text{const} - \beta' E_i. \end{aligned} \tag{3.14}$$

where,

$$\beta = \frac{\partial \ln \Omega'(E^{(0)})}{\partial E'} = \left.\frac{\partial \ln \Omega'(E')}{\partial E'}\right|_{E'=E^{(0)}} \tag{3.15}$$

Note that, in equilibrium, $\beta' = \beta = a/kT$. So,

$$p_i \propto \exp(-\beta E_i) \tag{3.16}$$

and finally,

$$p_i = \frac{\exp(-\beta E_i)}{\sum_r \exp(-\beta E_i)} \tag{3.17}$$

It also holds

$$p_i = C \exp(-\beta E_i) \tag{3.18}$$

which is useful to obtain a partition function of the canonical ensemble. Therefore, normalization of the probabilities is required and gives

$$\sum_i p_i = 1 = C \sum_i \exp(-\beta E_i) \quad \Leftrightarrow \quad C = \frac{1}{\sum\limits_i \exp(-\beta E_i)} \equiv \frac{1}{Z(\beta)} \tag{3.19}$$

where Z is the partition function of the canonical ensemble.

In relation to the other ensembles, a generalization of the canonical ensemble is a grand canonical ensemble, where the system can exchange particles and energy.

3.1.2.3 Partition function

It was already stated, that description of the physical system is based in statistical mechanics on the ensemble which represents all possible configurations of the system in question and the probabilities when each configuration is possible. Each ensemble is connected to the macroscopic properties of the system. Macroscopic quantities can be obtained by suitable averaging of the properties of the microscopic states in the ensemble, rather than as a time average over a dynamic trajectory. The key is to average with the correct weights. These weights are known as a partition function and have very descriptive name in German language (*zustandssumme*), meaning "sum over states". Due to the fact, that they normalize the weights, thus representing a sum over all microstates of the ensemble. Other important equations are bridge equations, which relate partition functions to their thermodynamic potentials. General form of the partition function for the classical system is

$$Z = \sum_{\text{all states}} \exp(\beta\, \mathcal{H}) \tag{3.20}$$

where $\mathcal{H}$ is the Hamiltonian of the system and $\beta = \frac{1}{k_\mathrm{B} T}$. The sum in equation (3.20) goes over all possible states of the system, [116]. The partition function also determines the probability of any particular state of the system. The probability that the system is in i-th state is

$$p_i = \exp\left(\frac{\beta\, \mathcal{H}(i)}{Z}\right) \tag{3.21}$$

where, $\mathcal{H}(i)$ is the Hamiltonian of the i-th state.

There exist several different types of the partition functions, each corresponding to their own statistical ensemble. For example, the canonical partition function applies to the canonical ensemble.

3.1.3 Ising Model

The Ising model is very simple statistical mechanics model used to imitate interaction of the individual elements with others in their neighbourhood. It was invented in 1920 by W. Lenz and solved in one dimension, where no phase change is permitted, in 1925 by his student E. Ising [119], after whom it is named. Model was originally invented as a mathematical model of a ferromagnetism, which is why it consists of discrete variables that can be in one of the two states e.g. 1 and $\bar{1}$. These variables are called spins and are arranged in a lattice where they can interact with its neighbours. Although the model was originally intended as a model of ferromagnetism it was soon discovered that it can be used for description of the condensation phenomena in the two dimensional systems, formed by adsorption of gases on the surfaces. The detailed analytic solution of the 2D square lattice Ising model was proposed in 1944 by L. Onsager, [120]. After that more simple and elegant methods involving a transformation matrix were proposed, [121, 122].

The 2D Ising model can be used for the phase transformations study. Furthermore, it is one of the simplest statistical models, which exhibits phase transformation. Ising model has been extensively used for modeling phase separation in the binary alloys. In the square lattice Ising model configuration with dimensions L, the total number of spins is equal to $N = L \times L$. In the simplest form, the interaction range is restricted to immediately adjacent sites with Hamiltonian for a specific spin site i given by

$$\mathcal{H}_i = -J_{ij} \sum_{ij} \sigma_i \sigma_j - H \sum_{i} \sigma_i \tag{3.22}$$

where, the sum ij runs over the nearest neighbours of i. J is the coupling constant between the nearest neighbours, and σ_i and σ_j are respective nearest neighbour spins with value either 1 or $\bar{1}$. H represents external influence on the model. When Ising model is adapted for crystalline systems, J_{ij} represents bond strength, σ represents either atom (1) or vacancy ($\bar{1}$), and H is equal to the chemical potential μ.

3.2 Boundary Conditions

Computer simulations are usually performed on a finite lattice systems with 10^3 to 10^8 atoms. These systems have boundaries or edges, and important question is how to treat boundaries of the lattice. The boundary condition problems can be avoided by employing a periodic boundary conditions, [123]. System in a box is replicated throughout the space to form infinite lattice. During simulation, when atom or molecule moves in the original box, its periodic image in each of the neighbouring boxes moves exactly the same. When atom leaves original box, one of its periodic images enters in, through the opposite face. If same condition is used on all free edges of the simulated system, full periodic boundary conditions are used. In figure 3.1, a 2D full periodic system is shown. Atoms can enter and leave each box, across each of the four edges.

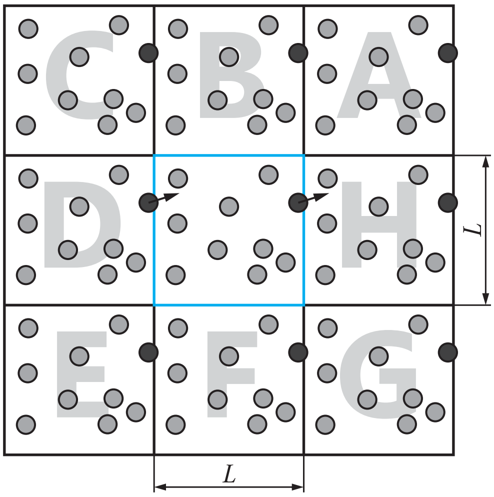

Figure 3.1: Two dimensional periodic conditions system.

With the periodic boundary conditions (PBC), simulation box of a finite size acts like a system of an infinite one. However, special care need to be put to recognize possible periodicity effects i.e. the simulation box must be large enough to avoid any such effects.

3.3 Monte Carlo methods

Modern use of the Monte Carlo methods began in Los Alamos laboratories during late 1940s and early 1950s [10, 11]. Name of these methods comes after casino in Monte

Carlo, due to use of the random numbers (true or pseudo random numbers) to accept or reject events. Nowadays, all methods based on the use of random numbers are called MC. Simulations based on the MC methods are used widely in science, [98, 99, 116, 124]. In molecular modeling these methods represent alternative to less averaged Molecular Dynamics. MC methods are distinguished from other deterministic algorithms by being stochastic, i.e. non deterministic due to use of the random numbers. In physical sciences, the Monte Carlo methods are useful for studying systems with a large number of coupled degrees of freedom, e.g. gases, liquids, disordered materials, strongly coupled solids, cellular structures, etc. They are also broadly used in mathematics for calculation of the definite integrals, especially complicated boundary conditions multidimensional integrals and in economics and business for risk modeling. Although, credit for invention of the Monte Carlo method is often given to Stanislav Ulam, the first sampling method was used long before, during the 18th century (Georges-Louis Leclerc, Comte de Buffon, 1777) and is known as Buffon's needle experiment. In Buffon's experiment a needle of lenght L was dropped many times onto a surface marked with equidistant parallel lines with distance between them d. If d is greater than L ($d > L$) the probability of the needle intersecting a line is

$$p = \frac{2L}{\pi d} \tag{3.23}$$

Laplace, pointed out years later that this experiment could be used as a crude tool for estimation of the value of π.

3.3.1 Monte Carlo integration

As already mentioned, the Monte Carlo methods were initially developed as a method for approximate calculation of complex definite integrals, usually multidimensional integrals, which could not be solved analytically. If we consider one dimensional integral on a closed interval $[a, b]$ given by equation

$$I = \int_a^b f(x)\mathrm{d}x \tag{3.24}$$

Figure 3.2 depicts function for which we want to obtain definite integral (grey area). To calculate an integral estimate, the simplest method to use is the use of *acceptance-rejection* method, named also hit-and-miss method. First, bounding box is needed, extending from $[a, b]$ and $[0, y_0]$, where y_0 needs to exceed maximum value of the function

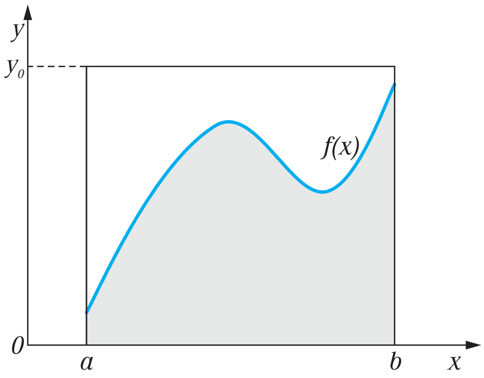

Figure 3.2: Schematic representation of MC integration method to determine grey area.

on the interval. From use of the uniformly distributed random numbers, we hit our box with N hits, and count the number of hits N_0, which fall below the curve $f(x)$, for each value x on our interval. The integral estimate is

$$I \approx I_E = \frac{N_0}{N} \times (y_0(b-a)) \tag{3.25}$$

given by the fraction of points which fall below the curve, multiplied by the area of the bounding box. The integral estimate converge to the exact value of integral as $N \to \infty$. This method for solving integrals is an example of the simple sampling Monte Carlo method. Simple problem often attacked using this method is numerical calculation of π.

Integral estimate can also be obtained by the mean value theorem following next equation

$$I_E = \frac{(b-a)}{N} \sum_{i=1}^{N} f(x_i) = (b-a)\bar{f} \tag{3.26}$$

where, x_i needs to cover range of the integration fully, and $\bar{f}$ is the mean value of f over the set of the sampled points. In the limit where $N \to \infty$, estimate converge to the exact value. Standard deviation of the integral estimate is given by

$$\sigma = \sqrt{\frac{\frac{(b-a)}{N} \sum_{i=1}^{N} f^2(x_i) - I_E^2}{N-1}} \tag{3.27}$$

Integration error decreases as $1/\sqrt{N}$ and is independent of the integral dimensionality.

3.3.2 Importance sampling

Simple Monte Carlo integration scheme uniformly sample points, and due to this can have low efficiency. Many functions have a significant weight only in a few regions. Low efficiency of the uniform sampling for such functions is overcome with an importance sampling. In statistics, importance sampling is a general technique for estimating properties of a particular distribution, while only having samples generated from a different distribution rather than the distribution of interest. For example, normal probability distribution function (Gaussian) have most of contributions to the integral near the central peak, while tails do not contribute much. Integration of Gaussian is much more efficient using importance sampling, where points are sampled with a non-uniform always positive distribution $w(x)$.

The integral I, is evaluated by selecting points from the probability distribution $p(x)$, given by

$$I = \int_a^b g(x)p(x)\mathrm{d}x \approx \frac{1}{N}\sum_{i=1}^{N} g(x_i) \tag{3.28}$$

where, $g(x) = f(x)/p(x)$. Sampling points x_i, are generated from the probability distribution $p(x)$, given by

$$p(x) = \frac{w(x)}{\int_a^b w(x)\mathrm{d}x} \tag{3.29}$$

Standard deviation defined in equation (3.27) is greatly reduced, if $f(x)$ is well described by $w(x)$ and integration procedure is much more efficient. Similar to uniform sampling method, integration error also decreases as $1/\sqrt{N}$.

3.4 Markov Master Equation

The system is evolved according to a stochastic algorithm in a way that the entire simulation space or all possible accessible states are explored. These stochastic attempts in order to change the system state are not connected to the underlying energy barriers. The MC methods follow a Markov process to evolve a given system towards equilibrium. Time evolution of the probability density is given by a Markov Master Equation, which is for evolution of the dynamical process, given by

$$\frac{\partial P(\sigma_f, t)}{\partial t} = \sum_{\sigma_i} P(\sigma_i, t)W(\sigma_i \to \sigma_f) - \sum_{\sigma_i} P(\sigma_f, t)W(\sigma_f \to \sigma_i) \tag{3.30}$$

where, σ_i and σ_f are initial and final, successive states of the system. $P(\sigma, t)$ is probability that the system is in the state σ at time t. $W(\sigma_f \rightarrow \sigma_i)$ is transition probability per unit time, where system undergoes transition from σ_i to σ_f. The strength of the Monte Carlo methods is in freedom of choosing allowed moves form $i \rightarrow f$. Due to this freedom, MC methods can be used to bridge various levels of description in the statistical mechanics, [125].

In steady-state, where $\partial P(\sigma_f, t)/\partial t = 0$, the system must ensure phenomenological argument of detailed balance, i.e. that sum of all transitions into the state σ, equals sum of all transitions out of the state. The detailed balance criterion given by equation (3.3), and must be obeyed, can be for this case written as

$$P(\sigma_i, t = \infty)W(\sigma_i \rightarrow \sigma_f) = P(\sigma_f, t = \infty)W(\sigma_f \rightarrow \sigma_i) \tag{3.31}$$

The probability of a system in steady-state is given with $P(\sigma_f, t = \infty) = P_{ss}(\sigma_f)$. The detailed balance criterion can be applied to any probability distribution. However, if the Boltzmann distribution is chosen, the transition probabilities are sensitive to an energy barrier $H(\sigma)$ scaled by thermodynamic factor β (cf. Nomenclature) and can be expressed as

$$P(\sigma, t = \infty) = \frac{1}{Z} \exp\left(-\beta H(\sigma)\right) \tag{3.32}$$

where, $H(\sigma)$ is the Hamiltonian of the system and Z is the partition function. Probability in equation (3.32) is usually not exactly known due to the partition function Z. This difficulty can be overcomed by generating a Markov chain of states, that is to generate new state from preceding. Furthermore, transition probability depends only on the difference of Hamiltonians of the initial and final states, therefore

$$\frac{W(\sigma_i \rightarrow \sigma_f)}{W(\sigma_f \rightarrow \sigma_i)} = \frac{P(\sigma_f, t = \infty)}{P(\sigma_i, t = \infty)} = \frac{\frac{1}{Z} \exp\left(-\beta H(\sigma_f)\right)}{\frac{1}{Z} \exp\left(-\beta H(\sigma_i)\right)} = \exp\left(-\beta \Delta E\right) \tag{3.33}$$

3.5 Monte Carlo methods in statistical physics

Monte Carlo (MC) methods are employed in many areas of statistical physics as a methods to solve master equation (3.30). They have been largely used to obtain equilibrium properties of the modeled systems, but in recent years they were also utilised for studying of the kinetic properties of the systems, [126].

Monte Carlo (MC) simulations are appropriate for the description of the precipitation on the atomic level, as they do not need assumptions about shape and composition of the nuclei. Usage of the method started in the fifties of the last century to calculate the thermodynamic quantities, [11]. Development of the system using the Metropolis Monte Carlo method is based on probabilities of possible events. Mayor step forward was development of the residence time algorithm, [127–129], which enabled a detailed study of kinetic decomposition and ordering in alloys, with comparison between the simulation time and the real time. From this point on, MC methods which describe time development of the system are called kinetic Monte Carlo (kMC). Progress was then introduction of vacancies in the systems, which in turn allowed simulation of the substitutional diffusion, [130, 131]. Introduction of equilibrium concentration of vacancies in the system, [12, 13], allowed the description of the actual kinetic pathways and comparison with experiments. This was first used for phase transformations in the binary alloys, [12, 17, 20, 22, 23], ternary alloys, [15, 16, 19, 26, 31, 38], quaternary alloys, [24, 132] and in alloys with even more substitutional elements, [14]. A further improvement was introduction of interstitials in the Fe-Nb-C alloy, [28], in the Fe-Y-O alloy, [36] and in the Fe-Ti-O alloy, [37], to study homogeneous precipitation. Next development step was introduction of dislocation and grain boundaries to study precipitation kinetics in the Fe-Nb-C alloy, [32, 33], in the Fe-C alloy, [34], and in the Ni-Al alloy, [35].

3.5.1 Metropolis Monte Carlo algorithm

There are many possible choices of the transition rate which satisfies the detailed balance criterion. Each of them, provides a dynamic method of generating an arbitrary probability distribution. The first transition rate choice used in statistical physics was proposed by Metropolis [11]. In his algorithm, configurations are generated from a previous state, using transitional probabilities dependant on the initial and final state energies. Metropolis MC can not be regarded as process that simulates real time, and evolution of the system is described using Monte Carlo Steps (MCS) and is non deterministic. Nevertheless, Metropolis MC (MMC) is useful as it generates correlated states due to the sequential Markov chain process. In brief, the Metropolis MC is an algorithm which determines whether a process will happen or not. In the Metropilis MC transition or walk from state σ_i to state σ_f, accompanied by an energy change $\Delta E = H(\sigma_f) - H(\sigma_i)$ is executed if $\Delta E \leq 0$. If $\Delta E > 0$ then random number $\rho \in [0, 1)$ decides if transition is executed or not based on

$$\rho < e^{-\beta \Delta E} \tag{3.34}$$

to accept and

$$\rho > e^{-\beta \Delta E}$$

to reject the transition. If one translates this to a diffusion process, the transition rates depend sensitively on the energy barrier ΔE scaled by thermodynamic β. Note, the fact that all transitions where $\Delta E \leq 0$ are accepted, the Metropolis algorithm does not express the real dynamics of the system.

In the Metropolis Monte Carlo method configurations are generated with Markov chain from previous state and depends solely on the energy difference between states. The sequence of states produced, follows a time ordered path. However, this time is non-deterministic and known as Monte Carlo time, [116]. All transition probabilities which satisfies detailed balance (equation (3.3)) are acceptable. Metropolis suggested following form of equations for the transition probabilities, [11]

$$\begin{aligned} W(\sigma_i \to \sigma_f) &= \tau^{-1} \exp\left(-\beta \Delta E\right) \qquad &\longrightarrow \qquad &\Delta E > 0 \\ W(\sigma_i \to \sigma_f) &= \tau^{-1} \qquad &\longrightarrow \qquad &\Delta E \leq 0 \end{aligned} \tag{3.35}$$

where $\Delta E = H(\sigma_f) - H(\sigma_i)$ and τ is the time required for transition. τ is often set equal to unity and is hence suppressed in the equations. If $H(\sigma_f) > H(\sigma_i)$ then it holds

$$\frac{W(\sigma_i \to \sigma_f)}{W(\sigma_f \to \sigma_i)} = \frac{\exp\left(-\beta(H(\sigma_f) - H(\sigma_i))\right)}{1} = \exp\left(-\beta(H(\sigma_f) - H(\sigma_i))\right) \tag{3.36}$$

else if $H(\sigma_f) < H(\sigma_i)$ then it holds

$$\frac{W(\sigma_i \to \sigma_f)}{W(\sigma_f \to \sigma_i)} = \frac{1}{\exp\left(-\beta(H(\sigma_i) - H(\sigma_f))\right)} = \exp\left(-\beta(H(\sigma_f) - H(\sigma_i))\right) \tag{3.37}$$

This shows that Metropolis Monte Carlo algorithm generates a new configuration σ_f from a previous configuration σ_i so that the transition probability $W(\sigma_i \to \sigma_f)$ satisfies the detailed balance condition. Simulations in which the Metropolis Monte Carlo algorithm is implemented follows next general scheme, [116]:

1. Choose an initial state,
2. Choose a event i,
3. Calculate the energy change ΔE associated with event i,
4. Generate random number ρ, which satisfies $0 < \rho \leq 1$,
5. If $\rho < \exp(-\beta \Delta E)$, execute event,

6. Go to the next event and repeat from 3.

3.5.2 Glauber and Kawasaki Dynamics

Other choices for determining the transition probabilities are Glauber and Kawasaki dynamics. The Glauber dynamics, [133] is a birth and death process, known also as spin-flip, where particles are constantly created and they also constantly disappear. The transition probability from initial to final state is given by

$$W(\sigma_i \to \sigma_f) = \frac{\exp(-\beta \Delta E)}{1 + \exp(-\beta \Delta E)} \tag{3.38}$$

Although, algorithm ensure convergence to the equilibrium, it does not always include sufficient accuracy of the kinetics compared to the real system. In the kinetic Ising model, Glauber transition probability is given as

$$W(\sigma_i \to \sigma_f) = \frac{1}{2}\left[1 - \sigma_i \tanh(\beta E_i)\right] \tag{3.39}$$

where $E_i = J \sum_{i,f} \sigma_f$. In general, the probability of an event depends on the configuration of all other spins and the heat bath temperature.

On the contrary in Kawasaki dynamics, [134] interacting particles are allowed to attempt simultaneous position exchange, so that the particle or spin number is conserved. Kawasaki model is also called spin-exchange. Exchange happens if the transition probability, given by

$$W(\sigma_i \to \sigma_f) = \frac{\exp\left(-\frac{\Delta E}{2T}\right)}{\exp\left(\frac{\Delta E}{2T}\right) + \exp\left(-\frac{\Delta E}{2T}\right)} \tag{3.40}$$

is larger than a random number $\rho \in [0, 1)$.

3.5.3 Thermally activated processes

Thermally activated processes are barrier controlled, where barrier depends on initial and final positions. The transition probability for thermally excited process is given as

$$W(\sigma_i \to \sigma_f) = \frac{\omega(\sigma_i \to \sigma_f)}{\tau} = \exp(-\beta E(\sigma_i, \sigma_f)) \tag{3.41}$$

where, $\omega(\sigma_i \to \sigma_f)$ is the probability of success, for thermally activate barrier crossing in average time τ.

3.6 Kinetic Monte Carlo method

Kinetic properties of the system requires establishment of definite relationship between Monte Carlo step and time. It will be shown that Poisson process addresses this relationship through the transition probabilities with physical background. Therefore, a kinetic Monte Carlo (kMC) or in chemistry dynamic Monte Carlo, addresses physical problems where outcome is governed by the local configuration of the system or energy barriers between possible states. Dynamics or evolution of the system is controlled by these transition rates. The kMC simulations have direct correlation to the real time, compared to Monte Carlo Steps (MCS) in Metropolis Monte Carlo simulations. Furthermore, kinetics of an individual atoms or molecules is modeled, but only in a coarse grained way representing average which could be obtained by the Molecular Dynamics simulations.

Compared to the Metropolis algorithm, the key element of kMC algorithm is the n-fold way algorithm or residence time algorithm [127–129]. The residence time algorithm enabled a detailed study of kinetic decomposition and ordering in alloys and utilizes deterministic time. From this point forward MC methods which describes time evolution of the system are called kinetic Monte Carlo (kMC). In the algorithm, an event i can be characterized by the transition probability or transition rate Γ_i. If the input transition probabilities are correct, the physical processes associated with states are stochastic, where events occur continuously and independent of one another (*Poisson process*). Associated times of the events must be constructed from the appropriately weighted probability distributions of all possible outcomes. Furthermore, this coarse graining of events and time, assumes that each event i, can be characterised with an average transition probability Γ_i. Considering this, any transition possible at time t is also possible at any later time $t + \Delta t$ with the uniform probability and independent of previous events. By the definition, this is a Poisson process, consistent with Master equation (3.30) and is given by the Poisson distribution

$$P(n_i) = \frac{(\Gamma_i t)^{n_i}}{n_i!}\, \mathrm{e}^{-\Gamma_i\, t} \tag{3.42}$$

where, n is a random variable counting number of the event i, occurred within time t. Useful feature of the Poisson process is that an ensemble of the independent processes will behave as one large process. That enables a formulation of the statistical properties of the ensemble in terms of the dynamics of the individual processes. For example, if there are k types of possible events with rates $\Gamma_1, \Gamma_2, \Gamma_3, \ldots, \Gamma_i, \ldots, \Gamma_k$ then total number of all events ($n = \sum_{i=1}^{k} n_i$) which occur in time t, is a Poisson distribution with the total rate $\Gamma = \sum_{i=1}^{k} \Gamma_i$. Thus, ensemble given by the Poisson distribution is following

$$P(n) = \frac{(\Gamma t)^n}{n!}\, \mathrm{e}^{-\Gamma t} \tag{3.43}$$

Events with larger transition probabilities will dominate, while possible events with lower transition probabilities will be rare. Simulation of thermodynamic equilibrium is possible, if transitions follow detailed balance, described earlier. Additional important attribute of the Poisson process is that the probability density of time t between successive event is

$$P(t) = \Gamma e^{-\Gamma t} \tag{3.44}$$

which, enables correlation between time and MC steps for evolution of the system. From the probability density can be shown, that mean time between successive events is $\bar{t} = 1/R$. Equation (3.44) gives an exponential distribution of time between the events, which can then be sampled to determine required time for the event to happen. This time $T(\tau)$, needed for the event to occur is obtained by integrating equation (3.44) over time

$$T(\tau) = \int_0^{\tau} \mathrm{d}t'\, \Gamma \mathrm{e}^{-\Gamma t'} = 1 - \mathrm{e}^{-\Gamma \tau} \tag{3.45}$$

where, a random variable $U = \mathrm{e}^{-\Gamma \tau}$ is uniformly distributed between $[0, 1]$ and allows us to obtain the MC time τ between successive events

$$\tau = \frac{-\ln U}{\Gamma} \tag{3.46}$$

This random sampling of the Poisson time distribution for each executed event, ensures establishment of a direct and unambiguous relationship between MC steps and MC time.

In the simulations, the following expression

$$\Delta t = -\frac{\ln \rho_2}{\Gamma} \tag{3.47}$$

yields residence time, where $\rho_2 \in (0, 1]$ is random number. The residence time is amount of time waited before the event occurs. Total time is sum of the all residence time increments of each step. Generated random numbers must never have value 0 as if $\rho_1 = 0$, there is no event to be executed. If $\rho_2 = 0$ we can not calculate time addition due to the nature of logarithmic function, which is not defined for argument 0. Special care is required toward generation of the random numbers, which need to satisfy several conditions:

- They need to be random or at least pseudo random.
- In order to reproduce results they need to be reproducible.
- In order to avoid interdependence of the results they need to be long periodic.

Although some might argue that by including the random number, the stochastic nature of the process can better be described, this is due to to the fact that the calculation of random numbers using some sort of the numerical algorithm, is time consuming and demanding, the same results can also be obtained using

$$\Delta t = \frac{1}{\Gamma} \tag{3.48}$$

For the thermally activated processes, studied in the framework of this thesis, the probability per unit time for transition to occur, depends sensitively on the energy barrier ΔE, scaled by temperature $\mathrm{k_B}T$, cf. section 3.5.3. The transition probabilities for each possible event i, at temperature T are given by

$$\Gamma_i = \nu_{ij} \exp\left(-\frac{\Delta E_{ij}}{k_\mathrm{B}T}\right) \tag{3.49}$$

where, ΔE_{ij} is energy barrier, needed to get from the stable position i, through the saddle point to the stable position j, cf. figure 2.10. ν_{ij} is an attempt frequency for possible event i, (cf. equation (2.31)). Figure 3.3 shows schematic representation of energies needed to calculate barrier energy ΔE_{ij}.

In the framework of kMC simulations of diffusion models for calculation of the transition probabilities it is important to distinguish between the energy difference between an initial and a final configuration $\Delta E = E_i - E_f$, and the migration barrier between the two configurations depending on direction $\Delta E_\mathrm{mig} = E_\mathrm{SP} - E_i$ or $\Delta E_\mathrm{mig} = E_\mathrm{SP} - E_f$, [135]. With the energy difference between an initial and a final configuration only equilibrium probabilities of the configurations are controlled. In the second case the migration barrier controls the equilibrium and kinetic properties of the configurations. Equation (3.49) is derived from the theory of thermally activated processes and can be used justifiable, if thermal fluctuations are smaller than the barrier energies ($k_\mathrm{B}T \ll \Delta E_{ij}$). The transition probabilities required as input data in the residence time kMC algorithm depends on the thermodynamic (E_i and E_f) and kinetic (ν an E_SP) parameters. The thermodynamic parameter is an interaction energy or an interatomic potential of the states needed to obtain an energy barrier between two states.

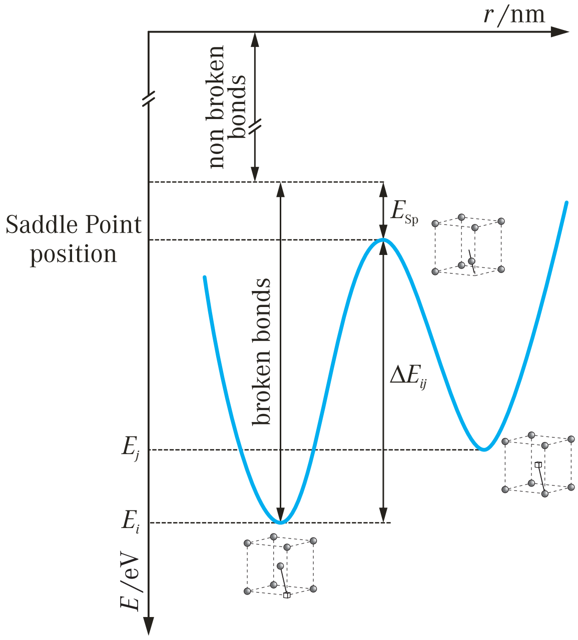

Figure 3.3: Schematic representation of migration barrier energy for broken bond model.

Estimation of the interaction energies can be done with help of the phase diagrams for various temperatures using mean field approximation. More accurate pairwise energies are calculated with the quantum methods like density functional theory (DFT) or temperature accelerated molecular dynamics (TAD). Other option include readings from the potential energy surfaces (PES).

Kinetic adjustment of the model can be achieved through the attempt frequencies ν_{ij}, and saddle point energies E_{Sp}, through evaluation of the diffusion coefficients.

The kMC method is appropriate for studying diffusion processes at the atomic scale in the material science. The residence time algorithm (cf. Fig. 3.4), essential for the kinetic Monte Carlo simulations of the real system dynamics, can be summarized as follows:

1. Set the time to zero; $t = 0$.
2. Form a list of all possible events and probability rates.
3. Calculate cumulative distribution rate $\Gamma = \sum_{i=1}^{k} \Gamma_i$ for $k = 1, \ldots, N$, where N is total number of possible events in one transitions.

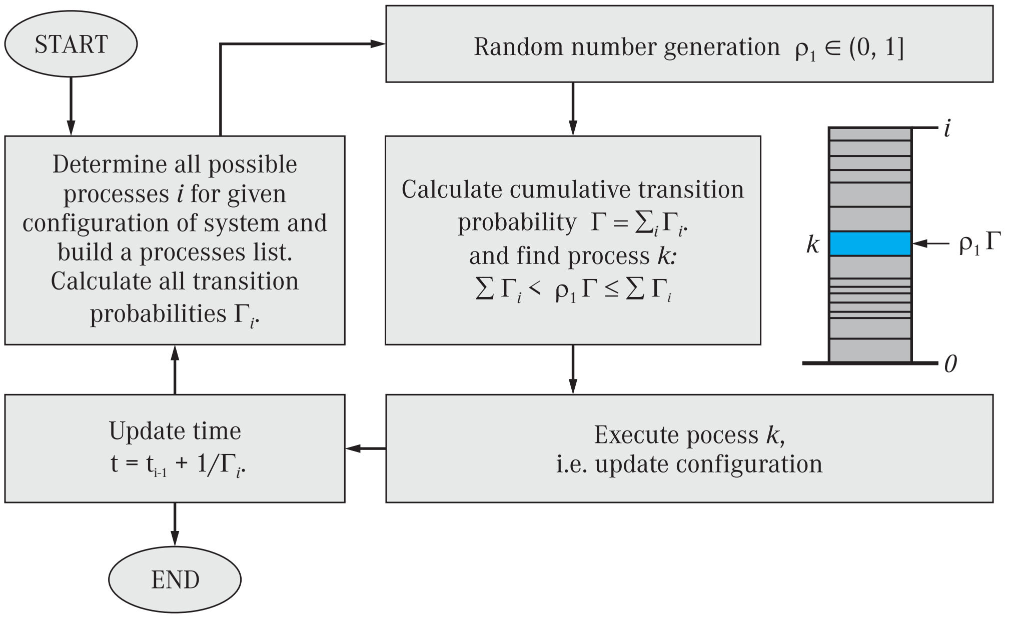
START
Random number generation $\rho_1 \in (0, 1]$
Determine all possible processes i for given configuration of system and build a processes list. Calculate all transition probabilities Γ_i.
Calculate cumulative transition probability $\Gamma = \sum_i \Gamma_i$. and find process k: $\sum \Gamma_i < \rho_1 \Gamma \leq \sum \Gamma_i$
i
k
$\rho_1 \Gamma$
0
Update time $t = t_{i-1} + 1/\Gamma_i$.
Execute pocess k, i.e. update configuration
END

Figure 3.4: Flow chart of kinetic Monte Carlo simulation

4. Get two uniform random numbers $\rho_1, \rho_2 \in (0, 1]$.
5. Find the event k to execute that satisfies $\Gamma_{i-1} < \rho_1 \Gamma \leq \Gamma_i$. Detailed representation of this step is depicted in Fig. 3.5 for process with eight possible events or transitions.
6. Execute event k.
7. Update the time with $t = t + \Delta t$.
8. Recalculate all probability rates Γ_i for changed system.
9. Iterate from step 2 until desired time is reached or finish simulation.

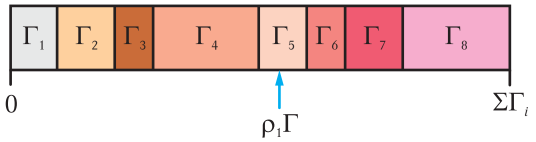
Γ_1
Γ_2
Γ_3
Γ_4
Γ_5
Γ_6
Γ_7
Γ_8
0
$\Sigma\Gamma_i$
$\rho_1\Gamma$

Figure 3.5: Schematic representation of step 5 for process with 8 possible events, e.g. diffusion in BCC lattice.

And now here is my secret, a very simple secret; it is only with the heart that one can see rightly, what is essential is invisible to the eye.

Antoine de Saint-Exupéry
(1900-1944)

4

Diffusion kinetic Monte Carlo model

4.1 Crystal lattice

An atomistic kinetic Monte Carlo simulations via vacancy mechanism consists from jumps on a lattice. Used lattice need to correctly describe crystal lattice of the real alloy. Since in this work only alloys exhibiting BCC or FCC crystal structure with or without interstitials will be simulated, the lattices used in simulations were build to correctly reproduce these two crystal structures. As a basic building blocks, simple cubes with the size of half a lattice parameter were used. A BCC or FCC lattice cell is then build with eight of this simple cubes. That enables introduction of an interstitial atoms on the octahedral positions if needed. The BCC and FCC crystal lattice cells,

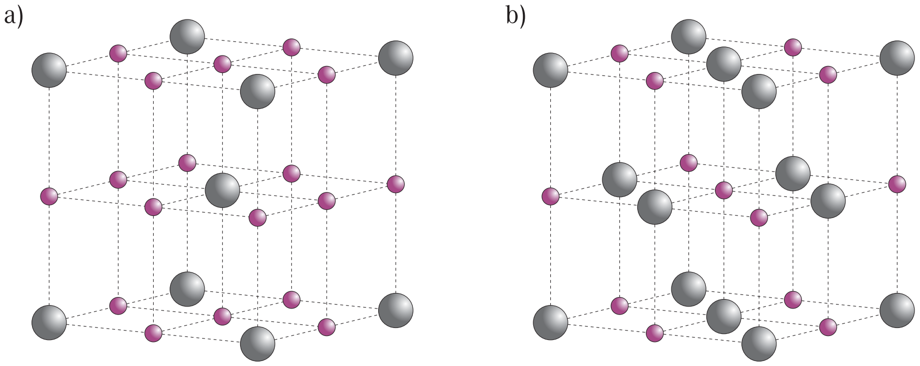

Figure 4.1: Simple cubic crystal structure with substitutional and interstitial atoms; a) body centred cubic (BCC) crystal and b) face centred cubic (FCC) crystal.

made with eight simple cubes and populated with atoms on all substitutional and interstitial positions are depicted in figure (4.1). The unit vectors used to locate the first and second substitutional neighbouring sites for BCC and FCC lattices built from simple cubic building blocks are summarized in Table 4.1 and Table 4.2, respectively.

Table 4.1: Unit vectors of the first nearest substitutional neighbours in the BCC and FCC lattices.

Lattice	First nearest neighbour vectors
BCC	$(1,1,1)$, $(1,1,-1)$, $(-1,1,1)$, $(-1,1,-1)$
	$(1,-1,1)$, $(1,-1,-1)$, $(-1,-1,1)$, $(-1,-1,-1)$
FCC	$(1,1,0)$, $(1,-1,0)$, $(-1,1,0)$, $(-1,1,0)$
	$(1,0,1)$, $(1,0,-1)$, $(-1,0,1)$, $(-1,0,-1)$
	$(0,1,1)$, $(0,1,-1)$, $(0,-1,1)$, $(0,-1,-1)$

Table 4.2: Unit vectors of the second nearest substitutional neighbours in the BCC and FCC lattices.

Lattice	Second nearest neighbour vectors
BCC	$(2,0,0)$, $(-2,0,0)$, $(0,2,0)$
	$(0,-2,0)$, $(0,0,2)$, $(0,0,-2)$
FCC	$(2,0,0)$, $(-2,0,0)$, $(0,2,0)$
	$(0,-2,0)$, $(0,0,2)$, $(0,0,-2)$

Developed lattice can be broken into two sublattices, one accommodating substitutional atoms and vacancies and other accommodating interstitials which is in practice nearly empty.

The number of possible interactions between the vacancy and atoms, must satisfy set of the system boundary conditions, as it is impossible to have more possible interactions than there is neighbouring sites. For example, on the substitutional sublattice with first and second neighbour interactions, following boundary conditions given by

$$\begin{aligned} n^{(1)}_{\mathrm{XX}} + n^{(1)}_{\mathrm{XY}} &= z_1 - 1 \\ n^{(2)}_{\mathrm{XX}} + n^{(2)}_{\mathrm{XY}} &= z_2 \\ n_{\mathrm{XV}} + n_{\mathrm{YV}} &= z_1 \end{aligned} \tag{4.1}$$

are applied, where $n^{(i)}_{\mathrm{XX}}$ is number of the nearest neighbours between the same type of atoms at i-th position, $n_{\mathrm{XY}}^{(i)}$ is number of the nearest neighbour between the X and Y atom types at i-th position, n_{XV} and n_{YV} are numbers of the X and Y atom types around the vacancy on its first neighbours shell. z_1 and z_2 quantify number of the possible nearest neighbour interactions between the first and second nearest neighbours, respectively. It holds $z_1 = 8$, $z_2 = 6$ for BBC lattice and $z_1 = 12$, $z_2 = 6$ for FCC lattice.

4.1.1 Rigid lattice

Ideally simulations should be executed on a fully relaxed lattice using position dependent interatomic energies. After system is relaxed, the positions of atoms will not be locked on the lattice points, in particular positions of atoms near defects (vacancies, grain boundaries, dislocations, ...) will fluctuate more. Position fluctuations of the atoms, causes change in their interatomic energies, which then needs to be computed for the every atom-vacancy exchange. This is computationally very demanding and time consuming. To avoid calculation of the position specific interatomic energies, a rigid lattice is usually used, where atoms are mapped onto a specific lattice positions. Consequently, constant interatomic energies can be used, and simulation time is severely reduced. The rigid lattice allows only exchanges on the lattice positions, for example movements of vacancies and substitutional atoms on the substitutional sublattice and jumps of interstitials on empty positions on the interstitial sublattice. However, since relaxations are dependent on the environment around exchanging atom, they can be to some extent introduced to the rigid lattice system with the use of environment dependant saddle point energies, [136, 137]. In this case, the atom-vacancy transition probability is dependant on the number of specific atom types around vacancy.

4.1.2 Lattice size

Simulations are performed with a finite size lattice, usually with L^3 basic BCC or FCC lattice cells and various boundary conditions. All simulations in this work were performed with the periodic boundary conditions described in detail in section 3.2. Furthermore, lattice also needs to allow relevant processes to happen, e.g. phase separation or phase ordering based on the thermodynamics of the simulated alloy. Time evolution of the alloy is based on the vacancy mechanism diffusion as thermally activated process, with the appurtenant transition probability.

It must be noted, that in simulations one Monte Carlo step (MCS) is completed after exchanges are repeated as many times as there is number of atoms in the simulation box.

Simulation is finished, after desired number of MCS is iterated, usually few thousand (10^3-10^7) iterations. Furthermore, with large simulation boxes, the computing time can become unreasonably long and compromise is needed, between computation time and size of the simulation box.

4.2 Transition probabilities models

In the previous chapter basics of the kinetic Monte Carlo method were laid out, where order of the event selection depends purely on the randomly selected transition probabilities Γ_i of possible events. In order to practically employ kMC method, a model for the transition probabilities is needed. Theoretically all quantities needed for transition probabilities from equations (3.49) and (2.10) can be computed using quantum chemical calculations for any given configuration. However, the computational cost with this approach is high. Another approach often used is to use the simplified models based on the experimental data, [138, 139]. Parametrization of the model is based on fitting appropriate quantities to the fore mentioned data, e.g. vacancy formation energies, diffusion coefficients, phase diagram data, etc. Furthermore, both approaches have their advantages and disadvantages. The most used method to obtain parameters with the quantum calculations is DFT, [7]. Main issue here is accuracy of the calculated parameters. However, errors in the energetics have smaller effect at higher temperature. Another important aspect of the quantum calculation of parameters, is that it can be used to obtain transition probabilities of systems that are hard or even impossible to experimentally asses. In the experiments, macroscopic properties are measured. In order to obtain transition probabilities from the experiments, one needs to know relation between the transition probabilities and macroscopic properties. When the system is well defined, the computation of the macroscopic features is quite straight forward. There exists several approaches to estimate the barrier energies

- **On-the-fly interaction energies with full atomic relaxations**, where the migration barrier energies are calculated for the specific local atomic configuration, using interatomic potentials with the lattice relaxation, [140–142]. Several methods exist for relaxation of the atom positions e.g. conjugate gradient, molecular statics or Monte Carlo, [135, 143]. There are also several algorithms for obtaining the migration energy barriers, with most widespread used beeing the drag, the nudged elastic band and the dimer methods, [142, 144, 145]. The advantage of the on-the-fly calculation of the migration energies, is that beside the chemical interactions also long range elastic interactions are accounted for, and their effects are included in the formation of precipitates. However, these methods are computationally very demanding and are used only in studies of simple diffusion properties and not widely applied for the microstructure evolution.

- **Advanced regression models**, where direct barrier calculations are substituted with regression of appropriate number of examples. An artificial intelligence based on the neural networks was successfully used for the regression of the migration barrier energies, [146–149]. Regression method produces formula, that describes complex relations between the barrier energy and the local atomic configuration. Lattice relaxation is accounted in the obtained barrier energy that depends on the chemical configuration and strain fields. In order to use the regression method, a number of the specific local configuration barrier energies is needed, [149].

- **Rigid lattice approximation with interaction energies**, where the total system energy is obtained as a sum of constant pair interaction energies ($\epsilon_{ij}^{(n)}$) on the rigid lattice with no relaxation. The vacancy formation and vacancy binding energies are obtained with the use of vacancy-atom interaction energies ($\epsilon_{iV}^{(n)}$). Moreover, using this approach, several broken bond models can be used.

  Model *i* An energy of possible configuration depends on a finite range (nearest, second or farther neighbours) of pair interactions $\epsilon_{\mathrm{XY}}^{i}$, where i is the range. The pair interaction energy is also known as chemical binding energy. Energy of any configuration is a sum of appurtenant pair interactions, where the migration energy has contributions of the two types of bonds. First bond type is modified by the jump while the second type is not. The energy of the bonds created in the saddle point configuration is designated as e_{SP}, and is taken as a constant. In the simplest version of this model it is assumed that e_{SP} does not depend on the composition in the surrounding of the saddle point and also does not depend on the atom type undergoing the exchange. This model is also called a Saddle Point Energy model, [150]. The migration barrier for X-V exchange is given as

  $$\Delta E_{\mathrm{mig}}^{X} = e_{\mathrm{SP}} - E_i = e_{\mathrm{SP}} - \sum_i \epsilon_{\mathrm{X}i} - \sum_j \epsilon_{\mathrm{V}j} \tag{4.2}$$

  The migration barrier has two contributions; the energy associated with saddle point binding energy which is taken as a constant, and the cohesive energy described as sum of the pair wise interactions of all the broken bonds associated with the vacancy-atom exchange.

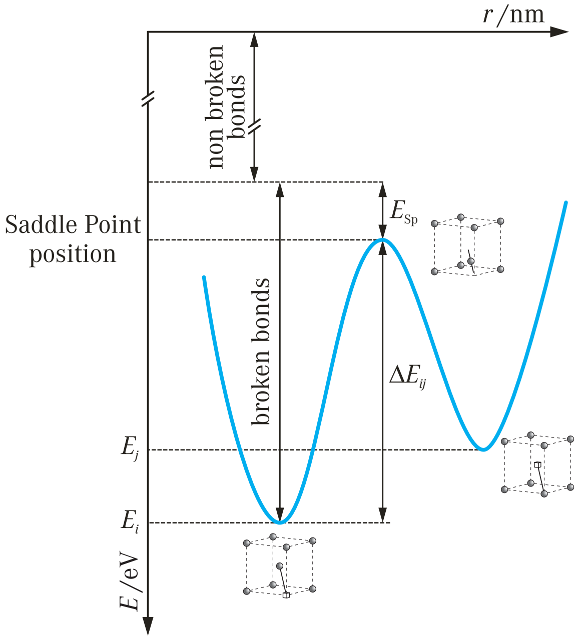

Figure 4.2: Schematic representation of migration barrier energy for broken bond model.

Model *ii* Transition probabilities are calculated in the same way as in the previous model. The only difference between the two is, that here e_{SP} depends on the atom type at the saddle point doing exchange. Through the saddle point energies, kinetics of the model can be influenced. Dependence of the saddle point energies on the atom type also causes some asymmetry effects, which will be explained later. Furthermore, dependence of the saddle point energies on the exchanging atom type, addresses contrasts in the diffusion of various chemical elements in the alloy, e.g. Ni-Cr-Al and mimics diffusion of real alloy better. This model was also used for coupling vacancy substitutional exchange and direct interstitial exchange mechanisms simultaneously in Fe-Nb-C alloy, [27, 28, 32, 33] and Fe-Y-O, [36] and Fe-Ti-O alloy, [37]. Equation for the migration barrier is similar to the previous model and is given as

$$\Delta E^X_{\mathrm{mig}} = e^X_{\mathrm{SP}} - E_i = e^X_{\mathrm{SP}} - \sum_i \epsilon_{\mathrm{X}i} - \sum_j \epsilon_{\mathrm{V}j} \tag{4.3}$$

In figure 4.2, the barrier energy for this model is schematically presented. This model is also suitable for simulations of interstitial atoms, if the empty spaces on the interstitial sublattice are treated as interstitial vacancies on the first nearest neighbour positions and will be addressed from now on as the Saddle Point Energy Model 2 (SPEM2).

Model *iii* This model is similar to the previous, with distinction that the e_{SP} is defined as a sum of the pair interactions. This model was used in kMC simulation of fully relaxed Fe-Cu alloy, based on the EAM potential, [136, 137] where contribution to the energy of the Fe atom at the saddle point, depends on the number of the Fe atoms at the nearest neighbour positions. The contribution of the Cu atom at the saddle point was independent of number of the Cu atoms at the nearest neighbour positions. Models described so far are variants of the Saddle Point Energy models.

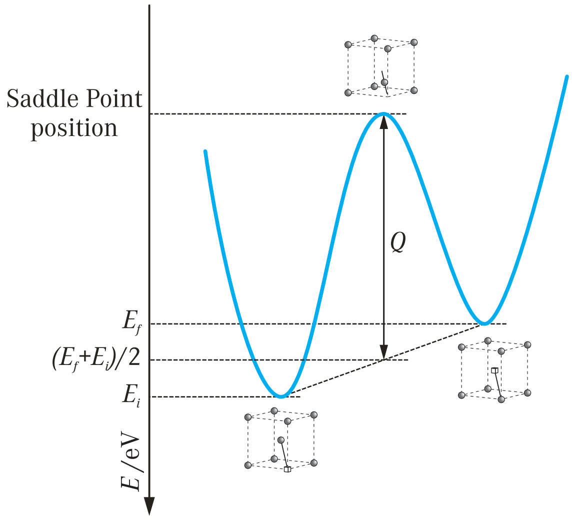

Figure 4.3: Schematic representation of migration barrier energy for kinetic Ising barrier energy model.

Model *iv* In the Final-Initial System Energy model, the saddle point energy and the migration barrier energy are given as

$$E_{\mathrm{SP}} = \frac{E_i - E_f}{2} + Q \tag{4.4}$$

$$\Delta E^X_{\mathrm{mig}} = \frac{E_f - E_i}{2} + Q \tag{4.5}$$

where, $E_f - E_i$ is the balance of the created and broken bonds at the stable lattice positions during exchange and Q is a constant parameter, independent of the initial configuration and the saddle point, [22, 24, 151]. However it depends on the exchanging atom type and is obtained from the diffusion coefficients in pure metals. Time scale is influenced by both, Q and ν. The energies of the final and initial state dependant on the position are given by

$$E = \sum_i N_{XX}^{(i)} \epsilon_{XX}^{(i)} + \sum_i N_{XV}^{(i)} \epsilon_{XV}^{(i)} \tag{4.6}$$

where, i corresponds to the nearest neighbour interaction number, N_{XX} is the number of bonds at the i-th neighbour position between X-X atom types, and N_{XV} is the number of bonds between vacancy and X atom type, ϵ_{XX} and ϵ_{XV} are the pair interaction energies between X-X and X-V species, respectively. This model is also referred as to kinetic Ising model, [135, 151]. Figure 4.3 shows migration barrier energy used in this model.

Model *v* The configurational energies, the saddle point energies and the vibrational frequencies are calculated using a many body interaction potential, [138]. The vibrational frequencies are in the range between 10^{12} s^{-1} and 10^{16} s^{-1}, and are often approximated with a fixed value in this range to save computational work of computing normal modes for every saddle point (cf. equation 2.31). For their estimation, the Einstein model or Debye approximation can be used, [20, 132]. Furthermore, the vibrational frequencies can also be calculated from the diffusion coefficients in an alloy as

$$\nu = \frac{D_0}{f_0 a^2} \tag{4.7}$$

where, f_0 is self diffusion correlation factor, D_0 is diffusion coefficient and a is lattice parameter, [28, 32, 33].

These listed models are computationally very efficient because of their simplicity. Furthermore, they are simple enough to be compared to the other analytical models. However, their biggest limitations are rigid lattice approximation and the extrapolation of various systems to one another is very limited and depends on the considered system. Some experiments on the relaxed lattices were done with the EAM potentials, [136].

Description of the models used in performed simulations, together with their detailed parametrization will be given for each alloy system simulated in the next chapters.

4.3 Vacancy concentration and time adjustment

4.3.1 Vacancy concentration

Vacancies are naturally present in all crystalline materials. Vacancies are generated and disappear on various discontinuities in crystals. Their concentration is very important variable and has large influence on many processes occurring in crystalline materials. The processes affected are among others diffusion and phase transformations. The total free energy of the material is dependent on the vacancy concentration, c_V. At any given temperature, an equilibrium vacancy concentration is defined. The equilibrium vacancy concentration $c_{V\mathrm{eq}}$ is temperature dependent and results in the lowest free energy. Furthermore, assuming the equilibrium vacancy concentration is very small ($c_{V\mathrm{eq}} \ll 1$), it can be calculated with minimisation of the free enthalpy as

$$c_{V\mathrm{eq}} = \exp\left(\frac{S_V}{k_\mathrm{B}}\right)\exp\left(\frac{-E_V}{k_\mathrm{B}T}\right)\left(1-\frac{pV_V}{k_\mathrm{B}T}\right) \tag{4.8}$$

where, since $T > 100\mathrm{K}$ and $p < 10^8\mathrm{Pa}$, it holds $pV_V/k_\mathrm{B}T \ll 1$. In equation (4.8), E_V is vacancy formation energy, S_V is formation entropy and V_V is formation volume from difference in energy, entropy and volume between a crystal with one vacancy and an ideal crystal with the same number of atoms, [132]. The equilibrium vacancy concentration is alternatively given as

$$c_{V\mathrm{eq}} = A\exp\left(\frac{-E_{\mathrm{V_{for}}}}{k_\mathrm{B}T}\right) \tag{4.9}$$

which is simplified version of equation (4.8), where A is constant, and $E_{\mathrm{V_{for}}}$ is vacancy formation energy. Value of the constant A varies between 1 and 280, [20, 136]. However, the equilibrium vacancy concentration can change dramatically in the real system undergoing phase transformation if the vacancy formation energies in various phases differ a lot. This has effect on time adjustment factor and the simplest solution is to assume some reference phase, where the vacancy formation energy is known, i.e. use of the equilibrium vacancy concentration of the base pure element. For example, in Fe based alloys, the time is adjusted according to the equilibrium vacancy concentration in the Fe.

In kMC simulations of the phase transformations, the diffusion and precipitation kinetics depends on the attempt frequencies and vacancy concentration. The vacancy concentration in simulations is usually kept constant, frequently only one vacancy is used. Depending on the simulation box size the corresponding vacancy concentration is much higher than equilibrium vacancy concentration in the real alloy. The difference in vacancy concentrations between the simulation and real alloys needs to be adjusted in order to obtain correct relation between the Monte Carlo time and real physical time. Time rescaling is based on the assumption, that kinetics is sufficiently slow and vacancy concentration is always at its equilibrium concentration, [20, 28, 33, 35, 36, 136].

4.3.2 Physical time

Time obtained from kMC simulations is Monte Carlo time t_{MC}, calculated with equations (3.47) or (3.48) and corresponds to the physical time of the simulated system. For example, at 873 K, the equilibrium vacancy concentration in iron, is $c_{\mathrm{Veq}} = 8.64 \times 10^{-10}$. In order to perform simulations at 873 K, with size of the simulation box where equilibrium vacancy concentration is always maintained, one would need approximately 10^9 atom sites, which means that the simulation box need would be around 835^3 BCC lattice constants. This is unrealistically large box size, therefore much smaller simulation box sizes are used. The diffusion is accelerated if the vacancy concentration is higher than equilibrium value. In order to get real physical time t_{real} with smaller simulation boxes, time rescaling factors are needed. These factors account for the difference in vacancy concentrations in the simulation boxes and in real alloys. Expression connecting the Monte Carlo time t_{MC} and real physical time t_{real} is

$$t_{\mathrm{real}} = \left(\frac{c_{\mathrm{Vsim}}}{c_{\mathrm{Veq}}} \right) t_{MC} \tag{4.10}$$

where, c_{Vsim} is vacancy concentration in the simulation box, and c_{Veq} is equilibrium vacancy concentration in the real alloy, [20, 136].

Since kinetics of the diffusion in alloy is governed by attempt frequencies, the real physical time can be obtained by adjusting the diffusion coefficients of the substitutional elements to account for difference in the diffusion rate. This is done through adjustment of the attempt frequencies, [28, 33, 35]. Furthermore, the simulation time (t_{MC}) then becomes equal to the real physical time. Adjustment of the diffusion coefficient through the attempt frequency is as follows

$$\nu = \nu_0 \frac{c_{\mathrm{Veq}}}{c_{\mathrm{Vsim}}} \tag{4.11}$$

where, ν_0 is original attempt frequency.

Previously described time rescaling techniques rely on the fixed number of vacancies in the simulations box. However, in the real alloys vacancies can be trapped inside precipitates and various vacancy sources, like grain boundaries or dislocations, then maintain vacancy concentration in the matrix close to the equilibrium value, [136, 152]. This effect, can also be used to rescale time, where vacancy source/sink is introduced on a given site in the simulation box, [28]. Vacancy is created on the vacancy source and placed in one of the neighbouring lattice sites with the vacancy creation probability. During diffusion through the simulation box, vacancy can reach one of the source/sink neighbouring lattice sites and can disappear with annihilation probability. This technique was mainly used in simulations of the heterogeneous precipitation, [28, 33, 35, 36].

4.4 Random number generator

As it was already mentioned, all Monte Carlo methods depend on the random numbers to choose occurring events. In the kinetic Monte Carlo simulations, the random number is needed to determine event with appurtenant transition probability, and calculate time needed for this event to happen, cf. section 3.6.

In the computer simulations, random numbers can be generated in several ways. Ideal would be use of the external generator based on the radioactive isotopes. However, such external devices are quite expensive. The random numbers, needed for the computer simulations are usually generated with deterministic algorithms, which generate sequence of the numbers with sufficient randomness. The random numbers generated with the deterministic algorithms are called pseudorandom numbers. Random numbers in all simulations presented here, were generated using a deterministic algorithm from the Numerical Recipes in C++ [153]. This algorithm is first initialized with seed number, obtained from the computer time. The seed number sets the initial state of the random number generator.

The random number generator needs to fulfil several essential properties to be good random generator. These properties are:

- Repeatability, where the same seed number needs to give same random number sequence.
- Randomness, meaning generated numbers should form uniform distribution and needs to be independent of each other.
- Long period. After some period, the sequence starts to repeat itself. This period should be number characteristically longer than the amount of numbers needed for the simulation.

- Portability. Algorithm should give same sequence on different computers if seed is the same.
- Fast. During the simulations, amount of generated random numbers is huge. Therefore, the deterministic algorithm should not slow down progress of the simulation a lot.
- Insensitive to seeds, where randomness and the period should not depend on the initial seed.

4.5 Complexity of the model used in this work

All processes that naturally occur in the real materials are impossible to be included into the computational model because of the computational time constraints. The generally accepted procedure when building computational models is first to define and simulate simple model with a few processes and parameters. Generalizations of the model are then made only after these initial steps. This protects model from becoming too complex and complicated from the beginning. Too complex and complicated models are very hard to handle, and make understanding and selection of the most important processes, occurring in the model too difficult.

The models built and used in this thesis, follow previously described model design guidelines. At first, a simple binary system based on the Fe-Cu alloy system was build. The choice of the Fe-Cu alloy system was deliberate, as this system was extensively studied experimentally and with various computer simulations. This enabled comparison of results from the literature, with new findings and orientation on the issues that were not given any attention. The simple binary model served as starting point and was afterwards made more complex by introduction of other substitutional elements. After substitutional diffusion processes were examined in detail, focus was turned to introduction of competing interstitial diffusion in the model.

Give me a lever long enough and a fulcrum on which to place it, and I shall move the world.

Archimedes (287 BC-212 BC)

5

Clustering in binary Fe-Cu alloy

This chapter deals with the kinetic Monte Carlo simulations of the binary Fe-Cu alloy system. After short review of previous experimental studies on this alloy system, detailed approach to the parametrization, based on the thermodynamic materials data is described. Extensive atomistic simulations were performed, first to address simulations box size issues. Then influence of various physical properties is analysed and described.

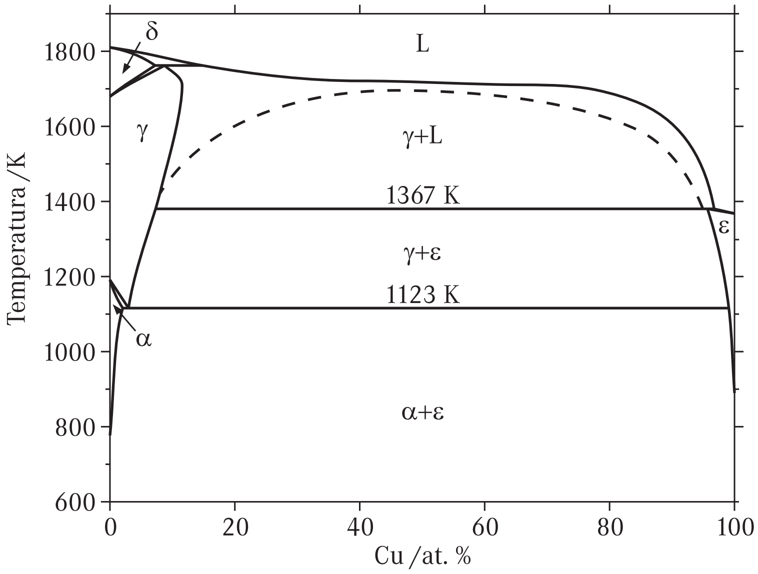

Figure 5.1: Equilibrium phase diagram of Fe-Cu alloys, [1]. Dashed line represents metastable miscibility gap of liquids.

Binary alloys are very interesting in the modeling and simulations as they offer compositional simplicity, which allows observation of physical phenomena where only one variable is changed, e.g. concentration, temperature and stress field. This chapter will present simulations performed on the binary Fe-Cu alloy with various compositions. Furthermore, this type of binary alloy has been extensively studied experimentally, [154–164] and by modeling, [12–14, 18, 20, 132, 135, 137, 147, 151, 165–167]. Alloying of steels with Cu is used in various classes of steel, from low-carbon to maraging and corrosion-resistant, as addition of Cu, improves steel strength and corrosion resistance, [168]. Understanding of the phase changes in the Fe-Cu alloys is therefore very important. Figure 5.1 shows equilibrium phase diagram of the Fe-Cu alloy, which exhibits eutectoid reaction at 2.8 at.% Cu and temperature at 1117 K, [1]. The solubility of Cu in iron based solid solution is limited. The precipitation of Cu clusters was first reported in 1933, [154]. First detailed study of copper precipitatates was performed with replicas of the thermaly aged Fe-1.23Cu alloy at 773 K, 873 K and 973 K for times up to 1000 h, [155]. Further studies have shown that Cu clusters precipitate with a metastable BCC structure coherent with the matrix and have spherical shape, [156]. Later studies showed that crystall structure of Cu precipitates is accompanied by a more compex crystall lattice rearangement from the initial coherent BCC → 9R → 3R → FCC structure, dependant on the prepipitate size, [158–164]. Initial Cu precipitates with radius up to 2 nm have BBC crystal structure, fully coherent with α-Fe matrix, [158–160]. Upon further growth, precipitates with radius between 2 nm and 9 nm undergo martensitic transformation from BCC to twinned 9R crystall structure, depicted in Figure 5.2a, [158, 162]. Precipitates larger than 9 nm possess a 3R structure, a distorted FCC structure which continually changes to ε-Cu FCC crystal structure, [161].

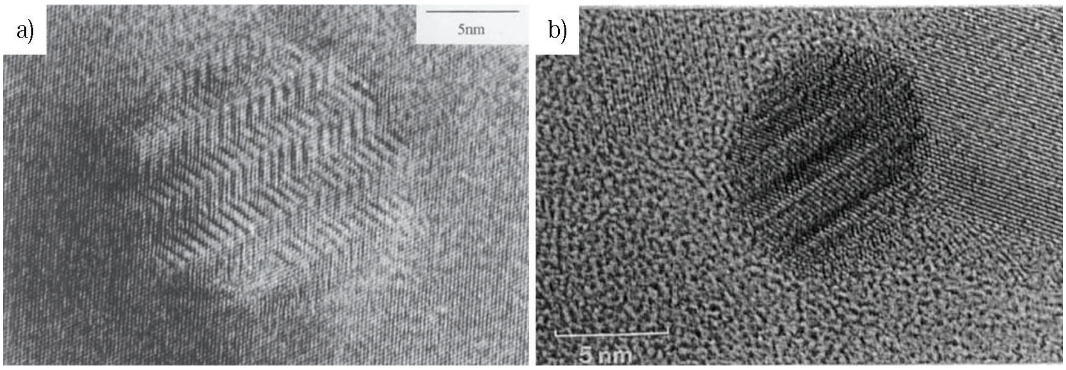

Figure 5.2: HREM micrograph of Cu precipitate; a) twinned 9R structure, [158] and b) structure partially transformed to FCC structure, [161].

Available published experimental data, can be used as confirmation of results obtained from the kinetic Monte Carlo simulations. The Fe-Cu alloy system is frequently used as a benchmark to test validity of the phase transformation models due to its relative simplicity to model. This system has large and almost symmetrical miscibility gap and differences in the atom sizes are small. Furthermore, experimentally obtained data confirmed that Cu clusters with sizes up to 2 nm are fully coherent with the α-iron matrix. The full coherency of Cu clusters and small atom size difference between Fe and Cu, justifies use of the rigid lattice in kMC simulations.

5.1 Parametrization of the simulation model

To calculate interatomic interaction energies needed for the transition probabilities, a thermodynamic materials properties were used. In Table 5.1, experimental data used for calculation of the interaction parameters is presented. Due to relatively symmetrical tracer diffusion properties of Fe and Cu in Fe, [172], symmetrical model can be used. In the symmetrical model, the binding energy of Cu is set equal to the binding energy of Fe. The interaction energies $\epsilon^{(i)}_{\mathrm{FeFe}}$ and $\epsilon^{(i)}_{\mathrm{CuCu}}$, where $i \in 1, 2$ were calculated from the cohesive energies in the pure metals

Table 5.1: Material properties of Fe and Cu used for calculation of interaction energies and kinetic parameters.

Lattice constant of α-Fe	a	0.287 nm, [169]
Number of first neighbours	z_1	8
Number of second neighbours	z_2	6
Cohesive energy of Fe	E_{cohFe}	-4.28 eV, [169]
Cohesive energy of Cu	E_{cohCu}	-3.49 eV, [169]
Mixing energy of Fe$-$Cu	E_{mixFeCu}	-0.515 eV, [170]
Vacancy formation energy of Fe	E_{VforFe}	1.60 eV, [152]
Vacancy formation energy of Cu	E_{VforCu}	1.28 eV, [152]
Vacancy migration energy of Fe	E_{VmigFe}	0.90 eV, [152]
Vacancy migration energy of Cu in Fe	E_{VmigCu}	0.70 eV, [152]
Diffusion constant of Fe	$\mathrm{D}_{0\_\mathrm{Fe}}$	$2.01\ 10^{-4}\ \mathrm{m}^2\ \mathrm{s}^{-1}$, [171]
Diffusion constant of Cu	$\mathrm{D}_{0\_\mathrm{Cu}}$	$2.16\ 10^{-4}\ \mathrm{m}^2\ \mathrm{s}^{-1}$, [171]
Attempt frequency of Fe	ν_{Fe}	$8.70 \times 10^{12}\ \mathrm{s}^{-1}$, [169]
Attempt frequency of Cu	ν_{Cu}	$6.67 \times 10^{12}\ \mathrm{s}^{-1}$, [169]

$$E_{\mathrm{cohX}} = \frac{z_1}{2}\epsilon^{(1)}_{\mathrm{XX}} + \frac{z_2}{2}\epsilon^{(2)}_{\mathrm{XX}} \tag{5.1}$$

where X is either Fe or Cu, z_1 and z_2 are number of first and second neighbours, respectively, [102]. Interaction energy of the second nearest neighbours is evaluated from interaction energy of first nearest neighbours as

$$\epsilon^{(2)}_{\mathrm{XX}} = d\epsilon^{(1)}_{\mathrm{XX}} \tag{5.2}$$

where X is either Fe or Cu and d is constant. Simulations presented here were performed with constant $d = 0.5$ in equation (5.2).

In figure 5.3, interaction energies between possible atom types and vacancy in the BCC crystal lattice on the first and second nearest neighbours shells are displayed.

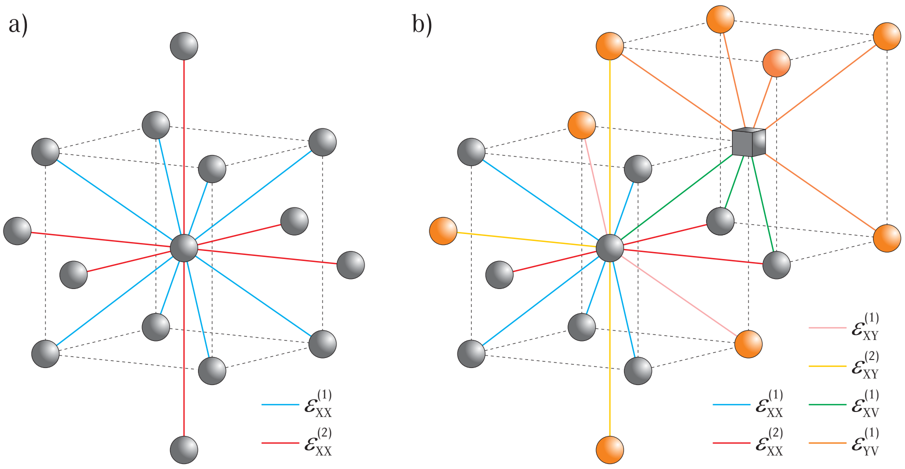
a)
b)
$\varepsilon^{(1)}_{\mathrm{XX}}$
$\varepsilon^{(2)}_{\mathrm{XX}}$
$\varepsilon^{(1)}_{\mathrm{XY}}$
$\varepsilon^{(2)}_{\mathrm{XY}}$
$\varepsilon^{(1)}_{\mathrm{XX}}$
$\varepsilon^{(1)}_{\mathrm{XV}}$
$\varepsilon^{(2)}_{\mathrm{XX}}$
$\varepsilon^{(1)}_{\mathrm{YV}}$

Figure 5.3: Schematic representation of the interaction energies in BCC crystal lattice; a) only X atoms on first $\epsilon^{(1)}_{\mathrm{XX}}$ and second $\epsilon^{(2)}_{\mathrm{XX}}$ nearest neighbour shells and b) mixed X and Y atoms on first and second nearest neighbour shells.

For the binary alloy systems, the mixing energy tells whether the system has tendency to precipitate when $E_{\mathrm{mixXY}} < 0$ or if the system has tendency to order. Heteroatomic interaction energies $\epsilon^{(i)}_{\mathrm{XY}}$ are associated with the mixing energy as

$$E_{\mathrm{mixXY}} = \frac{z_1}{2}\left(\epsilon^{(1)}_{\mathrm{XX}} + \epsilon^{(1)}_{\mathrm{YY}} - 2\epsilon^{(1)}_{\mathrm{XY}}\right) + \frac{z_2}{2}\left(\epsilon^{(2)}_{\mathrm{XX}} + \epsilon^{(2)}_{\mathrm{YY}} - 2\epsilon^{(2)}_{\mathrm{XY}}\right) \tag{5.3}$$

which is estimated from the solubility limit c^s_{Y} of element Y in X. For low solubilities holds

$$c^s_{\mathrm{Y}} \propto \exp\left(\frac{E_{\mathrm{mixXY}}}{k_{\mathrm{B}}T}\right) \tag{5.4}$$

For simulations of Cu clustering in α-Fe, equations (5.3) and (5.4) can be written as

$$E_{\mathrm{mixFeCu}} = \frac{z_1}{2}\left(\epsilon^{(1)}_{\mathrm{FeFe}} + \epsilon^{(1)}_{\mathrm{CuCu}} - 2\epsilon^{(1)}_{\mathrm{FeCu}}\right) + \frac{z_2}{2}\left(\epsilon^{(2)}_{\mathrm{FeFe}} + \epsilon^{(2)}_{\mathrm{CuCu}} - 2\epsilon^{(2)}_{\mathrm{FeCu}}\right) \tag{5.5}$$

$$c^{s}_{\mathrm{Cu}} \propto \exp\left(\frac{E_{\mathrm{mixFeCu}}}{k_{\mathrm{B}}T}\right) \tag{5.6}$$

To account for strengthening of the chemical bonds of less coordinated atoms, ghost interaction energies were introduced to the model. Athènes *et. al.*, [172] argued that ghost interactions does not change kinetic pathways of the vacancy, but has influence only the time spent at each configurations. This is not completely true since ghost interactions influences on the barrier energy, calculated with equation (4.3) and consequently changes transition probabilities (equation (3.49)), which has direct influence on the kinetic pathways of the vacancy. To calculate the ghost interaction energy between the atom X and vacancy ϵ_{XV} (c.f. figure 5.3, the vacancy formation energy was used. Method reflects the modification in the atomic bonding of atom X, due to absence of one atom, [173]. Formation energy of the vacancy in the pure X environment is then given as

$$E_{\mathrm{VforX}} = z_1\epsilon^{(1)}_{\mathrm{XV}} - E_{\mathrm{cohX}} \tag{5.7}$$

The diffusion coefficients follows Arrhenius equation and are calculated as

$$D_X = D_{0_X}\exp\left(\frac{-Q_X}{k_{\mathrm{B}}T}\right) \tag{5.8}$$

where, Q is activation energy given as $Q_X = E_{\mathrm{VforX}} + E_{\mathrm{VmigX}}$, and D_{0_X} is diffusion constant. The kinetic parameters were adjusted to the diffusion parameters, to accurately simulate diffusion processes, since diffusion coefficients obtained from the simulations must be equal to the experimental ones.

The saddle point energy E_{SpX}, is the total energy of the system at a saddle point. It was determined from the vacancy migration energy in pure phase X. At low solubility, thr saddle point energy can be assumed constant and independent of the nature of the jumping atom and local atomic arrangement. The saddle point energy was calculated from interactions between first and second nearest neighbours using following equation

$$\begin{aligned} E_{\mathrm{SpX}} = E_{\mathrm{VmigX}} + z_1\epsilon_{\mathrm{XV}} &+ c_{\mathrm{X}}\left[(z_1-1)\epsilon^{(1)}_{\mathrm{XX}} + z_2\epsilon^{(2)}_{\mathrm{XX}}\right] \\ &+ c_{\mathrm{Y}}\left[(z_1-1)\epsilon^{(1)}_{\mathrm{XY}} + z_2\epsilon^{(2)}_{\mathrm{XY}}\right] \end{aligned} \tag{5.9}$$

where, c_{X} and c_{Y} are concentrations of X and Y atoms, respectively. E_{VmigX} is the vacancy migration energy of X, and ϵ_{ij} are pair interaction energies. The saddle point energies used in all simulations were kept the same and concentration of Y used, was 1 at.%.

The attempt frequencies act as prefactor in equation (3.49) and were estimated from the Debye frequencies ν_{D} in the pure metals, [169]. Attempt frequencies were assumed to be equal and same to the highest Debye frequency of the elements in simulation, i.e. $\nu_{\mathrm{Fe}} = \nu_{\mathrm{Cu}} = \nu_{\mathrm{D_{Fe}}}$. The attempt frequencies are in the range between 10^{12} s^{-1} and 10^{16} s^{-1}. If differences of the prefactor is small, transition probabilities obtained with this assumption are not large and ratios between the transition probabilities are not changed. Influence of this assumption is only on the residence time, and consequently on the the kinetics and not on the kinetic pathways. Furthermore, self diffusion properties of Fe are used to obtain real time. If chemical concentration of Cu is low and vacancy does not have preferred environment, which is the case for the symmetric model, then obtained time is sufficiently accurate to justify assumption to use equal attempt frequencies. Rigorously, totally accurate attempt frequencies would be calculated from the phonon spectra in the particular environment. Almost always approximation with constant frequencies (Debye of Einstein) is used due to the high computational cost of the phonon spectra calculations.

From the experimental data summarized in Table 5.1, using procedure described above, the simulations parameters were calculated. They are presented in Table 5.2. The Cu-Cu interaction energies for first and second nearest neighbours obtained from the cohesive energy of Cu given in Table 5.1 are for pure FCC phase and yields, $\epsilon^{(1)}_{\mathrm{CuCu}} = -0.635$ eV and $\epsilon^{(2)}_{\mathrm{CuCu}} = -0.318$ eV, respectively. However, in simulations rigid lattice is used and expected precipitates have BCC crystal structure. Homointeraction energies of Cu were then adjusted according to the iron ones and this yields symmetrical model. Use of the symmetrical model is justified, since similar values of the $\epsilon^{i}_{\mathrm{CuCu}}$ are obtained

Table 5.2: Calculated interaction energies and kinetic parameters for binary FeCu alloy used in kMC simulations.

$\epsilon^{(1)}_{\mathrm{FeFe}} = -0.778$ eV	$\epsilon^{(2)}_{\mathrm{FeFe}} = -0.389$ eV
$\epsilon^{(1)}_{\mathrm{CuCu}} = -0.778$ eV	$\epsilon^{(2)}_{\mathrm{CuCu}} = -0.389$ eV
$\epsilon^{(1)}_{\mathrm{FeCu}} = -0.731$ eV	$\epsilon^{(2)}_{\mathrm{FeCu}} = -0.366$ eV
$\epsilon^{(1)}_{\mathrm{FeV}} = -0.335$ eV	$\epsilon^{(1)}_{\mathrm{CuV}} = -0.335$ eV
$E_{\mathrm{SpFe}} = -9.557$ eV	$E_{\mathrm{SpCu}} = -9.098$ eV
$\nu_{\mathrm{Fe}} = 8.70 \times 10^{12}$ s^{-1}	$\nu_{\mathrm{Cu}} = 8.70 \times 10^{12}$ s^{-1}

from the experimental precipitation kinetics, [12]. Used values of the Cu-Cu interaction energies at the corresponding nearest neighbour $\epsilon^i_{\mathrm{CuCu}}$ were set equal to the interaction energy of iron at the same neighbour shell, i.e. $\epsilon^{(1)}_{\mathrm{CuCu}} = \epsilon^{(1)}_{\mathrm{FeFe}} = -0.778$ eV and $\epsilon^{(2)}_{\mathrm{CuCu}} = \epsilon^{(2)}_{\mathrm{FeFe}} = -0.389$ eV. As already mentioned, equal attempt frequencies $\nu_{\mathrm{Fe}} = \nu_{\mathrm{Cu}}$ were used with Debye frequency in iron being used for both elements in simulations, which can be justified with low concentrations of Cu in simulated alloys which has negligent influence on the value of diffusion coefficient of Cu.

Migration barrier in the binary solid solution from all parameters given in Table 5.2 can be calculated with following equation

$$\Delta E_{\mathrm{X}} = E_{\mathrm{SpX}} - \sum_{i=1}^{k} n^{(i)}_{\mathrm{XX}} \epsilon^{(i)}_{\mathrm{XX}} - \sum_{i=1}^{k} n^{(i)}_{\mathrm{XY}} \epsilon^{(i)}_{\mathrm{XY}} - n_{\mathrm{XV}} \epsilon_{\mathrm{XV}} - n_{\mathrm{YV}} \epsilon_{\mathrm{YV}} \tag{5.10}$$

where, X is the exchanging atom, $n^{(i)}_{\mathrm{XX}}$, $\mathrm{X} \in \{\mathrm{A}, \mathrm{B}\}$ is number of the XX bonds (AA, BB or AB) at i-th nearest neighbour shell up to k. n_{YV}, $\mathrm{Y} \in \{\mathrm{A}, \mathrm{B}\}$ is number of AV and BV bonds at the first neighbour shell of the vacancy. The number of bonds must satisfy boundary conditions of the system, as it is impossible to have more bonds than there is neighbouring sites (c.f. equation (4.1).

5.1.1 Model Asymmetry

Although the tracer diffusion properties are almost equal in the used FeCu model, small difference still exists. This difference has influence on the model parametrization as can be seen from the saddle point energies which are diffusion dependant. The obtained values (cf. Table 5.2) are not equal, and asymmetry parameter

$$c* = E_{\mathrm{SpX}} - E_{\mathrm{SpY}} \tag{5.11}$$

can be defined. When the saddle point energies are set to be equal, the model asymmetry must be introduced through the atom-atom and atom-vacancy interaction parameters. In the second case the asymmetry parameter, dependant on the interatomic energies is defined as

$$a* = \sum_{i=1}^{k} \frac{\epsilon^i_{\mathrm{XX}} - \epsilon^i_{\mathrm{YY}}}{\epsilon^i_{\mathrm{XX}} + \epsilon^i_{\mathrm{YY}} - 2\epsilon^i_{\mathrm{XY}}} \tag{5.12}$$

The model asymmetry is very important property of the kMC model and has big influence on the kinetic pathways, [18]. Various sets of interatomic parameters ϵ^i_{XX}, ϵ^i_{YY}, ϵ^i_{XY}, E_{SpX}, E_{SpY}, ν_{X}, ν_{Y} can lead to the same mixing energy or give the same equilibrium phase diagrams and diffusivities of Y atoms in X. The diffusion mechanism of Y atoms can be different, meaning that alloy will exhibit different kinetic pathways. This happens because of the asymmetry effects, which are reflected with which type of the atom (X or Y) vacancy has preference to exchange. Several studies showed that asymmetry parameters have influence on the relative mobility of Y monomers and small clusters (dimers, trimers, . . .), [18, 172, 174].

5.2 Analysis of obtained atomic configurations

5.2.1 Identification and analysis of the clusters

Alloys exhibit various phase transformations when they are subjected to the thermal field variations. The phase transformations usually starts with precipitation. This process has influence on the mechanical properties of the alloys as precipitates acts as obstacles for dislocation motion. To predict changes of the mechanical properties, formed clusters need to be identified, characterized and analysed in terms of their chemical composition, shape, mean size, number density, . . . Trend of the solute atoms to form clusters, can be identified by measuring the short range order (SRO) parameter or atom pair correlations, cf. section 2.4.1. From the SRO parameter, time when clusters begin to grow can be easily identified. However, detailed informations regarding to the cluster chemical concentrations, size and their shape cannot be determined from it. In order to be able to determine the chemical concentration, size and shape of precipitates two mechanisms were used for post processing of obtained results.

After all clusters are identified, the procedures to obtain various size distributions are quite straightforward.

5.2.1.1 Identification with average concentrations

Method for the cluster identification with average concentrations can quickly characterizes non-pure precipitates which is very useful especially in alloys with other impurities, for example in the ternary or quaternary alloys. Concentration profiles of the solute atoms were defined by estimation of the average concentration of solutes over a certain volume for every lattice site in the matrix. The value for the 3D concentration of the solute atoms was obtained by using average concentration of an individual atom species in the sphere, centred at the lattice position with some radius up to the i-th nearest neighbour distance. After the local concentration at each lattice site is obtained, each of the clusters is defined by a given threshold concentration of the quested solute atoms in the cluster and belonging lattice sites are then attributed to the cluster. This is then basis for analysis of the shape, size and number density of the clusters from the spatial distribution of accepted lattice sites.

5.2.1.2 Identification with neighbouring atoms

In the binary alloys with strong tendency to element ordering, different approach based on the percolation theory, can be used, [93, 175, 176]. Instead of tracing local concentration within the i-th shell around the given lattice site, clusters are identified based on the occupation of the neighbouring sites. All lattice sites occupied by the searched solute atoms are looked for up to the i-th neighbour of the same atom type. Several algorithms exist which enable identification of the clusters, where the most known is Hoshen-Kopelman algorithm,[93], which is specialized application of the Union-Find algorithm, a simple method for a computation of equivalence classes.

The identification of clusters in this chapter were carried out for the first nearest neighbours only, since high resolution electron microscope and atom probe studies confirmed pure Cu precipitates, [161–164]. However, the desired boundary conditions can be easily changed, to include also atoms on sites beyond first neighbouring shell, as was the case for Ni-Cr-Al alloy sytem.

5.3 Results of the kMC simulations in the binary Fe-Cu system

The kMC simulations were performed according to the residence time procedure described in previous chapter using the developed algorithm presented in Appendix A and broken bond model SPEM2 (cf. section 4.2) with simulation parameters given in Table 5.2. Repeatability of the obtained results was confirmed with several simulation runs with the same starting conditions.

5.3.1 Influence of the simulation box size

In the previous chapter it was explained that computer simulations are performed on the finite simulation box size. The effect of the simulation box will be investigated in this section. Several simulations, with the same concentration and temperature, and various sizes of the simulation boxes were performed to determine its effect. Simulation box sizes, used to study influence of the box size on the clustering kinetics are given in Table 5.3. In the same table, number of all atom sites in the simulation box and number of Cu atoms used are given. All simulations were performed with 1 at.% Cu at 873 K and one vacancy.

Table 5.3: Various simulation box sizes used to investigate size effects.

No. of BCC lattice sites	Box size /nm	No. of all sites	No. of Cu atoms
20^3	5.74^3	16000	161
40^3	11.48^3	128000	1281
60^3	17.22^3	432000	4321
80^3	22.96^3	1024000	10241
100^3	28.70^3	2000000	20001
120^3	34.44^3	3456000	34561

The evolution of the number density of clusters larger than $n > 2$ is shown in figure 5.4. The number density evolution reveals that the smallest box is too small and contains far too few Cu atoms to be able to produce satisfactory results. Small number of atoms in the simulation box greatly accelerates simulations. However, since simulation box is small and number density of clusters should be the same in all box sizes, the monomer attachment and detachment causes large fluctuations of the number density of clusters. These fluctuations, seen in figure 5.4 for the smallest box size can be avoided with larger box sizes. Simulation box with 40^3 BCC lattice sites gives much

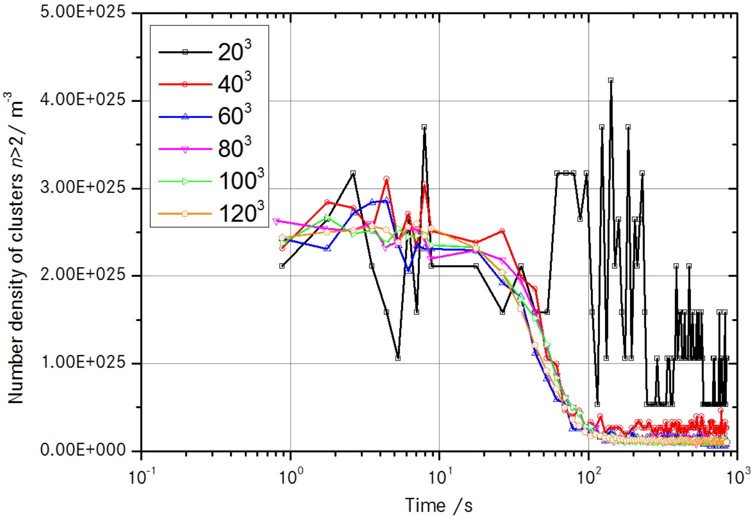

Figure 5.4: Influence of the simulation box size on the evolution of number density of clusters larger than $n > 2$.

better results. Some fluctuations of the number density can still be seen, especially towards the end of simulation. Larger box size offers with same the number density more formed clusters, which is better for the statistical analysis of obtained results. Larger the simulation box, the more smooth is the number density curve. However, this increases computational time needed for simulations and compromise between the simulation box size and computational time is needed.

The clustering kinetics of the system under investigation was investigated through time evolution of the short range parameter and average cluster size. Results obtained for all box sizes were carefully analysed and influence of the simulation box size on the clustering kinetics is discussed next.

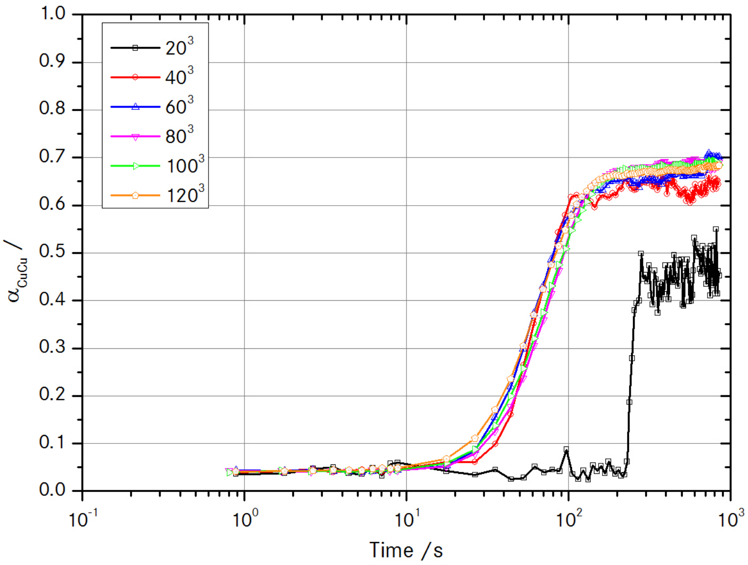

Figure 5.5: Evolution of the short range order parameter α^1_{CuCu} at various simulation box sizes.

The clustering of Cu atoms in the iron matrix can be analysed with evolution of the short range parameter α^1_{CuCu} in time, where Cu-Cu corresponds to the atom pairs under investigation and number one in superscript designates neighbouring shell. In the case of α^1_{CuCu}, the Cu-Cu pairs on the first neighbouring shell are considered. Time evolution of the SRO parameter for various simulation box sizes is depicted in figure 5.5. α^1_{CuCu} curves confirm that the smallest tested box size is not suitable for the cluster precipitation study. All essential features of the system under consideration were captured with box sizes 40^3 BCC lattice sites and above. However, toward the end of the simulation run, the SRO parameter α^1_{CuCu} still slightly fluctuates for box size 40^3 lattice sites, since number of clusters is relatively small.

In figure 5.6, influence of the simulation box size on the time evolution of the average cluster size is presented. In the same graph curves for the classical growth law ($t^{3/2}$) and LSW regime (t) are displayed. Figure 5.6 confirms previous findings, that box size 60^3 lattices describes essential features of the nucleation, growth and coarsening with sufficient accuracy. This box size also gives great compromise regarding the needed computation time for simulation run. Although, box with 60^3 lattice constants is sufficient for studied diffusion processes, majority of simulations presented in the thesis, were performed on the simulation box with 80^3 lattice constants to obtain higher number of clusters and improve subsequent statistical analysis, unless stated otherwise.

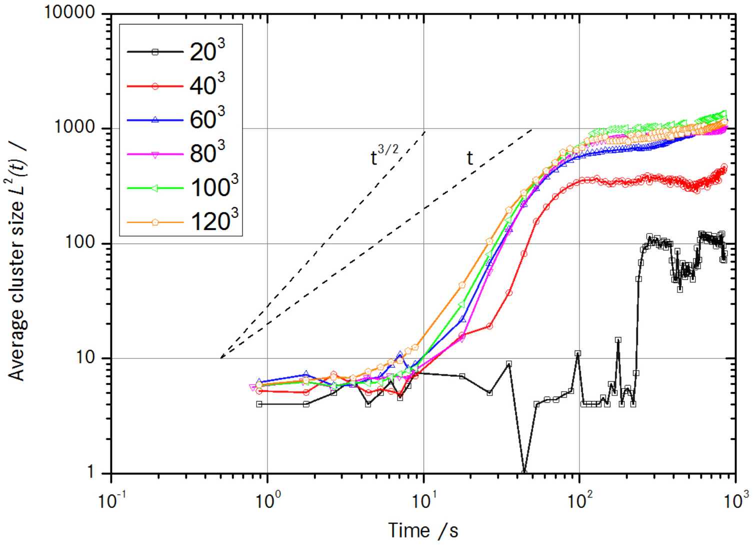

Figure 5.6: Influence of the simulation box size on the time evolution of the average cluster size.

5.3.2 Influence of the temperature and chemical composition

Influence of the temperature and chemical composition on the precipitation kinetics was investigated next. The kMC simulation runs were performed on the simulation box with 80^3 BCC lattices, which is equal to 23^3 nm. Full periodic boundary conditions were used. Total number of available atom position for the BCC crystal structure amounts to 10240000 positions. Simulations with 1 at.% Cu had 1 vacancy, 10241 Cu atoms and 1013759 Fe atoms. Simulations with 1.5 at.% Cu had 1 vacancy, 15361 Cu atoms and 1008639 Fe atoms. The temperature for each run was kept constant. The snapshots of obtained results, whith only Cu atoms shown, are presented in figures 5.7 - 5.11.

Results of obtained clusters for simulations with 1 at.% Cu are shown in figures 5.7, 5.8, 5.10 and 5.11 at temperatures 923 K, 874 K, 773 K and 673 K, respectively. In figure 5.9 results obtained with 1.5 at.% Cu at 873 K are depicted. Snapshot of the atom positions obtained from simulations were depicted and rendered with VMD - Visual Molecular Dynamics, molecular graphics software, [177]. Simulations started with totally disordered configuration where Cu atoms are randomly distributed in the Fe matrix. With evolution of the time, Cu atoms start to form clusters which then evolve through the growth and coarsening.

Formation of the Cu clusters causes depletion of the Cu in the matrix. In time, concentration of the Cu atoms in the matrix decreases and after very long times reaches equilibrium concentration $c_{eq\mathrm{Cu}}$ defined as,

$$c_{eq\mathrm{Cu}}(t \to \infty) \cong \exp\left(\frac{\Delta S}{k_\mathrm{B}}\right) \exp\left(\frac{E_\mathrm{mixFeCu}}{k_\mathrm{B}T}\right) \tag{5.13}$$

where, ΔS is the nonconfigurational entropy and was set according to the suggestions from literature, [167] as $\Delta S = 0.8k_\mathrm{B}$. The equilibrium matrix concentrations calculated with equation (5.13) for temperatures used in the kMC simulations are given in Table 5.4 for three mixing energies. Mixing energy value $E_\mathrm{mixFeCu} = -0.52$ eV was used and was for temperatures investigated obtained from the solubility of Cu in Fe, [170]. Different value ($E_\mathrm{mixFeCu} = -0.60$ eV) was also proposed, [151] and used in the kMC simulations. For these two mixing energies, complete simulation runs were performed to evaluate influence of the mixing energy on the clustering kinetics. For illustrative reasons, the equilibrium matrix concentrations at various temperatures were calculated for values of the mixing energy used in simulations and for middle value between those two.

Table 5.4: The equilibrium matrix concentrations at various temperatures for different mixing energies.

T /K	$c_{eq\mathrm{Cu}}$ /at.%		
	$E_\mathrm{mixFeCu} = -0.52$ eV	$E_\mathrm{mixFeCu} = -0.56$ eV	$E_\mathrm{mixFeCu} = -0.60$ eV
673 K	0.028	0.014	0.007
773 K	0.091	0.050	0.027
873 K	0.222	0.130	0.077
923 K	0.322	0.195	0.118

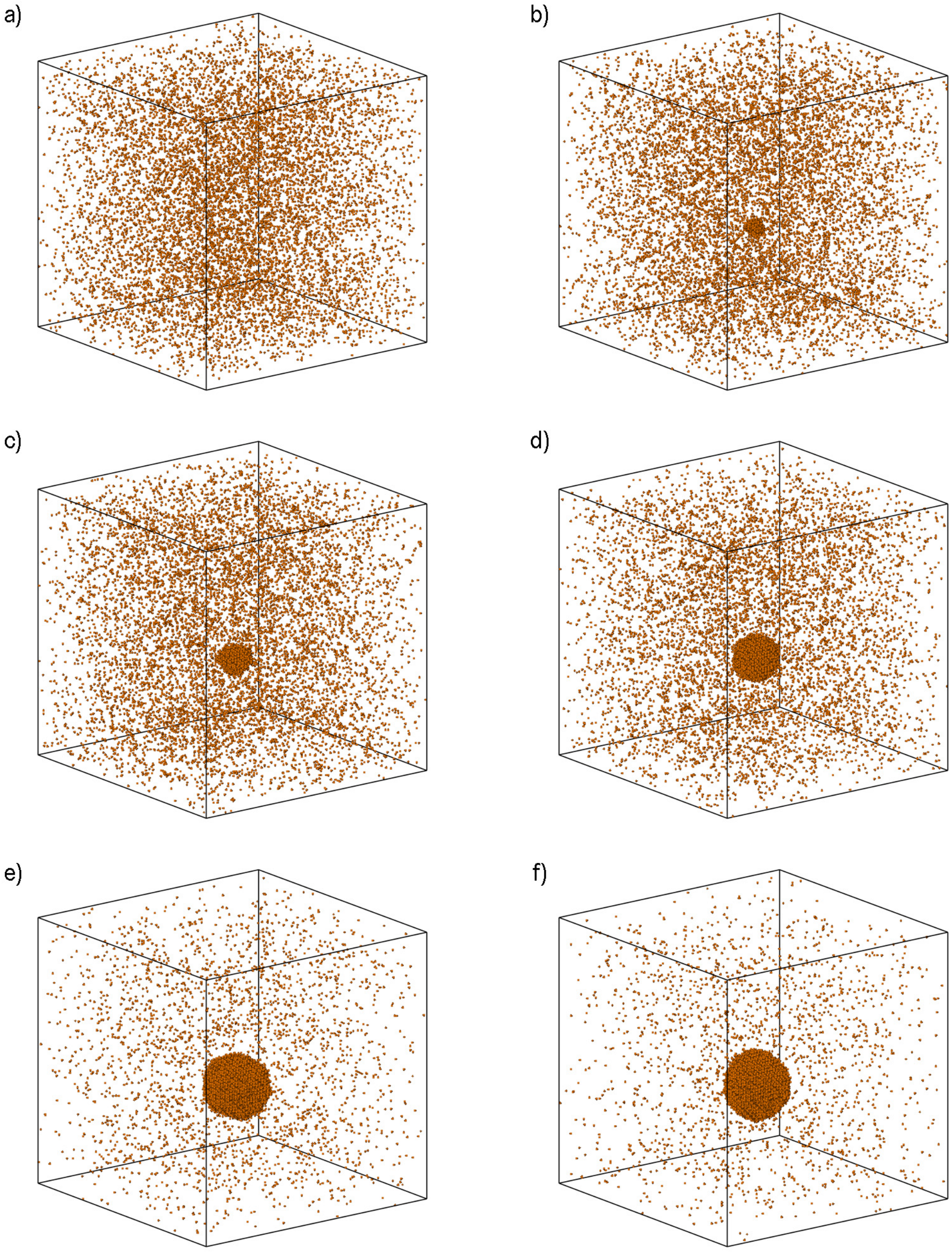

Figure 5.7: Snapshots of Fe-Cu alloy with 1 at.% Cu, obtained from kMC simulations during annealing at 923 K. Size of the simulation box is 80^3 BCC lattices (23^3 nm) and only Cu atoms are displayed due to visibility reasons; a) initial disordered configuration, b) at 4.5 s, c) at 15 s, d) at 30 s, e) at 90 s, f) at 227 s.

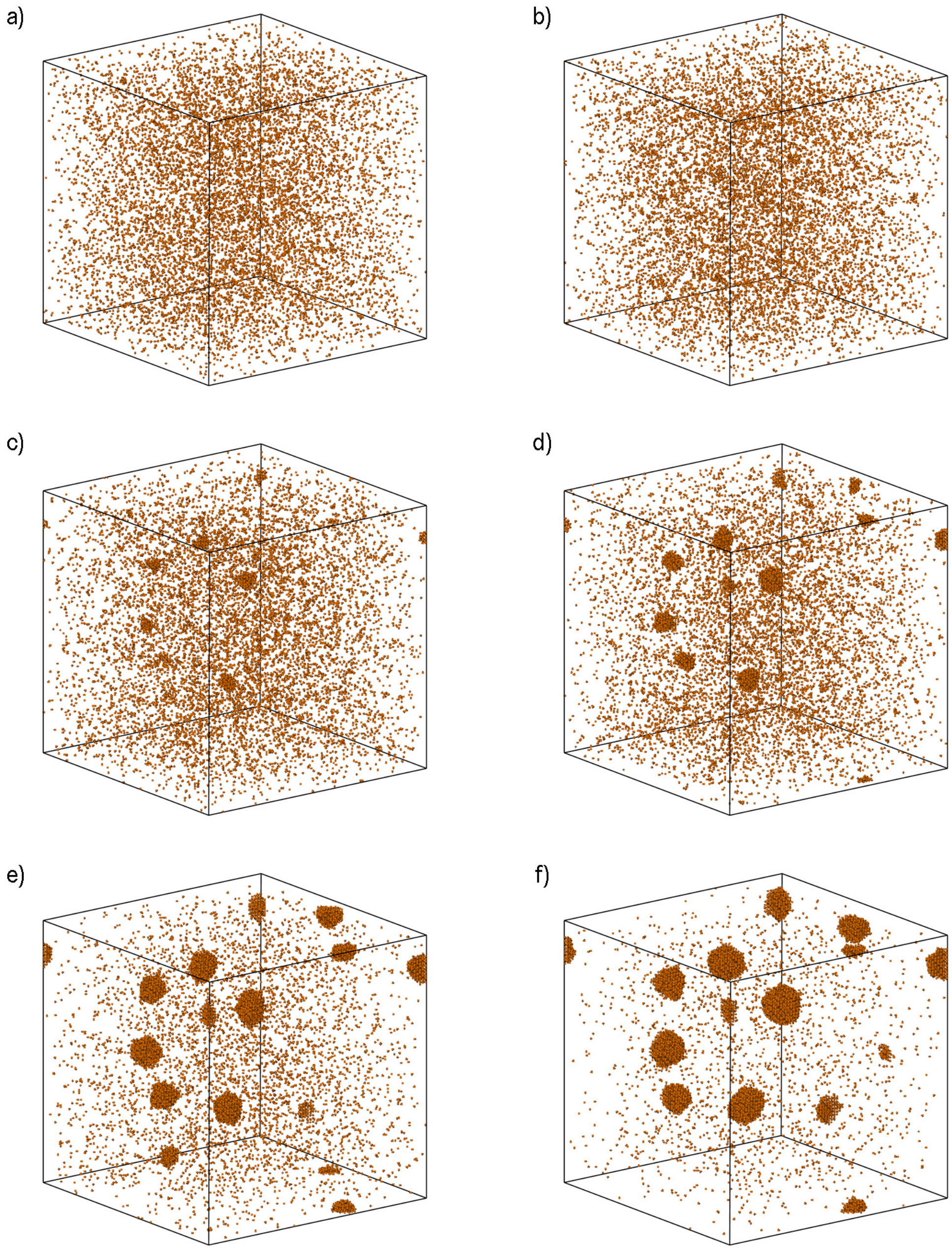

Figure 5.8: Snapshots of Fe-Cu alloy with 1 at.% Cu, obtained from kMC simulations during annealing at 873 K. Size of the simulation box is 80^3 BCC lattices (23^3 nm) and only Cu atoms are displayed due to visibility reasons; a) initial disordered configuration, b) at 9 s, c) at 26 s, d) at 44 s, e) at 87 s, f) at 850 s.

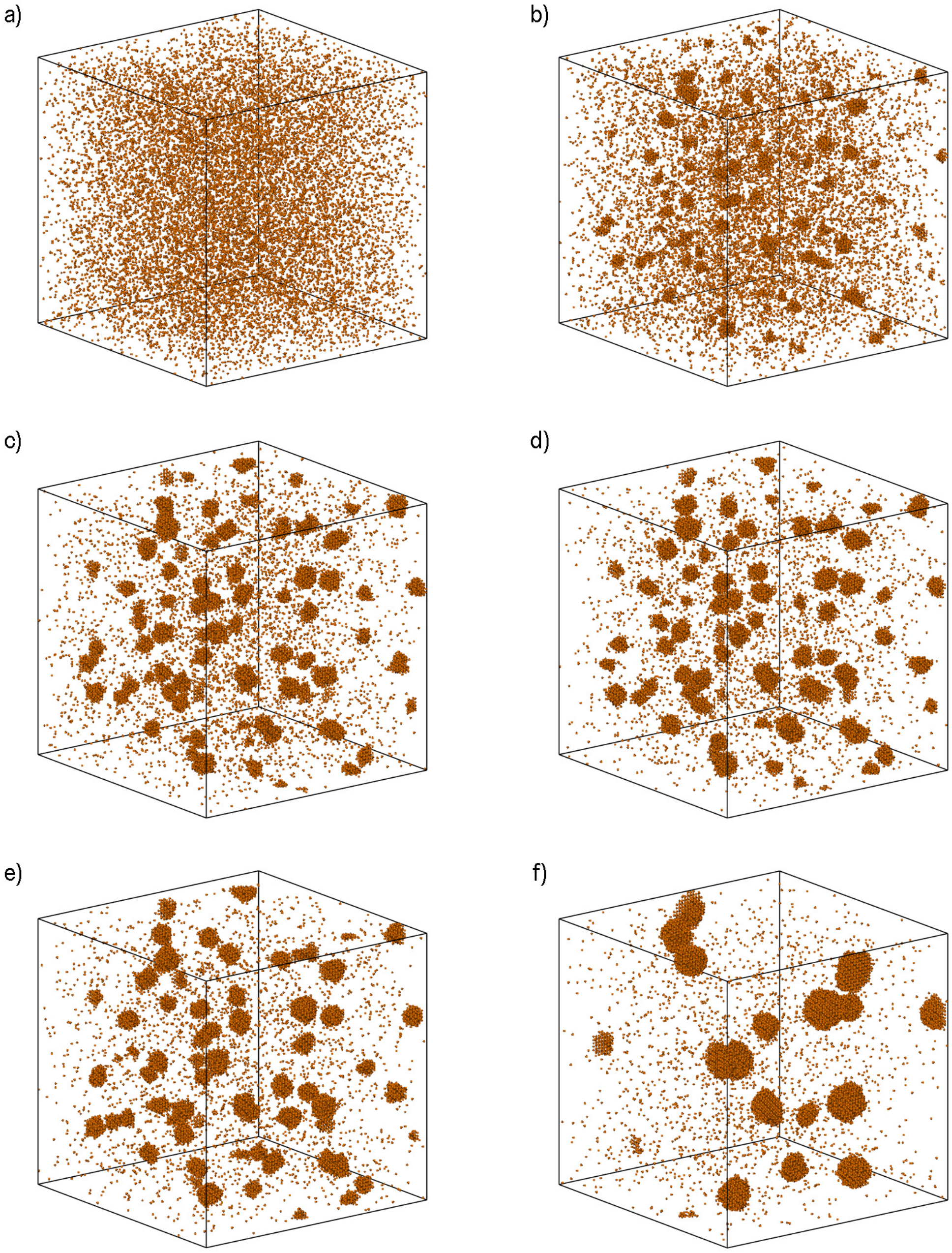

Figure 5.9: Snapshots of Fe-Cu alloy with 1.5 at.% Cu, obtained from kMC simulations during annealing at 873 K. Size of the simulation box is 80^3 BCC lattices (23^3 nm) and only Cu atoms are displayed due to visibility reasons; a) initial disordered configuration, b) at 8 s, c) at 24 s, d) at 40 s, e) at 79 s, f) at 790 s.

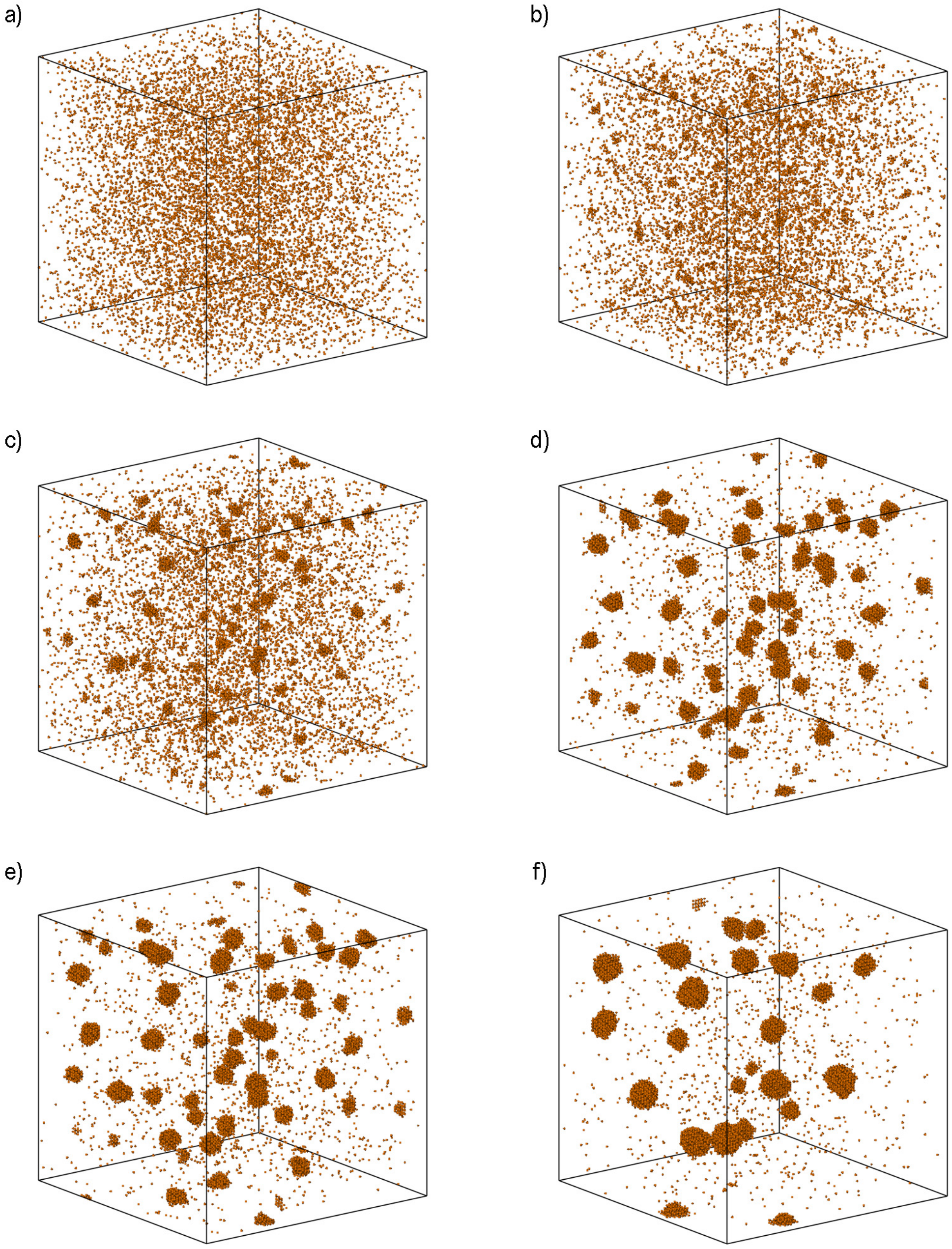

Figure 5.10: Snapshots of Fe-Cu alloy with 1 at.% Cu, obtained from kMC simulations during annealing at 773 K. Size of the simulation box is 80^3 BCC lattices (23^3 nm) and only Cu atoms are displayed due to visibility reasons; a) initial disordered configuration, b) at 181 s, c) at 596 s, d) at 2780 s, e) at 5431 s, f) at 53092 s.

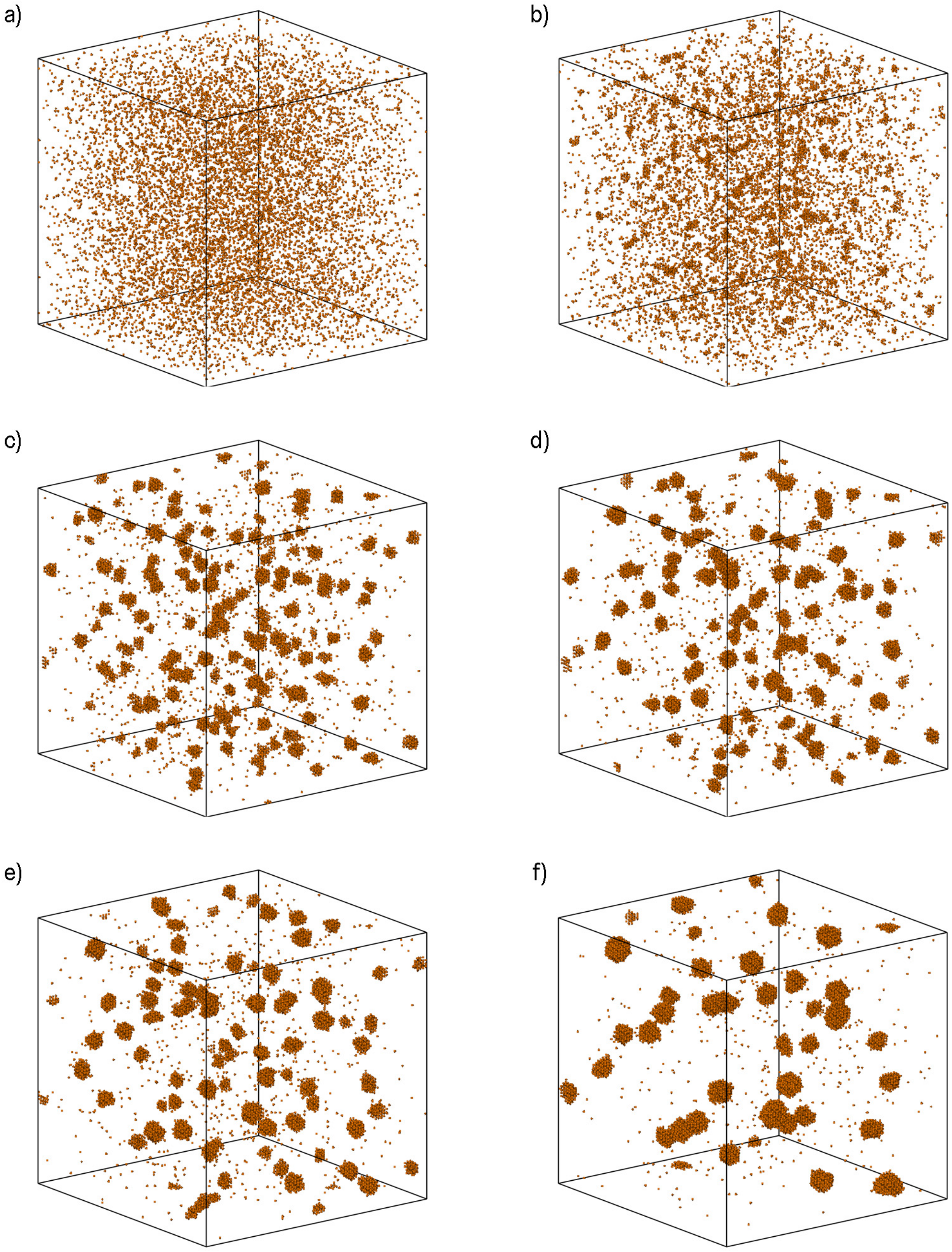

Figure 5.11: Snapshots of Fe-Cu alloy with 1 at.% Cu, obtained from kMC simulations during annealing at 673 K. Size of the simulation box is 80^3 BCC lattices (23^3 nm) and only Cu atoms are displayed due to visibility reasons; a) initial disordered configuration, b) at 28345 s, c) at 358598 s, d) at 1.1×10^6 s, e) at 2.2×10^6 s, f) at 9.6×10^6 s.

In figure 5.12, the short range order parameter α^1_{CuCu} calculated with equation (2.70) for the substitutional first nearest neighbours in Fe-Cu alloys isothermally aged at different temperatures and with various chemical compositions is presented. Clear influence of the temperature and composition on the precipitation kinetics is displayed. Incubation time is present in all starting conditions before α^1_{CuCu} starts to increase. The incubation time is influenced by the temperature and chemical composition as can be seen in figure 5.12. When stable nuclei start to form Cu clusters, the matrix becomes depleted with Cu atoms and SRO parameters starts to slowly rise i.e. the number of Cu-Cu bonds is increased. Subsequent growth of the nuclei causes sharp increase in α^1_{CuCu}, since more and more Cu atoms belong to the clusters. In figure 5.12 coarsening stage can be identified from the SRO parameter slope change. In this stage of the alloy evolution, the SRO parameter rises linearly and more moderate in time compared to the previous stage. In figure 5.13 time evolution of Cu concentration in the matrix $X_{\mathrm{Cu}}(t)$, at different temperatures and chemical compositions is shown. Graph exhibits mirrored properties compared to the time evolution of the SRO. Concentration of atoms in the matrix is decreasing very quickly, and at the end of simulations similar values, than those for equilibrium concentrations presented in Table 5.4 are reached. Growth rate of Cu clusters can be estimated from time evolution of Cu concentration in the matrix, where with higher initial concentration and temperature, growth rate

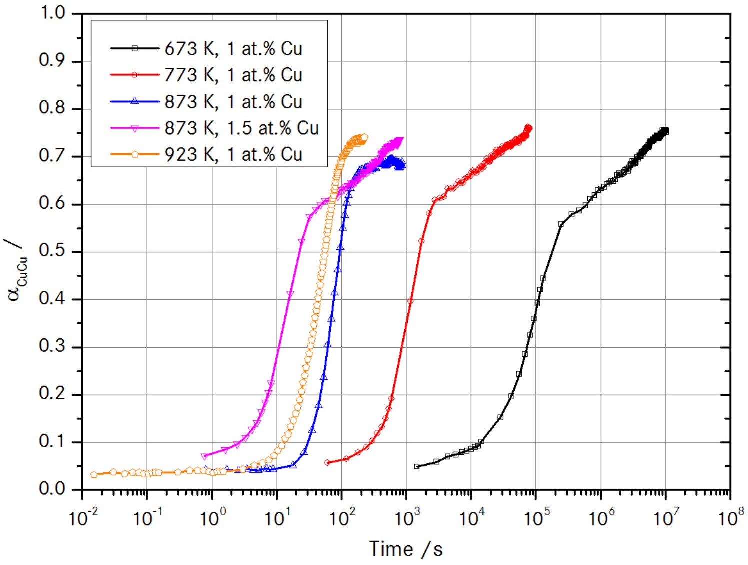

Figure 5.12: Evolution of the short range order parameter in Fe-Cu alloys at different temperatures and various chemical compositions.

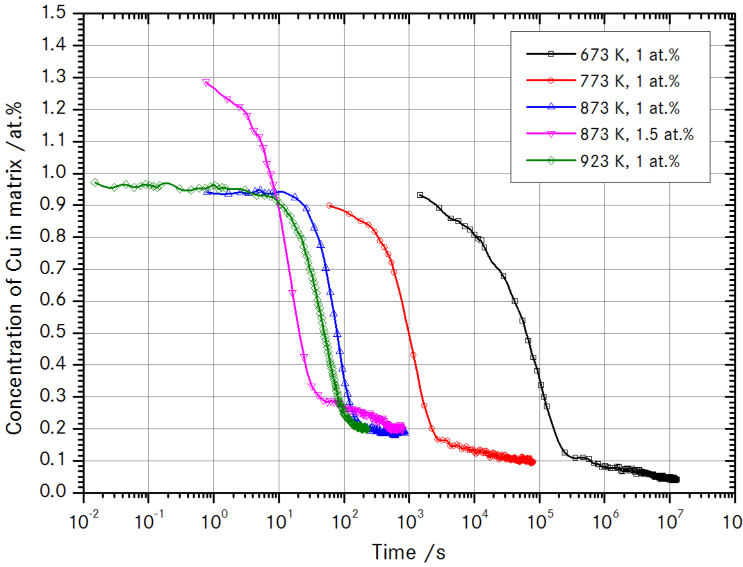

Figure 5.13: Time evolution of Cu concentration in the matrix at different temperatures and various chemical compositions.

increases. Characterization of the clustering process during simulations was also analysed through evolution of the number and size of formed clusters. In figure 5.14, the

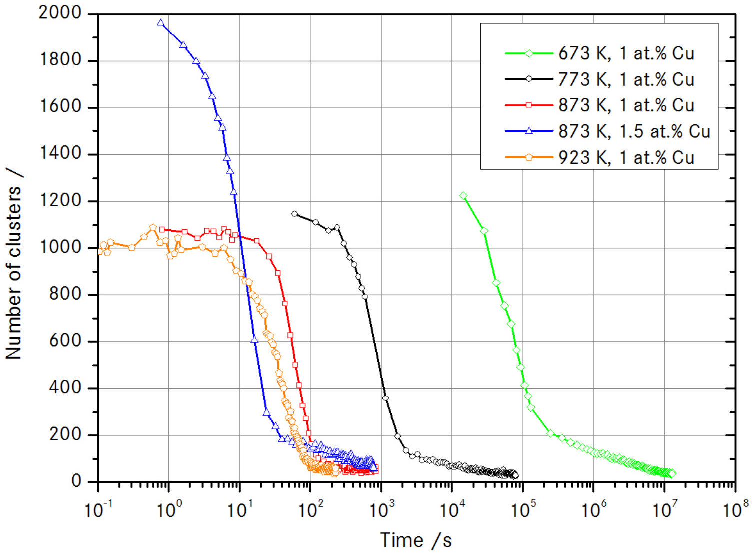

Figure 5.14: Number of clusters, including dimers in Fe-Cu alloys at different conditions.

number of clusters in time is displayed where all possible cluster sizes were included. At the beginning of the simulation, number of clusters strongly depends on the chemical composition. Number of clusters at the beginning of the simulations is presented in Table 5.5 and together with figure 5.14 confirms initial rise in the number of clusters after simulations are commenced. After certain period of time (100 MSC), number of the clusters sharply decrease as stable nuclei start to grow and stable cluster radii increases. The number of clusters toward the end of simulations is still decreasing, but with lower rate. Change in the slope of the number of precipitates is connected to the LSW regime of coarsening.

Table 5.5: Number of cluster at the initial disordered state ($t = 0$ s) for various temperature and chemical compositions.

Condition	Dimers	Trimer	Tetramers	Pentamers	Total
673 K, 1 at.% Cu	376	33	3	-	403
773 K, 1 at.% Cu	349	18	2	-	369
873 K, 1 at.% Cu	385	25	3	-	413
873 K, 1.5 at.% Cu	764	80	2	1	848
923 K, 1 at.% Cu	375	30	2	1	408

Beside following evolution of the number of clusters in time another important feature in the cluster microstructure evolution is change of its mean size. The average cluster size $L^2(t)$ is defined as a second moment of the cluster size distribution normalized by the first moment of the cluster size distribution (cf. section 2.4.1.2). Its evolution is followed in time and is shown in figure 5.15 for simulated Fe-Cu alloys, where cluster size is measured as dimensionless volume. In the same graph, also lines for the classical growth law and LSW regime are shown, where growth law is proportional to $t^{3/2}$ and curve for the LSW regime is proportional to t, due to use of volumes and not radii. If cube root is used on these expressions one yields well known power law coefficients for the growth ($t^{1/2}$) and coarsening ($t^{1/3}$) stages. At the beginning, nuclei are needed before growth can start. After initial clusters reach critical size they exhibit increased average size. In this stage for higher temperatures and 1 at.% Cu supersaturation, curves follow classical growth law quite well before plateau is reached and size becomes constant. Simulations at lower temperatures or higher superaturations exhibit change in the curve slope, coresonding to alternating growth and LSW regime. Toward the end of simulations these curves then exhibit clear LSW regime.

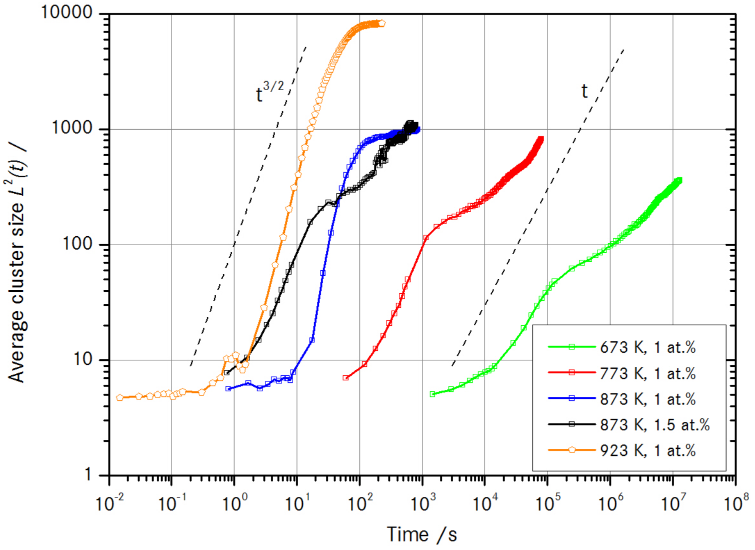

Figure 5.15: Evolution of the average cluster size in time for simulated conditions in Fe-Cu alloys.

5.3.3 Influence of the mixing energy

As already explained, the mixing energy has influence on the equilibrium matrix concentrations; cf. Table 5.4. Effects of temperature and chemical composition on the clustering were studied with the mixing energy $E_{\text{mixFeCu}} = -0.52$ eV, obtained from solubility of Cu in Fe, [170]. Different value ($E_{\text{mixFeCu}} = -0.60$ eV) was also proposed, [151] and used in kMC simulations. Since mixing energy E_{mixFeCu} is connected to the shape of the alloy phase diagrams, its effect on the clustering kinetics was analysed and compared. Simulations parameters for first set are given in Table 5.2. Second set of the simulation parameters were calculated with equations (5.1), (5.2), (5.1) and (5.5),

Table 5.6: Simulation parameters with mixing energy $E_{\text{mixFeCu}} = -0.60$ eV.

$\epsilon^{(1)}_{\text{FeFe}} = -0.778$ eV	$\epsilon^{(2)}_{\text{FeFe}} = -0.389$ eV
$\epsilon^{(1)}_{\text{CuCu}} = -0.778$ eV	$\epsilon^{(2)}_{\text{CuCu}} = -0.389$ eV
$\epsilon^{(1)}_{\text{FeCu}} = -0.7235$ eV	$\epsilon^{(2)}_{\text{FeCu}} = -0.3617$ eV
$\epsilon^{(1)}_{\text{FeV}} = -0.335$ eV	$\epsilon^{(1)}_{\text{CuV}} = -0.335$ eV
$E_{\text{SpFe}} = -9.557$ eV	$E_{\text{SpCu}} = -9.098$ eV
$\nu_{\text{Fe}} = 8.70 \times 10^{12}$ s^{-1}	$\nu_{\text{Cu}} = 8.70 \times 10^{12}$ s^{-1}

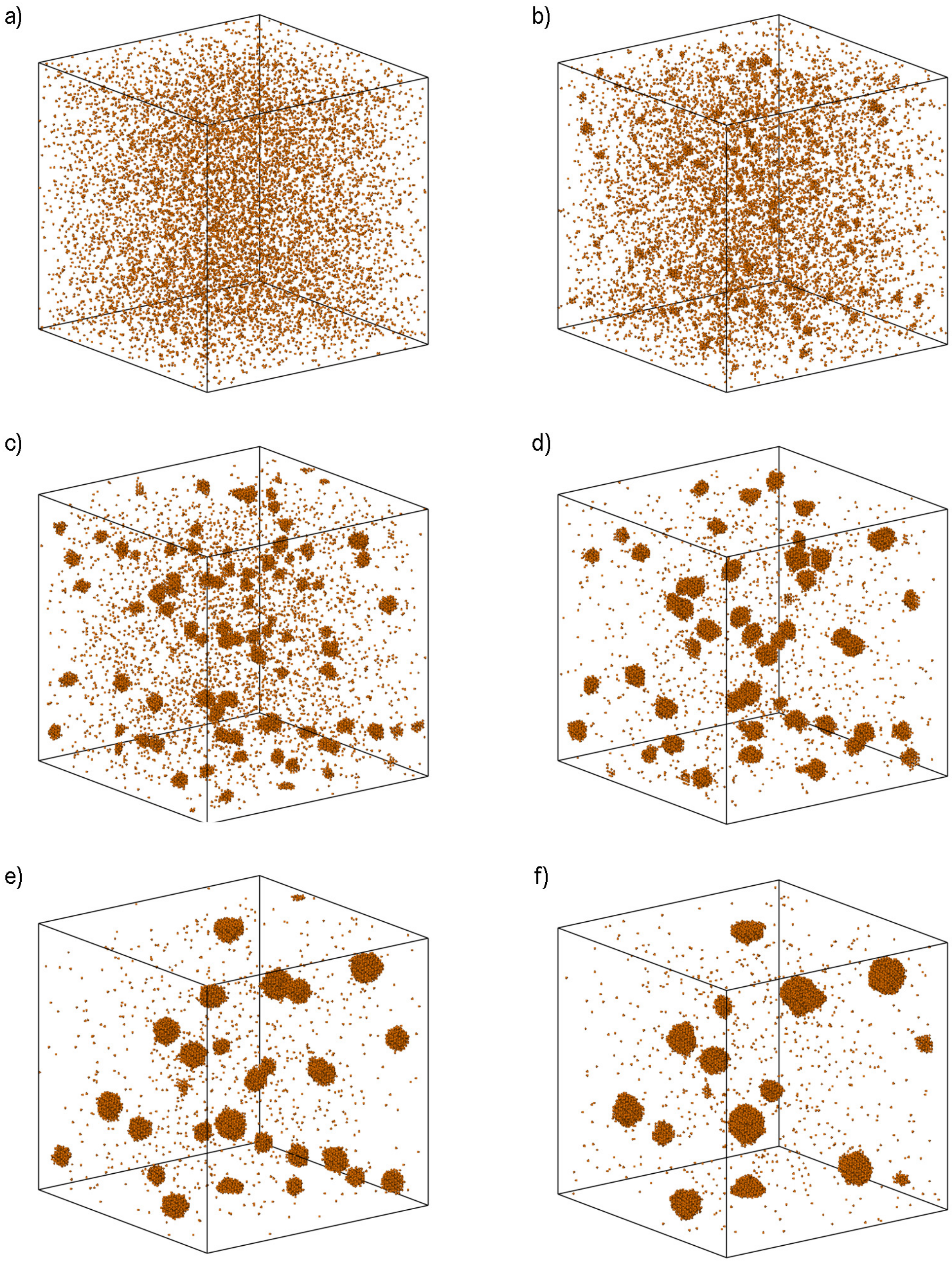

Figure 5.16: Snapshots of Fe-Cu alloy with 1 at.% Cu, obtained from kMC simulations during annealing at 873 K and increased mixing energy. Size of the simulation box is 80^3 BCC lattices (23^3 nm) and only Cu atoms are displayed due to visibility reasons; a) initial disordered configuration, b) at 1.7 s, c) at 7.9 s, d) at 73 s, e) at 289 s, f) at 724 s.

with value for the mixing energy taken as $E_{\mathrm{mixFeCu}} = -0.60$ eV and other material properties needed for calculation given in Table 5.1. This yields simulation parameters presented in Table 5.6. Influence of the mixing energy on the clustering process was analysed through comparison of the SRO parameter, the number of precipitates and average cluster size. 5.6. Two simulations with different set of parameters were executed. In the first simulation run, simulation parameters given in Table 5.2 were used, and then compared to the results obtained with run using simulation parameters in Table The same starting conditions were used, in Fe-Cu alloy with 1. at% Cu atoms isothermally aged at 873 K. Size of the simulation boxes for both runs was 80^3 BCC lattices.

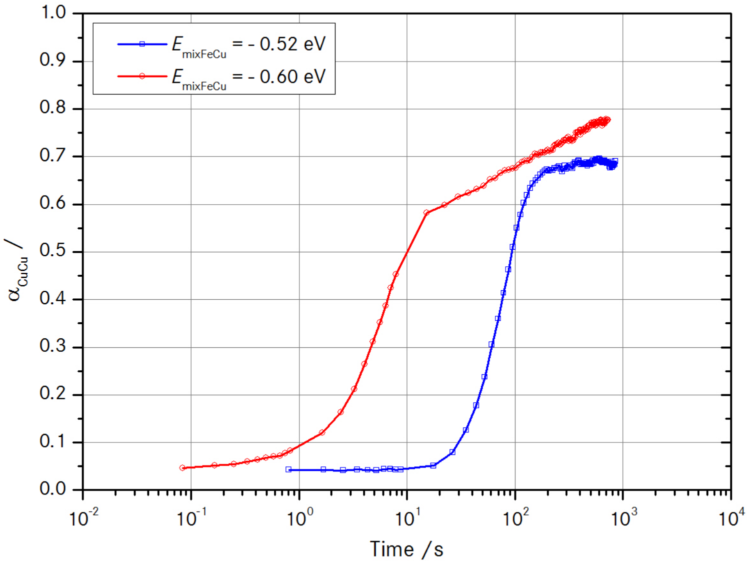

Figure 5.17: Influence of mixing energy on the evolution of the short range order parameter.

In figure 5.17 evolution of the short range parameter for both simulations is depicted. Similarity can be detected at the beginning of the simulations if the time difference is ignored. The clustering is quicker and incubation time shortens if the mixing energy is higher. With lower mixing energy, SRO parameter reaches plateau, where it remains constant, while for the higher mixing energy it still has tendency to increase. Figure 5.18 depicts number of clusters, including dimers for both mixing energies. Number of clusters is almost the same at the beginning and at the end. Higher mixing energy causes number of clusters to decrease faster in time, similar than in evolution of the short range order parameter.

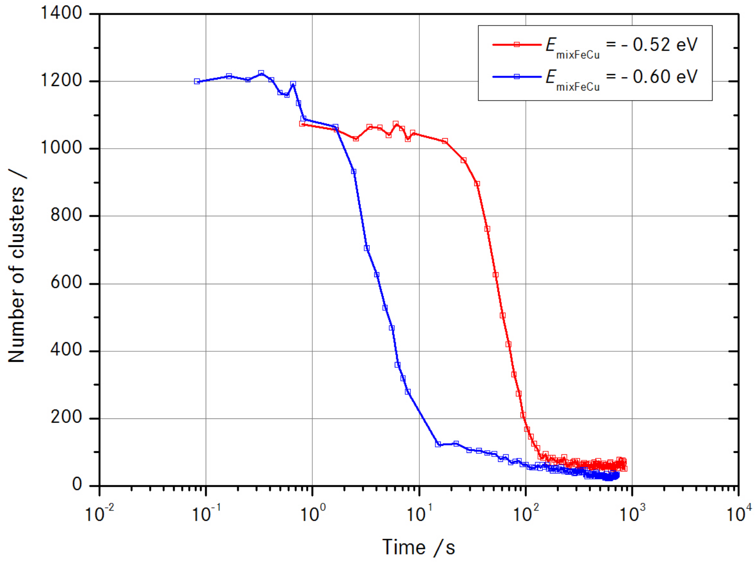

Figure 5.18: Influence of mixing energy on number of clusters in time.

In figure 5.19 comparison of average cluster sizes for two mixing energies is shown. With higher mixing energy, clear distinction between growth and coarsening stages can be identified. Furthermore, growth and coarsening is taking place according to the classical growth and LWS, respectively. When first simulation parameters set is

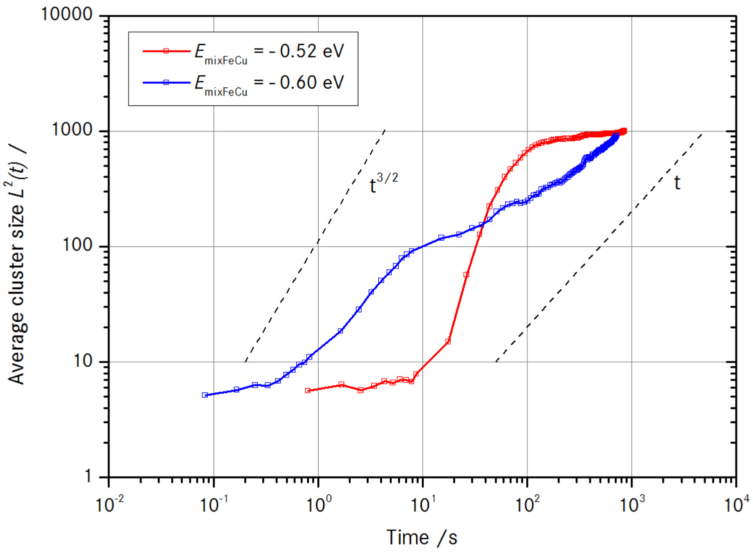

Figure 5.19: Influence of mixing energy on evolution of the average cluster size in time.

used, where mixing energy is lower, there is no clear distinction between growth and coarsening. Also growth is taking place much longer, compared to previous simulation set.

5.3.4 Influence of the model asymmetry

The literature review on the subject revealed strong influence of the asymmetry parameter on the nucleation and growth kinetics in various binary alloys, [17, 96, 172, 174]. The energetic model used in those studies was based on the kinetic Ising model, the ghost energies between vacancy and its first nearest neighbours were not considered and only nearest neighbour interaction were used. The adjusted SPEM2 broken bond model was used in another study with simulation parameters which exhibit asymmetry, however the influence of the model asymmetry parameter $a*$, was not investigated in this study, [167]. One of the findings of the aforementioned studies was that negative asymmetry parameter $a*$, influences vacancy trapping in the Cu clusters, which results in agglomeration or coagulation of clusters. This section addresses vacancy trapping effects in the Fe-Cu alloys system and its influence on the physical time, which were not studied before. When vacancy becomes trapped in the Cu rich cluster it causes mobility of this cluster even when cluster is large in its size. These moving Cu rich cluster can on its way meet another Cu rich cluster which causes agglomeration or coagulation of two clusters into single cluster. The single cluster shape then changes due to surface energy minimization into near spherical shape.

Table 5.7: Simulation parameters with asymmetry parameter $a* = 45.27$.

$\epsilon^{(1)}_{\mathrm{FeFe}} = -0.778$ eV	$\epsilon^{(2)}_{\mathrm{FeFe}} = -0.389$ eV
$\epsilon^{(1)}_{\mathrm{CuCu}} = -0.635$ eV	$\epsilon^{(2)}_{\mathrm{CuCu}} = -0.317$ eV
$\epsilon^{(1)}_{\mathrm{FeCu}} = -0.683$ eV	$\epsilon^{(2)}_{\mathrm{FeCu}} = -0.342$ eV
$\epsilon^{(1)}_{\mathrm{FeV}} = -0.335$ eV	$\epsilon^{(1)}_{\mathrm{CuV}} = -0.276$ eV
$E_{\mathrm{SpFe}} = -9.250$ eV	$E_{\mathrm{SpCu}} = -9.250$ eV
$\nu_{\mathrm{Fe}} = 8.70 \times 10^{12}\ \mathrm{s}^{-1}$	$\nu_{\mathrm{Cu}} = 8.70 \times 10^{12}\ \mathrm{s}^{-1}$

In the previous section symmetric model was used, where interatomic binding energies between Fe and Cu are assumed the same. No vacancy trapping was observed in the simulation where symmetrical model was employed. In order to investigate influence of the model asymmetry parameter $a*$, the cohesive energy of Cu was used as adjusting parameter. The asymmetry parameter $c*$ was set to zero in order not to overcomplicate model and parameter interdependencies. The saddle point energies used for Fe and Cu were set equal $E_{\mathrm{SpFe}} = E_{\mathrm{SpCu}} = -9.250$ eV. As explained before, small difference in the tracer diffusivity of Fe and Cu in Fe was addressed through the saddle point energies in the symmetrical model. When asymmetry parameter $a*$ take account of differences in the tracer diffusivity through the interatomic energies, the saddle point energy adjustments are not needed any more. Connection between the asymmetry parameter $a*$, the homoatomic interaction energies and mixing energy is given as

$$\epsilon^{(1)}_{\mathrm{CuCu}} = \frac{2E_{\mathrm{mixFeCu}}}{33} a * -\epsilon^{(1)}_{\mathrm{FeFe}} \tag{5.14}$$

Equation (5.14) was obtained with reordering of equations (5.1), (5.2), (5.5) and (5.12). The homoatomic energies of Fe were calculated from the cohesive energy; cf. section 5.1. The mixing energy used, was $E_{\mathrm{mixFeCu}} = -0.52$ eV, same as simulations where influences of temperature and chemical composition were analysed. For example, in Table 5.7 simulation parameters for Fe-Cu alloy system, if homoatomic energies of Cu are calculated from the cohesive energy of Cu in the pure FCC phase are given. With equation (5.12) and simulation parameters in Table 5.7, asymmetry parameter yields $a* = 45.27$, which is unrealistic asymmetry for Cu in BCC Fe.

To investigate influence of the asymmetry parameter $a*$, several simulations were performed on simulation box with 64^3 BCC lattices and varying $a*$. The chosen values of $a*$ were -2.5, -1, 0.25 and 0.5 and equation (5.14) was used to obtain simulation parameters with those predefined asymmetry values. The simulation parameters for the asymmetry values -2.5, -1, 0.25 and 0.5 are given in Tables 5.8, 5.9, 5.10 and 5.11, respectively. As control set, the simulation run was executed also with both asymmetry parameters ($a*$ and $c*$) set as zero. In simulations where influence of asymmetry on the phase ordering was studied, random alloy with 3 at.% Cu atoms was quenched from infinite temperature to a temperature $T = 873$ K. In order to increase statistics of the cluster properties in the focused regimes of growth and coarsening, higher number density of precipitates is desired. Therefore, to increase the number density of precipitates larger supersaturation was used (3 at.% Cu).

The asymmetry parameter $a*$, has large effect on simulations of the diffusion process and consequently influences cluster mobility. When $a*$ is negative, the vacancy spends more time in the Fe matrix. However, if the asymmetry parameter $a*$ is positive, vacancy prefers being near Cu atoms which leads to the vacancy trapping in Cu clusters. The vacancy trapping in Cu rich area influences the real time because the residence time algorithm still returns time increment, although microstucture is in not developing while vacancy is trapped in the Cu cluster. To reasonably adjust real time in simulations

Table 5.8: Simulation parameters with asymmetry parameter $a* = -2.5$.

$\epsilon^{(1)}_{\mathrm{FeFe}} = -0.778$ eV	$\epsilon^{(2)}_{\mathrm{FeFe}} = -0.389$ eV
$\epsilon^{(1)}_{\mathrm{CuCu}} = -0.700$ eV	$\epsilon^{(2)}_{\mathrm{CuCu}} = -0.350$ eV
$\epsilon^{(1)}_{\mathrm{FeCu}} = -0.653$ eV	$\epsilon^{(2)}_{\mathrm{FeCu}} = -0.327$ eV
$\epsilon^{(1)}_{\mathrm{FeV}} = -0.335$ eV	$\epsilon^{(1)}_{\mathrm{CuV}} = -0.281$ eV
$E_{\mathrm{SpFe}} = -9.250$ eV	$E_{\mathrm{SpCu}} = -9.250$ eV
$\nu_{\mathrm{Fe}} = 8.70 \times 10^{12}$ s^{-1}	$\nu_{\mathrm{Cu}} = 8.70 \times 10^{12}$ s^{-1}

Table 5.9: Simulation parameters with asymmetry parameter $a* = -1$.

$\epsilon^{(1)}_{\mathrm{FeFe}} = -0.778$ eV	$\epsilon^{(2)}_{\mathrm{FeFe}} = -0.389$ eV
$\epsilon^{(1)}_{\mathrm{CuCu}} = -0.747$ eV	$\epsilon^{(2)}_{\mathrm{CuCu}} = -0.373$ eV
$\epsilon^{(1)}_{\mathrm{FeCu}} = -0.700$ eV	$\epsilon^{(2)}_{\mathrm{FeCu}} = -0.350$ eV
$\epsilon^{(1)}_{\mathrm{FeV}} = -0.335$ eV	$\epsilon^{(1)}_{\mathrm{CuV}} = -0.313$ eV
$E_{\mathrm{SpFe}} = -9.250$ eV	$E_{\mathrm{SpCu}} = -9.250$ eV
$\nu_{\mathrm{Fe}} = 8.70 \times 10^{12}$ s^{-1}	$\nu_{\mathrm{Cu}} = 8.70 \times 10^{12}$ s^{-1}

Table 5.10: Simulation parameters with asymmetry parameter $a* = 0.25$.

$\epsilon^{(1)}_{\mathrm{FeFe}} = -0.778$ eV	$\epsilon^{(2)}_{\mathrm{FeFe}} = -0.389$ eV
$\epsilon^{(1)}_{\mathrm{CuCu}} = -0.786$ eV	$\epsilon^{(2)}_{\mathrm{CuCu}} = -0.393$ eV
$\epsilon^{(1)}_{\mathrm{FeCu}} = -0.739$ eV	$\epsilon^{(2)}_{\mathrm{FeCu}} = -0.370$ eV
$\epsilon^{(1)}_{\mathrm{FeV}} = -0.335$ eV	$\epsilon^{(1)}_{\mathrm{CuV}} = -0.340$ eV
$E_{\mathrm{SpFe}} = -9.250$ eV	$E_{\mathrm{SpCu}} = -9.250$ eV
$\nu_{\mathrm{Fe}} = 8.70 \times 10^{12}$ s^{-1}	$\nu_{\mathrm{Cu}} = 8.70 \times 10^{12}$ s^{-1}

Table 5.11: Simulation parameters with asymmetry parameter $a* = 0.5$.

$\epsilon^{(1)}_{\mathrm{FeFe}} = -0.778$ eV	$\epsilon^{(2)}_{\mathrm{FeFe}} = -0.389$ eV
$\epsilon^{(1)}_{\mathrm{CuCu}} = -0.794$ eV	$\epsilon^{(2)}_{\mathrm{CuCu}} = -0.397$ eV
$\epsilon^{(1)}_{\mathrm{FeCu}} = -0.747$ eV	$\epsilon^{(2)}_{\mathrm{FeCu}} = -0.373$ eV
$\epsilon^{(1)}_{\mathrm{FeV}} = -0.335$ eV	$\epsilon^{(1)}_{\mathrm{CuV}} = -0.346$ eV
$E_{\mathrm{SpFe}} = -9.250$ eV	$E_{\mathrm{SpCu}} = -9.250$ eV
$\nu_{\mathrm{Fe}} = 8.70 \times 10^{12}$ s^{-1}	$\nu_{\mathrm{Cu}} = 8.70 \times 10^{12}$ s^{-1}

where vacancy prefers Cu rich areas, and to maintain equilibrium vacancy concentration in Fe at its equilibrium value, time was corrected with the fraction of time, when vacancy resides in the Fe matrix. Time was advanced only when there were no Cu among its 8 nearest neighbours. For the asymmetry parameter $a* = -1$ effect of the time correction if time is advanced only when vacancy resides in the Fe matrix is shown in figure 5.20. The difference between adjusted time and time without adjustment, is increasing with number of the MCS. This happens due to the size of Cu clusters, which are larger toward the end of the simulation. As the clusters are larger time when vacancy is near them or trapped inside them increases.

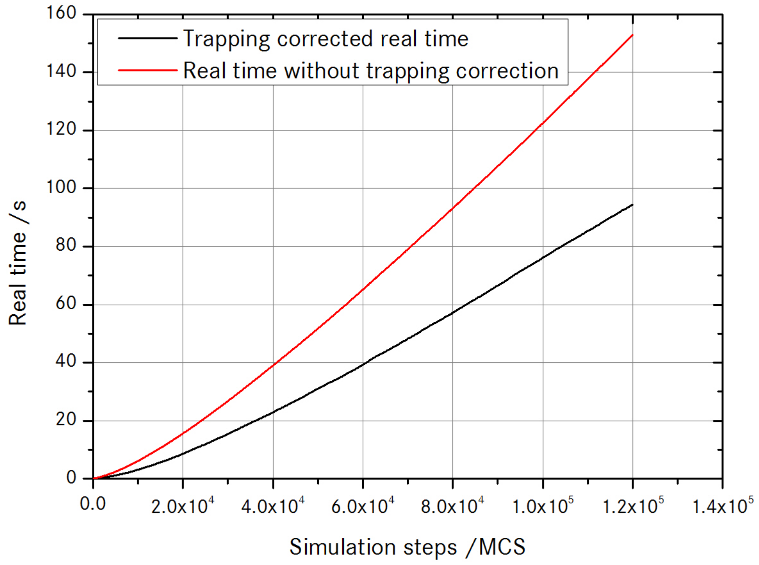

Figure 5.20: Influence on the real time for asymmetry parameter $a* = -1$, with and without vacancy trapping adjustment.

The diffusion of copper clusters, even large ones was observed at simulations with the negative asymmetry parameter. This is attributed to the vacancy trapping in Cu clusters which causes rearrangement of atoms in the cluster and consequently causes diffusion of the whole clusters. In figure 5.21 influence of the asymmetry parameter $a*$, on time evolution of the SRO parameter α^1_{CuCu} is shown. Figure 5.21 confirms influence of the asymmetry parameter on time before clustering commences. Also simulations with large $a*$, need to be run much longer to reach times where all relevant processes are sufficiently described. Although, simulation with $a* = -2.5$ was run approximately 3 times longer than the one with $a* = 0$, reached physical time was still very short. This happens due to influence of the model asymmetry, on where vacancy spends most of

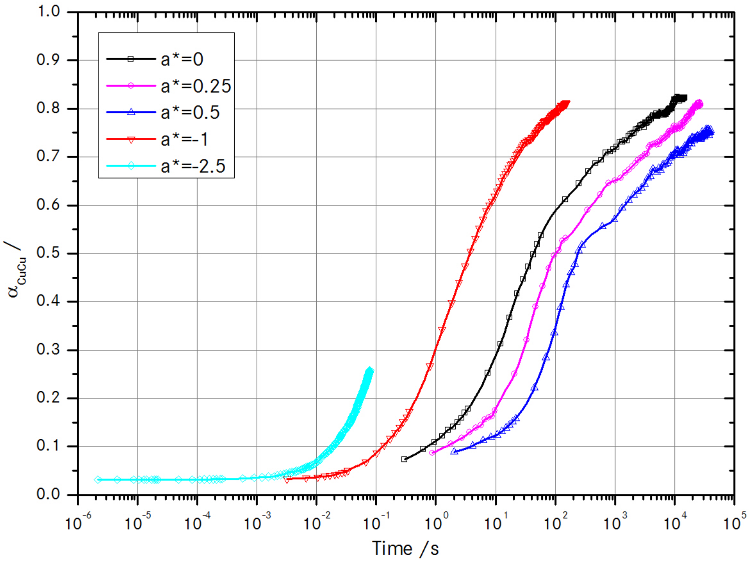

Figure 5.21: Influence of the asymmetry parameter $a*$ on the evolution of the SRO parameter α^1_{CuCu}.

its time. When $a* < 0$, the vacancy prefers Fe and this increases time before clustering of Cu atoms occurs.

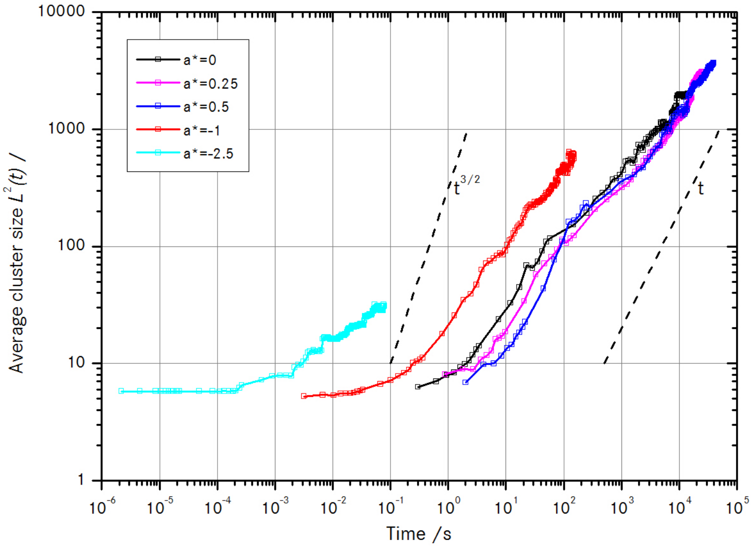

Figure 5.22: Influence of the asymmetry parameter $a*$ on the average cluster size evolution in time.

Figure 5.22, depicts influence of the asymmetry parameter $a*$ on evolution of the average cluster size. In figure 5.22, lines representing the classical growth ($t^{3/2}$) and the LSW regime (t) are also shown. If $a* \geq 0$, growth phase proceeds as predicted by the classical growth law. After the growth stage, growth rate of the clusters severely slows down and curves changes according to the $L^2(t) \propto t^x$, with values for the exponent $x \approx 0.2$, before coarsening starts obeying LSW law. However, clusters obtained with asymmetry $a* = -1$, experience growth according to the $L^2(t) \propto t^x$ with values for the exponent $x \approx 0.38$, before direct agglomeration or coagulation of formed clusters is observed. This is more clear for asymmetry $a* = -2.5$ where clusters starts to agglomerate as soon as they are stable enough. The agglomeration of clusters follows $L^2(t) \propto t^x$, with $x \approx 0.25$ and $x \approx 0.18$ for $a* = -1$ and $a* = -2.5$, respectively. The agglomeration of clusters was confirmed by following the number of atoms in clusters through time. The LSW regime where larger clusters grow on expense of the smaller, causes dissolution of smaller clusters. This is evident from figure 5.23, where influence of the asymmetry parameter $a*$ on the number of clusters larger than pentamers in time is shown. If agglomeration happens two clusters are simply joined and this causes instant reduction of one cluster in the simulation box. Contrary when following LSW regime clusters grow on the expense of smaller ones. Although, smaller clusters are dissolving, they are still present when results are analysed. Furthermore, they are

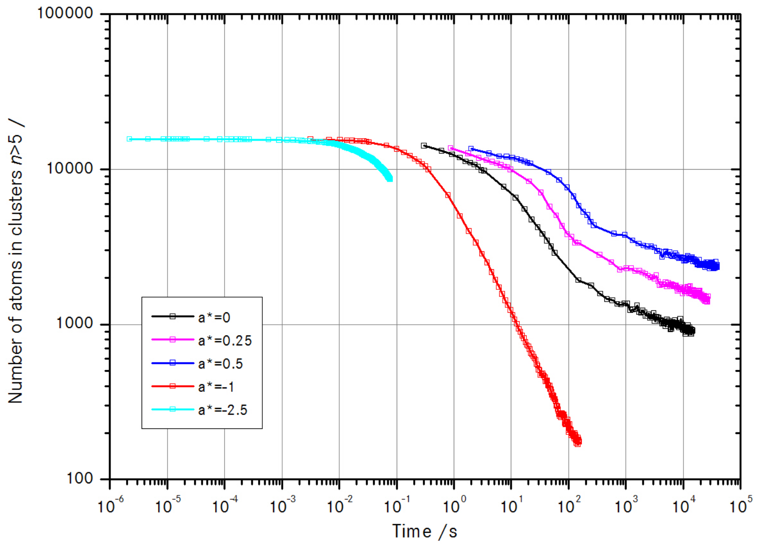

Figure 5.23: Influence the asymmetry parameter $a*$ on the number of clusters larger than pentamers.

beeing detected until their size becomes smaller than setted threshold, which was in this case at $n \geq 5$. This causes diminished decrease in the number of detected clusters as depicted in figure 5.23 for $a \geq 0$.

5.3.5 Evolution of seeded clusters

In previous sections quenching of the disordered distributions from infinite temperature to the predefined temperature caused random formation of clusters with broad distributions. In order, to study concentration profiles around clusters and to quantify their evolution and local environment, spherical clusters with the same dimension were seeded in mildly supersaturated solid solution. Isothermal evolution of the seeded Cu clusters with various sizes was performed with the kMC simulations using parameters in Table 5.2, and at temperature 873 K, simulations box size 50^3 BCC lattices (14.35^3 nm) and background concentration of 0.5 at.% Cu. At temperature 873 K and simulation parameters used, equlibrium concentration is approximately 0.22 at.%, which means that simulations were performed at slightly supersaturated conditions. However, used backgrund concentration causes small enough supersaturation such that no new clusters were percieved to nucleate. Eight clusters were seeded, each with distance 25 lattice constants (7.175 nm) from another in all directions. Radius of clusters was variable and all simulations were performed to 50×10^3 MCS. Radii of seeded clusters were 1.5, 2, 2.5, 3 and 3.5 lattice constants, yielding 0.4305 nm, 0.574 nm, 0.7175 nm, 0.861 nm and 1.0045 nm, respectively. Snapshots of initial, intermediate state at 10×10^3 MCS and final state (50×10^3 MCS) are depicted in figure 5.24. Seeded clusters with the smallest radius completely dissolve and no new clusters are found to nucleate. When radius is enlarged some clusters tend to dissolve, whereas some grow and become much larger than their initial size. Seeded clusters with radii 3.5 and 5 lattice sites only grow until equilibrium background concentration is reached. If simulation would be let run further, coarsening should be observed. Evolution of the average cluster size in time

Table 5.12: Coordinates of seeded clusters centre in lattice constants, used for subsequent analysis.

P1	P2	P3	P4
(12.5, 12.5, 12.5)	(12.5, 12.5, 37.5)	(12.5, 37.5, 12.5)	(12.5, 37.5, 37.5)
P5	P6	P7	P8
(37.5, 12.5, 12.5)	(37.5, 12.5, 37.5)	(37.5, 37.5, 12.5)	(37.5, 37.5, 37.5)

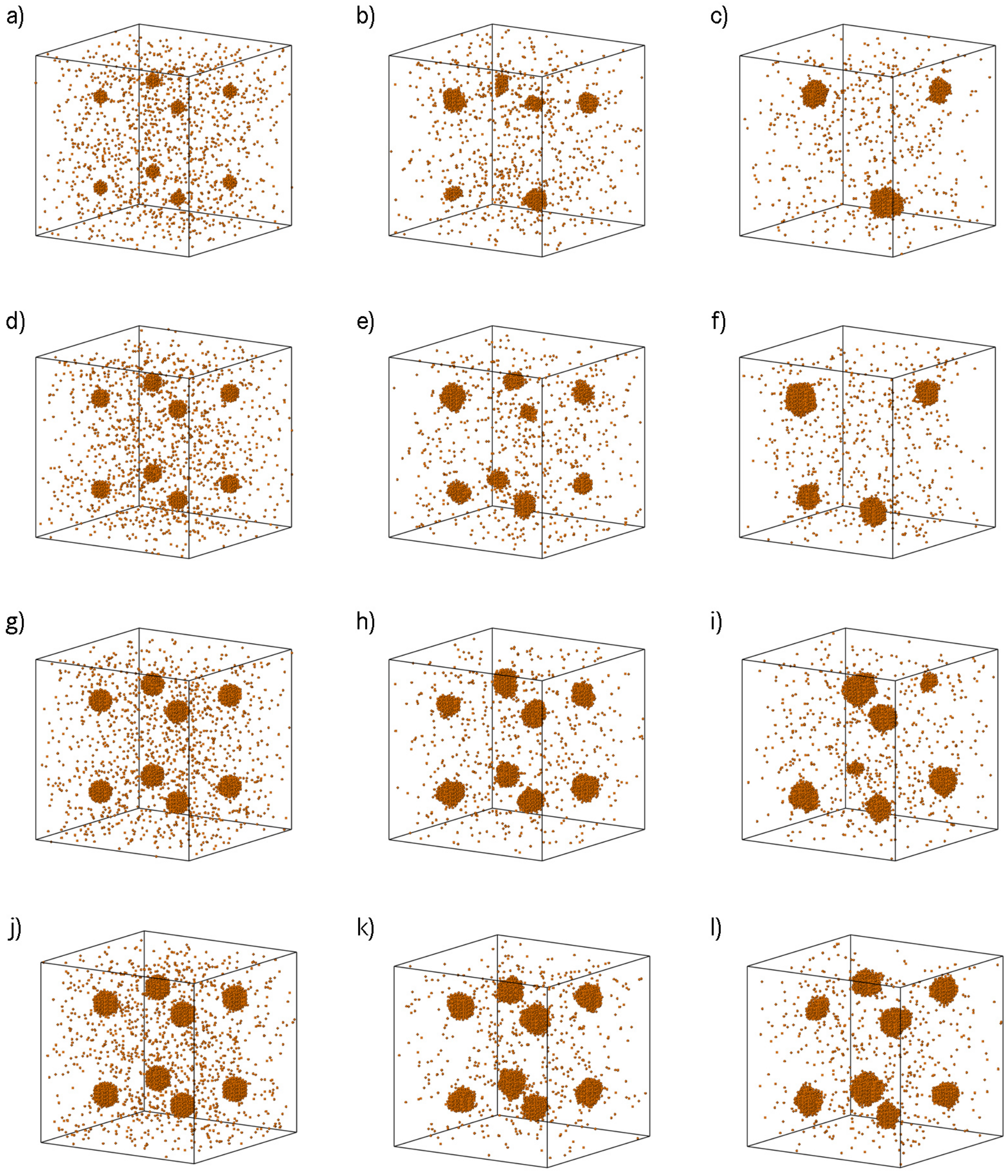

Figure 5.24: Snapshots of cluster evolution with seeded clusters of various dimensions in Fe-Cu alloy, obtained during annealing at 873 K. Size of the simulation box is 50^3 BCC lattices (14.35^3 nm) and only Cu atoms are displayed due to visibility reasons; a) initial configuration R=2, b) at 88.3 s, c) at 439 s, d) initial configuration R=2.5, e) at 84.6 s, f) at 423 s, g) initial configuration R=3, h) at 80 s, i) at 400 s, j) initial configuration R=3.5, k) at 77.8 s, l) at 388 s.

is depicted in figure 5.25 for all sizes of seeded clusters. All clusters dissolved in simulations where size of the seeded clusters radius was 1.5 lattice sites. This can be seen in figure 5.25 with sharp decline in detected cluster size for R=1.5 at approximately 10 s. The largest detected clusters are pentamers after seeded clusters dissolve. The average size of clusters does not increase much in time for size of the seeded clusters radii 3.5 and 5 lattice sites. The most interesting for further analysis are simulations where cluster seed radii were 2, 2.5 and 3 lattice sites, where growth, dissolution and coarsening can be seen. Evolution of clusters in time was analysed through change in the number of atoms used to build particular cluster. Clusters were marked depending on its seed position with P1-P8, with details about their coordinates given in Table 5.12.

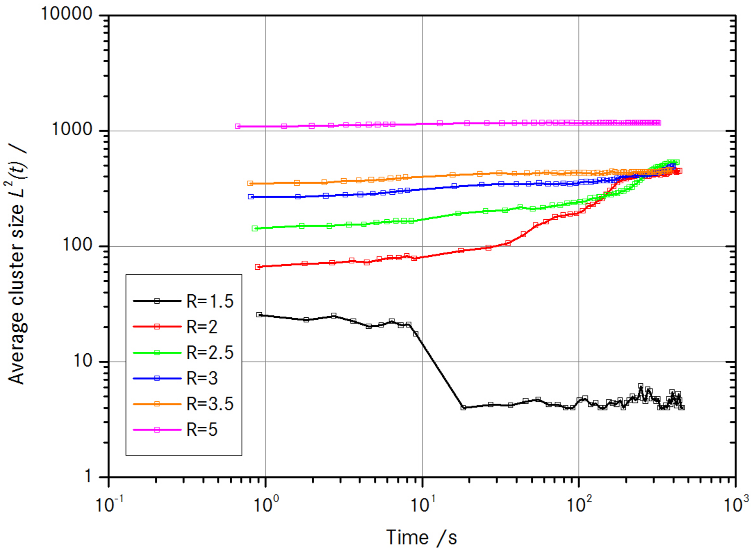

Figure 5.25: Evolution of the average cluster size for various initial sizes of seeded clusters.

In figure 5.26 size evolution of seeded clusters in time is presented for initial seed radius R=2 lattice sites. The seeded clusters are near critical size as most of them starts to grow. It is expected that the critical cluster radius will increase with depletion of background concentration. This was confirmed for Fe-Cu alloy system by Bombac and Kugler, with comparison of results obtained from the mean field and kinetic Monte Carlo simulations, [178]. Clusters which can follow this increase are growing, while others start to dissolve. At the end of the simulations only three clusters are present which are much larger than at the beginning. Two of those already started to dissolve

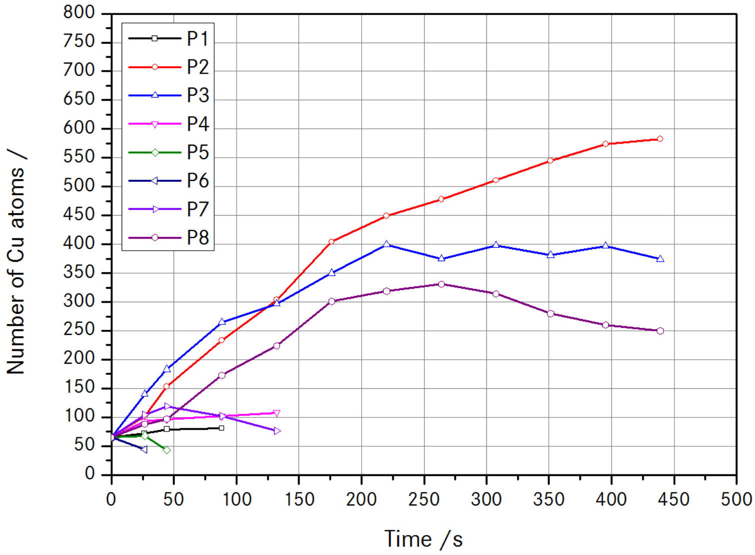

Figure 5.26: Size of clusters in time for seeded clusters with starting radius size R=2 lattice sites.

and would disappear if simulation would be let run further. Clusters moment of inertia for axis through their centre of the mass, calculated with equation (2.71) are displayed in figure 5.27a. This figure is very similar to time evolution of the number of Cu atoms in clusters, since only one type of atoms is presented and distance between the particular atoms and cluster centre of mass is connected to the size of the cluster. In figure 5.27b

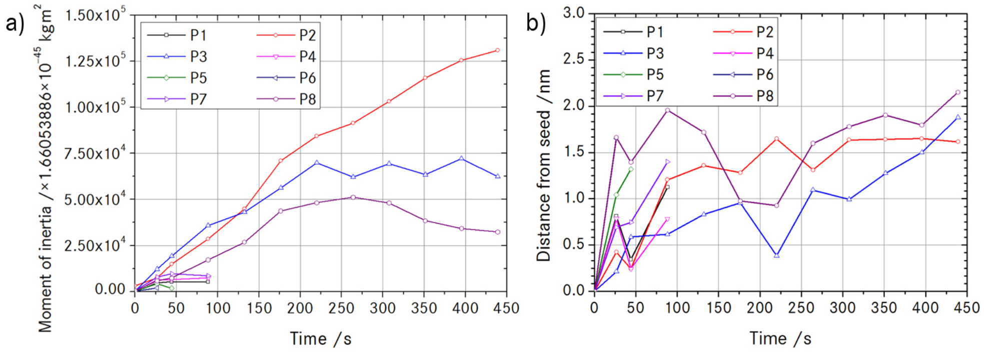

Figure 5.27: a) Moment of inertia evolution in time, b) clusters centre of mass deviation from seed position in time; for seeded clusters with starting radius size 2 lattice sites.

displacement of the clusters centre of mass from seed position in time is shown. This distance can be used to calculate diffusion of clusters with square displacements of the cluster centre of mass, $\left\langle \Delta r^2 \right\rangle$, according to $D_{\text{cluster}} = \left\langle \Delta r^2 \right\rangle / 6t$. The clusters number of atoms and its moments of inertia are good indicator which cluster is growing and which is dissolving. Moment of inertia around cluster mass centre or cluster number, offers no additional information about evolution of clusters shapes in time. However, changes of the cluster shape can be addressed with moment of inertia tensor, where moments of inertia for all possible directions are included. To obtain direction x, y or z in which cluster is growing, moment of inertia tensor can be diagonalized to obtain eigenvector values. The snapshots in figure 5.25 reveal some strange cluster shapes and confirms that they cannot be assumed spherical throughout their growth stage. Better indicator of the cluster shape is its moment of inertia tensor, represented in figure 5.28 for initial configuration and two later times along the snapshot of the cluster.

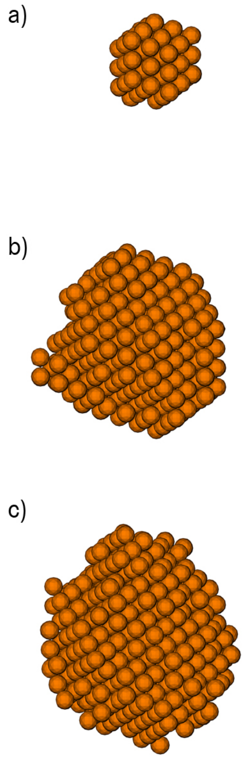

a)

$$\begin{pmatrix} 2114.31 & -41.2393 & -3.32 \times 10^{-14} \\ -41.2393 & 2196.79 & 3.15 \times 10^{-14} \\ -3.32 \times 10^{-14} & 3.15 \times 10^{-14} & 2196.79 \end{pmatrix}$$

b)

$$\begin{pmatrix} 46716.4 & -1002.17 & -695.892 \\ -1002.17 & 48848.6 & -4192.56 \\ -695.892 & -4192.56 & 46364.6 \end{pmatrix}$$

c)

$$\begin{pmatrix} 92122.3 & 1192 & 7914.91 \\ 1192 & 89493.7 & -2901.52 \\ 7914.91 & -2901.52 & 80122.3 \end{pmatrix}$$

Figure 5.28: Evolution of seeded cluster P2 with initial radius 2 lattice sites and its components of moment of inertia tensor in time at a) initial configuration with 66 Cu atoms and eigenvalues (2213.87, 2196.79, 2097.23), b) at 176.2 s with 404 Cu atoms and eigenvalues (52008.3, 47038.2, 42883.1), c) at 439 s with 583 Cu atoms and eigenvalues (96062.6, 90184.7, 75491).

At the beginning, as expected diagonal moments have almost same values, while non diagonal are practically zero. The shape then dramatically changes, with values of the nondiagonal elements being far from zero. Another proof of the nonspherical shapes was obtained with diagonalization of the moment of inertia tensor. Eigenvector values revealed large deviation between components and confirmed cluster flatness in x, y or z direction.

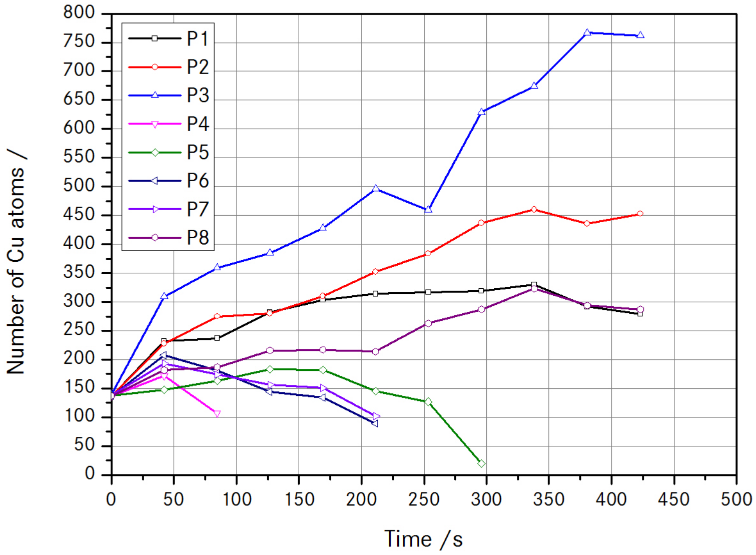

Figure 5.29: Size of clusters in time for seeded clusters with starting radius size R=2.5 lattice sites.

Similar was observed in simulations where radii of the seeded clusters were 2.5 and 3 lattice sites. In figure 5.29 evolution of the number of atoms in time, for particular cluster is depicted for seed radius 2.5 lattice sites. Initial radius is larger than critical since all clusters start to grow. Some of them then dissolve and at the end of simulation 4 clusters are observed, but two of them are already starting to dissolve. The moments of inertia and displacement of cluster centre of mass from seed position are shown in figure 5.30. Figure 5.31 depicts representation of the moment of inertia tensor at initial configuration and two later times. The non diagonal elements are not near zero from the beginning. This is due to an atom from background which was captured during cluster identification. Initial almost spherical shape then changes to the multifaceted shaped cluster far from the spherical shape. Figure 5.32 shows snapshots of the cluster P8, with initial radius R=2.5 lattice sites at various time increments. All individual snapshots are collected, each with different colour in figure 5.32a. The initial configuration exhibits

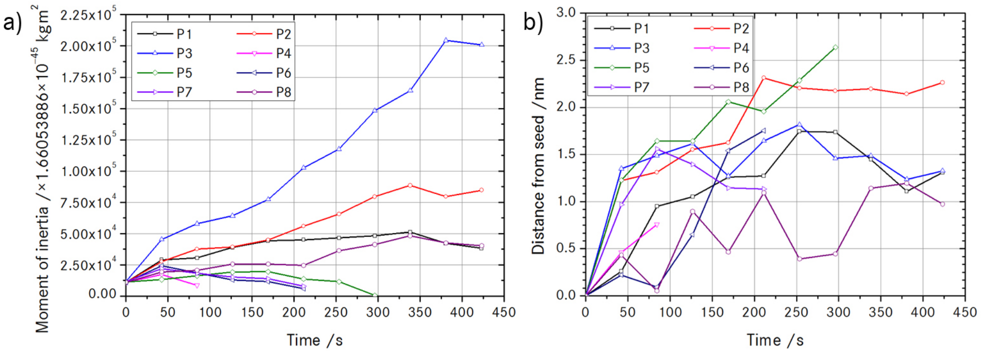

Figure 5.30: a) Moment of inertia evolution in time, b) clusters centre of mass deviation from seed position in time; for seeded clusters with starting radius size 2.5 lattice sites.

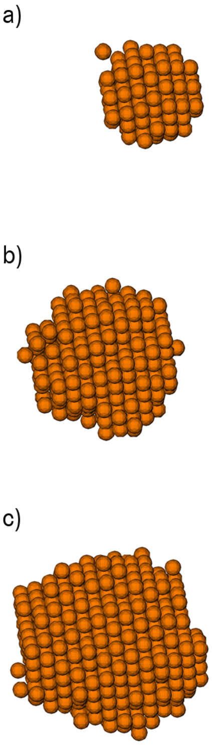

a)

$$\begin{pmatrix} 7859.03 & 130.295 & -35.8544 \\ 130.295 & 7524.64 & -24.8625 \\ -35.8544 & -24.8625 & 7818.65 \end{pmatrix}$$

b)

$$\begin{pmatrix} 49344.1 & 2684.96 & -131.981 \\ 2684.96 & 51113.7 & 1490.14 \\ -131.981 & 1490.14 & 54067.1 \end{pmatrix}$$

c)

$$\begin{pmatrix} 131675 & 4790.84 & -9916.95 \\ 4790.84 & 136877 & -2050.17 \\ -9916.95 & -2050.17 & 133238 \end{pmatrix}$$

Figure 5.31: Evolution of seeded cluster P3 with initial radius 2.5 lattice sites and its components of the moment of inertia tensor in time at a) initial configuration with 140 Cu atoms and eigenvalues (7921.07, 7801.8, 7479.45), b) at 169 s with 428 Cu atoms and eigenvalues (54891.2, 52377.6, 47256.1), c) at 423 s with 762 Cu atoms and eigenvalues (145193, 134421, 122176).

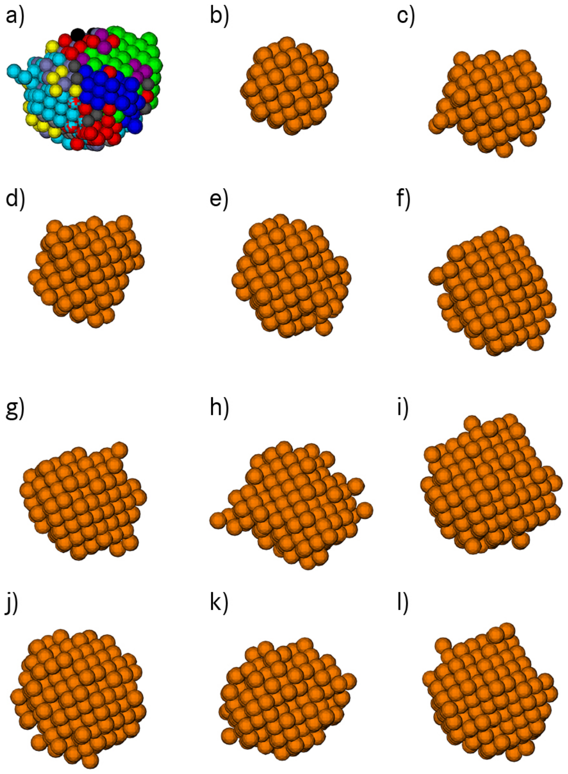

Figure 5.32: Snapshots seeded cluster P8 with initial radius R=2.5 lattice sites a) differently coloured superposition b)-k), b) initial configuration (137 atoms), c) at 42.2 s (182 atoms), d) at 84.6 s (187 atoms), e) at 126.8 s (216 atoms), f) at 169 s (217 atoms), g) at 211.2 s (214 atoms), h) at 253.5 s (263 atoms), i) at 296 s (287 atoms), j) at 338.2 s (323 atoms), k) at 380.5 s (294 atoms), l) at 423 s (287 atoms).

spherical cluster, composed from 137 Cu atoms. As diffusion causes movement of atoms through random motion, shape of the cluster changes in time. This particular cluster reaches largest size at 338.2 s, where it is composed from 323 Cu atoms. After 338.2 s cluster does not further grow or maintain its size, but starts slowly to dissolve. In figure 5.33, concentration profiles around seeded clusters P1-P8 at various time increments are shown. Concentration of Cu decreases with distance from the cluster centre of mass, as clusters are made only from Cu atoms. Local concentrations reach equilibrium value at distances much larger than the cluster sizes. The effect of clusters on the local concentration is diminished between 2.5 nm and 4 nm, confirming that chosen initial value between clusters was large enough.

In figure 5.34 time evolutions of the cluster sizes in number of Cu atoms are shown.

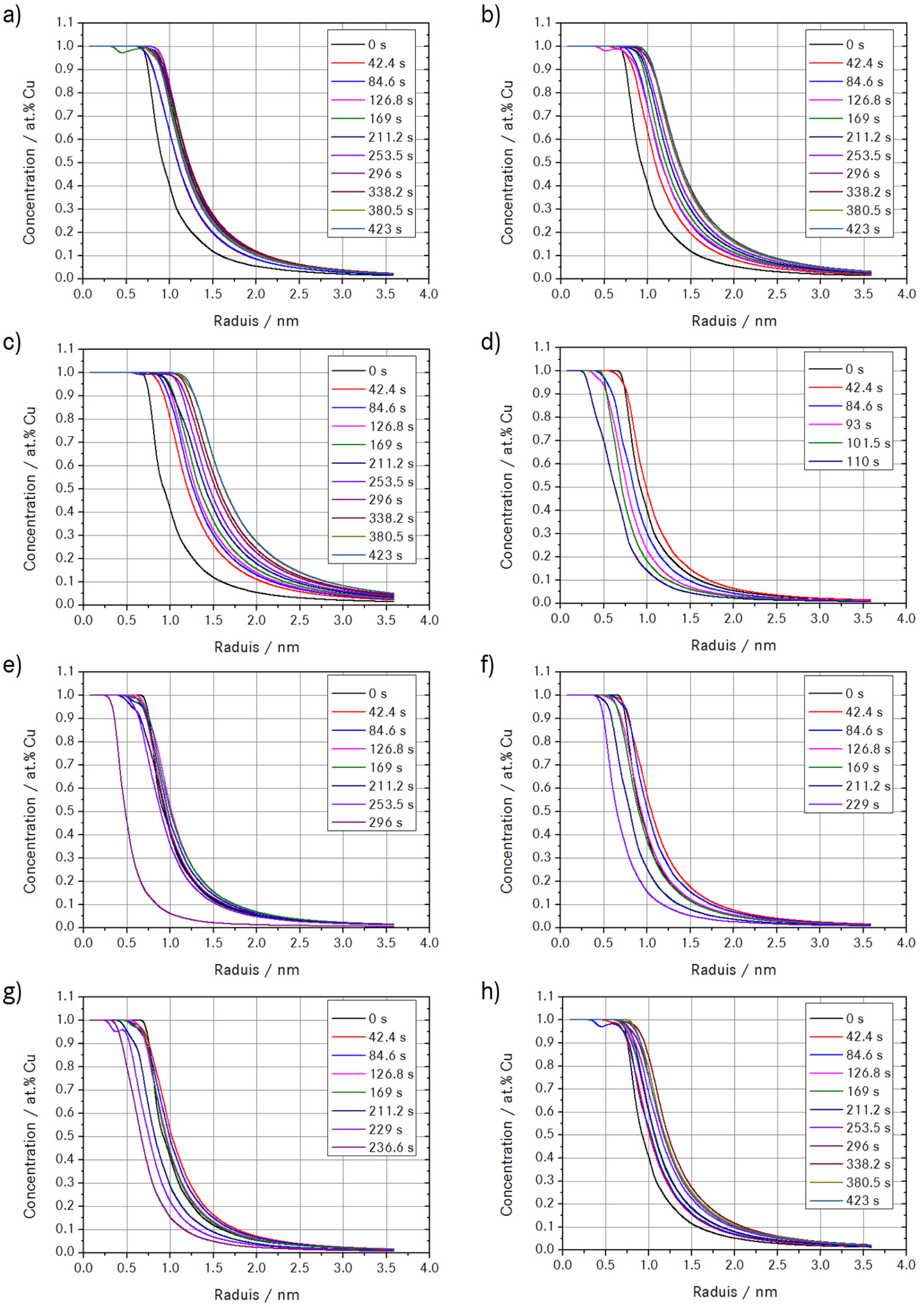

Figure 5.33: Concentration around seeded clusters with starting radius size 2.5 lattice sites at various times and following initial seed center coordinates; a) P1, b) P2, c) P3, d) P4, e) P5, f) P6, g) P7, h) P8.

Similar than in previous case, initial seed radius exceed critical radius and all clusters are observed to initialy enlarge. Although seven clusters were counted at the end of simulation, only five are larger than initial seed size, and three of them are already dissolving and would disappear if simulation would be let run further. Clusters without tendency to dissolve, have approximately at least two times more atoms at the end of the simulations than their initial seed size. Figure 5.35a shows evolution of the moment of inertia in time which is again very similar to the evolution of the cluster size

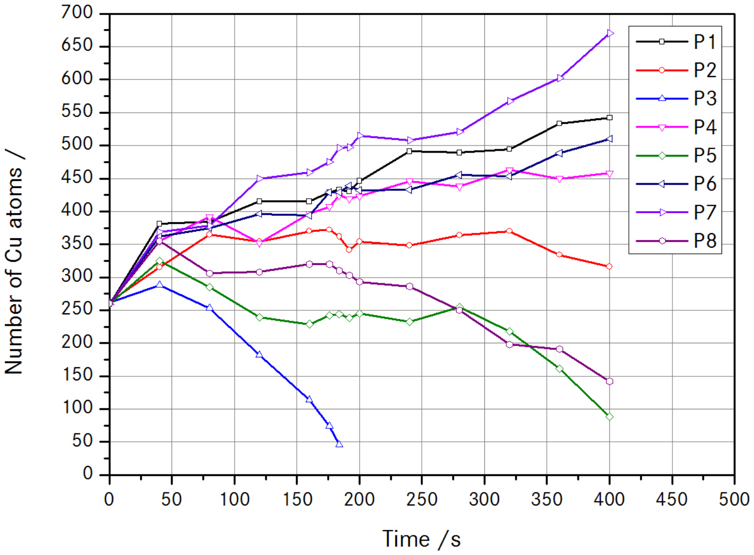

Figure 5.34: Size of clusters in time for seeded clusters with starting radius size R=3 lattice sites.

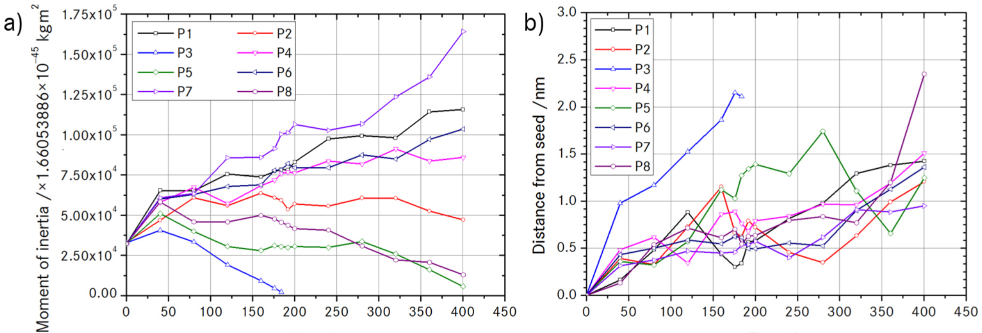

Figure 5.35: a) Moment of inertia evolution in time, b) clusters centre of mass deviation from seed position in time; for seeded clusters with starting radius size 3 lattice sites.

in time. Time evolution of the cluster centre of mass displacement from the initial seed positions given in Table 5.12, are depicted in figure 5.35b. Elements of the moment of inertia tensors are for the cluster P7 with starting size R=3 lattice sites, for initial and two subsequent configurations, along cluster snapshots shown in figure 5.36. At the beginning of the simulations the cluster is spherical, composed of 259 Cu atoms. The nondiagonal moments are zero and the diagonal moments of inertia are equal. Its shape is near spherical at 159.9 s, however it changes to faceted ellipsoid at 400.2 s.

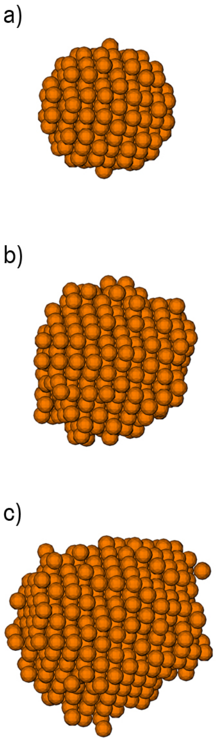

$$\begin{pmatrix} 21355.6 & 4.09\times10^{-14} & 2.19\times10^{-14} \\ 4.09\times10^{-14} & 21355.6 & 4.41\times10^{-14} \\ 2.19\times10^{-14} & 4.41\times10^{-14} & 21355.6 \end{pmatrix}$$

$$\begin{pmatrix} 58377.3 & 2348.44 & -1128.63 \\ 2348.44 & 57824.6 & 245.336 \\ -1128.63 & 245.336 & 55837.9 \end{pmatrix}$$

$$\begin{pmatrix} 103008 & 10564.2 & 7597.47 \\ 10564.2 & 111584 & 2046.23 \\ 7597.47 & 2046.23 & 113682 \end{pmatrix}$$

Figure 5.36: Evolution of seeded cluster P7 with initial radius 3 lattice sites and its components of moment of inertia tensor in time at a) initial configuration with 259 Cu atoms and eigenvalues (21355.6, 21355.6, 21355.6), b) at 159.9 s with 459 Cu atoms and eigenvalues (60567.4, 56659.7, 54812.8), c) at 400.2 s with 670 Cu atoms and eigenvalues (122955, 110917, 94401.7).

In this section clusters seeded to the predefined positions in slightly supersaturated medium in the Fe-Cu alloy system were isothermally annealed at 873 K. Their evolution is governed by attachment and detachment of Cu monomers. It was show that clusters initially grow before their dissolution commences. Largest clusters observed, are at the end of the simulation runs much larger than their initial seed size. Growth strongly influences their shapes, which changes from initial spherical shape into the compressed shape either in x, y or z directions.

5.3.6 Evolution of microstructure with initial conditions previously annealed at high temperature

Starting microstucture was obtained in simulations by random populating lattice sites with desired atoms. To study influence of unstable clusters on nucleation, simulations with different starting microstucture were performed. First random solid solution with 1 at.% Cu was isothermally annealed at 1123 K and then used as input microstucture for precipitation study at 873 K. In table 5.13 number of subcritical clusters obtained at the end of isothermal annealing at 1123 K is presented. If starting conditions used here, are compared to randomly distributed atoms used previously (cf. table 5.5), increased

Table 5.13: Number of cluster obtained from isothermal annealing at 1123 K.

Dimers	Trimer	Tetramers	Pentamers	Hexamers	Total
621	151	32	6	4	817

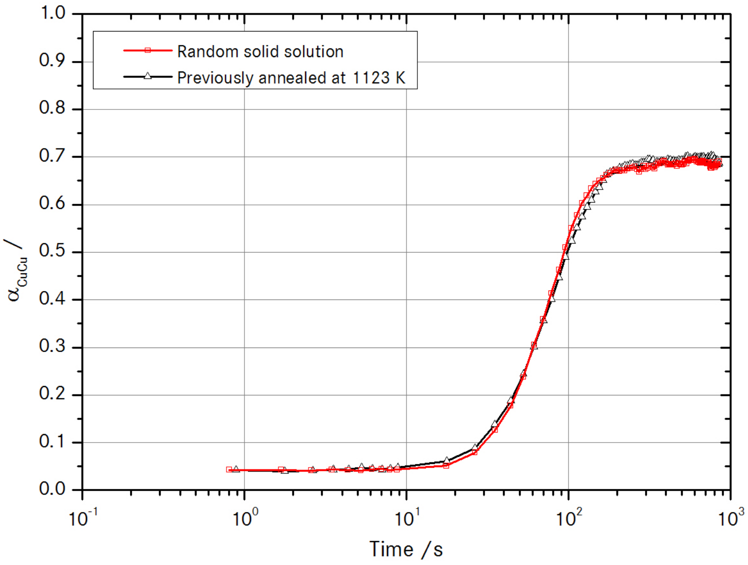

Figure 5.37: Evolution of the SRO parameter for random and previously annealed initial conditions in Fe-Cu alloys with 1 at.% Cu isothermally treated at 873 K.

number of subcritical clusters (dimmers, trimers, tetramers, ...) is noticed. Enlarged number of subcritical clusters is noticed in dimmers, trimers, tetramers, pentamers, hexamers and also in total number compared to random initial conditions.

In figure 5.37 comparison of evolution of the SRO parameters α_{CuCu} for random initial conditions and previously annealed solid solution at 1123 K is depicted. Small difference in the curves can be seen. After incubation time, Cu-Cu clustering rate is higher for previously annealed initial conditions. However, approximately at the middle of the growth stage clustering rate for random solid solution becomes greater.

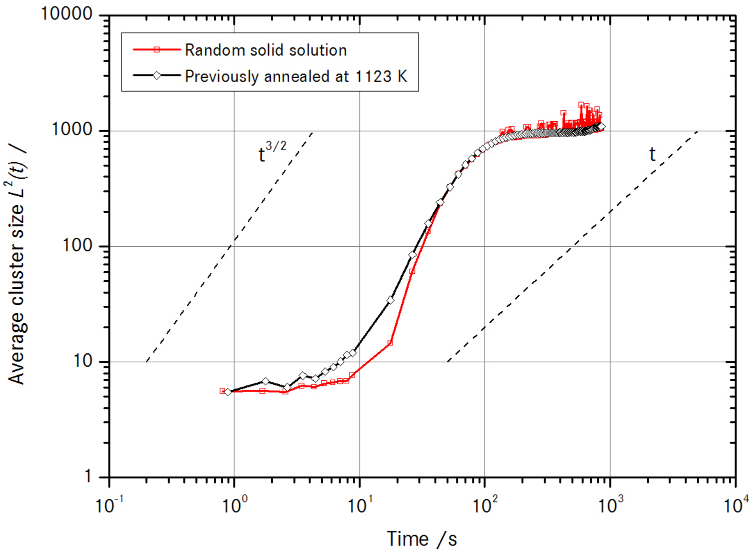

Figure 5.38: Evolution of the average cluster size for random and previously annealed initial conditions in Fe-Cu alloys with 1 at.% Cu isothermally treated at 873 K.

In figure 5.38 comparison of evolution of average cluster sizes for random initial conditions and previously annealed solid solution at 1123 K is shown. Simulations were performed with 1 at.% Cu and at 873 K. When solid solution is previously annealed incubation time for nucleation is shorter. Furthermore, growth rate is lower compared to the randomly distributed solid solution. Shorter incubation time is attributed to increased number of subcritical clusters in previously annealed microstucture. Furthermore, distinction between nucleation and growth stages is for previously annealed starting conditions diminished. In the second part of the growth stage and for coarsening stage, curves are almost identical. This shows that unstable clusters influences kinetic pathways at the beginning of precipitation (nucleation and growth commencement) while average sizes of particles are at the end are almost identical.

Let the future tell the truth, and evaluate each one according to his work and accomplishments. The present is theirs; the future, for which I have really worked, is mine.

Nikola Tesla (1856-1943)

6

Clustering in the ternary Fe-Cu-Ni and Fe-Cu-Mn and in the quaternary Fe-Cu-Ni-Mn alloys

Extension of the binary model to simulate Cu precipitation, described in previous chapter are a ternary Fe-Cu-Ni or Fe-Cu-Mn and a quaternary Fe-Cu-Ni-Mn simulations models.

6.1 Model parametrization

The ternary and quaternary model systems can be treated as an appropriate number of binary models. The parametrization of separate binary models is then performed as described in previous chapter. The thermodynamic material properties used in parametrization are presented in Table 6.1. Symmetrical model was used, where binding energies of Cu, Ni and Mn were set equal to the binding energy of Fe, which was calculated from the cohesive energy in the pure metal.

Heteroatomic interaction energies $\epsilon^{(i)}_{\mathrm{XY}}$, associated with mixing energy as E_{mixXY} (cf. equation (5.3)) were obtained from separate binary systems, in the ternary systems from three and in the quaternary system from six. For example, in the Fe-Cu-Ni, heteroatomic interaction energies were calculated from mixing energies of Fe$-$Cu, Fe$-$Ni and Cu$-$Ni. The saddle point energies were determined from the vacancy migration energy in pure phases and the same values were used in the ternary and quaternary

Table 6.1: Material properties of Fe, Cu, Ni and Mn used for calculation of interaction energies and kinetic parameters.

Lattice constant of α-Fe	a	0.287 nm, [169]
Number of first neighbours	z_1	8
Number of second neighbours	z_2	6
Cohesive energy of Fe	E_{cohFe}	-4.28 eV, [169]
Cohesive energy of Cu	E_{cohCu}	-3.49 eV, [169]
Cohesive energy of Ni	E_{cohNi}	-2.92 eV, [169]
Cohesive energy of Mn	E_{cohMn}	-4.44 eV, [169]
Mixing energy of Fe$-$Cu	E_{mixFeCu}	-0.52 eV, [170]
Mixing energy of Fe$-$Ni	E_{mixFeNi}	-0.02 eV, [132]
Mixing energy of Fe$-$Mn	E_{mixFeMn}	-0.17 eV, [132]
Mixing energy of Cu$-$Ni	E_{mixCuNi}	-0.05 eV, [132]
Mixing energy of Cu$-$Mn	E_{mixCuMn}	0.0 eV, [132]
Mixing energy of Ni$-$Mn	E_{mixNiMn}	0.32 eV, [132]
Vacancy formation energy of Fe	E_{VforFe}	1.60 eV, [152]
Vacancy formation energy of Cu	E_{VforCu}	1.28 eV, [152]
Vacancy formation energy of Ni	E_{VforNi}	1.79 eV, [152]
Vacancy formation energy of Mn	E_{VforMn}	1.60 eV, [152]
Vacancy migration energy of Fe	E_{VmigFe}	0.90 eV, [152]
Vacancy migration energy of Cu in Fe	E_{VmigCu}	0.70 eV, [152]
Vacancy migration energy of Ni in Fe	E_{VmigNi}	1.04 eV, [152]
Vacancy migration energy of Mn in Fe	E_{VmigMn}	0.90 eV, [152]
Diffusion constant of Fe	$\mathrm{D}_{0\_\mathrm{Fe}}$	2.01 10^{-4} m^2 s^{-1}, [171]
Diffusion constant of Cu	$\mathrm{D}_{0\_\mathrm{Cu}}$	2.16 10^{-4} m^2 s^{-1}, [171]
Diffusion constant of Fe	$\mathrm{D}_{0\_\mathrm{Fe}}$	1.40 10^{-4} m^2 s^{-1}, [171]
Diffusion constant of Cu	$\mathrm{D}_{0\_\mathrm{Cu}}$	1.49 10^{-4} m^2 s^{-1}, [171]
Attempt frequency of Fe	ν_{Fe}	8.70×10^{12} s^{-1}, [169]
Attempt frequency of Cu	ν_{Cu}	6.67×10^{12} s^{-1}, [169]
Attempt frequency of Ni	ν_{Fe}	8.02×10^{12} s^{-1}, [169]
Attempt frequency of Mn	ν_{Cu}	8.54×10^{12} s^{-1}, [169]

systems. The saddle point energy is in quaternary system given as

$$\begin{aligned}
E_{\mathrm{SpX}} = E_{\mathrm{VmigX}} + z_1\epsilon_{\mathrm{XV}} &+ c_{\mathrm{X}}\left[(z_1-1)\epsilon^{(1)}_{\mathrm{XX}} + z_2\epsilon^{(2)}_{\mathrm{XX}}\right] \\
&+ c_{\mathrm{Y}}\left[(z_1-1)\epsilon^{(1)}_{\mathrm{XY}} + z_2\epsilon^{(2)}_{\mathrm{XY}}\right] \\
&+ c_{\mathrm{W}}\left[(z_1-1)\epsilon^{(1)}_{\mathrm{XW}} + z_2\epsilon^{(2)}_{\mathrm{XW}}\right] \\
&+ c_{\mathrm{Z}}\left[(z_1-1)\epsilon^{(1)}_{\mathrm{XZ}} + z_2\epsilon^{(2)}_{\mathrm{XZ}}\right]
\end{aligned} \tag{6.1}$$

where c_{X}, c_{Y}, c_{W} and c_{Z} are concentrations of X, Y, W and Z atoms, respectively. E_{VmigX} is a vacancy migration energy of X and ϵ_{ij} are pair interaction energies. The saddle point energies were calculated with concentrations of Y, W and Z at 1 at.% for all species. Attempt frequencies were assumed to be equal and Debye frequency of iron was used in the simulations, i.e. $\nu_{\mathrm{Fe}} = \nu_{\mathrm{Cu}} = \nu_{\mathrm{Ni}} = \nu_{\mathrm{Mn}} = \nu_{\mathrm{D_{Fe}}}$. These assumption does not change the kinetic pathways and influences only on the kinetics and consequently the obtained time. Calculated simulations parameters (interaction energies and kinetic parameters) are presented in Table 6.2.

Table 6.2: Calculated simulations parameters used in ternary and quaternary alloy systems.

$\epsilon^{(1)}_{\mathrm{FeFe}} = -0.778$ eV	$\epsilon^{(2)}_{\mathrm{FeFe}} = -0.389$ eV
$\epsilon^{(1)}_{\mathrm{CuCu}} = -0.778$ eV	$\epsilon^{(2)}_{\mathrm{CuCu}} = -0.389$ eV
$\epsilon^{(1)}_{\mathrm{NiNi}} = -0.778$ eV	$\epsilon^{(2)}_{\mathrm{NiNi}} = -0.389$ eV
$\epsilon^{(1)}_{\mathrm{MnMn}} = -0.778$ eV	$\epsilon^{(2)}_{\mathrm{MnMn}} = -0.389$ eV
$\epsilon^{(1)}_{\mathrm{FeCu}} = -0.731$ eV	$\epsilon^{(2)}_{\mathrm{FeCu}} = -0.366$ eV
$\epsilon^{(1)}_{\mathrm{FeNi}} = -0.776$ eV	$\epsilon^{(2)}_{\mathrm{FeNi}} = -0.388$ eV
$\epsilon^{(1)}_{\mathrm{FeMn}} = -0.763$ eV	$\epsilon^{(2)}_{\mathrm{FeMn}} = -0.381$ eV
$\epsilon^{(1)}_{\mathrm{CuNi}} = -0.774$ eV	$\epsilon^{(2)}_{\mathrm{CuNi}} = -0.387$ eV
$\epsilon^{(1)}_{\mathrm{CuMn}} = -0.778$ eV	$\epsilon^{(2)}_{\mathrm{CuMn}} = -0.389$ eV
$\epsilon^{(1)}_{\mathrm{NiMn}} = -0.807$ eV	$\epsilon^{(2)}_{\mathrm{NiMn}} = -0.404$ eV
$\epsilon^{(1)}_{\mathrm{FeV}} = -0.335$ eV	$\epsilon^{(1)}_{\mathrm{CuV}} = -0.335$ eV
$\epsilon^{(1)}_{\mathrm{NiV}} = -0.335$ eV	$\epsilon^{(1)}_{\mathrm{MnV}} = -0.335$ eV
$E_{\mathrm{SpFe}} = -9.556$ eV	$E_{\mathrm{SpCu}} = -9.129$ eV
$E_{\mathrm{SpNi}} = -9.547$ eV	$E_{\mathrm{SpMn}} = -9.415$ eV
$\nu_{\mathrm{Fe}} = 8.70 \times 10^{12}\ \mathrm{s}^{-1}$	$\nu_{\mathrm{Cu}} = 8.70 \times 10^{12}\ \mathrm{s}^{-1}$
$\nu_{\mathrm{Ni}} = 8.70 \times 10^{12}\ \mathrm{s}^{-1}$	$\nu_{\mathrm{Mn}} = 8.70 \times 10^{12}\ \mathrm{s}^{-1}$

The migration barriers were from appropriate parameters given in Table 6.2 calculated with equation (5.10) adapted to the ternary or quaternary systems.

As in the case of binary system, also here two asymmetry parameters can be defined, $a*$ and $c*$ with equations (5.12) and (5.11), respectively. However, since ternary and quaternary models can be build from simple binary, the number of asymmetry parameters depends on the number of simple binary models used for particular ternary or quaternary model system. Simulations were performed with $a* = 0$, and asymmetry was introduced through the saddle point energies. Table 6.3 represents all asymmetry parameter $c*$ introduced into simulations with ternary and quaternary models.

Table 6.3: Possible asymmetry parameters $c*$ for simulated alloy systems.

Fe-Cu-Ni	Fe-Cu-Mn	Fe-Cu-Ni-Mn
$c*_{FeCu}$	$c*_{FeCu}$	$c*_{FeCu}$
$c*_{FeNi}$	$c*_{FeMn}$	$c*_{FeMn}$
$c*_{CuNi}$	$c*_{CuMn}$	$c*_{FeMn}$
		$c*_{CuNi}$
		$c*_{CuMn}$
		$c*_{NiMn}$

6.2 Results

In this section results obtained with the kMC simulations in the ternary Fe-Cu-Ni and Fe-Cu-Mn and in the quaternary Fe-Cu-Ni-Mn alloys are presented. The kMC simulations were performed according to the residence time procedure and broken bond model SPEM2 (cf. section 4.2) using the developed algorithm presented in Appendix A and simulations parameters presented in Table 5.2. Results from several runs did not reveal significantly different results for each alloy system. Simulations were performed with chemical conditions presented in Table 6.4 where content of Fe is base.

Table 6.4: Chemical compositions in at.% used in kMC simulations.

Fe-Cu-Ni	Fe-Cu-Mn	Fe-Cu-Ni-Mn
1 at.% Cu	1 at.% Cu	1 at.% Cu
1 at.% Ni	1 at.% Mn	1 at.% Ni
		1 at.% Mn

Size of the simulation box for the ternary alloys was 80^3 BCC lattices (23^3 nm). In figure 6.1 snapshots of obtained clusters in Fe-Cu-Mn alloy with 1 at.% Cu and 1 at.% Mn are presented. Figure 6.2 depicts extracted cluster and induvidual atom groups. At approximately 30 s, Cu atoms form nucleus which then starts to grow in time.

In figure 6.3 evolution of the short range order parameters α_{CuCu}, α_{MnMn}, and α_{CuMn} from kMC simulations of Fe-Cu-Mn alloy are shown. In order to quantify influence of the Mn impurity, figure 6.3 depicts the SRO parameter α_{CuCu} obtained

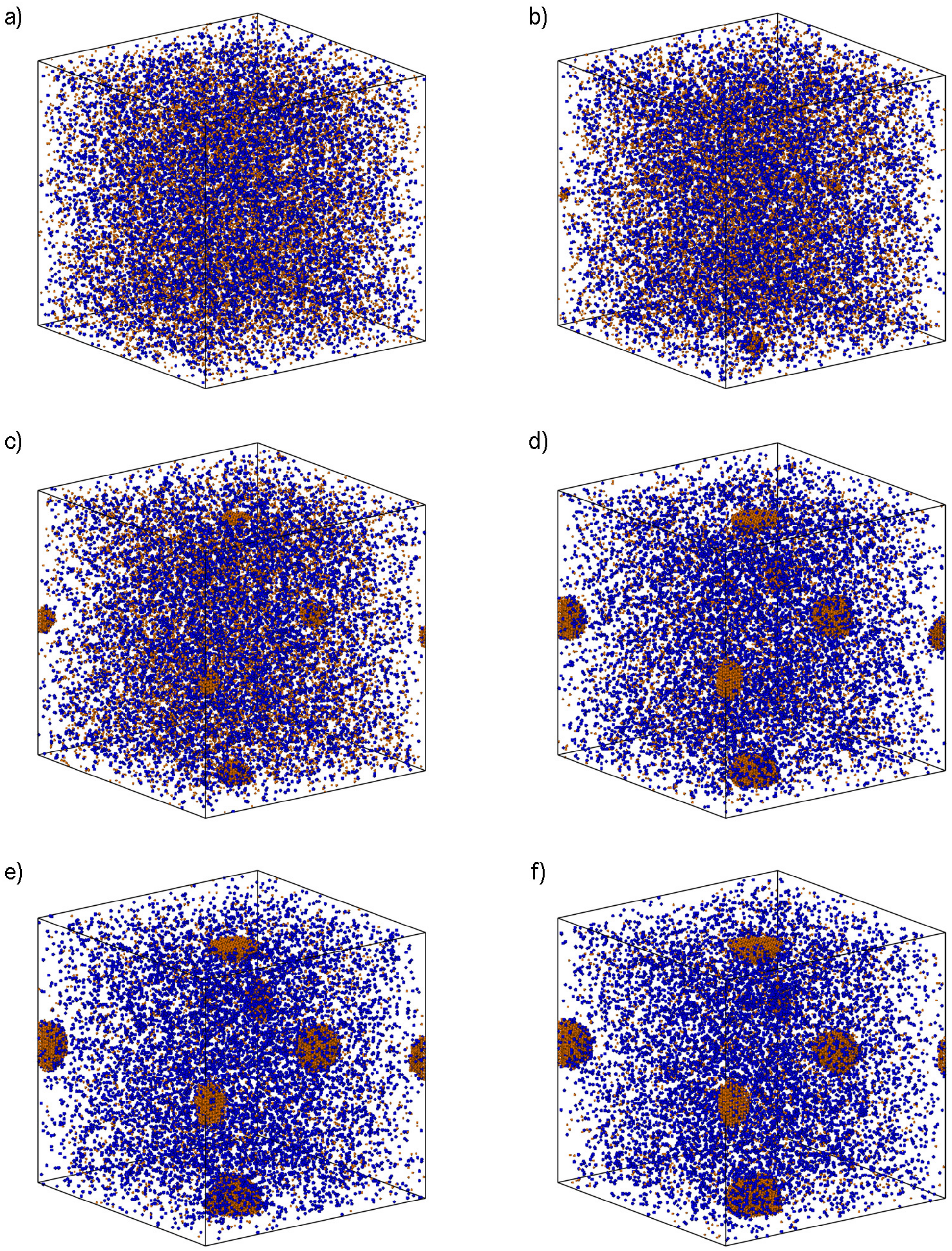

Figure 6.1: Snapshots of clusters in Fe-Cu-Mn alloy with 1 at.% Cu and 1 at.% Mn, obtained from kMC simulations during annealing at 873 K. Size of the simulation box is 80^3 BCC lattices (23^3 nm), Cu atoms are orange and Mn are blue. Fe atoms are not shown due to visibility reasons; a) initial disordered configuration, b) at 66.5 s, c) at 133.2 s, d) at 334.7 s, e) at 1356 s, f) at 2720 s.

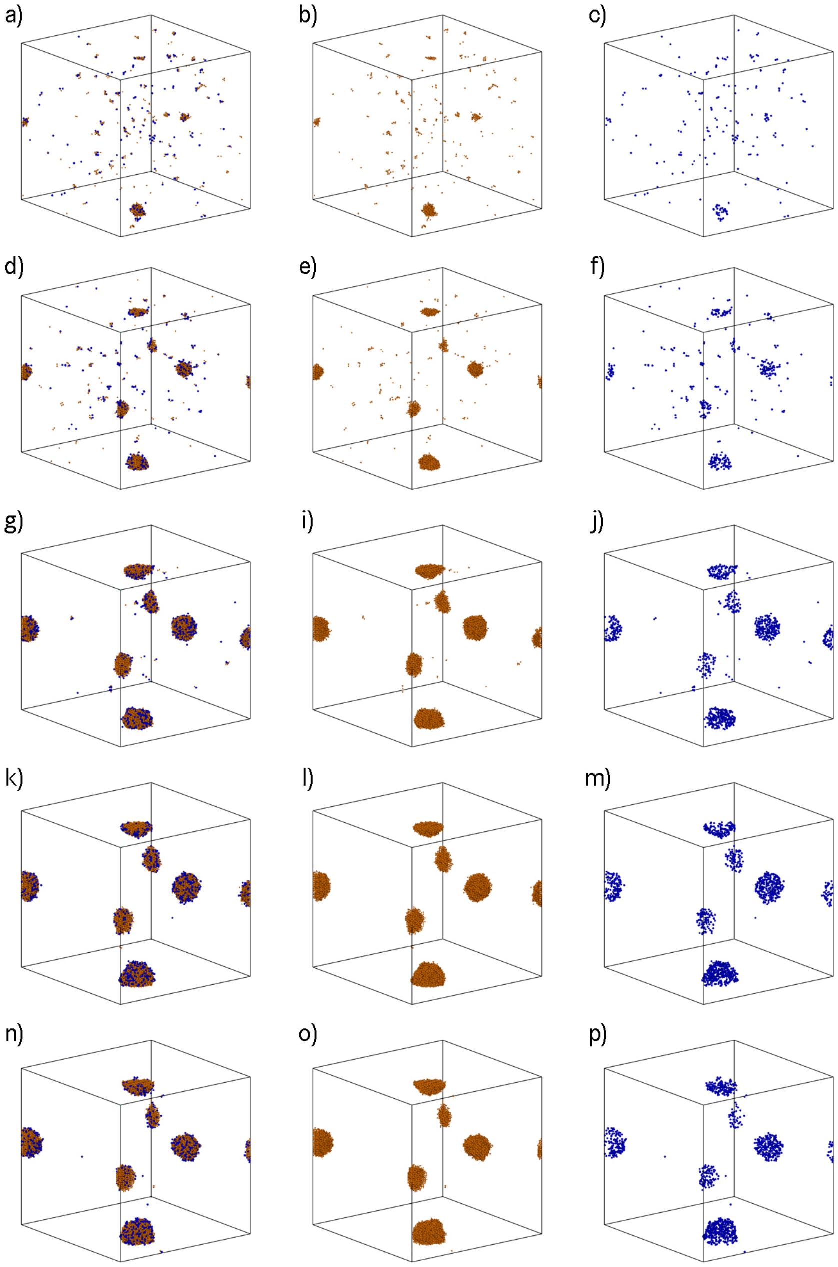

Figure 6.2: Snapshots of individual atom group clusters from kMC simulations during isothermal treatment at 873 K for Fe-Cu-Mn alloy with 1 at.% Cu and 1 at.% Mn. Size of the simulation box is 80^3 BCC lattices (23^3 nm), Cu atoms are orange and Mn atoms are blue; a)-c) at 66.5 s, d)-e) at 133.2 s, f)-h) at 334.7 s, i)-k) at 1356 s, l)-m at 2720 s.

in binary Fe-Cu alloy with dashed line. Both curves are similar and follows S curve shape. At the beginning incubation time is present before SRO parameter α_{CuCu} starts to increase. Compared to the binary Fe-Cu alloy, incubation time becomes longer when Mn impurities are added. Mixing energies of Fe-Mn (-0.17 eV) and Fe-Cu (-0.52 eV) should cause phase separation of both phases and competition between both has influence on the incubation time and impede increase rate of the SRO parameter.

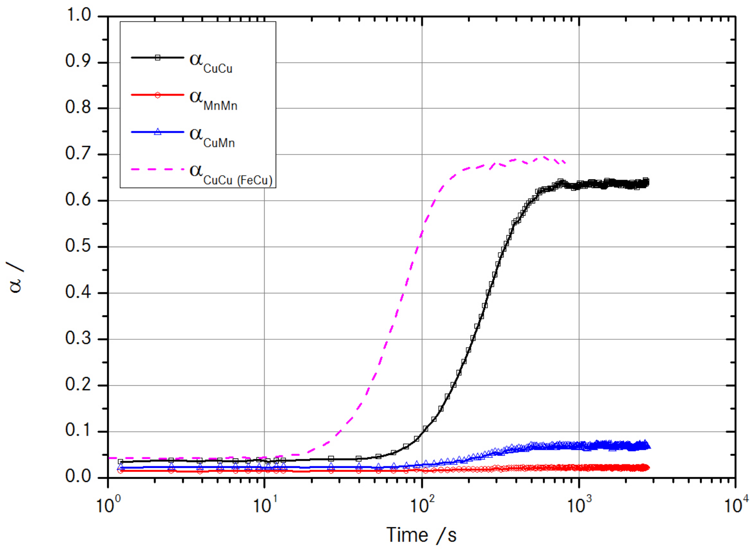

Figure 6.3: Evolution of the short range order parameters in Fe-Cu-Mn alloy with 1 at.% Cu and 1 at.% Mn at 873 K. Dashed line presents evolution of the short range order parameter in binary Fe-Cu alloy at same conditions.

From figure 6.2 slight mixing of the Cu and Mn in outer shell of formed precipitate is seen, which is confirmed with rise of the value of SRO parameter α_{CuMn} in figure 6.3.

Beside evolution of the short range order parameter α_{XX}, evolution of the average cluster size in time was used to analyse obtained results. In figure 6.4 evolution of the average cluster size, together with lines for classical growth law ($t^{3/2}$) and LSW regime (t) are presented. At the beginning, the average cluster size does not change in time until stable nuclei are formed. After that, the average cluster size starts to slowly increase. Approximately at the middle of the simulation the average cluster size start to follow classical growth law. During growth stage the the mean average cluster increases according to $L^2(t) \propto t^x$ with $x \approx 1/1.25$ in the range between 30 s and 200 s. Following the growth period at times longer than 200 s, the growth stalls and average cluster size reaches plateau. When average cluster size is reached, the equilibrium concentration

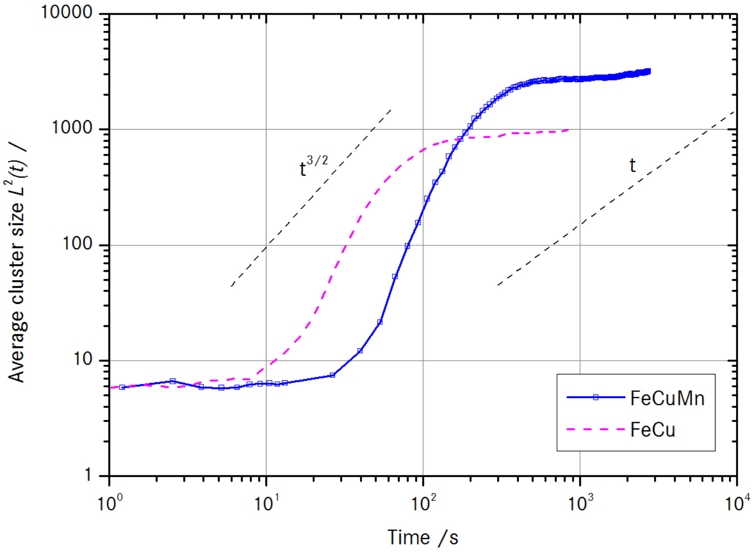

Figure 6.4: Evolution of the average cluster size in time for Fe-Cu-Mn alloy isothermally annealed at 873 K.

in the matrix is attained. Slight increase of the average cluster size curve at the end is indication of slow commencement of the LSW regime.

In the case of the ternary Fe-Cu-Mn alloy, the addition of Mn causes significant changes in the clustering kinetics. Before influence of two impurities on the clustering kinetics was analysed, the second impurity was introduced into Fe-Cu alloy similar than in the case of Fe-Cu-Mn alloy. Second impurity used was Ni with snapshots obtained from kMC simulations presented in figure 6.5. Beside change in impurity atom type and its influence on the simulation parameters, both simulation runs were performed at same starting conditions. Size of the simulation box used was 80^3 BCC lattices which yields 23^3 nm. Snapshots of extracted clusters and their individual atom groups are shown in figure 6.6. Comparison of formed clusters reveal very little mixing between Cu and Ni in the outer shell of formed clusters. Amount of Ni mixed with Cu in the outer shell of the precipitate is much smaller than in case of added Mn. Evolution of the SRO parameter α is depicted in figure 6.7, where it is compared to the evolution of the short range order parameter obtained in binary Fe-Cu alloy at same conditions. The curves are very similar if much longer incubation time in the case of Fe-Cu-Ni alloy is neglected. Values of the SRO parameter when its peak is reached are also very similar. Evolution of the mean cluster size in time is shown in figure 6.8. The average cluster size is almost constant for very long time before exhibits sharp increase in size. During the growth stage approximately between 180 s and 400 s, curve changes according to $L^2(t) \propto t^x$ with $x \approx 0.93$. Between 400 s and 1000 s, the growth rate slows down before becomes constant where equilibrium matrix is attained. The LSW regime can not proceed as only one cluster was formed during simulation. Addition of Ni causes significant changes in clustering kinetics. The amount of time before stable nuclei are formed is very long due to influences of the mixing energies as explained in the case of ternary Fe-Cu-Mn alloy. However, when stable nuclei are finally formed the growth rate is almost linear in time.

Simulations performed with ternary alloy model reveal that additions of various impurities has significant effects on the clustering kinetics. The ternary alloy simulation model was then made a bit more complex by addition of another element. That allowed to study influence of both impurities at the same time. Obtained results are first presented only for quaternary model and then also compared to the ternary model for both impurities. The model for quaternary Fe-Cu-Ni-Mn alloy was build like previous ones with used simulation parameters given in Table 6.2. Size of the simulation box was 80^3 BCC lattices (23^3 nm). At the beginning the disordered quaternary alloy with 1 at.% Cu, 1 at.% Ni and 1 at.% Mn atoms and one vacancy was quenched at 873 K and then isothermally anneald at the same temperature. In figure 6.9 snapshots obtained from kMC simulation at various times are presented. Although only Cu, Ni and Mn atoms are depicted the amount of atoms makes visibility of formed clusters very difficult. Extracted clusters and induvidual atom groups are shown in figure 6.10. Clustering starts with stable nuclei of Cu atoms. These nuclei then grow and attract Mn and Ni atoms on outer shells. Figure 6.10 reveals that amount on Ni atoms is lower than Mn atoms in clusters. Evolution of SRO parameter α in simulated quaternary Fe-Cu-Ni-Mn alloy is shown in figure 6.11 where dashed line coresponds to the SRO parameter of the binary Fe-Cu alloy simulated at same conditions. Both curves are almost identical with some minor distinctions. Differences are in the incubation time period before α_{CuCu} increases and peak values of α_{CuCu}. The average cluster size evolution in time is depicted in figure 6.12 and follows S curve shape. Cluster size is up to 60 s almost constant. After that cluster growth begins and size evolves according to $L^2(t) \propto t^x$ with $x \approx 0.62$. The growth stage takes place between 80 s and 200 s, following by slow transition into coarsening regime, which at the very end starts to follow classical LSW coarsening law.

In previous paragraph results from ternary and quaternary alloys were compared to the well analysed binary Fe-Cu alloy. In order to reveal true influence of each impurity separately or combined, curves for SRO parameter α were collected in one

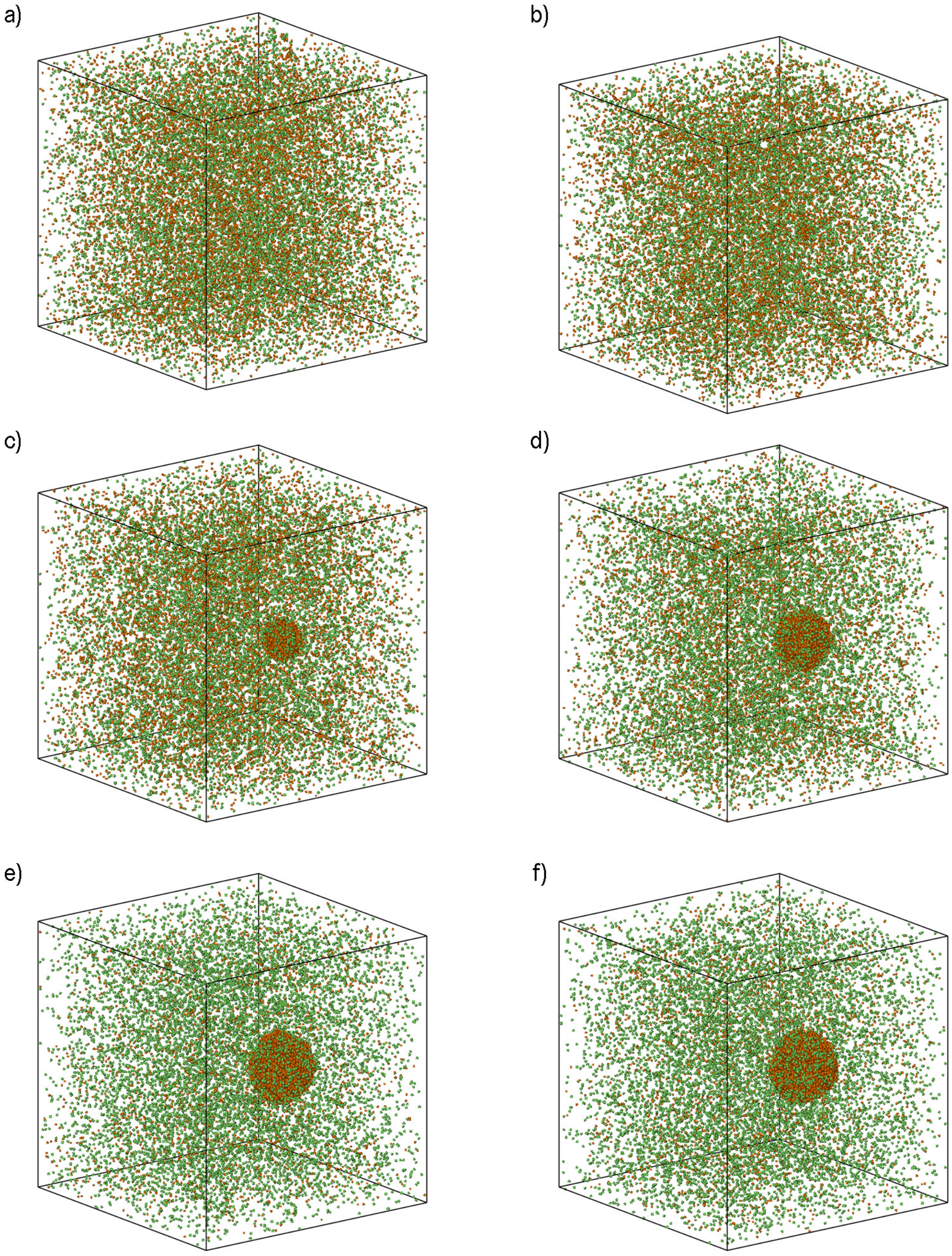

Figure 6.5: Snapshots from kMC simulations of Fe-Cu-Ni alloy with 1 at.% Cu and 1 at.% Ni, obtained from kMC simulations during annealing at 873 K. Size of the simulation box is 80^3 BCC lattices (23^3 nm), Cu atoms are orange and Ni atoms are green. Fe atoms are not shown due to visibility reasons; a) initial disordered configuration, b) at 67.9 s, c) at 244.5 s, d) at 680.7 s, e) at 1368 s, f) at 2743 s.

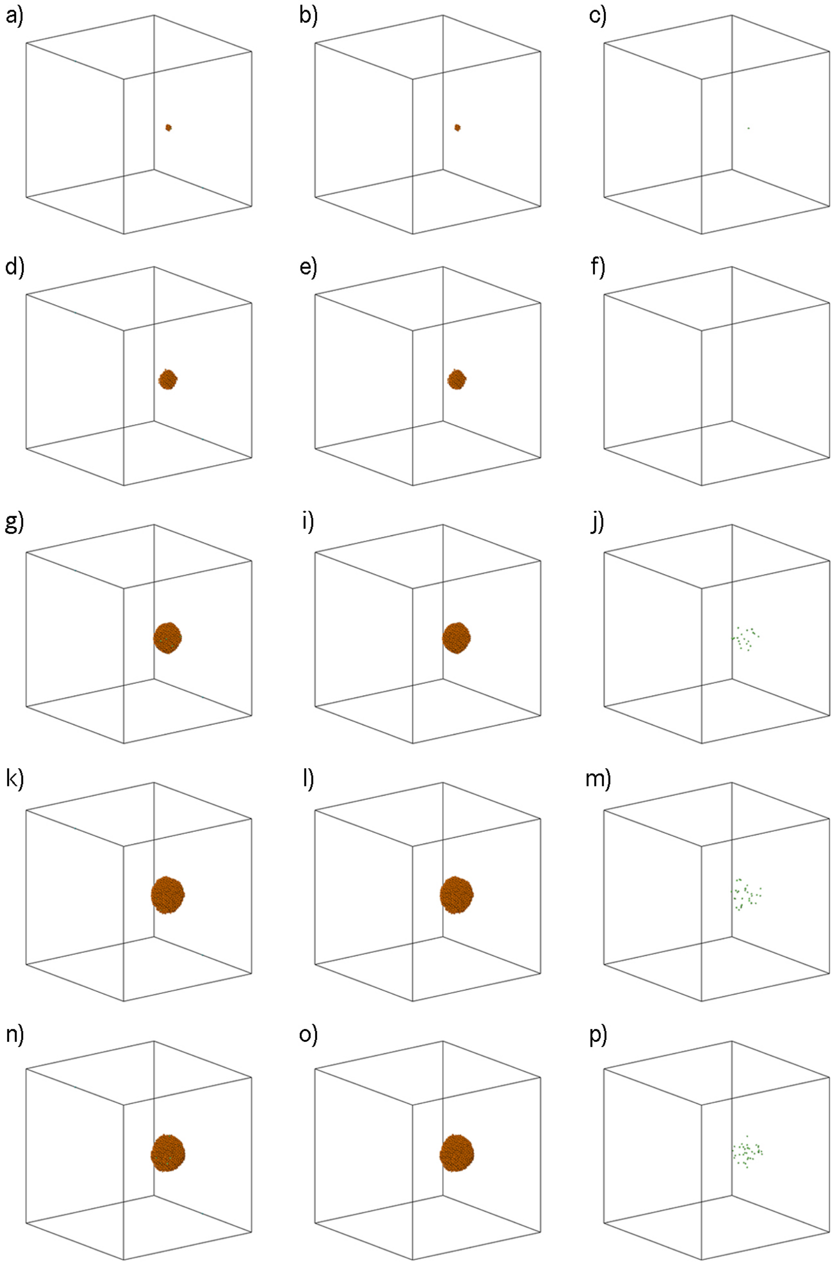

Figure 6.6: Snapshots of individual atom group clusters from kMC simulations during isothermal treatment at 873 K for Fe-Cu-Ni alloy with 1 at.% Cu and 1 at.% Ni. Size of the simulation box is 80^3 BCC lattices (23^3 nm), Cu atoms are orange and Ni atoms are green; a)-c) at 67.9 s, d)-e) at 244.5 s, f)-h) at 680.7 s, i)-k) at 1368 s, l)-m at 2743 s.

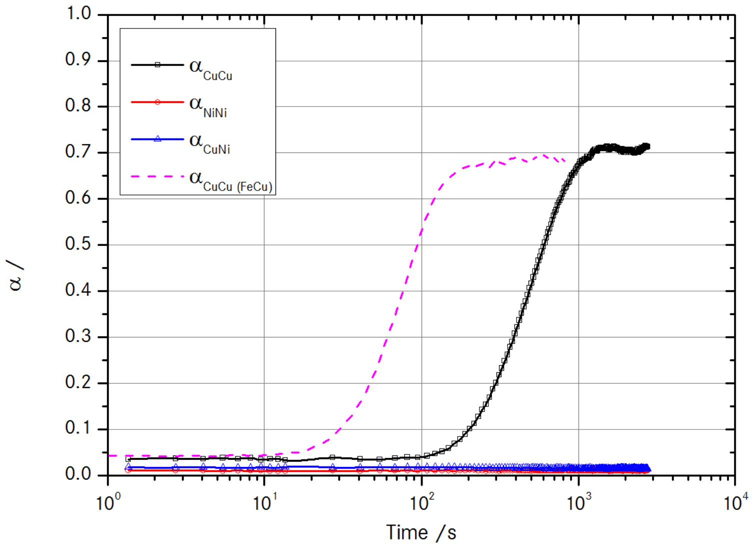

Figure 6.7: Evolution of the short range order parameter in Fe-Cu-Ni alloy with 1 at.% Cu and 1 at.% Ni at 873 K. Dashed line presents evolution of the short range order parameter in binary Fe-Cu alloy at same conditions.

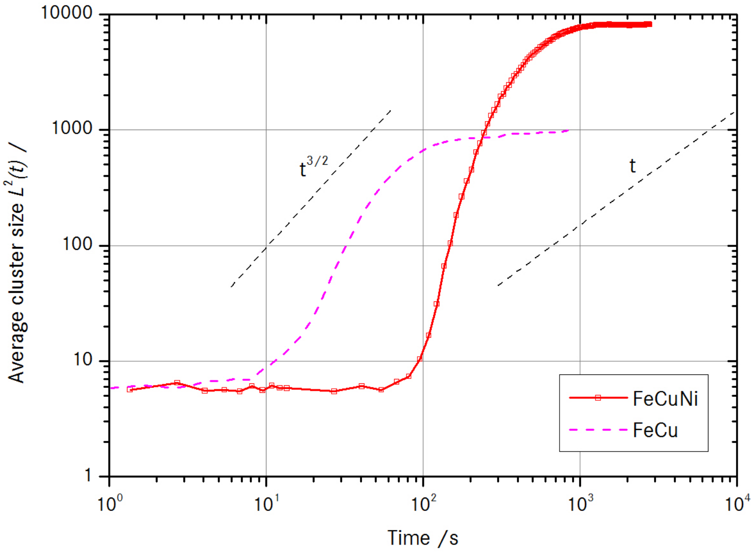

Figure 6.8: Evolution of the average cluster size in time for Fe-Cu-Ni alloy isothermally annealed at 873 K.

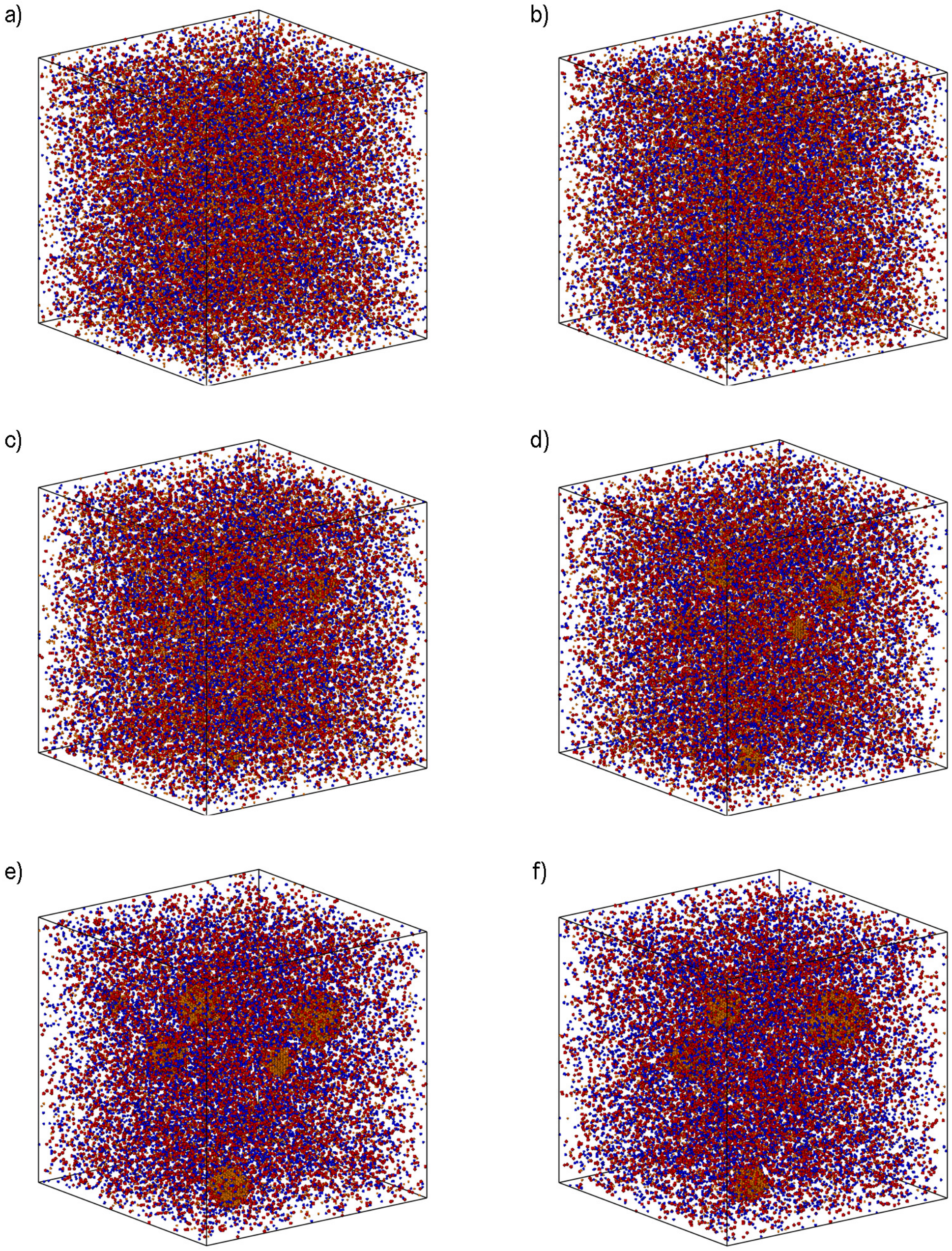

Figure 6.9: Snapshots of precipitation in Fe-Cu-Ni-Mn alloy with 1 at.% Cu, 1 at.% Ni and 1 at.% Mn, obtained from kMC simulations during isothermal treatment at 873 K. Size of the simulation box is 80^3 BCC lattices (23^3 nm), Cu atoms are orange, Ni atoms are blue and Mn atoms are red, Fe atoms are not shown due to visibility reasons; a) initial disordered configuration, b) at 80.7 s, c) at 134.7 s, d) at 202 s, e) at 476 s, f) at 2623 s.

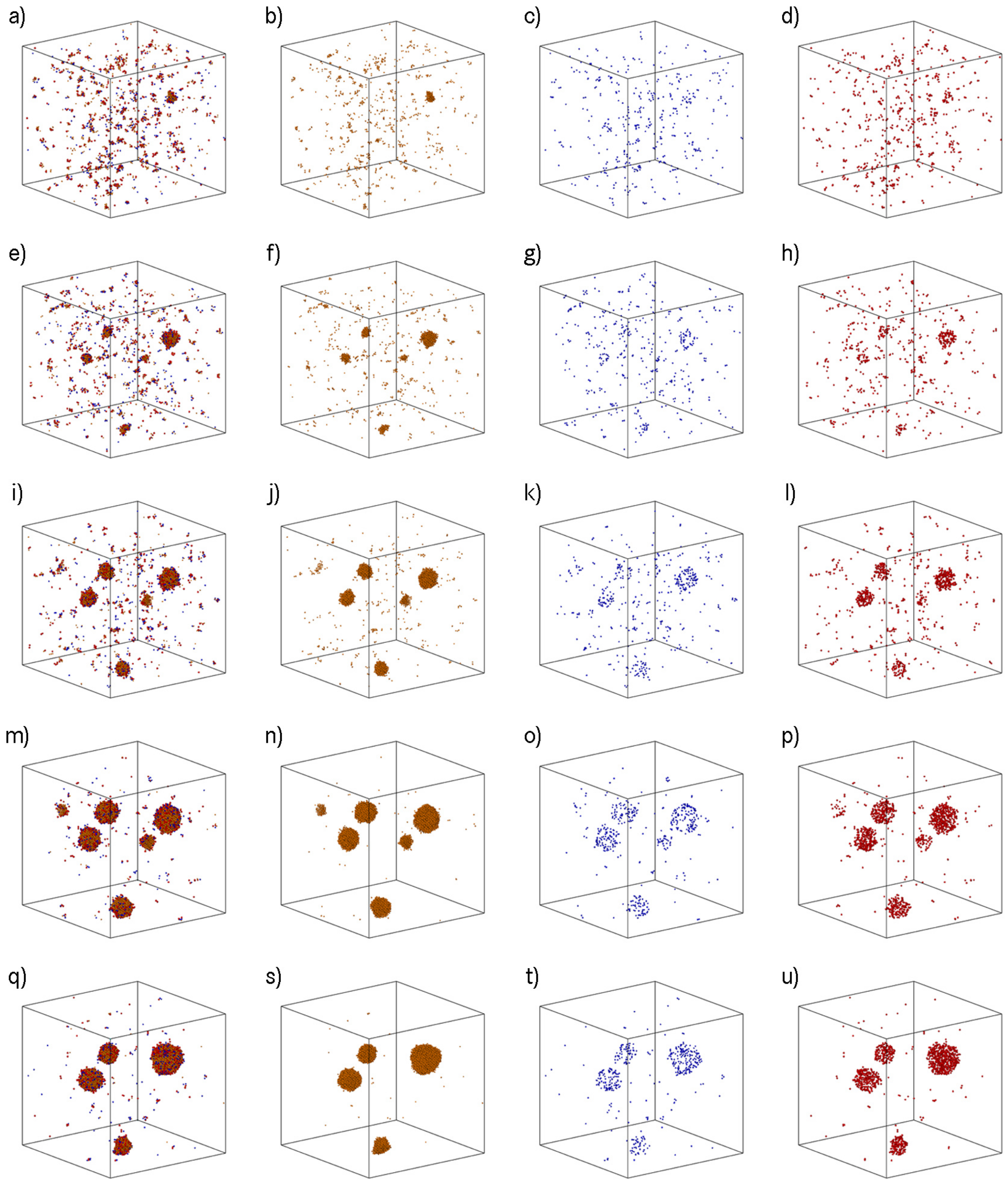

Figure 6.10: Snapshots of individual atom group clusters from kMC simulations during isothermal treatment at 873 K for Fe-Cu-Ni-Mn alloy with 1 at.% Cu, 1 at.% Ni and 1 at.% Mn. Size of the simulation box is 80^3 BCC lattices (23^3 nm), Cu atoms are orange, Ni atoms are blue and Mn atoms are red; a)-d) at 80.7 s, e)-h) at 134.7 s, i)-l) at 202 s, m)-p) at 476 s, q)-u) at 2623 s.

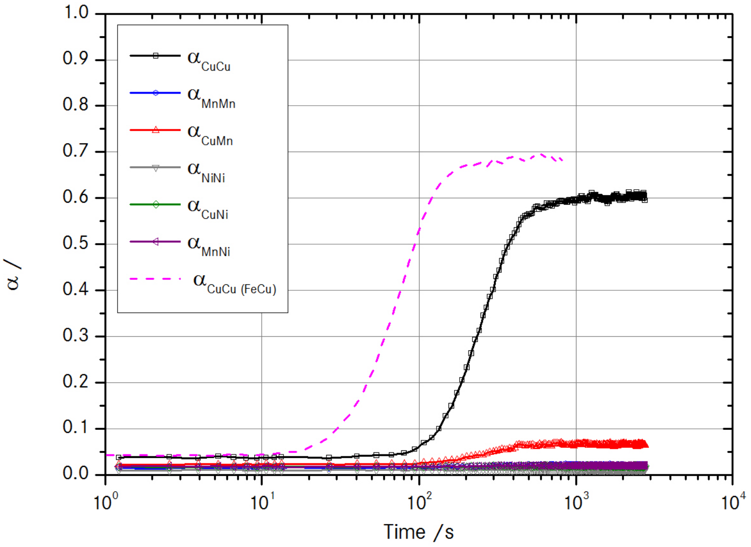

Figure 6.11: Evolution of the short range order parameter in Fe-Cu-Ni-Mn alloy with 1 at.% Cu, 1 at.% Ni and 1 at.% Mn at 873 K. Dashed line presents evolution of the short range order parameter in binary Fe-Cu alloy at same conditions.

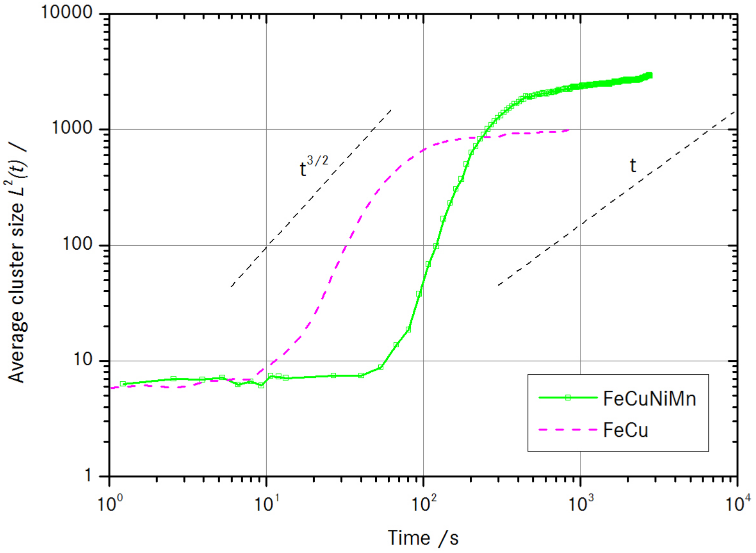

Figure 6.12: Evolution of the average cluster size in time for Fe-Cu-Ni-Mn alloy isothermally annealed at 873 K.

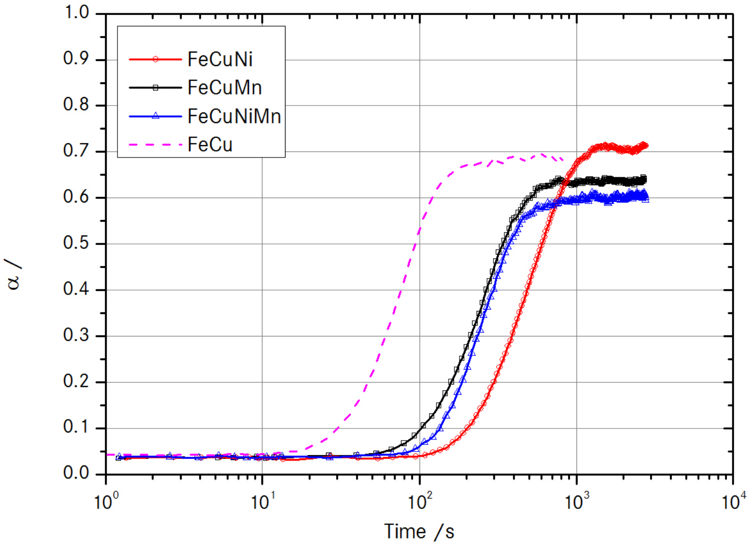

Figure 6.13: Evolution of the short range order parameter α^1_{CuCu} in time for Fe-Cu-Ni, Fe-Cu-Mn and Fe-Cu-Ni-Mn alloy systems. Dashed line presents evolution of the short range order parameter in binary Fe-Cu alloy at same conditions.

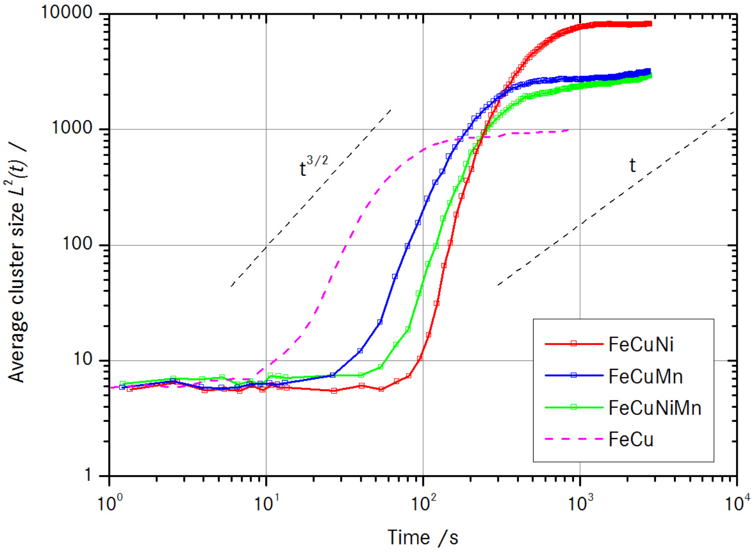

Figure 6.14: Evolution of the average cluster size in time for Fe-Cu-Ni, Fe-Cu-Mn and Fe-Cu-Ni-Mn alloy systems.

graph. Although, various simulation box sizes does not influences evolution of the SRO parameter α and average cluster size; cf. section 5.3.1, the same simulation box sizes were used in all simulations (80^3 BCC constants) compared here. Figure 6.13 shows evolution of SRO parameter α^1_{CuCu} for ternary Fe-Cu-Ni, ternary Fe-Cu-Mn and quaternary Fe-Cu-Ni-Mn alloys. The same figure also depicts SRO parameter α^1_{CuCu} for binary Fe-Cu alloy with dashed line. Clear distinctions are visible between all curves displayed. Addition of Ni atoms causes significant increase of incubation time before clustering occurs. This incubation time is much smaller when only Mn is added to binary Fe-Cu alloy or when both Mn and Ni are introduced, albeit compared to the pure binary Fe-Cu alloy still significantly increased.

Nucleation, growth and coarsening stages can be identified with evolution of the average cluster size. Figure 6.14 shows evolution in time of the average precipitate size for all three alloys simulated in this chapter. Curve representing evolution of mean size of the quaternary alloy is for nucleation and growth stage located between curves where Mn was added and curve where Ni was used as impurity. Average size of the clusters at the end of the simulations is lower for quaternary alloy. Both ternary systems exhibit almost identical sizes. Addition of the Mn impedes growth rate, while Ni impurity causes increase of the growth rate. Size of the clusters change according to the $L^2(t) \propto t^x$ with values for the exponent x for particular alloy system presented in Table 6.5, where $L^2(t)$ are expressed as radii. The highest growth rates exhibit ternary Fe-Cu-Ni system. A little slower growth is observed in ternary Fe-Cu-Mn system, while quaternary Fe-Cu-Ni-Mn system grows according to the $L^2(t) \propto x = 0.62$, which is very near to the classical growth rate ($x = 0.5$).

Table 6.5: Values of exponent x for growth stage according to the $L^2(t) \propto t^x$, with average cluster size expressed as radii.

Alloy	x
Fe-Cu-Ni	0.93
Fe-Cu-Mn	0.8
Fe-Cu-Ni-Mn	0.62

Research is what I'm doing when I don't know what I'm doing.

Wernher Von Braun (1912 - 1977)

7

The phase separation in Ni-Cr-Al alloy

Alloys with high content of Ni are called nickel superalloys and are intended for parts under heavy thermal stresses. The decomposition of supersaturated NiCrAl solid solutions involves two processes, ordering and phase separation. The equilibrium microstructure exhibits face centred cubic (FCC) matrix with various carbides, and ordered $L1_2$, γ' phase like Ni_3Al or Ni_3Cr , depending on the alloy chemical composition. The transformation FCC → $L1_2$ crystal structure is typical first order transition. In figure 7.1 ternary phase digram for Ni-Cr-Al system at 873 K is depicted, [179].

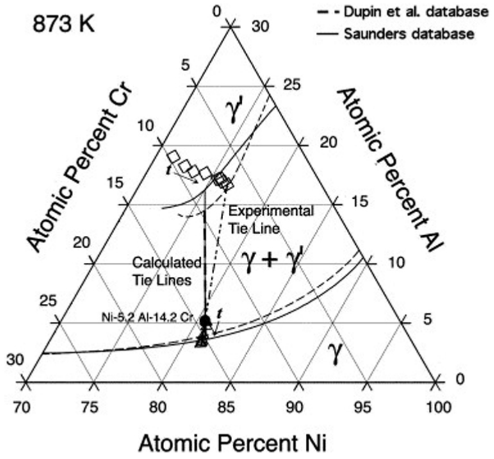
873 K
- - Dupin et al. database
— Saunders database
Atomic Percent Cr
Atomic Percent Al
Atomic Percent Ni
γ'
γ + γ'
γ
Experimental Tie Line
Calculated Tie Lines
Ni-5.2 Al-14.2 Cr
0
5
10
15
20
25
30
70
75
80
85
90
95
100

Figure 7.1: Ni part of equilibrium ternary phase diagram of Ni-Cr-Al alloy at 873 K, [179].

Nickel superalloys with various chemical compositions were extensively studied experimentally, [15, 16, 179–186] and theoretically with phase field and Monte Carlo methods, [15, 16, 31, 35, 38, 186–189].

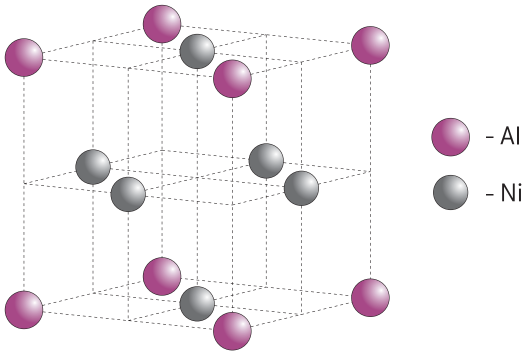

Figure 7.2: Schematic presentation of Ni_3Al with $L1_2$ crystallographic structure.

Small lattice mismatch between FCC matrix and ordered γ' precipitates with $L1_2$ structure, shown in figure 7.2 justifies use of the rigid lattice for the kMC simulations. The mismatch is around 1 %, therefore at initial stages coherency can be kept and elastic strains neglected, [35]. Lattice constant of pure FCC nickel is $a = 0.352$ nm, [190]. The γ' unit cell consists of nickel atoms at the face centres, and Al atoms at the cube corners. Each nickel atom is surrounded by eight other Ni atoms and four Al atoms. Every Al atom has two Ni atoms as its first nearest neighbours, and no other Al atom, [187]. Phase diagram in figure 7.1 show that solubility of Cr is large in Ni and Al, therefore large amount of Cr can be accommodated in Ni_3Al phase. This was previously confirmed by other studies, [16, 180], where was also suggested that Cr can substitute both Al and Ni, and that beside expected Ni_3Al phase, also Ni_3Cr $L1_2$ crystal structure is possible.

7.1 Model parametrization

Parameters used in kMC simulations are presented in Table 7.1. Full Ni-Cr-Al alloy thermodynamics needs to be embodied in the simulation parameters and was based on the data from literature, [16, 31]. Interatomic parameters taken from reference [31] were deduced from a cluster expansion of the cohesive energy of Ni(Al,Cr) supercells computed with density functional theory, local density approximation, combined with non-local, norm-conserving pseudopotentials, and plane-wave expansions. Calculations used the band-by-band conjugate gradient technique to minimize the total energy with

Table 7.1: Simulation parameters used for kMC simulations in NiCrAl alloy

$\epsilon^{(1)}_{\mathrm{NiNi}} = -0.7485$ eV	$\epsilon^{(2)}_{\mathrm{NiNi}} = -0.0135$ eV
$\epsilon^{(1)}_{\mathrm{CrCr}} = -0.6845$ eV	$\epsilon^{(2)}_{\mathrm{CrCr}} = -0.0112$ eV
$\epsilon^{(1)}_{\mathrm{AlAl}} = -0.5786$ eV	$\epsilon^{(2)}_{\mathrm{AlAl}} = -0.0265$ eV
$\epsilon^{(1)}_{\mathrm{NiCr}} = -0.7582$ eV	$\epsilon^{(2)}_{\mathrm{NiCr}} = 0.0258$ eV
$\epsilon^{(1)}_{\mathrm{NiAl}} = -0.7495$ eV	$\epsilon^{(2)}_{\mathrm{NiAl}} = 0.0349$ eV
$\epsilon^{(1)}_{\mathrm{CrAl}} = -0.6963$ eV	$\epsilon^{(2)}_{\mathrm{CrAl}} = 0.0225$ eV
$\epsilon^{(1)}_{\mathrm{NiV}} = -0.178$ eV	$\epsilon^{(1)}_{\mathrm{CrV}} = -0.223$ eV
$\epsilon^{(1)}_{\mathrm{AlV}} = -0.221$ eV	
$E_{\mathrm{SpNi}} = -9.750$ eV	$E_{\mathrm{SpCr}} = -9.862$ eV
$E_{\mathrm{SpAl}} = -9.412$ eV	$\nu_{\mathrm{Ni}} = 1.10 \times 10^{15}$ s^{-1}
$\nu_{\mathrm{Cr}} = 8.70 \times 10^{14}$ s^{-1}	$\nu_{\mathrm{Al}} = 1.10 \times 10^{15}$ s^{-1}

respect to plane-wave coefficients. Kinetic parameters, E_{SpX} and ν_X were taken from reference [16] and they reproduce the impurity diffusion of Al and Cr in Ni accurately.

7.2 Results

In this section results obtained with kMC simulation on Ni-5.2Al-14.2Cr at.% alloy are presented. Size of the simulation box used, was 78 × 78 × 39 FCC lattices or 27.46 × 27.46 × 13.73 nm. This amounts to total of 949104 available atom positions, which were populated with 764977 Ni atoms, 134773 Cr atoms, 49354 Al atoms and one vacancy. Total random atom distribution was quenched from infinite temperature to 873 K and then isothermally annealed at that temperature. In figure 7.3 snapshots obtained from kMC simulations at different times are presented. Ni atoms are omitted due to visibility reasons. Snapshots reveal, that initial disordered configuration is gradually changing as $L1_2$ phase precipitates an grows. From obtained results, the ordered γ' phase with $L1_2$ structure (cf. figure 7.2) was extracted. Two possible variants of the γ' precipitates are possible, Ni_3Al and Ni_3Cr and their evolution in time is shown in figure 7.4. The Ni_3Cr variant is in obtained results present from the very early stage, which indicates that Cr starts to order with respect to Al atoms. Its amount slightly increases at first, before starts do decreasing. The Ni_3Al phase variant was not detected in a early stage of the simulations. After Ni_3Al phase was formed, its amount very quickly reached maximum value.

Snapshots of extracted Ni_3Al and Ni_3Cr precipitates at four different times are

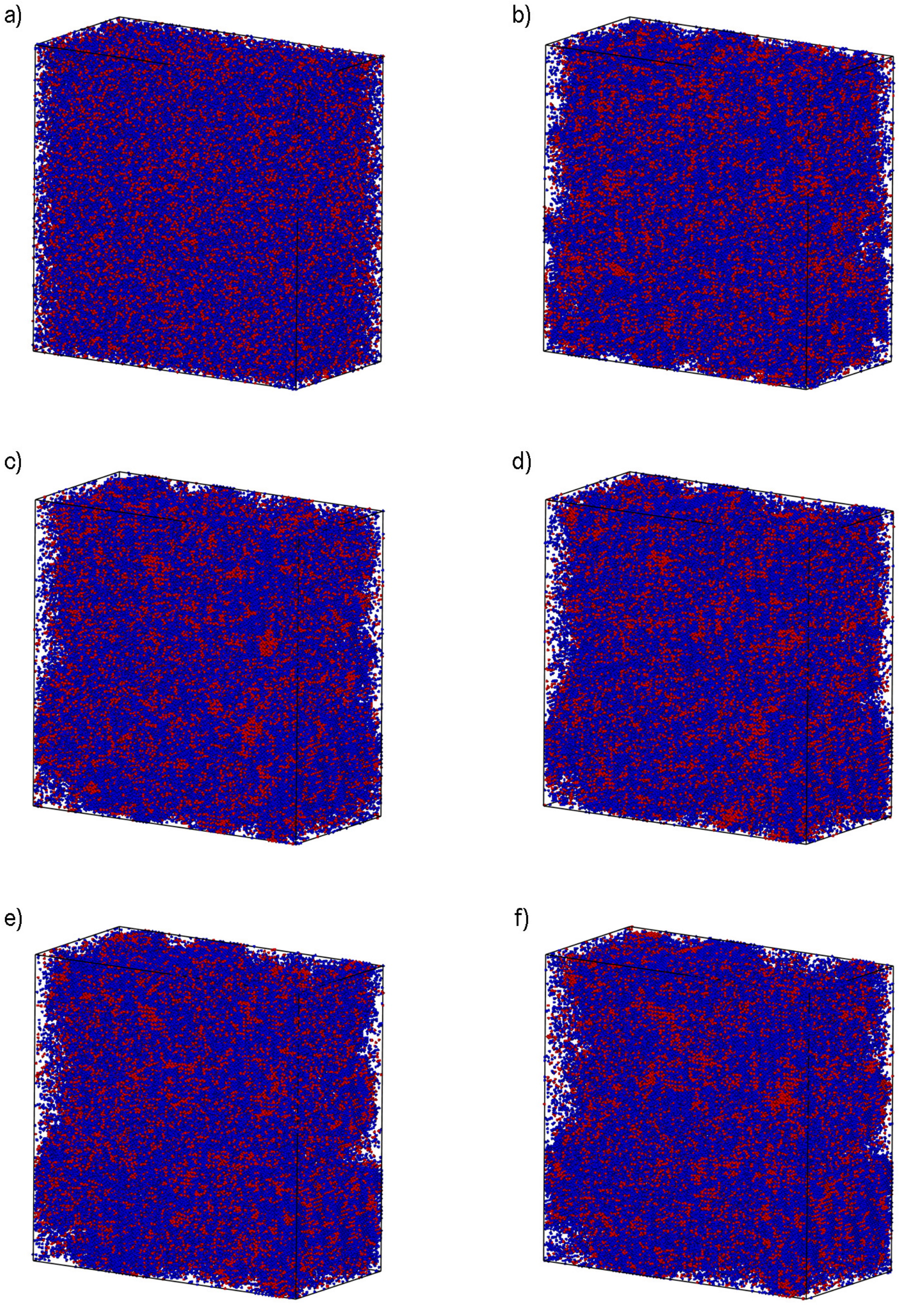

Figure 7.3: Snapshots of isothermally treated Ni-Cr-Al alloy with 15.2 at% Cr, 5.2 at% Al, at 873 K obtained from kMC simulations. Due to visibility reasons only Cr (blue) and Al (red) atoms are displayed; a) initial disordered configuration, b) at 0.04 s, c) at 0.18 s, d) at 0.28 s, e) at 0.39 s, f) at 0.49 s.

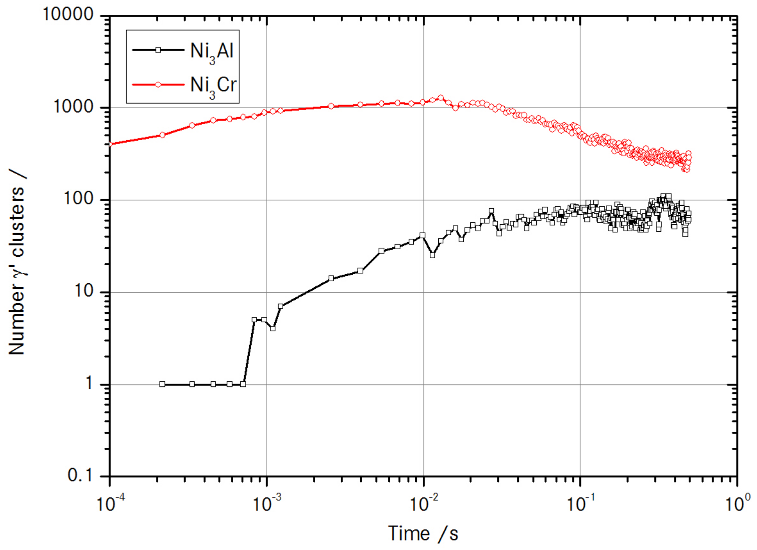

Figure 7.4: Time evolution of the amount of Ni_3Al and Ni_3Cr precipitates.

shown in figures (7.5) and (7.6), respectively. Optical comparison of both figures reveal higher amount of the Ni_3Cr precipitates, which are smaller compared to the extracted Ni_3Al precipitates.

In figure 7.7 are depicted γ' precipitates extracted from microstructures obtained from isothermal annealing at 873 K of Ni-Cr-Al alloy with 15.2 at% Cr, 5.2 at% Al using threshold concentration 0.66 around Ni atoms. If these snapshots are compared to snaphots of extracted exact $L1_2$, γ' phases Ni_3Al and Ni_3Cr shown in figures 7.5 and 7.6, yielded results are diffrent. This difference is attributed to concentration threshold arround searched atoms which collects whole sorroundings belonging to that particular treshold. When search is executed for exact crytal structure only those atoms are collected. The severe difference in obtained results suggests that special care must be put into analysis of obtained data either from computer or real experiments.

Similar than in the case of Fe-Cu alloys, short range order parameter can be used to investigate precipitation kinetics. In the case of ternary Ni-Cr-Al alloys several SRO parameters are possible to be defined which enable insight into the phases evolution, simulated with kMC. The precipitation kinetics in Ni-Cr-Al alloy simulated in this chapter was investigated through time evolution of α^1_{AlAl}, α^2_{AlAl}, α^1_{CrCr}, α^2_{CrCr}, α^1_{AlNi}, α^2_{AlNi}, α^1_{CrNi} and α^2_{CrNi} SRO parameters. In figure 7.8 evolution of SRO parameters α^1_{AlAl}, α^2_{AlAl}, α^1_{CrCr} and α^2_{CrCr} in time are depicted. All SRO parameters are increasing, with α^2_{AlAl} exhibiting highest increase rate, which indicates that Al atoms are positioning

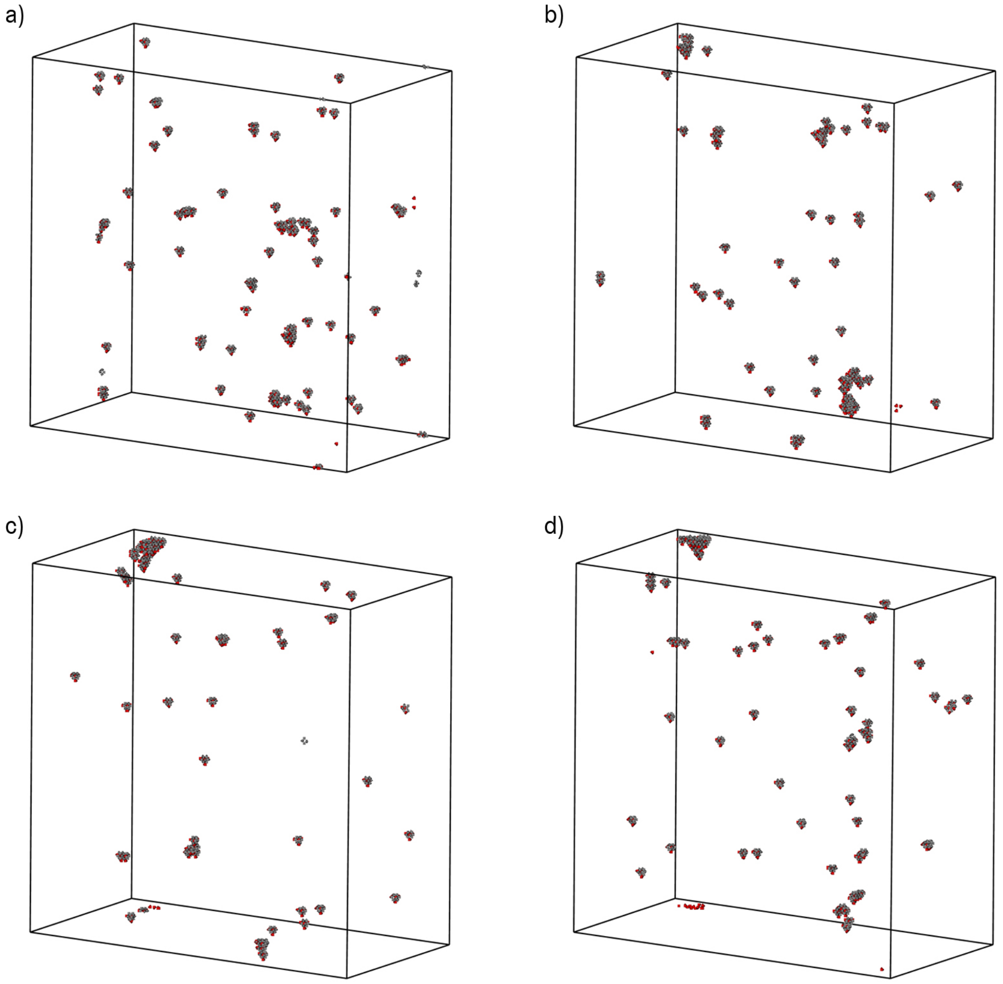

Figure 7.5: Snapshots of obtained Ni_3Al precipitates in isothermally treated Ni-Cr-Al alloy with 15.2 at% Cr, 5.2 at% Al, at 873 K. Al atoms are red and Ni atoms are silver; a) at 0.18 s, b) at 0.28 s, c) at 0.39 s, d) at 0.49 s.

themselves for Ni_3Al phase, where Al is present on the FCC cube corner sites. Similar behaviour was observed also for Cr atoms, which also tend to form γ' precipitates. The ordering of Al atoms on first neighbouring positions was not noticed. However, α^1_{CrCr} starts to increase towards the end of the simulation, suggesting that Ni is being replaced on the face centre sites of the FCC cells. This happens because of high solubility of Cr in Ni and was previously confirmed with experimental observations, [180] and kMC simulations, [16].

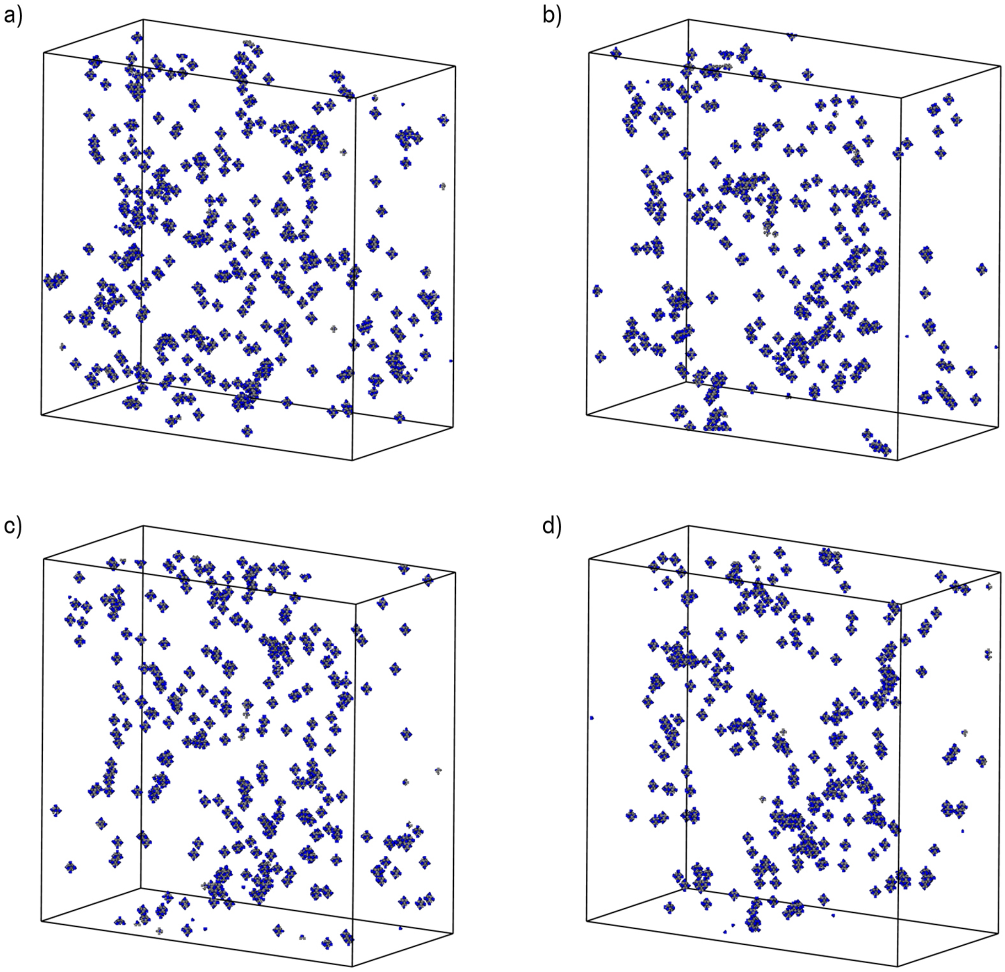

Figure 7.6: Snapshots of obtained Ni_3Cr precipitates in isothermally treated Ni-Cr-Al alloy with 15.2 at% Cr, 5.2 at% Al, at 873 K. Cr atoms are blue and Ni atoms are silver; a) at 0.18 s, b) at 0.28 s, c) at 0.39 s, d) at 0.49 s.

In figure 7.9 heteroatomic short range order parameters α^1_{AlNi}, α^2_{AlNi}, α^1_{CrNi} and α^2_{CrNi} are shown. SRO parameters α^1_{AlNi} and α^1_{CrNi} describes tendency of Al and Cr to form bonds on first neighbour positions with Ni. Both parameters are constant at the beginning and start to decrease toward the end of the simulation. As expected, SRO parameters α^2_{AlNi} and α^2_{CrNi} are decreasing from the beginning, with α^2_{AlNi} exhibiting higher decrease rate. When γ' precipitates are formed, Ni atoms are expected on their firs nearest neighbour positions. With increasing amount of γ' phase, the SRO

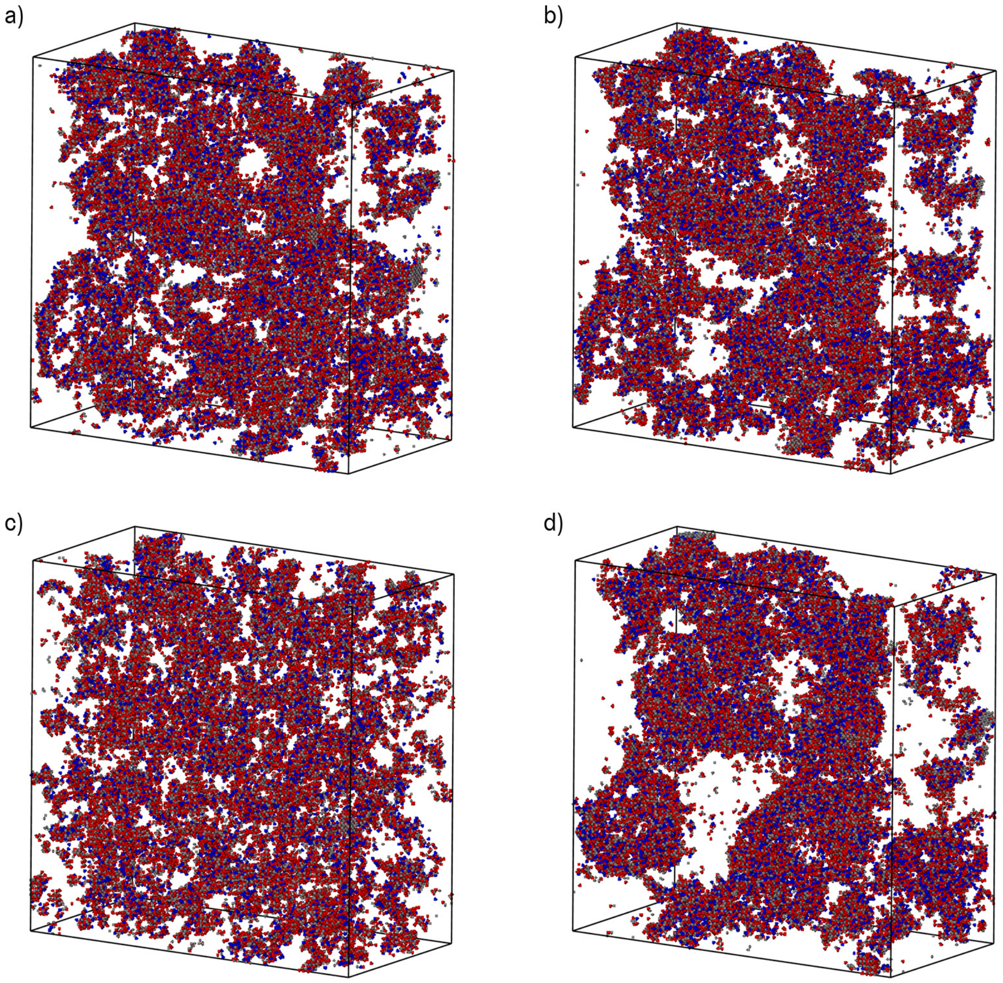

Figure 7.7: Snapshots of obtained γ' precipitates using threshold concentration around Ni atoms in isothermally treated Ni-Cr-Al alloy with 15.2 at% Cr, 5.2 at% Al, at 873 K. Cr atoms are blue, Al atoms are red and Ni atoms are silver; a) at 0.18 s, b) at 0.28 s, c) at 0.39 s, d) at 0.49 s.

parameters α^2_{AlNi} and α^2_{CrNi} should decrease.

Parts made from nickel superalloys are often used in very demanding environment and exposed to high thermal loadings. The strength of nickel superalloys is derived from the presence on γ' precipitates, which then in the presence of thermal loads grow and coarsen. This can have undesired effects, therefore simulations to predict life span of Ni-superalloys are welcomed. Simulations performed here on the highly supersaturated Ni-Cr-Al alloy, nucleation of ordered γ' precipitates was observed from the beginning.

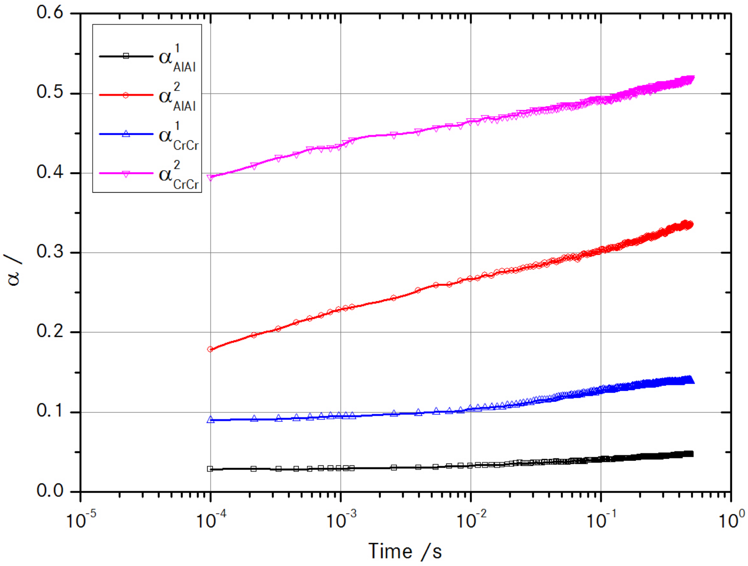

Figure 7.8: Evolution of the short range order parameter in Ni-Cr-Al alloy at 873 K for homoatomic combinations.

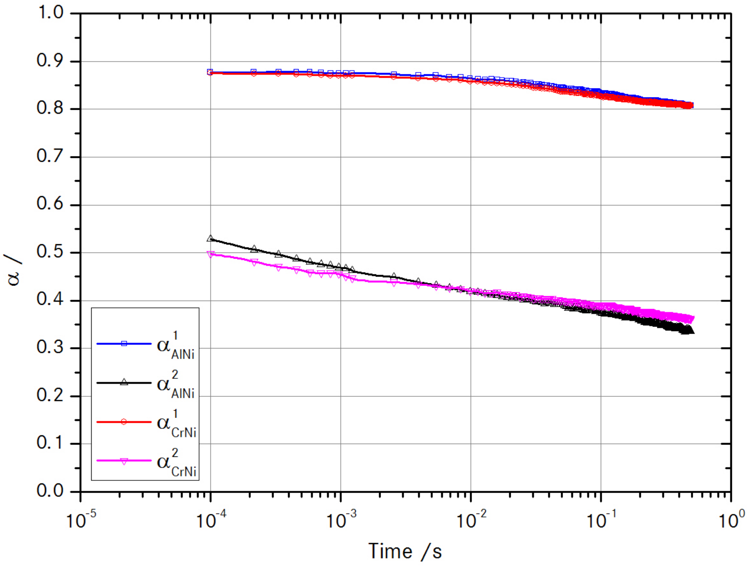

Figure 7.9: Evolution of the short range order parameter in Ni-Cr-Al alloy at 873 K for heteroatomic combinations.

At the early stages of phase separation by kMC simulations, two types of ordered γ' precipitates (Ni_3Al and Ni_3Cr) were detected and their time evolution was analysed. Detection of both variants of the γ' precipitates is in agreement with previous experimental and modeling studies, [16, 31, 35, 38, 180, 183–186, 186, 188]. Comparison of matrix and γ' precipitates with 3D atom probe (3D APT) confirms very small mismatch between their lattice parameters and confirms justification to perform simulations with the use of rigid lattice diffusion model. Furthermore, similar kinetic pathways were also observed with 3D APT studies, which confirms used simulation parameters.

The scientist is not a person who gives the right answers, he's one who asks the right questions.

Claude Lévi-Strauss
(1908-2009)

8

The simulation of coupled interstitial/substitutional diffusion in Fe-C alloy

The precipitation of carbides is very important and helps to control physical properties of the steels. Other chemical elements (e.g. Nb, Ti, V, ...) which enhances carbide precipitation are often added to steels. In order to obtain given microstructure adequate processing is needed. To better choose thermal treatments for desired phase composition it is important to predict the precipitation kinetics. The Fe-C phase diagram, shown in figure 8.1 provides valuable foundation on which to build knowledge of steels in their immense variety, [191].

This chapter focuses on the homogeneous precipitation in α-iron. The simulations model used in previous chapters was made even more complicated with addition of simultaneous diffusion of the interstitial atoms. Therefore, the simulations model combines vacancy diffusion of the substitutional elements (Fe) and interstitial diffusion of C atoms. If plain carbon steel is aged at 473 K or above, the orthorhombic cementite Fe_3C is formed, [191]. This is also evident from the Fe-C phase diagram, where phase composition below 1000 K is made from ferrite and cementite.

8.1 Model parametrization

Rigid lattice used for simulations in previous chapters needs to be changed to account interstitials. Since carbon atoms diffuse on different lattice sites than substitutional elements, it is logical to define two separate sublattices. First sublattice accommodates

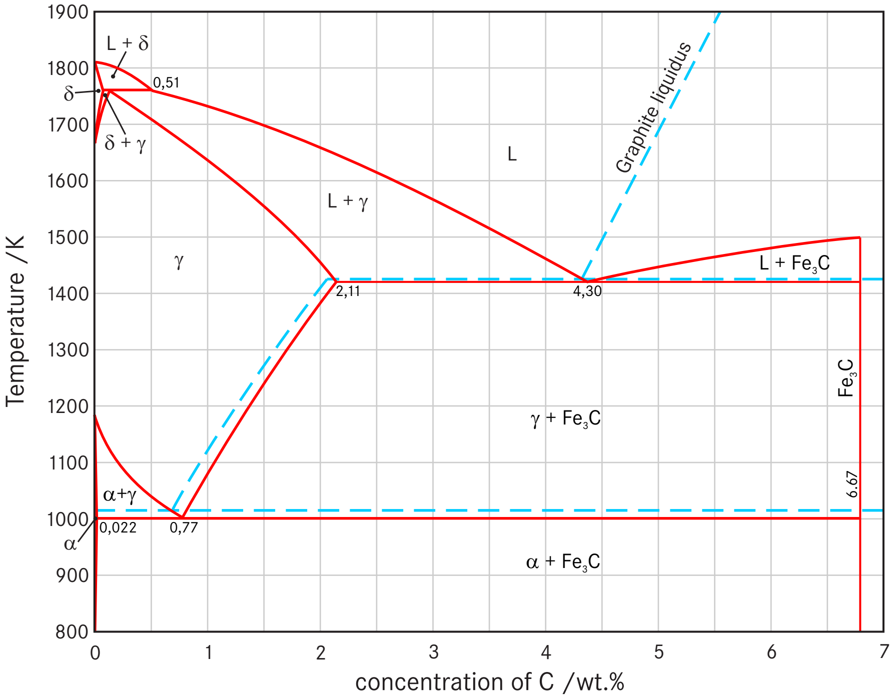

Figure 8.1: The Fe-C phase diagram, [191].

Fe atoms and substitutional vacancy, while other sublattice responsible for diffusion of C atoms is almost empty and represents 3/4 of all sites. Nearest neighbours in the coupled substitutional and interstitial kinetic Monte Carlo simulations are defined on a simple cubic lattice as follows

- First nearest neighbours are between two sites on interstitial sublattice with distance between them one half of base BCC lattice, $r_1 = 0.1435$ nm
- Second nearest neighbours are also between two interstitial sites on the diagonal of simple cubic cube with distance, $r_2 = 0.20294$ nm
- Third nearest neighbours are first nearest neighbours on substitutional sublattice, defined same as in previous simulations, $r_3 = 0.2486$ nm
- Fourth nearest neighbours are second nearest neighbours on substitutional sublattice, already defined in previous simulations, $r_4 = 0.287$ nm

Simulations of cementite precipitation from supersaturated ferrite with carbon represents several difficulties if rigid lattices are used. The cementite has orthorhombic,

$D0_{11}$ crystal structure with lattice parameters $a = 0.4525$ nm, $b = 0.5087$ nm and $c = 0.6743$ nm, [192] and ferrite has body centred cubic, A2 crystal structure with lattice parameter $a = 0.287$ nm. This mismatch of lattice parameters makes impossible to accurately reproduce the Fe-C phase diagram with rigid lattice approximation. The Fe_3C phase is thus replaced by approaching FeC phase and interaction parameters are fitted to the real Fe-C system. In the cubic stoichiometric FeC phase, C atoms occupy 1/3 of the interstitial sites and can be build in several variants, shown in figure 8.2.

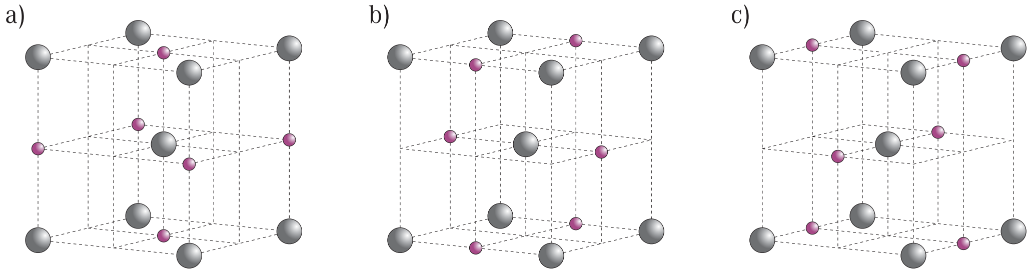

Figure 8.2: Schematic presentation of Fe_3C structure on the simple cubic lattice. Three variants, a), b), and c) are possible, with C atoms occupying various interstitial positions.

Table 8.1: Interaction energies and kinetic parameters used for the kMC simulations of Fe-C alloy.

$\epsilon_{\mathrm{CC}}^{(1)} = 0.10$ eV	$\epsilon_{\mathrm{CC}}^{(2)} = 0.10$ eV
$\epsilon_{\mathrm{CC}}^{(3)} = -0.09$ eV	$\epsilon_{\mathrm{CC}}^{(4)} = -0.09$ eV
$\epsilon_{\mathrm{FeFe}}^{(3)} = -0.611$ eV	$\epsilon_{\mathrm{FeFe}}^{(4)} = -0.611$ eV
$\epsilon_{\mathrm{FeC}}^{(1)} = 0$ eV	$\epsilon_{\mathrm{FeC}}^{(2)} = 0$ eV
$\epsilon_{\mathrm{CV}}^{(1)} = -0.30$ eV	$\epsilon_{\mathrm{CV}}^{(2)} = 0$ eV
$\epsilon_{\mathrm{FeV}}^{(3)} = -0.34$ eV	$\epsilon_{\mathrm{FeV}}^{(4)} = 0$ eV
$E_{\mathrm{SpFe}} = -9.31$ eV	$E_{\mathrm{SpC}} = 0.88$ eV
$\nu_{\mathrm{Fe}} = 10^{16}$ s^{-1}	$\nu_{\mathrm{C}} = 1.46 \times 10^{14}$ s^{-1}

Simulation parameters used for coupled substitutional and interstitial diffusion are presented in Table 8.1. It can be seen that interactions are not possible on first and second nearest positions for substitutional atoms. The carbon solubility depends only on $\epsilon_{\mathrm{CC}}^{(3)}$ and $\epsilon_{\mathrm{CC}}^{(4)}$ and was fitted to correspond to the Fe-C phase diagram. Slightly repulsive interactions $\epsilon_{\mathrm{CC}}^{(1)}$ and $\epsilon_{\mathrm{CC}}^{(2)}$ do not effect carbon solubility and were fitted to the simple pair potential, [193]. Fe interaction energies were fitted to the cohesive energy of iron as was also the case in previous chapters. Similar parametrization for homogeneous precipitation model was used in previous work by Dominique Gendt, [28] for Fe-Nb-C alloy. The kinetic parameters, jump frequencies and saddle point energies were based on the values from previous work by D. Gendt, [28]. The pair interaction energies $\epsilon^1_{\mathrm{XY}i}$ and ϵ^2_{XY} are parameters for reactions with 1st and 2nd nearest neighbours on interstitial part of rigid lattice.

8.2 Results

In this section results obtained with kinetic Monte Carlo simulations are presented. Simulations, performed on 32^3 BCC lattice sites (9.18^3 nm) in Fe-C alloy with 1 at.% C atoms and single vacancy. In figure 8.3 snapshots of initial disordered configuration and obtained microstructures at two times are depicted. Only C atoms are depicted for visibility reasons. Quick ordering of C atoms can be observed and in figure 8.3c almost all C atoms are in FeC clusters.

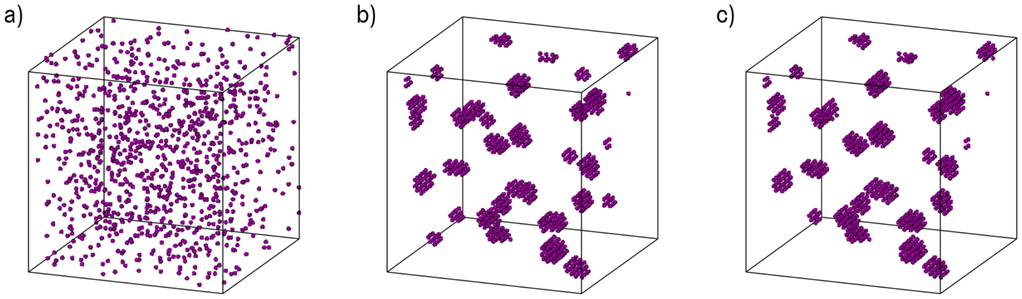

Figure 8.3: Snapshots of Fe-C alloy with 1 at.% C, obtained from kMC simulations during annealing at 873 K. Size of the simulation box is 32^3 BCC lattices (9.2^3 nm), only C atoms are displayed due to visibility reasons; a) initial disordered configuration, b) at 0.9 s, c) at 2 s.

The C-C pair correlation function of the initial disordered state in shown in figure 8.4. Initial configuration is sufficiently disordered although slight correlations can be observed at short distances, at around $r \approx 0.25$ nm with value $g(r) \approx 5$, which corresponds to third nearest neighbours.

The carbon clusters are formed very quickly due to fast diffusion of interstitial carbon and driving force for iron carbide precipitation (activity of carbon in iron). The composition and crystal structure of obtained precipitates are cubic FeC crystal

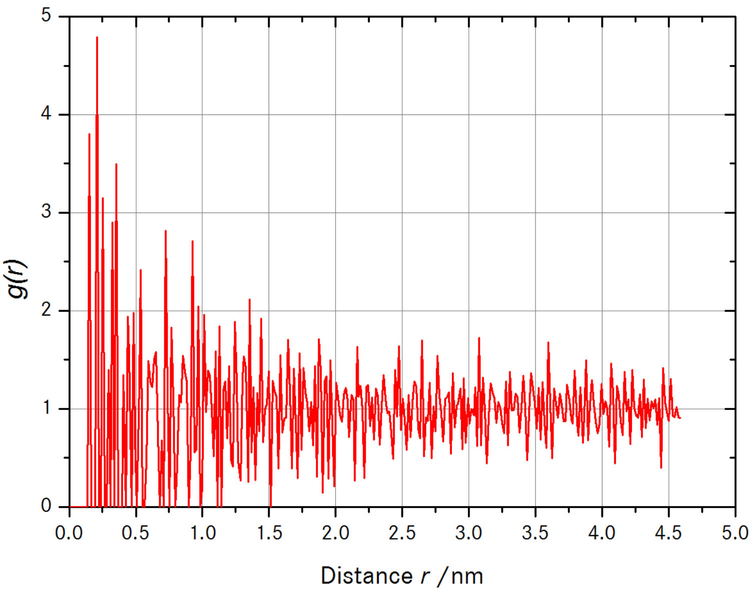

Figure 8.4: Carbon-carbon pair correlation function of initial disordered state.

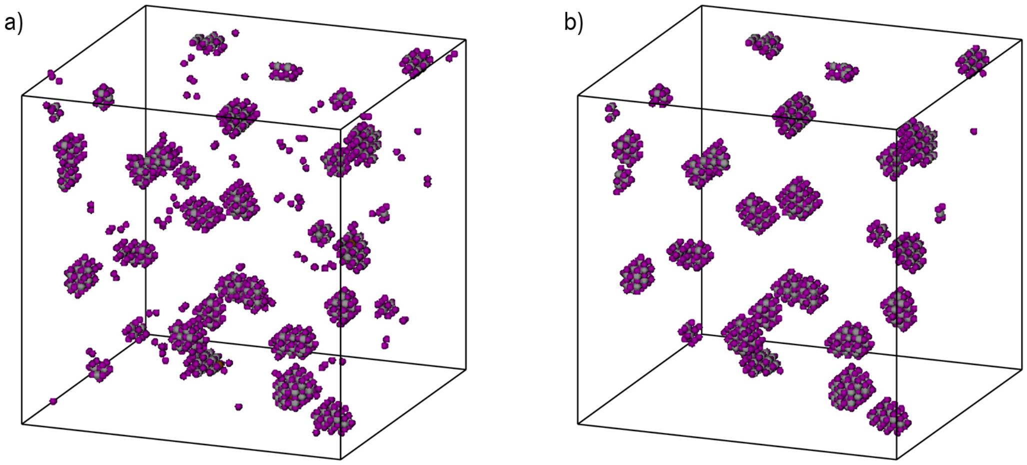

Figure 8.5: Snapshots of FeC precipitates in Fe-C alloy with 1 at.% C, obtained from kMC simulations during annealing at 873 K; a) at 0.9 s, b) at 2 s.

structure and not expected Fe_3C cementite phase, due to use of the rigid lattice approximation. Also associated lattice mismatches are not accounted for. However, obtained

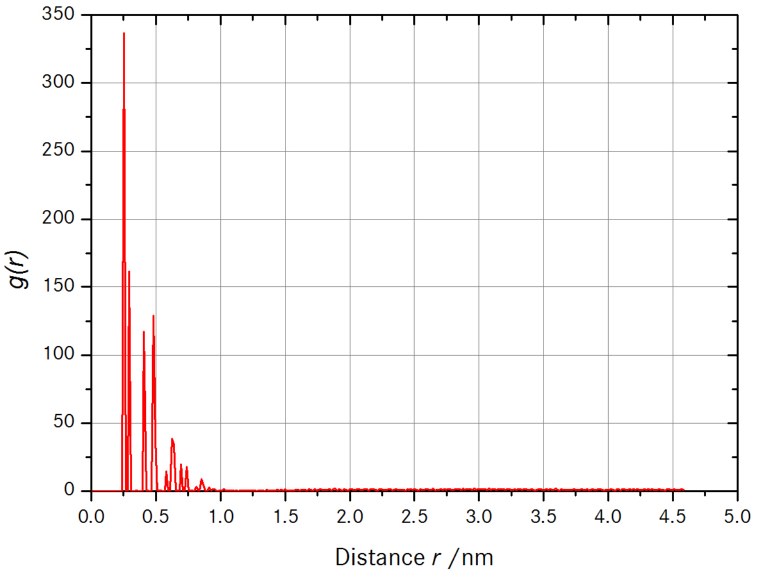

Figure 8.6: Carbon-carbon pair correlation function at 0.9 s.

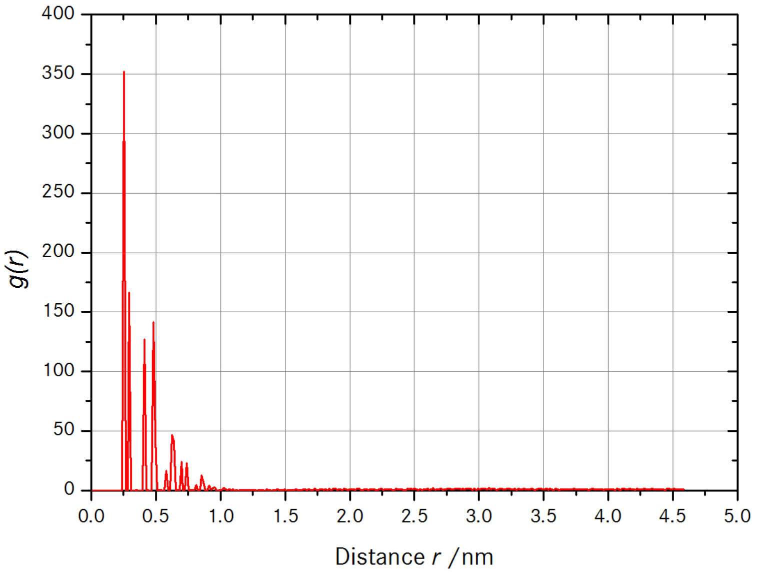

Figure 8.7: Carbon-carbon pair correlation function at 2 s.

precipitation kinetics should qualitatively describe diffusion of carbon in iron and its rapid clustering. Extracted clusters with cubic FeC structure are depicted in figure 8.5. When both both snapshots are compared, coarsening of obtained FeC clusters is revealed. In figure 8.5a very small amount of C atoms is seen in the matrix, while in figure 8.5b all C atoms are bind into clusters. This can be studied with pair correlation function of both states. In figures 8.6 and 8.7 pair correlation function corresponding to snapshots in figures 8.5a and 8.5b are shown, respectively. Strong correlation are observed at distance $r \approx 0.25$ nm which relates to third nearest neighbours and is correct according to the chosen simulation parameters. Value of the pair correlation function increases even more at distance $r \approx 0.25$ for snapshot in figure 8.5b, confirming that C atoms started to form larger clusters.

Rigid lattice model used in this chapter for simulation of cementite precipitation offers some insight into precipitation kinetics. Model reproduces naturally much faster occurring diffusion of carbon atoms and slower diffusion of iron. As explained, expected orthorhombic Fe_3C phase was replaced by cubic FeC phase and solubility limit of carbon was fitted to follow Fe-C phase diagram.

No amount of experimentation can ever prove me right; a single experiment can prove me wrong.

Albert Einstein (1879-1955)

9

Conclusions

Alloys used in everyday life are mainly used in nonequilibrium states where certain physical properties of such states are exploited. The processing path to desired properties often leads through precipitation of the new phases. The kinetic pathways to optimal processing route, require a huge amount of expensive experimental work and are not straightforward. Precipitation and its kinetics is classically divided into nucleation, growth and coarsening, which are then studied as separate processes. Classical theories for these three idealized stages are based on minimization of the free energy potential and solving diffusion equation, where several assumptions are needed for analytical solutions. In the real alloys those idealized stages overlap and assumptions used causes problems in prediction of the kinetic pathways leading to the desired physical properties with classical theories. Fore mentioned assumptions are not needed, if diffusion processes leading to precipitation are treated explicitly on the atomistic level. The main purpose of the presented thesis was to use atomistic simulations, which explicitly treat diffusion of the atoms, to simulate phase transformations in supersaturated solid solutions. Simulations were performed with a kinetic Monte Carlo method on several alloy compositions, where various processes were studied.

In the scope of this thesis a diffusion model, based on the rigid lattice approximation for kinetic Monte Carlo simulations was developed. Its validity was tested and confirmed on the simple binary alloy system. The developed simple binary model offers very good description of the diffusion processes and accurate description of nucleation, growth and coarsening stages. Although a lot of kinetic Monte Carlo simulations can be found in literature, the simulation box size effects were not addressed before. Majority of simulations were performed on the binary Fe-Cu alloy where influence of the box size, temperature, chemical compositions, mixing energy and asymmetry were tested. Influence of the model asymmetry on the vacancy trapping was also investigated. Negative values of the asymmetry parameter change kinetic pathways at late stages, where coarsening was not observed. Negative asymmetry parameter causes agglomeration or direct coagulation of formed clusters and has influence on their mobility, even when they are large. Increased mobility of subcritical clusters have influences on incubation time, nucleation and growth rates and also growth mechanism. Controlled study of the cluster evolution was performed with computer experiments where various initial cluster sizes were seeded in slightly supersaturated medium. The moment of inertia tensors were calculated for several obtained cluster shapes which revealed, that initial spherical shape can deviate a lot. Also displacement of the clusters centre of mass in time and concentration profiles at various times were addressed and discussed. Influence of subcritical clusters was assessed using at high temperature previously annealed microstructure as initial conditions. Here number of subcritical clusters with more than five atoms were detected and their influence is in shorter incubation time and diminished growth rate. However, after some time growth rate and mean cluster size start to behave as in the case with initial random solid solution. The simple binary BCC model served as a starting point, and was made more complex by introduction of other substitutional elements. First ternary Fe-Cu-Mn and Fe-Cu-Ni alloys and then also quaternary Fe-Cu-Ni-Mn alloy were simulated. Effects of additional impurities on the nucleation, growth and coarsening stages were studied. The rigid lattice approximation accurately described clustering, even after introduction of other chemical elements, and obtained results were discussed and compared to the binary Fe-Cu alloy system. This diffusion model was then adjusted for simulations of the phase separation in ternary Ni-Cr-Al alloys with FCC crystal structure. Obtained results are in agreement with 3D atom probe and high resolution microscope experimental studies and with other kinetic Monte Carlo studies. Two variants of γ' precipitates, Ni_3Al and Ni_3Cr were observed and their time evolutions analysed and discussed. After substitutional diffusion processes were examined in detail on several alloy systems, focus was turned to develop kinetic Monte Carlo diffusion model, where substitutional diffusion is competing with interstitial diffusion. Kinetic Monte Carlo simulations with the rigid lattice approximation were then performed on the binary Fe-C alloy, where interstitial positions were populated with carbon atoms. The competing substitutional and interstitial diffusion processes are operating at very different speeds which further complicates model. Furthermore, realistic orthorhombic Fe_3C cementite phase can not be accurately reproduced with rigid lattice approximations and was replaced by approaching cubic FeC crystal structure. Pair correlations of obtained results reveal very quick clustering of carbon on third nearest neighbour positions.

From the presented results, we can conclude that the main goal of this work, which was to develop and implement an atomistic simulation package based on the kinetic Monte Carlo method, that is able to study at a detailed atomistic, spatial scale the diffusion processes, leading to the nucleation, growth, ripening and coalescence of precipitates, was successfully achieved. Furthermore, influence of the subcritical clusters on the incubation time, nucleation rate and growth was also studied. The developed kinetic Monte Carlo simulations package and used atomic potential models enables accurate forecasting of the clustering kinetics from nucleation, growth and coarsening stages.

The developed rigid lattice kinetic Monte Carlo model can be used for fundamental study of diffusion processes and with some further development also for determination of adequate processing routes in industry. There are still points for improvements which could not be implemented due to the limited resources and given time-frame.

Various processes and physical properties could be studied with the developed computer experiment code and underlying model with some improvements and adaptations. However, they were not considered as their treatment would exceed the scope of the thesis. They are as follows

- During material processing, cooling rates can have large effects on the obtained microstructures and consequently mechanical properties of alloys. Developed model was used only for isothermal simulations and could be adjusted also for anisothermal simulations.
- The kinetic Monte Carlo of diffusion model presented in this thesis avoids assumptions common to the phenomenological models. Especially in the multicomponent alloys, it is assumed that the off-diagonal terms of the Onsager matrix can be neglected. However, the diffusion matrix is in general nondiagonal and off-diagonal terms can effect the kinetic pathways. Full diffusion matrix could be calculated from results of kMC simulations with some effort.

In order to obtain an even more realistic description of the kinetic pathways, the following improvements can be made in future

- Simulations in this thesis were performed with simple potentials. Interatomic potentials calculated with *ab-initio* methods would be an improvement. In order to obtain even more realistic kinetic pathways full atomic relaxations should be taken into account. However, this dramatically increases computational time and some trade off between atomic relaxations and simplicity is needed.
- Calculation of the position dependant interatomic energies, using density functional theory (DFT) methods requires enormous computing power. A possible

improvement is the use of optimized interaction energies obtained by using neural networks from a pool of large number of cases previously calculated.

- It was assumed that formed clusters keep coherency with matrix. However, especially in the case of Fe-C and precipitation of Fe_3C cementite phase this is not true. Furthermore, loss of coherency is associated with elastic energies due to lattice mismatches which can have large effect of precipitation. Semi rigid lattice model could be build which would improve lattice mismatch effects.
- Time needed for typical simulations is very long. Although some efforts were put into parallelization of the developed model, better parallelization techniques would greatly improve computing time efficiency.

The problems of language here are really serious. We wish to speak in some way about the structure of the atoms. But we cannot speak about atoms in ordinary language.

Werner Heisenberg
(1901-1976)

A

Description of the developed kMC code

To perform atomic kinetic Monte Carlo simulations on crystal lattice simulations package is needed. During the course of doctoral study simulations package in C++ programming language was developed, tested and evaluated. Simulation package was made from several object which were then put together into bigger building blocks used in the main function. In the main function chemical concentration and atoms names are selected first. Next very important parameter is the size and type of the simulation box. At the moment two crystal lattice types with or without interstitials are available, BCC and FCC. The chosen lattice structure is then populated with desired concentrations of atoms. After lattices are populated initialization function is called, which calculate initial transition probabilities from simulation parameters. One Monte Carlo step (MSC) is completed after same number of exchanges are performed as there is number of all atoms in the simulation box using residence time algorithm described previously. Intermediate results are recorded after several hundred MCS and simulation is run until desired number of MCS is reached, usually around one hundred thousand, depending on the size of simulation box, asymmetry and temperature.

Higher the simulations temperature, more MCS steps is needed to reach reasonable scaled real time relevant for diffusion processes. The simulations software itself consists from following files:

kMCmain.cpp - function main

kMCsim.h and kMCsim.cpp - calculation of transition probabilities and residence time algorithm

kMCgrid.h and kMCgrid.cpp - building of grids and recording of results

kMCsosedi.h and kMCsosedi.cpp - positions of neighbours and simulation parameters

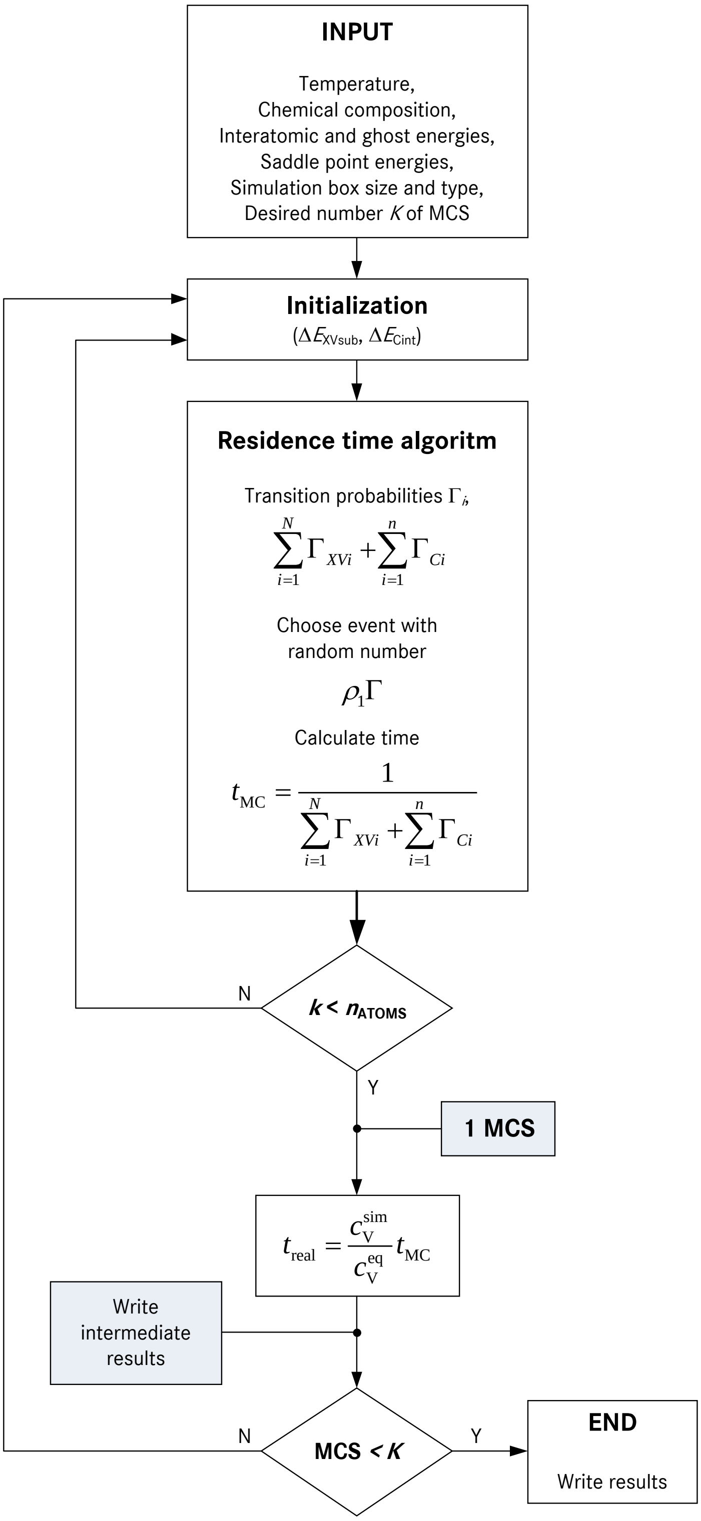
INPUT
Temperature,
Chemical composition,
Interatomic and ghost energies,
Saddle point energies,
Simulation box size and type,
Desired number K of MCS
Initialization
($\Delta E_{\mathrm{XVsub}}$, ΔE_{Cint})
Residence time algoritm
Transition probabilities Γ_i,
$\sum_{i=1}^{N}\Gamma_{XVi}+\sum_{i=1}^{n}\Gamma_{Ci}$
Choose event with random number
$\rho_1\Gamma$
Calculate time
$t_{\mathrm{MC}}=\frac{1}{\sum_{i=1}^{N}\Gamma_{XVi}+\sum_{i=1}^{n}\Gamma_{Ci}}$
$k < n_{\mathrm{ATOMS}}$
N
Y
1 MCS
$t_{\mathrm{real}}=\frac{c_{\mathrm{V}}^{\mathrm{sim}}}{c_{\mathrm{V}}^{\mathrm{eq}}}t_{\mathrm{MC}}$
Write intermediate results
MCS < K
N
Y
END
Write results

Figure A.1: Flowchart of the developed kMC simulation software

Rand.h and Rand.cpp - random number generation

Pri vseh zadevah je zdravo tu pa tam obesiti vprašaj na vse, kar imaš že dolgo za samoumevno.

Bertrand Russell (1872-1970)

B

Extended summary in Slovene (Povzetek v slovenskem jeziku)

Lastnosti mnogih industrijsko pomembnih zlitin so močno odvisne od izločanja delcev drugih faz. Mehanske lastnosti mnogih jekel so odvisne od mikrostrukture karbidov, ki se pri visokih temperaturah izločajo iz avstenitne faze, pri nizkih pa iz feritne faze. Malooglјičnim jeklom, kot so na primer visokotrdna malo legirana (HSLA) jekla, se z dodatkom Nb, V ali Ti zviša napetost tečenja, z izločanjem karbidov teh elementov pa lahko vplivamo tudi na kinetiko rekristalizacije. Med zlitine, pri katerih igra izločevanje zelo pomembno vlogo, spada tudi skupina tehnološko zelo pomembnih Al zlitin z dodatkom Mg in Si (6xxx) in druge Al zlitine z dodatkom Cu, za katere je značilno kompleksno zaporedje tvorbe in razpada metastabilnih faz v odvisnosti od temperature, časa in kemične sestave zlitine. Za te zlitinske sisteme je bilo v preteklosti opravljenih veliko eksperimentalnih in teoretičnih študij. Še posebej velik napredek pri razumevanju izločevalnih mehanizmov je prinesel razvoj modernih preiskovalnih metod, kot so vrstična elektronska mikroskopija (SEM), presevna elektronska mikroskopija (TEM), rentgenska difrakcija (XRD), 3D tomografija z atomsko konico (3DAP), itn. Pri študiju izločanja v prenasičenih metastabilnih trdnih raztopinah ponavadi ločimo tri različne faze: *(i)* nukleacijo stabilnih gruč atomov izločene faze, *(ii)* difuzijsko rast nastalih gruč in *(iii)* nato še njihovo ogrobitev (Ostwaldovo zorenje) in koalescenco, ki vključuje rast večjih izločkov na račun manjših zaradi zmanjšanja površinske energije sistema. V realnih sistemih se ti trije idealizirani kinetični režimi največkrat prekrivajo, kar posledično zelo oteži interpretacijo rezultatov. Znano je, da je z ustrezno izbiro parametrov v okviru modelov, ki temeljijo na klasični teoriji nukleacije, mogoče zadovoljivo opisati časovni potek števila in velikosti izločkov v fazi njihove rasti in ogrobitve. Vendar ti modeli temeljijo na mnogih poenostavitvah in vprašljivih privzetkih kot na primer o sferičnosti in stehiometričnosti izločkov, da so površinske energije neodvisne od temperature in velikosti izločkov, itn. V obstoječih modelih je površinska energija ponavadi uporabljena kot prilagoditveni parameter. Poleg tega obstoječi modeli upoštevajo le rast izločkov nadkritične velikosti (večji od kali), medtem ko popolnoma zanemarijo vlogo velikega števila nestabilnih podkritičnih gruč (embriji). Le te zaradi nenehnega nastajanja in razpada celo v nenasičenih trdnih raztopinah tvorijo stacionarno porazdelitev, kar vpliva na kinetiko izločanja. Pri višjih temperaturah in/ali pri nizkih površinskih energijah lahko te gruče znatno vplivajo na koncentracijo raztopljenih atomov v zlitini, kar posledično vpliva tako na nukleacijo, kot tudi na rast in ogrobitev izločkov. Nasprotno pri atomističnih simulacijah, temelječih na eksplicitni obravnavi difuzije posameznih atomov, niso potrebne omenjene poenostavitve in predpostavke. Zato lahko atomistične simulacije kinetike izločanja v odvisnosti od temperature, časa in od kemične sestave pomembno prispevajo k globljemu razumevanju nastanka kali in nadaljne rasti. Simulacije izločanja na atomističnem nivoju so zato orodje z odlično sposobnostjo napovedovanja in v pomoč pri načrtovanju modernih zlitin z boljšimi lastnostmi, še posebej za sisteme pri ekstremnih pogojih (npr. ekstremni tlaki, temperature, radioaktivni elementi, itn), kjer je eksperimentalno delo zahtevno, težavno ali celo nemogoče.

V okviru naloge je poudarek na simulacijah dinamičnega razvoja sistema atomov. Razvoj atomističnih simulacij se je pričel v petdesetih in šestdesetih letih dvajsetega stoletja z molekularno dinamiko (MD), pri kateri integriramo Newtonove enačbe gibanja atomov po času. Zaradi upoštevanja termičnih nihanj atomov morajo biti pri MD integracijski koraki dovolj majhni, približno 10^{-15} s. Naslednja stopnja razvoja so bile metode izračuna elektronske strukture, z namenom dosega še bolj natančnih rezultatov, ki temeljijo na reševanju Schrödingerjeve enačbe, [4] in so dandanes znane kot *ab-initio*. Največkrat uporabljena metoda v znanosti o materialih je teorija gostotnih funkcionalov (DFT). Korenine DFT izhajajo iz Thomas-Fermijevega modela [5, 6], vendar so temelji postali trdni šele z Hohenberg-Kohnovimi izreki, [7]. Navkljub povečani natančnosti zaradi upoštevanja elektronske strukture, je slabost *ab-initio* metod potreba po izredno visoki računalniški moči. Za dosego še daljših časov, potrebnih za študij difuzijsko pogojenih procesov, so potrebne metode, ki omogočijo večje povprečenje. Atomistične simulacije, pri kateri je možno razširiti velikost in časovno skalo, so skupina Monte Carlo (MC) metod, ki so v uporabi od poznih štiridesetih let dvajsetega stoletja [10, 11]. Njihova uporaba se je začela v petdesith letih dvajsetega stoletja kot Metropolis Monte Carlo, kjer je časovni razvoj sistema pogojen z izračunom verjetnosti posameznega dogodka. MC metoda uporabljena v okviru te naloge je kinetična Monte Carlo (kMC) metoda, ki omogoča simulacije v realnem času. Metoda je primerna za študij kinetike nukleacije, saj ne zasleduje natančnih termičnih nihanj atomov, ampak difuzijske preskoke med stanji. To omogoča večje velikosti in časovne skale, pomembne pri študiju nukleacije in rasti izločkov v realnih zlitinah [12–38]. Naloga se osredotoča na uporabo kMC metode za podrobno proučevanje nukleacije, rasti, ogrobitve in koalescence izločkov, s posebnim poudarkom na kinetiki tvorbe in razpada nestabilnih gruč podkritičnih velikosti ter njihov vpliv na kinetiko izločanja, ki jih obstoječi modelu ne upoštevajo.

Delo je mogoče v grobem razdeliti na tri dele; in sicer na splošni uvod, teoretični del in modeliranje. Splošnemu uvodu, v katerem so zastavljeni cilji in metode, sledi teoretični pregled, v katerem so prestavljene klasična teorija nukleacije, osnove statistične mehanike s poudarkom na MC metodah in difuzijski model za simulacije izločanja z metodo kMC. V delu kjer je predstavljeno modeliranje so opisani posameznih zlitinski sistemi in njihova parametrizacija ter detajlno obdelani dobljeni rezultati simulacij. Zaključkom sledi dodatek v katerem je predstavljena shema izdelanega programa za simulacije. Razvit in izdelan program za simulacije omogoča študij difuzijskih faznih transformacij na atomistični skali. V okviru doktorske naloge so bile izvedene različne simulacije, s katerimi je bil ugotovljen vpliv temperature, kemične sestave, asimetrije medatomskih potencialov, mešalne energije in začetne mikrostrukture na kinetični razvoj izločkov in njihovo gostoto, volumski delež elementov, velikost in obliko izločkov, koncentracijske profile, parameter reda kratkega dosega in parsko korelacijsko funkcijo. Detajlna študija je bila najprej narejena na enostavnem binarnem modelu z telesno centrirano kristalno (t.c.k.) strukturo na Fe-Cu zlitinskem sistemu. Dobljene mikrostrukture so zelo podobne tipičnim mikrostrukturam pridobljenimi z 3D APT ali HRTEM. Ugotovljeno je bilo, da je vpliv mešalne energije na razvoj parametra reda kratkega dosega in števila izločkov podoben vplivu temperature. Zvišana mešalna energija pospeši izločanje in posledično zviša vrednosti parametra reda kratkega dosega. Nadalje, pri zvišani mešalni energiji je opaziti jasni območji rasti in ogrobljenja izločkov. Simulacije so pokazale, da sta izločanje in kinetične poti občutljivi na asimetričnost medatomskih potencialov, kar je bilo študirano z definicijo parametrov asimetrije. V doktorski nalogi je predlagan nov model za asimetrijo, ki poleg medatomskih energij upošteva tudi navidezne (ghost) energije med praznino in atomi. Pri negativnem parametru asimetrije prevladuje direktna koagulacija izločkov, medtem ko v primeru simetričnega modela in modela s pozitivnim parametrom asimetrije prevladuje Ostwaldovo zorenje. Časovni eksponenti za razvoj povprečnega radija izločkov, dobljeni iz simulacij, so bili za dolge čase primerjani z napovedmi LSW teorije. Razlike med LSW teorijo in dobljenimi rezultati so pripisane vplivom mobilnosti gruč. Nadalje je bilo ugotovljeno, da negativni parameter asimetrije povzroči povečanje časa simulacije za dosego enakega realnega časa. To je povezano z preferenčnim okoljem, kjer se zadržuje praznina ali tako imenovanemu efektu ujetja lete v bakrovih izločkih. Za podrobnejšo pojasnitev kinetike izločanja so bile izvedene računalniške simulacije, pri katerih so bili izločki predhodno zasejani v rahlo prenasičeno trdno raztopino. Namen študija je bil pojasnitev vpliva izločkov z različnimi začetnimi oblikami na obliko in velikost izločkov med njihovo rastjo. Vizualno opažene velike razlike med začetno sferično obliko in dobljenimi končnimi oblikami in velikostmi izločkov so bile dodatno preverjene še s pomočjo tenzorjev vztrajnostnih momentov izločkov. Mikrostrukture dobljene iz računalniških eksperimentov, izvedenih nad temperaturo topnosti Cu v železu pri kateri so bili v večjem številu prisotne gruče atomov podkritičnih velikosti (dvojčkov, trojčkov, ...) so bile uporabljene za določitev vpliva podkritičnih gruč na inkubacijski čas in hitrost nukleacije in rasti izločkov. V primeru prisotnosti večjih podkritičnih gruč (več kot pet atomov v gruči) je inkubacijski čas krajši in hitrost nukleacije in rasti manjša. Vpliv teh podkritičnih gruč se s časom izniči in tudi povprečna velikost izločkov je enaka, kot v primeru brez prisotnih večjih gruč. Dodatno je bil preverjen vpliv možnih periodičnosti na dobljene rezultate, saj so bili v vseh simulacijah uporabljeni popolni periodični robni pogoji. Ugotovljeno je bilo, da so rezultati pridobljeni s simulacijsko škatlo velikosti 40^3 t.c.k rešetk zadovoljivi in omogočajo ponovljivost. Vendar so bile uporabljene večje simulacijske škatle, da je bilo dobljeno večje število izločkov, kar omogoča natančnejšo statistično analizo dobljenih rezultatov.

Razviti paket za računalniške eksperimente je bil zastavljen tako, da omogoča dodajanje poljubnega števila kemijskih elementov in uporabo različne globine simulacijskih modelov (števila najbližjih sosedov). Sam model je bil preverjen na dveh ternarnih in eni kvaternarni zlitini z t.c.k kristalno strukturo. Kinetika izločanja v ternarnih Fe-Cu-Mn in Fe-Cu-Ni zlitinah ter kvaternarni Fe-Cu-Ni-Mn zlitini, je bila primerjana z rezultati predhodno simulirane binarne Fe-Cu zlitine. Pri temperaturi 873 K je bil spremljan razvoj parametra reda kratkega dosega in povprečna velikost izločkov. Ugotovljeno je bilo, da dodatek Ni in Mn atomov v zlitino, poveča inkubacijski čas za nukleacijo in ima vpliv na hitrost rasti izločkov. Najvišja hitrost rasti je bila opažena, v primeru ko je bil dodan samo Ni. Najnižja hitrost rasti je bila opažena v primeru, ko je bil dodan samo Mn, medtem ko je hitrost rasti izločkov je za kvaternarno zlitino leži med obema skrajnima vrednostma ternatnih zlitin med obema do sedaj omenjenima v primeru kvaternarnega sistema.

Za simulacije razmešanja je bil razvit simulacijski paket nadgrajen tako, da omogoča simulacije tudi za zlitine s ploskovno centrirano kristalno strukturo. Z njim so bili narejeni računalniški eksperimenti na zlitini Ni-Cr-Al pri 873 K. Pri tej temperaturi sta bila zaznana dva tipa γ' faze, in sicer Ni_3Al in Ni_3Cr, kar je v skladu s 3D APT eksperimenti iz literature. Simulacije so pokazale, da se delež Ni_3Al vseskozi povečuje s časom, medtem ko delež Ni_3Cr najprej narašča in nato po dosegu največje vrednosti začne padati. Za detekcijo teh dveh faz sta bili razviti in testirani dve metodi. Pri prvi so bile faze določene na podlagi izračuna povprečnih koncentracij okoli iskanih elementov, druga pa temelji na natančni določitvi točno določene kristalne strukture. Dobljeni delež in položaj faz se za obe metodi razlikuje, zaradi česar je potrebna posebna previdnost pri analizi podatkov tako računalniških simulacij, kot tudi rezultatov eksperimentov z atomsko konico. Namreč, pri eksperimentih z atomsko konico se delež posameznih faz določa na osnovi povprečnih koncentracij.

Zmožnosti razvitega simulacijskega paketa so bile preverjene tudi s simulacijami kinetike izločanja v zlitinah, z atomi legirnih elementov na intersticijskih in substitucijskih mestih kristalne mreže in sicer z uporabo Fe-C zlitinskega sistema. Čeprav kot pričakovano Fe_3C faze in mogoče reproducirati s približkom toge mreže, sta bili reproducirani mnogo hitrejša difuzija intersticijskih elementov in počasnejša difuzija substitucijskih elementov. Za ta primer so bile izračunane parske korelacijske funkcije za začetno neurejeno stanje in dve poznejši stanji. Ugotovljeno je bilo, da ogljikovi pari tvorijo vezi na mestu tretjih najbližjih sosedov, kar je pričakovano in v skladu z izbranimi interakcijskimi energijami.

V okviru doktorske naloge razviti model temelji na upoštevanju navideznih (ghost) energij med praznino in atomi, in sicer preko definicije asimetrije medatomskih potencialov. Kohezivna enegija topljneca je bila uporabljena kot prilagoditveni parameter, pri čemer smo v modelu zahtevali ohranitev energije mešanja, saj slednja določa obliko faznega diagrama. Na podlagi tega modela je bila za dano asimetrijo medatomskih potencialov določena celotna energetika. V pričujočem delu smo upoštevali prve in druge najbližje sosede danega atoma, sam model pa omogoča določitev celotne energetike do n-tih sosedov, kjer je n poljubno naravno število. V primeru izbire simetričnih medatomskih potencialov, nam model da podobne vrednosti energetike, kot jih najdemo v literaturi.

Iz predstavljenih rezultatov je mogoče ugotoviti, da je glavni cilj te naloge, ki je bil uporabiti difuzijski model za simulacije s kinetično Monte Carlo metodo, ki temelji na eksplicitni obravnavi difuzije posameznih atomov brez dodatnih poenostavitev in predpostavk, značilnih za klasične teorije nukleacije, rasti in ogrobitve, uspešno dosežen. Razviti model je mogoče uporabiti kot napovedno orodje in omogoča natančno napovedovanje kinetike izločanja v odvisnosti od temperature, kemične sestave in začetne mikrostrukture. Nadalje je bil s predlaganim pristopom študiran vpliv gruč atomov podkritične velikosti na inkubacijski čas ter hitrost nukleacije in rasti izločkov. Ugotovljeno je bilo, da je mobilnost gruč atomov močno odvisna od asimetrije medatomskih potencialov. Negativna asimetrija vpliva na povečanje mobilnosti gruč atomov, pri čemer lahko njihova mobilnost preseže mobilnost monomerov, kar smo pripisali ujetju vakance v gručo. Povečana mobilnost teh podkritičnih gruč atomov, vpliva na skrajšanje inkubacijskega časa za nukleacijo, zmanjšanje hitrosti nukleacije, vpliva pa tudi na mehanizem rasti izločkov. Slednji zaradi povečanja mobilnosti gruč poteka manj z kondenzacijo posameznih atomov in v vse večji meri z združevanjem posameznih gruč.

Seznam količin in procesov, ki jih je mogoče z razvitim atomističnim modelom simulirati brez bistvenih izboljšav ali prilagoditev, pa ni bil obravnavan, ker bi takšna obravnava presegla zastavljene naloge, je naslednji:

- Hitrost ohlajanja ima velik vpliv na mikrostrukturo in posledično na mehanske lastnosti. Razviti model je bil uporabljen za izotermne simulacije. Z nekaterimi prilagoditvami bi ga bilo mogoče nadgraditi za neizotermne simulacije.
- Predstavljen in uporabljen difuzijski model ne potrebuje posebnih predpostavk značilnih za fenomenološke modele. Pri večkomponentnih zlitinah ostali klasični modeli ponavadi zanemarijo nediagonalne komponente Onsagerjeve matrike. Difuzijska matrika je v splošnem nediagonalna in zanemarjeni členi lahko vplivajo na kinetične poti posameznih elementov. Z dodatnimi nadgradnjami simulacijskega programa in programov za analizo rezultatov, bi bil omogočen izračun vseh komponent difuzijske matrike iz rezultatov kMC simulacij.

Z nekaterimi izboljšavami, bi bilo mogoče v prihodnosti izdelati še bolj realističen model, za kar je potrebno sledeče:

- Uporabljeni potenciali so bili enostavni. Nadaljnja izboljšava bi bila izračun potencialov z metodami za funkcionale elektonske gostote. Za še bolj natančne kinetične poti, pa bi bile potrebne celovite atomske relaksacije odvisne od medatomskih razdalj.
- Izračun medatomskih energij v odvisnosti od položaja atomov z metodami za funkcionale elektonske gostote zahteva ogromno računalniško moč. Možna izboljšava je uporaba optimiziranih energij, pridobljenih z uporabo nevronskih mrež na bazenu velikega števila predhodno izračunanih primerov.
- V doktorskem delu je bila predpostavljena popolna koherentnost izločkov z matrico, kar v primeru izločanja cementita ne drži. Elastične napetosti, ki nasta-

nejo pri izgubi koherentnosti lahko vplivajo na dobljene rezultate, zato bi bilo potrebno izboljšati neskladja kristalnih struktur, ki nastanejo pri izgubi koherentnosti izločkov.

- Čas tipične simulacije je precej dolg. Nekaj korakov je bilo narejenih v smeri paralelizacije, vendar so na temu področju ostale še precejšne možnosti za izboljšave.

References

[1] Baker, H., ed., *ASM Handbook Volume 3: Alloy Phase Diagrams.* ASM International, 10 ed., December 1992. 1, 78

[2] Alder, B. J. and Wainwright, T. E., "Studies in Molecular Dynamics. I. General Method," *Journal of Chemical Physics*, vol. 31, no. 2, pp. 459–466, 1959. 3, 38

[3] Rahman, A., "Correlations in the motion of atoms in liquid argon," *Physical Review*, vol. 136, pp. A405–A411, Oct 1964. 3

[4] Schrödinger, E., "An Undulatory Theory of the Mechanics of Atoms and Molecules," *Physical Review*, vol. 28, pp. 1049–1070, Dec 1926. 4, 166

[5] Thomas, L., "The calculation of atomic fields," *Mathematical Proceedings of the Cambridge Philosophical Society*, vol. 23, pp. 524–548, 1927. 4, 166

[6] Fermi, E., "Un metodo statistico per la determinazione di alcune priopprieta dell'atomo," *Rendiconti Accademia Nazionale dei Lincei*, vol. 6, pp. 602–607, 1927. 4, 166

[7] Hohenberg, P. and Kohn, W., "Inhomogeneous electron gas," *Physical Review*, vol. 136, pp. B864–B871, Nov 1964. 4, 68, 166

[8] Kohn, W. and Sham, L. J., "Self-Consistent Equations Including Exchange and Correlation Effects," *Physical Review*, vol. 140, p. A1138, Nov 1965. 4

[9] Car, R. and Parrinello, M., "Unified Approach for Molecular Dynamics and Density-Functional Theory," *Physical Review Letters*, vol. 55, no. 22, pp. 2471–2474, 1985. 4, 38

[10] Metropolis, N. and Ulam, S., "The monte carlo method," *Journal of the American Statistical Association*, vol. 44, pp. 335–341, Sep 1949. 4, 52, 166

[11] Metropolis, N., Rosenbluth, A. W., Rosenbluth, M. N., Teller, A. H. and Teller, E., "Equation of State Calculations by Fast Computing Machines," *Journal of Chemical Physics*, vol. 21, no. 6, pp. 1087–1092, 1953. 4, 52, 57, 58, 166

[12] Soisson, F., Barbu, A. and Martin, G., "Monte Carlo simulations of copper precipitation in dilute iron-copper alloys during thermal ageing and under electron irradiation," *Acta Materialia*, vol. 44, no. 9, pp. 3789–3800, 1996. 4, 57, 78, 83, 167

[13] Athènes, M., Bellon, P., Martin, G. and Haider, F., "A Monte-Carlo study of B2 ordering and precipitation via vacancy mechanism in b.c.c. lattices," *Acta Materialia*, vol. 44, no. 12, pp. 4739–4748, 1996. 57

[14] Liu, C. L., Odette, G. R., Wirth, B. D. and Lucas, G. E., "A lattice Monte Carlo simulation of nanophase compositions and structures in irradiated pressure vessel Fe-Cu-Ni-Mn-Si steels," *Materials Science and Engineering: A*, vol. 238, no. 1, pp. 202–209, 1997. 57, 78

[15] Pareige-Schmuck, C., Soisson, F. and Blavette., D., "Ordering and phase separation in low supersaturated Ni-Cr-Al alloys: 3D atom probe and Monte Carlo simulation," *Materials Science and Engineering A*, vol. 250, no. 1, pp. 99–103, 1998. 57, 140

[16] Pareige, C., Soisson, F., Martin, G. and Blavette., D., "Ordering and phase separation in Ni-Cr-Al: Monte Carlo simulations vs three-dimensional atom probe," *Acta Materialia*, vol. 47, no. 6, pp. 1889–1899, 1999. 57, 140, 141, 144, 148

[17] Athènes, M., Bellon, P. and Martin, G., "Effects of atomic mobilities on phase separation kinetics: a Monte-Carlo study," *Acta Materialia*, vol. 48, no. 10, pp. 2675–2688, 2000. 34, 57, 102

[18] Soisson, F. and Martin, G., "Monte Carlo simulations of the decomposition of metastable solid solutions: Transient and steady-state nucleation kinetics," *Physical Review B*, vol. 62, pp. 203–214, Jul. 2000. 78, 83, 84

[19] Pareige, C. and Blavette, D., "Simulation of the FCC → FCC + $L1_2$ + DO_{22} kinetic reaction," *Scripta Materialia*, vol. 44, no. 2, pp. 243–247, 2001. 57

[20] Schmauder, S. and Binkele, P., "Atomistic computer simulation of the formation of Cu-precipitates in steels," *Computational Materials Science*, vol. 24, pp. 42–53, 2002. 33, 57, 72, 73, 74, 78

[21] Binkele, P. and Schmauder, S., "An atomiscit Monte Carlo simulation of precipitation in a binary system," *Zeitschrift für Metallkunde*, vol. 94, no. 8, pp. 858–863, 2003.

[22] Khrushcheva, O., Zhurkin, E. E., Malerba, L., Becquart, C. S., Domain, C. and Hou, M., "Copper precipitation in iron: a comparison between metropolis monte carlo and lattice kinetic monte carlo methods," *Nuclear Instruments and Methods in Physics Research B*, vol. 202, pp. 68–75, 2003. 57, 72

[23] Clouet, E., Nastar, M. and Sigli, C., "Nucleation of Al_3Zr and Al_3Sc in aluminum alloys: From kinetic Monte Carlo simulations to classical theory," *Physical Review B*, vol. 69, p. 064109, 2004. 57

[24] Sha, G. and Cerezo, A., "Kinetic Monte Carlo simulation of clustering in an Al–Zn–Mg–Cu alloy (7050)," *Acta Materialia*, vol. 53, pp. 907–917, February 2005. 57, 72

[25] Clouet, E., Hin, C., Gendt, D., Nastar, M. and Soisson, F., "Kinetic monte carlo simulations of precipitation," *Advanced Engineering Materials*, vol. 8, pp. 1210–1214, December 2006.

[26] Clouet, E., Laé, L., Épicier, T., Lefebvre, W., Nastar, M. and Deschamps, A., "Complex precipitation pathways in multicomponent alloys," *Nature Materials*, vol. 5, no. 6, pp. 482–488, 2006. 57

[27] Gendt, D., Maugis, P., Martin, G., Nastar, M. and Soisson, F., "Monte Carlo Simulation of NbC Precipitation Kinetics in α-Fe," *Defect and Diffusion Forum*, vol. 194–199, pp. 1779–1786, 2001. 70

[28] Gendt, D., *Cinétiques de précipitation du carbure de niobium dans la ferrite (Kinetics of Niobium Carbide precipitation in Ferrite)*. PhD thesis, Université de Paris 11, Orsay, 2001. 57, 70, 72, 74, 75, 152

[29] Binkele, P., Kizler, P. and Schmaudel, S., "Atomistic Monte Carlo simulation of the diffusion of P and C neat grain boundaries in bcc iron," in *30. MPA-Seminar 'Safety and reliability in energy technology' in conjunction with the 9th German-Japanese seminar, Volume 1* (Roos, E., ed.), (Stuttgart), pp. 25.1–25.22, Staatliche Materialprüfungsanstalt (MPA) Universität Stuttgart, 6-7 October 2004.

[30] Binkele, P., Kizler, P. and Schmaudel, S., "Atomistic kinetic monte carlo simulations of segregation of phosphorus and carbon at grain boundaries in bcc-iron." 2007.

[31] Mao, Z., Sudbrack, C. K., Yoon, K. E., Martin, G. and Seidman, D. N., "The mechanism of morphogenesis in a phase-separating concentrated multicomponent alloy," *Nature Materials*, vol. 6, pp. 210–216, 2007. 57, 140, 148

[32] Hin, C., Bréchet, Y., Maugis, P. and Soisson, F., "Kinetics of heterogeneous dislocation precipitation of NbC in alpha-iron," *Acta Materialia*, vol. 56, no. 19, pp. 5535–5543, 2008. 57, 70, 72

[33] Hin, C., Bréchet, Y., Maugis, P. and Soisson, F., "Kinetics of heterogeneous grain boundary precipitation of NbC in α-iron: A monte carlo study," *Acta Materialia*, vol. 56, no. 19, pp. 5653–5667, 2008. 57, 70, 72, 74, 75

[34] Hin, C., Brechet, Y., Maugis, P. and Soisson, F., "Heterogeneous precipitation on dislocations: effect of the elastic field on precipitate morphology," *Philosophical Magazine*, vol. 88, pp. 1555–1567, April 2008. 57

[35] Hin, C., "Kinetics of heterogeneous grain boundary precipitation of Ni_3Al in nickel alloy," *Journal of Physics D: Applied Physics*, vol. 42, no. 22, p. 225309, 2009. 57, 74, 75, 140, 148

[36] Hin, C., Wirth, B. D. and Neaton, J. B., "Formation of Y_2O_3 nanoclusters in nanostructured ferritic alloys during isothermal and anisothermal heat treatment: A kinetic Monte Carlo study," *Physical Review B*, vol. 80, p. 134118, Oct 2009. 57, 70, 74, 75

[37] Hin, C. and Wirth, B., "Formation of oxide nanoclusters in nanostructured ferritic alloys during anisothermal heat treatment: A kinetic Monte Carlo study," *Materials Science and Engineering A*, vol. 528, pp. 2056–2061, 2011. 57, 70

[38] Mao, Z., Booth-Morrison, C., Sudbrack, C. K., Martin, G. and Seidman, D. N., "Kinetic pathways for phase separation: An atomic-scale study in Ni-Al-Cr alloys," *Acta Materialia*, vol. 60, pp. 1871–1888, February 2012. 4, 57, 140, 148, 167

[39] Gibbs, J. W., "On the equilibrium of heterogeneous substances," *Transactions of the Connecticut Academy of Arts and Sciences*, vol. 3, pp. 108–248 and 343–524, 1874 and 1877. 7

[40] Slezov, V. V., *Kinetics of First-order Phase Transitions.* Weinheim: Wiley-VCH Verlag, 2009. 8, 16

[41] Volmer, M. and Weber, A., “Kiembildung in Übersättigen Gebilden (Germ-formation in oversaturated figures),” *Zeitschrift für Physikalische Chemie*, vol. 119, no. 3/4, pp. 277–301, 1926. 8, 17

[42] Farkas, L., “Keimbildungsgeschwindigkeit in übersättigten Dämpfen (The speed of germinitive formation in over saturated vapours),” *Zeitschrift für Physikalische Chemie*, vol. 125, no. 3/4, pp. 236–242, 1927. 8, 16

[43] Becker, R. and Döring, W., “Kinetische behandlung der keimbildung in übersättigten Dämpfern (Kinetic treatment of germ formation in supersaturated vapour),” *Annalen der Physik*, vol. 24, no. 8, pp. 719–752, 1935. 8, 17

[44] Zeldovich, Y. B., “On the theory of new phase formation: Cavitation (Eng. Transl.),” *Zhurnal eksperimentalnoi i teoreticheskoi fiziki (Journal of Experimental and Theoretical Physics)*, vol. 12, no. 11/12, p. 525–538, 1942. 8, 17

[45] Kampmann, R. and Wagner, R., *Decomposition of alloys: the early stages*, ch. Kinetics of precipitation in metastable binary alloys - theory and application to Cu-1.9 at% Ti and Ni-14 at% Al, pp. 91–103. Pergamon Press, 1984. 8, 17

[46] Christian, J. W., *The Theory of Transformations in Metals and Alloys.* Pergamon, 3rd ed., 2002. 9, 10, 24

[47] Doherty, R. D., *Physical Metallurgy*, ch. Diffusive phase transformations in the solid state, p. 2888. North Holland, 4th ed., 1996. 9

[48] Fultz, B. and Hoyt, J. J., *Alloy Physics*, ch. Phase Equilibria and Phase Transformations, p. 1003. Wiley-VCH, 2007. 11, 39, 40

[49] Reed-Hill, R. E. and Abbaschian, R., *Physical Metallurgy Principles.* PWS Publishing Company, 3rd ed., 1994. 11, 13

[50] Porter, D. A. and Esterling, K. E., *Phase Transformations in Metals and Aloys.* Chapman and Hall, 2nd ed., 1992. 11, 28

[51] Cahn, J. W., “The kinetics of grain boundary nucleated reactions,” *Acta Metallurgica*, vol. 4, no. 5, pp. 449–459, 1956. 14

[52] Kashchiev, D., *Nucleation: basic theory with applications.* 978-0750646826: Butterworth-Heinemann, 2000. 16

[53] Kelton, K. F. and Greer, A. L., *Nucleation in Condensed Matter.* Pergamon, 2010. 16

[54] Philbert, J., “One and a half century of diffusion: Fick, Einstein, before and beyond,” *Diffusion Fundamentals*, vol. 2, pp. 1.1–1.10, 2005. 18

[55] Allnatt, A. R. and Lidiard, A. B., *Atomic Transport in Solids.* Cambridge University Press, 2003. 19

[56] Belova, I. V. and Murch, G. E., *Cellular and Porous Materials: Thermal Properties Simulation and Prediction*, ch. Thermal Properties of Composite Materials and Porous Media: Lattice-Based Monte Carlo Approaches, p. 439. Wiley-VCH, 2008. 19, 24

[57] Smigelskas, A. D. and Kirkendall, E. O., “Zinc Diffusion in Alpha Brass,” *Transactions of the American Institute of Mining, Metallurgical and Petroleum Engineers*, vol. 171, pp. 130–142, 1947. 19, 20

[58] Huntington, H. B. and Seitz, F., “Mechanism for Self-Diffusion in Metallic Copper,” *Physical Review*, vol. 61, pp. 315–325, Mar 1942. 19

[59] Huntington, H. B., “Self-Consistent Treatment of the Vacancy Mechanism for Metallic Diffusion,” *Physical Review*, vol. 61, pp. 325–338, Mar 1942. 19

[60] Fick, A., “V. On liquid diffusion,” *Philosophical Magazine Series 4*, vol. 10, no. 63, pp. 30–39, 1855. 20

[61] Mehrer, H., Bakker, H., Bonzel, H. P., Bruff, C. M., Dayananda, M. A., Gust, W., Horvath, J., Kaur, I., Kidson, G. V., LeClaire, A. D., Mehrer, H., Murch, G. E., Neumann, G., Stolica, N. and Stolwijk, N. A., *Diffusion in Solid Metals and Alloys*, vol. 26 of *Landolt-Börnstein.* Springer, 1990. 20

[62] Balluffi, R. W., Allen, S. M. and Carter, W. C., *Kinetics of Materials.* Wiley-Interscience, 2005. 20

[63] Wert, C. and Zenner, C., “Interstitial atomic diffusion coefficients,” *Physical Review*, vol. 76, no. 8, pp. 1169–1175, 1949. 21

[64] Vineyard, G. H., “Frequency factors and isotope effects in solid state rate processes,” *Journal of Physics and Chemistry of Solids*, vol. 3, pp. 121–127, 1957.

[65] Sólyom, J. and Piróth, A., *Fundamentals of the Physics of Solids: Structure and dynamics.* Fundamentals of the Physics of Solids, Springer, 2007. 21

[66] Flynn, C. P., *Point defects and diffusion.* Clarendon Press Oxford, 1972. 21

[67] Voter, A. F., *Radiation Effects in Solids*, ch. Introduction to the Kinetic Monte Carlo Method, p. 24. NATO Science Series, Springer, 2007. 22

[68] Dove, M. T., *Introduction to Lattice Dynamics.* Cambridge topics in Mineral Physics and Chemistry, Cambridge University Press, 1993. 22

[69] Jackson, K. A., *Kinetic Processes: Crystal Growth, Diffusion, and Phase Transitions in Materials.* Wiley-VCH, 2004. 23

[70] Everett, D. H., “Manual of Symbols and Terminology for Physicochemical Quantities and Units, Appendix II: Definitions, Terminology and Symbols in Colloid and Surface Chemistry,” *Pure and Applied Chemistry*, vol. 31, no. 4, pp. 577–638, 1972. 23

[71] Einstein, A., *On the Movement of Small Particles Suspended in a Stationary Liquid Demanded by the Molecular-Kinetic Theory of Heat.* Dover Publications, 1956. 23

[72] Einstein, A., “Über die von der molekularkinetischen Theorie der Wärme geforderte Bewegung von in ruhenden Flüssigkeiten suspendierten Teilchen,” *Annalen der Physik*, vol. 322, no. 8, pp. 549–560, 1905. 23

[73] Limoge, Y. and Bocquet, J. L., “Temperature behavior of tracer diffusion in amorphous materials: A random-walk approach,” *Physical Review Letters*, vol. 65, pp. 60–63, Jul 1990. 23

[74] Murch, G. E., *Materials Science and Technology: Phase Transformations in Materials*, vol. 5, ch. Diffusion in Crystaline Solids, p. 649. Wiley-WCH, 1996. 24

[75] Kempen, A. T., Sommer, F. and Mittemeijer, E. J., “The kinetics of the austenite–ferrite phase transformation of Fe-Mn: differential thermal analysis during cooling,” *Acta Materialia*, vol. 50, no. 14, pp. 3545–3555, 2002. 24

[76] Ostwald, W., *Lehrbuch der Allgemeinen Chemie*, vol. 2, part 1. Leipzig, Germany: W. Engelmann, 1896. 25, 29

[77] Ratke, L. and Voorhees, P. W., *Growth and Coarsening: Ostwald Ripening in Material Processing.* Springer, 2002. 25

[78] Zener, C., "Theory of Growth of Spherical Precipitates from Solid Solution," *Journal of Applied Physics*, vol. 20, no. 10, pp. 950–953, 1949. 26, 27

[79] Frank, F. C., "Radially Symmetric Phase Growth Controlled by Diffusion," *Proceedings of the Royal Society of London. Series A. Mathematical and Physical Sciences*, vol. 201, no. 1067, pp. 586–599, 1950. 27

[80] Ham, F. S., "Theory of diffusion-limited precipitation," *Journal of Physics and Chemistry of Solids*, vol. 6, no. 4, pp. 335–351, 1958. 28

[81] Horvay, G. and Cahn, J. W., "Dendritic and spheroidal growth," *Acta Metallurgica*, vol. 9, no. 7, pp. 695 – 705, 1961. 28

[82] Hilert, M., "Role of interfacial energy during solid–state phase transformations," *Jernkontorets Annaler*, vol. 141, pp. 757–789, 1957. 28

[83] Perez, M., "Gibbs-Thomson effects in phase transformations," *Scripta Materialia*, vol. 52, pp. 709–12, 2005. 28

[84] Lifshitz, I. M. and Slyozov, V. V., "The kinetics of precipitation from supersaturated solid solutions," *Journal of Physics and Chemistry of Solids*, vol. 19, pp. 35–50, 1961. 29, 30

[85] Wagner, C., "Theorie der Alterung von Niederschlägen durch Umlösen (Ostwald-Reifung)," *Zeitschrift für Elektrochemie, Berichte der Bunsengesellschaft für physikalische Chemie*, vol. 65, pp. 581–591, 1961. 29, 30

[86] Bray, A. J., "Theory of phase-ordering kinetics," *Advances in Physics*, vol. 51, pp. 481–587, 2002. 30

[87] Kahlweit, M., "Ostwald ripening of precipitates," *Advances in Colloid and Interface Science*, vol. 5, no. 1, pp. 1–35, 1975. 30

[88] Speight, M. V., "Growth kinetics of grain-boundary precipitates," *Acta Metallurgica*, vol. 16, no. 1, pp. 133–135, 1968. 32

[89] Kreye, H., "Einfluß von Versetzungen auf die Umlösung von Teilchen," *Zeitschrift für Metallkunde*, vol. 61, pp. 108–112, 1970. 32

[90] Ardell, A. J., "On the coarsening of grain boundary precipitates," *Acta Metallurgica*, vol. 20, no. 4, pp. 601–609, 1972. 32

[91] Ossi, P. M., *Disordered Materials.* Springer Berlin Heidelberg, 2006. 32

[92] Binder, K. and Müller-Krumbhaar, H., "Investigation of metastable states and nucleation in the kinetic Ising model," *Physical Review B*, vol. 9, pp. 2328–2353, Mar 1974. 33, 34

[93] Hoshen., J. and Kopelman, R., "Percolation and cluster distribution. i. Cluster multiple labeling technique and critical concentration algorithm," *Physical Review B*, vol. 14, pp. 3438–3445, Oct 1976. 33, 85

[94] Volmer, M., *Kinetik der Phasenbildung.* Dresden: T. Steinkopff, 1939. 33

[95] Nishioka, K., "Kinetic and thermodynamic definitions of the critical nucleus in nucleation theory," *Physical Review E*, vol. 52, pp. 3263–3265, Sep 1995. 33

[96] Roussel, J.-M. and Bellon, P., "Vacancy-assisted phase separation with asymmetric atomic mobility: Coarsening rates, precipitate composition, and morphology," *Physical Review B*, vol. 63, p. 184114, Apr 2001. 34, 102

[97] Family, F. and Meakin, P., "Scaling of the Droplet-Size Distribution in Vapor-Deposited Thin Films," *Physical Review Letters*, vol. 61, pp. 428–431, Jul 1988. 34

[98] Allen, M. P. and Tildesley, D. J., *Computer Simulation of Liquids.* Oxford University Press, 1987. 34, 35, 53

[99] Frenkel, D. and Smit, B., *Understanding Molecular Simulation: From Algorithms to Applications.* Computational science, Academic Press, 2002. 35, 53

[100] Hansen, J.-P. and McDonald, I. R., *Theory of Simple Liquids.* Academic Press, 3$^{\text{rd}}$ ed., 2006. 35, 36

[101] Cowley, J. M., "An Approximate Theory of Order in Alloys," *Physical Review*, vol. 77, pp. 669–675, Mar 1950. 36

[102] Ducastelle, F., *Order and phase stability in alloys.* Cohesion and structure, Amsterdam: North-Holland, 1991. 36, 80

[103] Yip, S., *Handbook of Materials Modeling*, vol. 1 and 2 of *Theoretical, Mathematical and Computational Physics.* Dordrecht: Springer, 2005. 40

[104] Clouet, E., Barbu, A., Laé, L. and Martin, G., "Precipitation kinetics of Al_3Zr and Al_3Sc in aluminum alloys modeled with cluster dynamics," *Acta Materialia*, vol. 53, no. 8, pp. 2313–2325, 2005. 40

[105] Barbu, A. and Clouet, E., "Cluster dynamics modeling of materials: advantages and limitations," *Solid State Phenomena*, vol. 129, pp. 51–58, 2007. 40

[106] Raabe, D., *Computational Materials Science: the simulation of materials, microstructures and properties.* Wiley-VCH, 1998. 42

[107] Cahn, J. W. and Hilliard, J. E., "Free Energy of a Nonuniform System. I. Interfacial Free Energy," *Journal of Chemical Physics*, vol. 28, no. 2, pp. 258–267, 1958. 42

[108] Allen, S. M. and Cahn, J. W., "A microscopic theory for antiphase boundary motion and its application to antiphase domain coarsening," *Acta Metallurgica*, vol. 27, no. 6, pp. 1085–1095, 1979. 42

[109] Onsager, L., "Reciprocal Relations in Irreversible Processes. I.," *Physical Review*, vol. 37, pp. 405–426, Feb 1931. 42

[110] Onsager, L., "Reciprocal Relations in Irreversible Processes. II.," *Physical Review*, vol. 38, pp. 2265–2279, Dec 1931. 42

[111] Landau, L. D., "Theory of phase changes. I," *Physikalische Zeitschrift der Sowjetunion*, vol. 11, pp. 26–47, 1937. 42

[112] Landau, L. D., "Theory of phase transformation. II," *Physikalische Zeitschrift der Sowjetunion*, vol. 11, pp. 545–555, 1937. 42

[113] Boltzmann, L. E., *Lectures on Gas Theory; Translated by S.G. Brush.* Berkley and Los Angeles: University of California Press, 1964. 43, 44, 46

[114] Guénault, T., *Statistical Physics.* Springer Verlag, 2^{nd} ed., 2007. 44

[115] Bovier, A., *Statistical Mechanics of Disordered Systems; A Mathematical Perspective.* Cambridge University Press, 2006.

[116] Landau, D. P. and Binder, K., *A Guide to Monte Carlo Simulations in Statistical Physics.* Cambridge University Press, 3^{rd} ed., 2009. 44, 50, 53, 58

[117] Gibbs, J. W., *Elementary Principles of Statistical Mechanics.* New York: Charles Scribner's Sons, 1902. 44

[118] Clausius, R., *The mechanical theory of heat: with its applications to the steam-engine and to the physical properties of bodies.* J. Van Voorst, 1867. 46

[119] Ising, E., "Beitrag zur Theorie des Ferromagnetismus," *Zeitschrift für Physik A Hadrons and Nuclei*, vol. 31, no. 1, pp. 253–258, 1925. 51

[120] Onsager, L., "Crystal Statistics. I. A Two-Dimensional Model with an Order-Disorder Transition," *Physical Review*, vol. 65, pp. 117–149, Feb 1944. 51

[121] Stanley, H. E., *Introduction To Phase Transitions and Critical Phenomena.* Oxford University Press, 1987. 51

[122] Zinn-Justin, J., *Phase Transitions and Renormalization Group.* Oxford University Press, 2007. 51

[123] Born, M. and von Karman, T., "Über Schwingungen in Raumgittern," *Physikalische Zeitschrift*, vol. 13, p. 297, 1912. 52

[124] Newman, M. E. J. and Barkema, G. T., *Monte Carlo Methods in Statistical Physics.* New York: Oxford University Press, 2001. 53

[125] Kratzer, P., *Multi-scale Simulation Methods in Molecular Sciences*, vol. 42 of *NIC Series*, ch. Monte Carlo and kinetic Monte Carlo methods, p. 26. Institute for Advanced Simulation, Forschungszentrum Jülich, 2009. 56

[126] Fichthorn, K. A. and Weinberg, W. H., "Theoretical foundations of dynamical Monte Carlo simulations," *Journal of Chemical Physics*, vol. 95, no. 2, pp. 1090–1096, 1991. 56

[127] Young, W. M. and Elcock, E. W., "Monte Carlo studies of vacancy migration in binary ordered alloys: I," *Proceedings of the Physical Society*, vol. 89, p. 735, 1966. 57, 60

[128] Bortz, A. B., Kalos, M. H. and Lebowitz, J. L., "A new algorithm for Monte Carlo simulation of Ising spin systems," *Journal of Computational Physics*, vol. 17, no. 1, pp. 10–18, 1975.

[129] Gillespie, D. T., "A general method for numerically simulating the stochastic time evolution of coupled chemical reactions," *Journal of Computational Physics*, vol. 22, pp. 403–434, 1976. 57, 60

[130] Yaldram, K. and Binder, K., "Monte Carlo simulation of phase separation and clustering in the ABV model," *Journal of Statistical Physics*, vol. 62, no. 1-2, pp. 161–175, 1991. 57

[131] Fratzl, P. and Penrose, O., "Kinetics of spinodal decomposition in the Ising model with vacancy diffusion," *Physical Review B*, vol. 50, pp. 3477–3480, Aug 1994. 57

[132] Binkele, P., *Atomistische Modellierung und Computersimulation der Ostwald-Reifung von Ausscheidungen beim Einsatz von kupferhaltigen Stählen.* PhD thesis, Institut für Materialprüfung, Werkstoffkunde und Festigkeitslehre (IMWF); Universität Stuttgart, 2006. 57, 72, 73, 78, 122

[133] Glauber, R. J., "Time-Dependent Statistics of the Ising Model," *Journal of Mathematical Physics*, vol. 4, no. 2, p. 294, 1963. 59

[134] Kawasaki, K., "Diffusion Constants near the Critical Point for Time-Dependent Ising Models. I," *Physical Review*, vol. 145, pp. 224–230, May 1966. 59

[135] Soisson, F., Becquart, C. S., Castin, N., Domain, C., Malerba, L. and Vincent, E., "Atomistic Kinetic Monte Carlo studies of microchemical evolutions driven by diffusion processes under irradiation," *Jounal of Nuclear Materials*, vol. 406, pp. 55–67, 2010. 62, 68, 72, 78

[136] Le Bouar, Y. and Soisson, F., "Kinetic pathways from embedded-atom-method potentials: Influence of the activation barriers," *Physical Review B*, vol. 65, no. 9, pp. 94–103, 2002. 67, 71, 72, 73, 74, 75

[137] Le Bouar, Y. and Walle, S., "Diffusion in dilute $Fe_{1-x}Cu_x$ alloys: Comparison between a rigid lattice model and static EAM simulations," *Defect Diffusioun Forum*, vol. 194–199, pp. 139–144, 2001. 67, 71, 78

[138] Martin, G. and Soisson, F., *Handbook of Materials Modeling*, vol. 2 of *Theoretical, Mathematical and Computational Physics*, ch. Kinetic Monte Carlo Method to Model Diffusion Controlled Phase Transformations in the Solid State, p. 26. Dordrecht: Springer, 2005. 68, 72

[139] Geuser, F. D., Gable, B. M. and Muddle, M. C., "CALPHAD based kinetic Monte Carlo simulation of clustering in binary Al-Cu alloy," *Philosophical Magazine*, vol. 91, no. 2, pp. 315–336, 2011. 68

[140] Xu, L. and Henkelman, G., "Adaptive kinetic monte carlo for first-principles accelerated dynamics," *Journal of Chemical Physics*, vol. 129, no. 11, p. 114104, 2008. 68

[141] Bleda, E., Gao, X. and Daw, M. S., "Calculations of diffusion in FCC binary alloys using on-the-fly kinetic Monte Carlo," *Computational Materials Science*, vol. 43, no. 4, pp. 608–615, 2008.

[142] Xu, H., Osetsky, Y. N. and Stoller, R. E., "Simulating complex atomistic processes: On-the-fly kinetic Monte Carlo scheme with selective active volumes," *Physical Review B*, vol. 84, no. 13, p. 132103, 2011. 68

[143] Gupta, H., Weinkamer, R., Fratzl, P. and Lebowitz, J. L., "Microscopic computer simulations of directional coarsening in face-centered cubic alloys," *Acta Materialia*, vol. 49, no. 1, pp. 53–63, 2001. 68

[144] Henkelman, G. and Jonsson, H., "A dimer method for finding saddle points on high dimensional potential surfaces using only first derivatives," *Journal of Chemical Physics*, vol. 111, no. 15, pp. 7010–7022, 1999. 68

[145] Fan, Y., Kushima, A., Yip, S. and Yildiz, B., "Mechanism of Void Nucleation and Growth in bcc Fe: Atomistic Simulations at Experimental Time Scales," *Physical Review Letters*, vol. 106, p. 125501, Mar 2011. 68

[146] Djurabekova, F., Domingos, R., Cerchiara, G., Castin, N., Vincent, E. and Malerba, L., "Artificial intelligence applied to atomistic kinetic Monte Carlo simulations in Fe-Cu alloys," *Nuclear Instruments and Methods in Physics Research Section B: Beam Interactions with Materials and Atoms*, vol. 255, no. 1, pp. 8–12, 2007. ¡ce:title¿Computer Simulation of Radiation Effects in Solids¡/ce:title¿ ¡ce:subtitle¿Proceedings of the Eighth International Conference on Computer Simulation of Radiation Effects in Solids (COSIRES 2006)¡/ce:subtitle¿ ¡xocs:full-name¿Computer Simulation of Radiation Effects in Solids¡/xocs:full-name¿. 69

[147] Castin, N., Malerba, L., Bonny, G., Pascuet, M. I. and Hou, M., "Modelling radiation-induced phase changes in binary FeCu and ternary FeCuNi alloys using an artificial intelligence-based atomistic kinetic Monte Carlo approach," *Nuclear Instruments and Methods in Physics Research Section B: Beam Interactions with Materials and Atoms*, vol. 267, no. 18, pp. 3002–3008, 2009. 78

[148] Terentyev, D., Bonny, G., Castin, N., Domain, C., Malerba, L., Olsson, P., Moloddtsov, V. and Pasianot, R. C., "Further development of large-scale atomistic modelling techniques for Fe–Cr alloys," *Journal of Nuclear Materials*, vol. 409, no. 2, pp. 167–175, 2011.

[149] Pascuet, M., Castin, N., Becquart, C. and Malerba, L., "Stability and mobility of Cu-vacancy clusters in Fe-Cu alloys: A computational study based on the use of artificial neural networks for energy barrier calculations," *Journal of Nuclear Materials*, vol. 412, no. 1, pp. 106–115, 2011. 69

[150] Martin, G., "Atomic mobility in Cahn's diffusion model," *Physical Review B*, vol. 41, pp. 2279–2283, Feb 1990. 69

[151] Vincent, E., Becquart, C. S., Pareige, C., Pareige, P. and Domain, C., "Precipitation of the FeCu system: A critical review of atomic kinetic Monte Carlo simulations," *Journal of Nuclear Materials*, vol. 373, pp. 387–401, 2008. 72, 78, 89, 98

[152] Ullmaier, H., ed., *Atomic Defects in Metels*, vol. 25 of *Landolt-Börnstein*. Springer-Verlag, 1991. 75, 79, 122

[153] Press, W. H., Flannery, B. P., Teukolsky, S. A. and Vetterling, W. T., *Numerical Recipes in C: The Art of Scientific Computing*. Cambridge University Press, 2^{nd} ed., 1992. 75

[154] Smith, C. S. and Palmer, E. W., "Precipitation hardening of copper steels," *Transactions of AIME*, vol. 105, pp. 133–168, 1933. 78

[155] Hornbogen, E. and Glenn, R. C., "A metallographic study of precipitation of copper from alpha iron," *Transactions of the Metallurgical Society of AIME*, vol. 218, pp. 1064–1070, 1960. 78

[156] Hornbogen, E., "The role of strain energy during precipitation of copper and gold from alpha iron," *Acta Metallurgica*, vol. 10, no. 5, pp. 525–533, 1962. 78

[157] Goodman, S., Brenner, S. and Low, J., "An fim-atom probe study of the precipitation of copper from lron-1.4 at. pct copper. part ii: Atom probe analyses," *Metallurgical and Materials Transactions B*, vol. 4, pp. 2371–2378, 1973.

[158] Othen, P. J., Jenkins, M. L. and Smith, G. D. W., "High-resolution electron microscopy studies of the structure of Cu precipitates in α-Fe," *Philosophical Magazine A*, vol. 70, no. 1, pp. 1–24, 1994. 78

[159] Pizzini, S., Roberts, K. J., Phythian, W. J., English, C. A. and Greaves, G. N., “A fluorescence EXAFS study of the structure of copper-rich precipitates in Fe-Cu and Fe-Cu-Ni alloys,” *Philosophical Magazine Letters*, vol. 61, no. 4, pp. 223–229, 1990.

[160] Othen, P. J., Jenkins, M. L., Smith, G. D. W. and Phythian, W. J., “Transmission electron microscope investigations of the structure of copper precipitates in thermally-aged Fe-Cu and Fe-Cu-Ni,” *Philosophical Magazine Letters*, vol. 64, no. 6, pp. 383–391, 1991. 78

[161] Duparc, H. A. H., Doole, R. C., Jenkins, M. L. and Barbu, A., “A high-resolution electron microscopy study of copper precipitation in Fe-1.5 wtvol. 71, no. 6, pp. 325–333, 1995. 78, 85

[162] Monzen, R., Jenkins, M. L. and Sutton, A. P., “The bcc-to-9R martensitic transformation of Cu precipitates and the relaxation process of elastic strains in an Fe-Cu alloy,” *Philosophical Magazine A*, vol. 80, no. 3, pp. 711–723, 2000. 78

[163] Schober, M., Eidenberger, E., Staron, P. and Leitner, H., “Critical Consideration of Precipitate Analysis of Fe–1 at.% Cu Using Atom Probe and Small-Angle Neutron Scattering,” *Microscopy and Microanalysis*, vol. 17, pp. 26–33, 2011.

[164] Takahashi, J., Kawakami, K. and Kobayashi, Y., “Consideration of particle-strengthening mechanism of copper-precipitation-strengthened steels by atom probe tomography analysis,” *Materials Science and Engineering: A*, vol. 535, pp. 144–152, February 2012. 78, 85

[165] Ludwig, M., Farkas, D., Pedraza, D. and Schmauder., S., “Embedded atom potential for Fe-Cu interactions and simulations of precipitate-matrix Interfaces,” *Modelling and Simulation in Materials Science and Engineering*, vol. 6, pp. 19–28, 1998. 78

[166] Marian, J., Wirth, B., Odette, G. and Perlado, J., “Cu diffusion in α-Fe: determination of solute diffusivities using atomic-scale simulations,” *Computational Materials Science*, vol. 31, pp. 347–367, 2004.

[167] Soisson, F. and Fu, C. C., “Cu-precipitation kinetics in α-Fe from atomistic simulations: Vacancy-trapping effects and Cu-cluster mobility,” *Physical Review B*, vol. 76, p. 214102, Dec 2007. 78, 89, 102

[168] Urtsev, V., Mirzaev, D., Yakovleva, I., Tereshchenko, N. and Okishev, K., "On the mechanism of nucleation of copper precipitates upon aging of Fe-Cu alloys," *The Physics of Metals and Metallography*, vol. 110, pp. 346–355, 2010. 78

[169] Kittel, C., *Introduction to solid state physics.* Wiley, 1996. 79, 82, 122

[170] Salje, G. and Feller-Kniepmeier, M., "The diffusion and solubility of copper in iron," *Journal of Applied Physics*, vol. 48, no. 5, pp. 1833–1839, 1977. 79, 89, 98, 122

[171] Mehrer, H., ed., *Diffusion in Solid Metals and Alloys*, vol. 26 of *Landolt-Börnstein.* Springer-Verlag, 1991. 79, 122

[172] Athènes, M., Bellon, P. and Martin, G., "Identification of novel diffusion cycles in B2 ordered phases by Monte Carlo simulation," *Philosophical Magazine A*, vol. 76, no. 3, pp. 565–585, 1997. 79, 81, 84, 102

[173] Doyama, M. and Koehler, J. S., "The relation between the formation energy of a vacancy and the nearest neighbor interactions in pure metals and liquid metals," *Acta Metallurgica*, vol. 24, no. 9, pp. 871–879, 1976. 81

[174] Athènes, M. and Bellon, P., "Antisite-assisted diffusion in the L12 ordered structure studied by Monte Carlo simulations," *Philosophical Magazine A*, vol. 79, no. 9, pp. 2243–2257, 1999. 84, 102

[175] Stauffer, D. and Aharony, A., *Introduction to Percolation Theory.* Taylor & Francis, 2nd ed., 2003. 85

[176] Hoshen, J., Stauffer, D., Bishop, G. H., Harrison, R. J. and Quinn, G. D., "Monte carlo experiments on cluster size distribution in percolation," *Journal of Physics A*, vol. 12, no. 8, pp. 1285–1307, 1979. 85

[177] Humphrey, W., Dalke, A. and Schulten, K., "VMD – Visual Molecular Dynamics," *Journal of Molecular Graphics*, vol. 14, pp. 33–38, 1996. 89

[178] Bombac, D. and Kugler, G., "Precipitation in alloys: a kinetic Monte Carlo and Class model study," in *The 19th Annual International Conference on Composites/Nano Engineering (ICCE- 19), Shanghai, China*, pp. 129–130, World journal of engineering, Vol. 8, supp. 1, July 24–30 2011. 110

[179] Sudbrack, C. K., Yoon, K. E., Noebe, R. D. and Seidman, D. N., "Temporal evolution of the nanostructure and phase compositions in a model Ni-Al-Cr alloy," *Acta Materialia*, vol. 54, no. 12, pp. 3199–3210, 2006. 139, 140

[180] Ochial, S., Oya, Y. and Suzuki, T., "Alloying behaviour of Ni3Al, Ni3Ga, Ni3Si and Ni3Ge," *Acta Metallurgica*, vol. 32, no. 2, pp. 289–298, 1984. 140, 144, 148

[181] Chellman, D. J. and Ardell, A. J., "The coarsening of γ' precipitates at large volume fractions," *Acta Metallurgica*, vol. 22, no. 5, pp. 577–588, 1974.

[182] Schmuck, C., Caron, P., Hauet, A. and Blavette, D., "Ordering and precipitation of γ' phase in low supersaturated Ni-Cr-Al model alloy: An atomic scale investigation," *Philosophical Magazine A*, vol. 76, no. 3, pp. 527–542, 1997.

[183] Sudbrack, C. K., Noebe, R. D. and Seidman, D. N., "Direct observations of nucleation in a nondilute multicomponent alloy," *Physical Review B*, vol. 73, p. 212101, Jun 2006. 148

[184] Seidman, D. N., Sudbrack, C. K. and Yoon, K. E., "The use of 3-d atom-probe tomography to study nickel-based superalloys," *JOM Journal of the Minerals, Metals and Materials Society*, vol. 58, pp. 34–39, 2006. 10.1007/BF02748493.

[185] Sudbrack, C. K., Noebe, R. D. and Seidman, D. N., "Compositional pathways and capillary effects during isothermal precipitation in a nondilute Ni-Al-Cr alloy," *Acta Materialia*, vol. 55, no. 1, pp. 119–130, 2007.

[186] Booth-Morrison, C., Weninger, J., Sudbrack, C. K., Mao, Z., Noebe, R. D. and Seidman, D. N., "Effects of solute concentrations on kinetic pathways in Ni-Al-Cr alloys," *Acta Materialia*, vol. 56, no. 14, pp. 3422–3438, 2008. 140, 148

[187] Plati, A., "Modelling of γ' Precipitation in Superalloys," Master's thesis, University of Cambridge, 2003. 140

[188] Wu, K., Chang, Y. A. and Wang, Y., "Simulating interdiffusion microstructures in Ni-Al-Cr diffusion couples: a phase field approach coupled with CALPHAD database," *Scripta Materialia*, vol. 50, no. 8, pp. 1145–1150, 2004. 148

[189] Lu, Y. L., Chen, Z., Wang, Y. X., Zhang, J. and Yang, K., "Phase-field study the effect of elastic strain energy on the incubation period of Ni-Cr-Al

alloys," *Computational Materials Science*, vol. 50, no. 6, pp. 1925–1931, 2011. 140

[190] Working Group Electron Microscopy, *Atlas of Precipitates in Steels.* Materials Comittee Steel Institute VDEh, Verlag Stahleisen, 2003. 140

[191] Bhadeshia, H. K. D. H. and Honeycombe, R. W. K., *Steels Microstructure and Properties.* Butterworth-Heinemann, 3rd ed., 2006. 149

[192] Bhadeshia, H. K. D. H., *Bainite in Steels.* IOM Communications, 2nd ed., 2001. 151

[193] Johnson, R. A., "Interstitials and Vacancies in α Iron," *Physical Review*, vol. 134, pp. A1329–A1336, Jun 1964. 152